The effects of non-Hermiticity and non-linearity on topological phenomena investigated in electric networks

Dissertation zur Erlagung des naturwissenschaftlichen
Doktorgrades der Julius-Maximilians-Universität Würzburg

vorgelegt von

Stefan Michael Imhof
aus Würzburg

Würzburg 2022

Eingereicht am:

bei der Fakultät für Physik und Astronomie

1. Gutachter: AOR Dr. Tobias Kießling

2. Gutachter: Prof. Dr. Ronny Thomale

3. Gutachter:

der Dissertation

Vorsitzender:

1. Prüfer: AOR Dr. Tobias Kießling

2. Prüfer: Prof. Dr. Ronny Thomale

3. Prüfer:

im Promotionskolloquium

Tag des Promotionskolloquiums:

Doktorurkunde ausgehändigt am:

Table of contents

Zusammenfassung **1**

Summary **5**

1 Introduction **9**

2 Connecting tight binding models with electrical circuit networks **13**
2.1 Electric network analysis 13
2.1.1 Nodal analysis 14
2.1.2 The grounded circuit Laplacian 16
2.1.3 Matrix properties of the grounded circuit Laplacian 17
2.2 Translating a tight binding Hamiltonian into an electrical circuit 21
2.2.1 Commonalities and differences in the descriptions of solid state crystals and electrical circuits 21
2.2.2 The Su-Schrieffer-Heeger model 23
2.2.3 Electric circuit representation of the SSH model 27
2.3 Experimental investigation of tight binding Hamiltonians in circuits . . . 33
2.3.1 Imperfections appearing in circuits and their impact on the grounded circuit Laplacian 33
2.3.2 Lock-in technique for phase sensitive detection of AC voltages . . 35
2.3.3 AC impedance measurements 36
2.3.4 Electrical investigation methods and their insights 38
2.3.5 Speeding up the measurement process 44
2.4 Symmetries and their impacts on grounded circuit Laplacians 48

3 Topological phenomena in Hermitian systems **53**
3.1 Edge states and band structure of the SSH model 53
3.1.1 10 unit cell SSH circuit 54
3.1.2 20 unit cell SSH circuit 58
3.1.3 Conclusions 61
3.2 Band structure studies of the honeycomb lattice 62
3.2.1 Graphene-like admittance band structure 62
3.2.2 Carbon nanotube-like admittance band structure 65
3.2.3 Conclusions 66
3.3 Quadrupolar topological insulator 67
3.3.1 Hopping model of the quadrupolar topological insulator 67
3.3.2 Circuit implementation and measurement results 70
3.3.3 Conclusions 72

4 Topological phenomena beyond linear Hermitian systems 73
4.1 $\mathcal{PT}$-SSH model . . . 74
4.1.1 Consequences of $\mathcal{PT}$ symmetry in the SSH model . . . 74
4.1.2 Circuit implementation . . . 77
4.1.3 Experimental investigation . . . 79
4.1.4 Topological protected localized states . . . 80
4.1.5 Theoretical description of the topological states . . . 84
4.1.6 Conclusions . . . 89
4.2 Non-Hermitian, non-reciprocal SSH model . . . 91
4.2.1 Circuit implementation . . . 91
4.2.2 Non-local voltage response as an indicator of mode localization . . . 98
4.2.3 Extended circuit investigation . . . 100
4.2.4 Bulk mode localization: The non-Hermitian skin effect . . . 102
4.2.5 Distorted topological phase transitions . . . 108
4.2.6 Conclusions . . . 111
4.3 Non-linear SSH model . . . 113
4.3.1 Non-linear van der Pol differential equation . . . 113
4.3.2 Circuit implementation . . . 117
4.3.3 1D non-linear topological lattice . . . 120
4.3.4 2D non-linear topological lattice . . . 125
4.3.5 Conclusions . . . 129

5 Conclusion and outlook 131

A Circuit diagrams, board designs and parts lists 137
A.1 $\mathcal{PT}$-SSH circuit . . . 137
A.2 Non-Hermitian, non-reciprocal SSH circuit . . . 139
A.3 Circuit boards for measurement automation . . . 144
A.4 Non-linear SSH circuit . . . 147

Bibliography 151

Acknowledgements 161

Zusammenfassung

Die vorliegende Dissertation befasst sich mit der Realisierung, dem Nachweis und der Charakterisierung topologieinduzierter Zustände und Phänomene in elektrischen Schaltkreisen, den sogenannten „topolectric circuits“, motiviert durch Erkenntnisse aus der Festkörperphysik.
Hierfür wird die Beschreibung eines elektrischen Schaltkreises mithilfe des Knotenpotentialverfahrens verwendet, welches Potentiale und extern zugeführte Ströme von Schaltungen bestehend aus linearen elektrischen Bauelementen kompakt durch eine Admittanzmatrix miteinander verknüpft.
Aufgrund der Äquivalenz eines mithilfe von konzentrierten Bauteilen beschreibbaren Schaltkreises und eines gewichteten Graphens wird der Matrixformalismus in Bezug auf die zugrundeliegende Graphentheorie zum grounded circuit Laplacian Formalismus erweitert. Dieser dient anschließend als Grundlage für die Verknüpfung von elektrischen Schaltkreisen und festkörperphysikalischen Modellsystemen mit topologieinduzierten Phänomenen, die nicht auf der quantenphysikalischen Natur des Festkörpers beruhen. Denn der den Kristall beschreibende, quantenmechanische Hamiltonoperator in tight binding (engl. für: enge Bindung) Näherung kann in ähnlicher Matrixschreibweise dargestellt werden. Dadurch können anschließend durch Messungen im Schaltkreisäquivalent aufgrund der Ähnlichkeit der beiden Matrizen Rückschlüsse auf Elektron-Wellenfunktionen, deren Energien und die elektronische Bandstruktur des Festkörpers gezogen werden.

Weiterhin werden die verschiedenen Messmethoden zur Untersuchung der Schaltkreise, die zugehörigen Annahmen und die daraus folgernden Rückschlüsse auf die Admittanzmatrix, ihre Eigenwerte und Eigenvektoren sowie die aus einem periodischen Schaltkreis ableitbare Admittanzbandstruktur vorgestellt.

Um die oben beschriebenen Parallelen zwischen Festkörperkristall und Schaltkreis testen zu können, werden drei lineare hermitesche Festkörpersysteme in Schaltkreise übertragen und untersucht. Dabei werden obendrein allgemeine Vorschläge für ein solches Schaltungsdesign erarbeitet, mit dem Ziel ungewollte Kopplungseffekte und parasitäre Admittanzen im Schaltkreis minimieren zu können.
Während der Studie des Su-Schrieffer-Heeger (SSH) Modells lassen sich dabei die räumliche Struktur eines topologischen Randzustands, seine energetische Lage innerhalb der Bandlücke des Festkörpers, die Bandstruktur und der topologische Phasenübergang in Verbindung mit dem Schließen der Bandlücke anhand des Schaltkreisäquivalents ermitteln.
Durch die Bestimmung der Admittanzbandstruktur einer elektrischen Schaltung basierend auf einem Honigwabengitter, welches als vereinfachtes Modell des Werkstoffs Graphen angesehen werden kann, wird weiterhin die Äquivalenz zwischen Schaltung und Festkörper auch für größere Systeme in höheren Dimensionen bestätigt. Zusätzlich wird

die Flexibilität der Plattform ausgenutzt, um die Periodizität jener Schaltung in einer Dimension aufzuheben. Damit können anschließend die Bandstrukturen eindimensional periodischer Honigwabengitter mit verschiedenen Terminierungen am nicht-periodischen Rand gemessen werden. Dies entspricht der Untersuchung von Kohlenstoffnanoröhrchen im Festkörperbild.
Um auch die Relevanz der Untersuchung topologischer Phänomene in elektrischen Schaltungen für die aktuelle Forschung darlegen zu können, wird mithilfe eines elektrischen Schaltkreises ein festkörperphysikalisches Konzept für topologische Isolatoren höherer Ordnung untersucht und ein Modell eines quadrupolaren topologischen Isolators, also ein zweidimensionales System mit topologisch lokalisierten Moden in dessen Ecken, experimentell realisiert und die Existenz einer solchen Mode nachgewiesen.

Die besonderen Vorteile der experimentellen Untersuchung nicht ausschließlich topologischer Phänomene mit Hilfe von elektrischen Schaltungen zeigen sich bei der Realisierung nichthermitescher und nichtlinearer Modelle, auch wenn in diesen die Stabilität des Schaltkreises, welche zuvor durch Hermitizität und daraus resultierenden reellen Eigenwerten der Admittanzmatrix inhärent gegeben war, durch vorherige Betrachtung und eventuelle Kompensation sichergestellt werden muss.
Durch die Erforschung nichthermitescher und nichtlinearer Physik erweitern sich die potenziellen Anknüpfpunkte dieser Forschung vom ursprünglich festkörperphysikalischen Kontext auf eine Vielzahl an sowohl klassischen Phänomenen aus Bereichen der Optik, Biologie, aktiver Materie etc., als auch quantenmechanischen Sachverhalten aus dem Gebiet offener Quantensysteme.
Für die Untersuchung jener Themengebiete innerhalb dieser Arbeiten wird das bereits genannte SSH Modell auf unterschiedliche Arten erweitert, um verschiedene Aspekte und Fragestellungen im Zusammenhang mit Nichthermitizität und Nichtlinearität betrachten zu können.

Mithilfe der $\mathcal{PT}$-symmetrischen Erweiterung des SSH Schaltkreises durch lokale Gewinn- und Verlustterme können die Bandstrukturen des Modells in allen drei Bereichen des Parameterraums, im $\mathcal{PT}$-symmetrischen, $\mathcal{PT}$-gebrochenen und $\mathcal{APT}$-symmetrischen Regime, gemessen und das Schließen der komplexen Bandstruktur an den exceptional points (engl. für: Ausnahmepunkte), an denen die definierende Matrix eine Singularität aufweist, festgestellt werden.
Außerdem wird die Existenz von topologischen Randzuständen unabhängig von Parameteränderungen und damit verbundenem Schließen und Öffnen der komplexen Bandstruktur gezeigt. Im Gegensatz dazu kann das Verschwinden und Wiederkehren eines topologischen Defektzustandes während derselben Parameteränderung nachgewiesen werden. Demzufolge ist die bulk-boundary correspondence (engl. für: Volumen-Rand Korrespondenz), wie sie aus hermiteschen Systemen bekannt ist, in $\mathcal{PT}$-symmetrischen Systemen nur eingeschränkt anwendbar.

Darüber hinaus wird durch Messungen an einem SSH Modell mit gleichzeitiger Brechung von Hermitizität und Reziprozität durch ein aktives Schaltelement mit richtungsabhängiger positiver und negativer Impedanz neben lokalisierten topologischen Randmoden, auch die Lokalisation von allen weiteren Moden im System an einem Rand, entsprechend

dem theoretischen Konzept des nichthermiteschen Skin-Effekts (von engl. *skin* für Haut), experimentell nachgewiesen.
Dank der einfachen experimentellen Manipulierbarkeit jeder Admittanz des Schaltkreises kann gezeigt werden, dass sich während der experimentellen Verkleinerung einer einzelnen Admittanz im periodischen Schaltkreis bis hin zu null die Volumenmoden immer stärker auf einer der beiden Seiten um diese Stelle konzentrieren. Zusätzlich geht die Lage der Admittanzeigenwerte von geschlossenen Kurven, die einen nichtleeren Bereich einschließen (periodische Schaltung), zu offenen Kurven (offene Schaltung) in der komplexen Ebene über, was in hermiteschen oder reziproken Systemen nicht der Fall sein kann, da deren periodischen Spektren bereits auf offenen Kurven liegen.
Des Weiteren wird das Konzept komplexer Wellenvektoren zur Beschreibung von lokalisierten Volumenmoden experimentell für verschiedene Lokalisationslängen bestätigt. Durch unterschiedliche Skalierung der Admittanzen in Abhängigkeit der Messfrequenz können unterschiedliche Verhältnisse zwischen reziproker und nichtreziproker Kopplung im SSH-Modell realisiert und die Stärke der Lokalisation der Volumenmoden sowie deren Position variiert werden.
Aus der unterschiedlichen Lage der Admittanzeigenwerte von Volumenmoden im periodischen und offenen Schaltkreis und den zugehörigen Parameterwerten für das Erscheinen und Verschwinden topologischer Randmoden werden andere Zusammenhänge zwischen topologischen Zuständen und Volumeneigenschaften des Systems festgestellt, als sie durch die Volumen-Rand Korrespondenz im hermiteschen Fall erwartbar wären.

Abschließend wird neben der Hermitizität auch die Linearität durch das Einfügen eines nichtlinearen, resistiven Schaltungselements in das SSH Modell gebrochen. Dadurch kann der auf linearen Gleichungssystemen beruhende grounded circuit Laplacian Formalismus nicht mehr auf den Schaltkreis, welcher nun durch ein gekoppeltes, nichtlineares Differentialgleichungssystem beschrieben werden muss, angewandt werden. Durch schwache Nichtlinearität und stark unterschiedliche Kopplungen innerhalb und zwischen den SSH Einheitszellen kann das elektrische Verhalten des Systems separiert und einerseits lokal durch die zugrundeliegende, nichtlineare Van der Pol Differentialgleichung, andererseits global durch die Topologie, festgelegt durch die Kopplungen im System, beschrieben werden.
Als Resultat können selbsterregende und selbsterhaltende Moden im Schaltkreis ermittelt werden, welche an den Rändern als topologische Randmoden mit höherfrequenter, sinusförmiger Oszillation auftreten, wohingegen im Inneren des Modells für die stark gekoppelten Knoten phasensynchrone, niederfrequente Relaxationsoszillationen auftreten. Es kann außerdem nachgewiesen werden, dass diese Art der Beschreibung auch im Zweidimensionalen anwendbar bleibt und dass die Präsenz der topologischen Randmoden auch durch Anwesenheit von Rand- oder Volumendefekten nicht beeinträchtigt wird.

Summary

The presented thesis deals with the realization, proof and characterization of topology-induced states and phenomena via electric circuits - termed topolectric circuits in this context - motivated by scientific insights in solid state physics.
For this purpose the electric circuit is described using nodal analysis, enabling the connection of voltages and external input currents of the circuit by an admittance matrix. Due to the equivalence of a circuit with lumped components and a weighted graph, the matrix formalism is transferred to the terminology of graph theory and termed grounded circuit Laplacian formalism. This formalism subsequently serves as a basis for the linkage between electrical circuits and solid state models showing topology-induced phenomena that are not based on the quantum nature of the solid. Parallels can be drawn because of the similarities to the matrix representation of the crystal's Hamilton operator in thight-binding approximation. Thus, by measurements in a circuit with similar matrix description, insights about electron wave functions, their energies and the electronic band structure of the solid can be found.

The used electrical measurement methods, the related assumptions and the resulting insights on the admittance matrix, its eigenvalues and eigenvectors and the admittance band structure, determined using a periodic version of the circuit, are presented.

In order to test these parallels, three linear Hermitian solid state systems are transferred and investigated in circuits. By doing so, general suggestions on designing those types of circuits are worked out with the aim of minimizing unwanted coupling effects and parasitic admittances in the circuit.
During the study of the Su-Schrieffer-Heeger (SSH) model, the spatial structure of a topological edge state, its energetic location within the band gap of the solid, the model's band structure and the topological phase transition associated with the closing of the band gap can be determined based on the circuit equivalent.
By measuring the admittance band structure of an electric circuit with the connectivity of a honeycomb lattice, which can be considered as a simplified model of graphene, the parallels between circuit and solid can be approved for even lager systems in higher dimensions. On top of that, the flexibility of the circuit platform is exploited to adapt the two dimensional periodic circuit to have periodicity in only one dimension. Subsequently, admittance band structures for different edge terminations can be recorded equaling the electronic band structures of carbon nanotubes.
To be able to also demonstrate the relevance of the investigation of topological phenomena in electric circuits to current research, a solid state theory predicting higher order topological insulators is explored. Therefore, the existence of a localized topological corner mode in a two-dimensional electrical system, i.e. a quadrupolar topological insulator, is demonstrated.

The particular advantages of the experimental investigation of non-exclusively topological phenomena by means of electric circuits come to light in the realization of non-Hermitian and non-linear models, even if the stability of those kinds of circuits must be ensured by prior considerations and compensation, which was inherently given by real eigenvalues of the admittance matrix due to Hermiticity before.

By studying non-Hermitian and non-linear physics, the points of contact with other research topics expand from the original solid state context to a variety of both, classical phenomena from optics, biology, active matter, etc., and quantum mechanical aspects arising in open quantum systems.
For the investigation of those topics within this work, the previously mentioned SSH model is extended in different ways to be able to consider several aspects and issues related to non-Hermiticity and non-linearity.

Using a $\mathcal{PT}$ symmetric extension of the SSH circuit introduced by local gain and loss terms, the model's band structure in all three regions of its parameter space, in the $\mathcal{PT}$ symmetric, the $\mathcal{PT}$ broken and the $\mathcal{APT}$ symmetric regime, together with the closing of the complex band structure at exceptional points, where the defining matrix is singular, can be determined.
Moreover, the existence of topological boundary states is shown independent from parameter changes, which lead to closings and re-openings of the complex band structure. In contrast, the disappearance and recurrence of a topological defect state can be found during the same parameter change. Consequently, bulk-boundary correspondence, as known from Hermitian systems, has limited applicability in $\mathcal{PT}$ symmetric systems.

Furthermore, measurements on an SSH model with simultaneous breaking of Hermiticity and reciprocity implemented by an active circuit element with direction-dependent positive and negative impedance are performed. Hereby a localization of all bulk modes together with the localization of topological protected edge modes can be shown experimentally. This feature was previously predicted in theory and termed the non-Hermitian skin effect.
Thanks to the easy experimental manipulability of each circuit admittance, it can be shown that during the reduction of a single admittance of the periodic chain, the bulk modes localize more and more on one of the sides next to this admittance. In addition, the location of the admittance eigenvalues in the complex plane swaps from closed curves with non-zero internal area (periodic circuit) to open curves (open circuit), which cannot be the case in Hermitian or reciprocal systems because their periodic spectra are already located on open curves.
Moreover, the complex wave vector concept used to describe the localized bulk modes is experimentally confirmed for different localization lengths. Due to different scaling of the admittances as a function of measurement frequency, various ratios between reciprocal and non-reciprocal hoppings can be realized and the strength of the localization of the bulk modes as well as their position can be changed.
Due to the distinct admittance eigenvalues for a periodic and open circuit and the related parameter values needed to achieve the (dis-)appearance of the topological states, the

relations between topological states and bulk properties are found to deviate from the bulk-boundary correspondence, which would be expected in the Hermitian case.

Finally, linearity is also broken in addition to Hermiticity by inserting a non-linear resistive circuit element into the SSH model. As a result, the grounded circuit Laplacian formalism based on systems of linear equations can no longer be used to describe the circuit, which now is characterized by a system of coupled non-linear differential equations. Due to the operation with weak non-linearity and strongly differing intra- and intercell couplings the electrical behaviour of this SSH model can be separated and described locally by the underlying non-linear van der Pol differential equation, and globally by the topology determined by the system's couplings.
This results in self-excited and self-sustained modes in the circuit, which appear as high frequency sinusoidal oscillating topological edge modes at the boundaries, whereas phase-synchronous low frequency relaxation oscillations occur in the interior of the model for the strongly coupled nodes.
Furthermore, this description is proven to remain valid in two dimensions and, moreover, the existence of topological boundary modes can also be verified even under the presence of boundary or volume defects.

1 Introduction

The mathematical concept of topology which we will encounter in this work, is a research topic dealing with properties of geometric objects that do not depend on the exact shape of the objects and are preserved under continuous deformations.
It made its way into solid state physics in the 1980s when von Klitzing found a quantization in Hall resistance measured in a two dimensional electron gas formed in a MOSFET (metal oxide semiconductor field effect transistor) device at low temperatures and high magnetic fields [1]. The magnetic field forces the electrons on quantized cyclotron orbits with equidistant energy values, the so called Landau levels [2]. Each Landau level is extensively degenerate and the number of states in one level is proportional to the applied magnetic field. Because of disorder in the sample the bulk states of the Landau levels are localized, and only the chiral edge states contribute to the conductivity. With an increasing magnetic field the number of filled Landau levels decreases step by step, leading to decreased Hall conductivity. Due to the energetic gaps between them the change in the number of filled levels is discretized and results in quantized Hall plateaus. The origin of this quantization phenomenon could be mapped back onto topological properties of the underlying parameter space by Thouless, Kohmoto, Nightingale and den Nijs (TKNN) [3]. When the wave vector $\vec{k}$ is varied sufficiently slow and no energy level crossings take place, the adiabatic theorem [4] ensures that the system will not change its energetic eigenstate, which only picks up a phase. This seems to be irrelevant at first glance because only the absolute square of an eigenstate is measurable in a quantum mechanical system. But when a closed curve in parameter space is passed through, the state reaches its initial configuration and an acquired phase difference due to the topology of the parameter space, called the geometric or Berry phase [5], is quantized and can have physical significance.
For a two dimensional model, as it is the case in the quantum Hall effect, the unit cell in momentum space, the Brillouin zone, forms a torus and can therefore lead to nontrivial Berry phases. In such a periodic model an integer-valued topological invariant, the TKNN invariant, can be calculated from the Berry curvature, which is a gauge field associated with the Berry phase. This invariant connects the existence of localized edge modes in a finite sample directly to the geometric properties of a periodic model for the bulk and therefore is a prime example for the bulk-boundary correspondence in topological systems.
Based on these first findings, many other discoveries regarding solid state phenomena in combination with topological effects have been made. Additional plateaus in the Hall conductance for fractional numbers of the Von Klitzing constance $R_K = e^2/h$ were found [6] and theoretically explained by many-particle states [7–9]. Further progress was made by the discovery of the quantum anomalous Hall effect [10, 11], where an internal magnetization and spin-orbit coupling lead to a spin-polarized edge state and the quantum spin Hall effect [12–14] with spin-orbit coupling resulting in a pair of

counter-propagating edge states with opposite spin polarization. Together with a lot of further research these milestones have paved the rapidly proceeding way of the field of topological insulators [15, 16] in condensed matter physics with possible applications in photo-detectors, magnetic devices, transistors, lasers [17] as well as in the fields of spintronics [18] and quantum computing [19].

Retrospectively it is clear that quantization effects due to topological properties are not restricted to solid state materials or quantum mechanical systems at all, because the Berry phase does not depend on the non-commutativity of the quantum mechanical Hilbert space, but rather depends on the evolution of states in the underlying parameter space. But it took almost three decades until Haldane and Raghu came up with an idea to translate the quantum Hall edge states into magneto-optic photonic crystals to achieve unidirectional wave guidance [20]. The proposed optical metamaterial obeys the Faraday effect and is based on a solid state model, which was set up earlier by Haldane [10] to host the quantum anomalous Hall effect.
Building on this transfer, topological modes where found and investigated in a plethora of other material classes. Besides the wide field of topological photonics [21–25] with results such as robust optical delay lines [26], optical insulators [27], topological insulator lasers [28, 29] etc. topological concepts have also been investigated in ultracold atomic gases [30–33], acoustic [34–36] and mechanical metamaterials [37–40], in engineered microsystems hosting polaritons [41–43] or superconducting qubits [44, 45] and electrical circuit networks [46, 47], to list the most prominent examples.
The parallels between topological concepts in solid state physics and electric circuit networks, which are the platform of choice in the present work, may not be as evident as in other metamaterials, which are quantum mechanical systems or resemble the underlying Schrödinger equations. But the electric circuit platform stands out in accessibility and tunability, industrial-grade manufacturing processes and an extremely versatile range of commercially available circuit components. With these advantages it provides a powerful tool to investigate the impact of topology on translation invariant lattices on an experimental basis.
Working in the low frequency limit allows us to describe the circuit's impedances in a lumped element model, i.e. all impedance contributions are localized at the circuit components, so that the circuit's lines and spacial arrangement do not alter the model. This leads to an unparalleled flexibility in extending and rearranging a circuit network, which also allows to set the boundary conditions at will. The ability to switch between periodic and open boundary conditions is a key ingredient for investigating the bulk-boundary correspondence in topological systems. Moreover, any number of model dimensions, as well as complex and long range connections, can be introduced.

Nowadays, new challenges in research on topological effects lie in the investigation of models involving non-Hermiticity and non-linearity. They have to be considered when thinking about open quantum systems [48], but also lead to essential insights in metamaterial research such as unidirectional invisibility [49], coherent perfect absorbers [50], enhanced sensitivity [51], non-reciprocal light propagation [52], loss-induced transparency [53] in photonics, the investigation of friction in mechanical metamaterials [54], or a better understanding of biological localization processes [55] and learning

dynamics in neural networks [56].
Here another important advantage of investigating non-Hermitian models in an electric equivalent comes into play: the complex nature of admittance. Non-Hermitian models, which in general contain complex hopping elements, therefore can be readily implemented in an electric circuit. In other metamaterials it is often easy to introduce loss terms, but to add gain to the system an external energy input is needed, which often is hard to realize and can also alter the Hermitian couplings in the network. On the other hand, in circuits which can be described by a lumped element model an active subcircuit can be added to shift the phase of a complex admittance at will. Due to the flexibility in spacial arrangement of the circuit elements the joint system can be made to not alter the Hermitian couplings. Although active circuit elements have the ability to drive the network unstable, a way to pre-check and stabilize the theoretical circuit model without altering the underlying physical phenomena exists [57]. In addition, a variety of circuit elements with non-linear current-voltage relation and the ability of constructing arbitrary current-voltage relations using active circuitry also allow the straight forward investigation of non-linear models. Therefore, electric circuits serve as an ideal experimental test bed to address currently unsolved questions regarding topological phenomena beyond Hermitian systems.

To combine topological phenomena with non-Hermitian physics on the versatile topolectrical circuit platform [68] in this thesis, we first introduce the grounded circuit Laplacian matrix formalism in chapter 2, based on nodal analysis, a method known from electrical engineering to analyze admittances of linear circuits, and the Laplacian matrix known from graph theory describing the connectivity of a graph. After that, we briefly elaborate on the matrix properties of the grounded circuit Laplacian and how they are used to translate topological phenomena found in solid state physics into electric circuit networks. Based on an instructive example, the Su-Schrieffer-Heeger (SSH) model, we explain in detail the development of an electric circuit network resembling this solid state model. We furthermore describe the experimental investigation of such a circuit, the measurement technique, the investigation methods and the insights that can be found with them. We close this chapter with a quick overview of several symmetries known from solid state physics and their effects on an electrical circuit.
In chapter 3 we start with the experimental investigation of three Hermitian circuits and work out some general design rules for topolectrical circuits. First, we find topological edge modes and the band structure of the SSH model (sec. 3.1, published in [68]), then we measure the band structure equivalent of solid state models for graphene and carbon nanotubes (sec. 3.2, published in [59]), and finally we can prove a theoretical prediction [60] of higher order topological states in a circuit equaling a so called quadrupolar topological insulator (sec. 3.3, published in [61]).
Equipped with the measurement principles, which were validated in the previous chapter, we are able to address unanswered questions in non-Hermitian physics in chapter 4. We begin our study of non-Hermitian systems with a $\mathcal{PT}$-symmetric extension of the SSH model (sec. 4.1, published in [62]). We investigate differences between topological edge and defect states and their contradictions to the Hermitian bulk-boundary correspondence, the complex-valued band structure, the appearance of exceptional points, i.e. gap closings in the complex band structure, etc.

Subsequently, we use a negative impedance converter to also break reciprocity in the SSH model and obtain an extensive mode localization, which is termed the non-Hermitian skin effect (sec. 4.2, published in [63]). We directly observe the process of bulk mode localization by incremental switching between open and periodic boundary conditions, measure and explain the spectral flow of the eigenvalues in the complex plane, find distorted topological phase transitions and derive a generalized bulk-boundary correspondence for those systems.
Lastly, we add non-linearity to our model system, which prevents the application of linear algebra, the basis of the grounded circuit Laplacian, and leads to coupled non-linear van der Pol differential equations [64] (sec. 4.3, published in [65]). Therefore, we have to investigate the explicit time dependent behaviour and frequency components of the measurement signals and find self-activated and self-sustained topologically protected sinusoidal oscillations at the edges of the system, while strongly coupled bulk pairs show low frequency in-phase relaxation oscillations. On top of that, this joint effort of non-linear and topological features can be validated in higher dimensionality and in the presence of lattice defects.
In chapter 5 we summarize the results that our experimental investigation of electrical circuits contributes to the research on topological and non-Hermitian phenomena. We further point out several research frontiers where topolectrical circuits can be used to gain new insights and to open up new fields of application. On top of that we elaborate on additional investigation methods and potential applications of circuits exhibiting topologically induced edge modes.
Drawings of the circuit diagrams, board designs and parts lists of the non-Hermitian circuits can be found in appendix A and for the Hermitian circuits these can be found in the appendix of the author's master thesis [66].

2 Connecting tight binding models with electrical circuit networks

Due to the focus on the experimental implementation and investigation of the so called topolectrical circuits in this thesis, we start the elaborations on the connections between solid state physics and circuits from the electrical point of view. Circuit analysis is a common topic in most textbooks dealing with electrical engineering and will be discussed only in a short manner. The explanation of the fundamental electrical concepts are based on the educational book *Introduction to Electrical Circuit Analysis* [67], whereas the Grounded Circuit Laplacian formalism (see section 2.1.2), used to investigate tight binding Hamiltonians by electrical measurements of a circuit, was introduced in [68]. Another experimental introduction with focus on resonant circuits can be found in the author's master thesis [66].

2.1 Electric network analysis

The electric circuits investigated in this work will be described in the lumped element model, meaning that the electrical properties of the circuits are concentrated in their circuit elements. The networks are analyzed in terms of voltages V at the circuit nodes and currents I flowing between them. In this context a node describes an interconnection of perfectly conducting traces and therefore a region of equivalent potential.
The voltage, as it is defined as the difference of the electric potential of two points (more descriptive: the work applied on a particle of unit charge by moving it from one to the other point), is a relative quantity. Consequently, for a unique definition of voltages a reference potential has to be defined, which will be called ground or ground potential in the following.
The nodes in the network are connected by the circuit elements, which are characterized by their current voltage relation. In linear circuits this relation is given by the corresponding resistances/impedances $Z := V/I$ or conductances/admittances $Y := Z^{-1}$ for direct current (DC)/alternating current (AC).
The distribution of current and voltage in the circuit is determined by Kirchhoff's current and voltage law

$$\sum_{n=1}^{N} I_n = 0 \qquad\qquad \sum_{n=1}^{N} V_n = 0 \tag{2.1}$$

stating that the sum of all currents I_n flowing through a node and all voltages V_n applied to the elements on a loop of the circuit add up to zero, i.e. charge is conserved in the network and there is no electromagnetic coupling (internally and externally) other than described by the circuit elements.

2.1.1 Nodal analysis

To analyze complex electrical networks we are going to use a common tool in electrical engineering called nodal analysis. In this section the circuits are assumed to be reciprocal, i.e. the current entering at one side of a circuit element equals the current leaving at the other side (see section 2.4). The procedure will be explained based on the circuit in Fig. 2.1, a simple example that cannot be analyzed by combing serial and parallel circuits anymore.

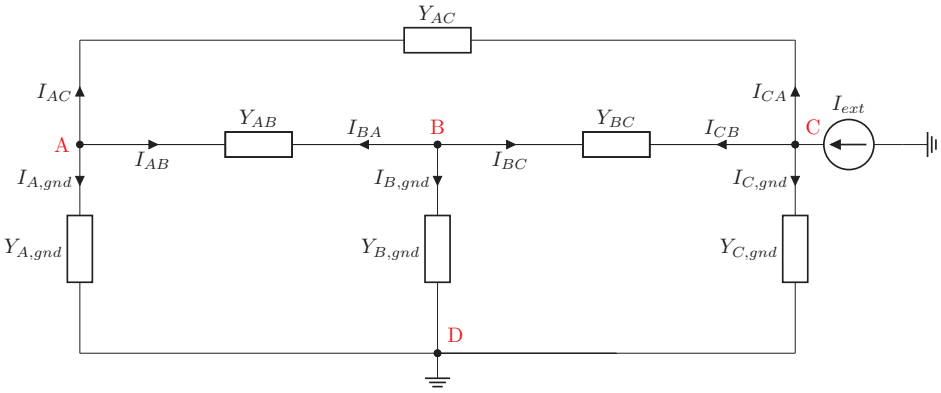

Figure 2.1: An electrical circuit network containing four nodes (red letters) connected by six circuit elements which are described by their admittances Y. Node D is chosen as the circuit ground. Node C is fed by an external current source.

First of all, one node has to be chosen as a circuit ground. To keep the circuit analysis simple, a node with multiple connections should be used (in our case we pick node D). In the following, a current flowing from node A to node B is labeled I_{AB}, the admittances connecting these nodes are labeled Y_{AB} accordingly. Due to reciprocity ($I_{AB} = -I_{BA}$) $Y_{AB} = Y_{BA}$ applies. The voltage of a node A measured with respect to ground is denoted by V_A.
The main framework in nodal analysis is to set up the equations for every node (except ground) determined by Kirchhoff's current law:

$$\begin{aligned} I_{A,ext} &= I_{A,gnd} + I_{AB} + I_{AC} = 0 \\ I_{B,ext} &= I_{BA} + I_{B,gnd} + I_{BC} = 0 \\ I_{C,ext} &= I_{CA} + I_{CB} + I_{C,gnd} = I_{ext} \end{aligned} \tag{2.2}$$

After that all internal currents will be expressed in terms of the admittances connecting the nodes and the corresponding voltages.

$$\begin{aligned} I_{A,ext} &= Y_{A,gnd} \cdot V_A + Y_{AB} \cdot (V_A - V_B) + Y_{AC} \cdot (V_A - V_C) = 0 \\ I_{B,ext} &= Y_{AB} \cdot (V_B - V_A) + Y_{B,gnd} \cdot V_B + Y_{BC} \cdot (V_B - V_C) = 0 \\ I_{C,ext} &= Y_{AC} \cdot (V_C - V_A) + Y_{BC} \cdot (V_C - V_B) + Y_{C,gnd} \cdot V_c = I_{ext} \end{aligned} \tag{2.3}$$

This set of equations can be combined into a matrix equation connecting the node voltages and the external input currents via the network admittances.

$$\vec{I}_{ext} \;=\; \boldsymbol{Y}\vec{V} \tag{2.4}$$

$$\begin{pmatrix} 0 \\ 0 \\ I_{ext} \end{pmatrix} = \begin{pmatrix} Y_{A,gnd}+Y_{AB}+Y_{AC} & -Y_{AB} & -Y_{AC} \\ -Y_{AB} & Y_{B,gnd}+Y_{AB}+Y_{BC} & -Y_{BC} \\ -Y_{AC} & -Y_{BC} & Y_{C,gnd}+Y_{AC}+Y_{BC} \end{pmatrix} \cdot \begin{pmatrix} V_A \\ V_B \\ V_C \end{pmatrix} \tag{2.5}$$

By inverting the admittance matrix ($\boldsymbol{G} := \boldsymbol{Y}^{-1}$) the voltages of all nodes caused by the external current input can be determined. The internal currents can be calculated by using the definition of the admittances $I_{AB} = (V_A - V_B) \cdot Y_{AB}$.
Assuming a current I_{ext} entering at A and leaving at B, the two-point impedance Z_{AB} between the two nodes can be defined as

$$\begin{aligned} Z_{A,B} \;&=\; \frac{V_A - V_B}{I_{ext}} \;=\; \frac{G_{AA}\cdot I_{ext} - G_{AB}\cdot I_{ext} - (G_{BA}\cdot I_{ext} - G_{BB}\cdot I_{ext})}{I_{ext}} \\ &=\; G_{AA} + G_{BB} - G_{AB} - G_{BA}\,. \end{aligned} \tag{2.6}$$

Here the two capital indices of G indicate row and column in the admittance matrix.
For linear circuit analysis using alternating currents (AC) the relations between voltage and current are expressed by a set of linear (differential) equations.
When using only resistive elements (resistance R), voltage and current are related at any time by Ohm's law:

$$V_R(t) \;=\; R \cdot I_R(t) \tag{2.7}$$

In contrast, capacitive (capacitance C) or inductive elements (inductance L) relate the current (voltage) with the voltage (current) derivative according to Maxwell's equations giving rise of differential equations in time:

$$I_C(t) \;=\; C \cdot \frac{\mathrm{d}V_C(t)}{\mathrm{d}t} \qquad V_L(t) \;=\; L \cdot \frac{\mathrm{d}I_L(t)}{\mathrm{d}t} \tag{2.8}$$

Each circuit made of capacitive, inductive and resistive elements will thus lead to a set of ordinary second order differential equations with constant coefficients which can be written as

$$\boldsymbol{\Gamma}\,\frac{\mathrm{d}^2\vec{V}(t)}{\mathrm{d}t^2} \;+\; \boldsymbol{\Sigma}\,\frac{\mathrm{d}\vec{V}(t)}{\mathrm{d}t} \;+\; \boldsymbol{\Lambda}\,\vec{V}(t) \;=\; \frac{\mathrm{d}\vec{I}(t)}{\mathrm{d}t}\,. \tag{2.9}$$

Here the matrices $\boldsymbol{\Gamma}$, $\boldsymbol{\Sigma}$ and $\boldsymbol{\Lambda}$ represent the capacitances, resistors and inductors connecting the voltage and current vectors of length N for a circuit with $N+1$ nodes due to the additional ground node.
From the experimental point of view there are two main ways to investigate these systems: Either using pulse excitation and observing the system's dynamics or, as it is used most time in this work, by a continuous excitation with a time-harmonic function to study the steady state solution of the circuit by using the impedance/admittance definition. Therefore, a Fourier transformation is applied

$$I_C(\omega) \;=\; \underbrace{i\omega C}_{Y_C}\cdot V_C(\omega) \qquad I_R(\omega) \;=\; \underbrace{\frac{1}{R}}_{Y_R}\cdot V_R(\omega) \qquad I_L(\omega) \;=\; \underbrace{\frac{1}{i\omega L}}_{Y_L}\cdot V_L(\omega) \tag{2.10}$$

resulting in a set of algebraic equations

$$i\omega\mathbf{\Gamma}\,\vec{V}(\omega) \,+\, \mathbf{\Sigma}\,\vec{V}(\omega) \,+\, \frac{1}{i\omega}\mathbf{\Lambda}\,\vec{V}(\omega) \,=\, \vec{I}(\omega)\,. \tag{2.11}$$

2.1.2 The grounded circuit Laplacian

In graph theory the Laplacian matrix $\boldsymbol{L}$ describing the connectivity of a graph can be identified with a finite and discrete version of the Laplace operator which appears in a lot of differential equations describing a plethora of physical models. It is defined by $\boldsymbol{L} \,=\, \boldsymbol{D}_L - \boldsymbol{A}_L$ with the degree matrix $\boldsymbol{D}_L$ counting the number of edges connected to each vertex and the adjacency matrix $\boldsymbol{A}_L$ representing the connections between the vertices.
In the lumped-element model a circuit represents a weighted graph. Consequently, the grounded circuit Laplacian $\boldsymbol{J}$, introduced in [68] and explained in detail in [69–71], connects the admittance matrix $\boldsymbol{Y}$ with the Laplacian matrix $\boldsymbol{L}$. It was first set up to investigate topological features of tight-binding models in condensed matter physics. But it can be used to examine the properties of any set of complex-valued linear circuit equations.
$\boldsymbol{J}$ equals the admittance matrix $\boldsymbol{Y}$ known from nodal analysis introduced in section 2.1.1 and is split into three different matrices:

$$\boldsymbol{Y} \,=:\, \boldsymbol{J} \,=\, (\boldsymbol{D} - \boldsymbol{C}) + \boldsymbol{W} \tag{2.12}$$

The total node conductance matrix $\boldsymbol{D}$ corresponds to the degree matrix $\boldsymbol{D}_L$ from graph theory and contains the sum of all admittances connected to the node on the matrix diagonal. In the adjacency matrix $\boldsymbol{C}$ the admittance Y_{ij} of the connection from node i to j is filled in, similar to the connections of a graph's vertices in the adjacency matrix $\boldsymbol{A}_L$. The ground matrix $\boldsymbol{W}$ is a diagonal matrix and lists the admittances connected to ground.
To make the link to nodal analysis somewhat clearer we devise the matrices in terms of the general current voltage relation:

$$\begin{aligned} I_n \,&=\, \sum_{m=1}^{N} Y_{n,m}\,(V_n - V_m) + Y_{n,0}V_n \\ &=\, \sum_{m=1}^{N} \left(\sum_{k=1}^{N} Y_{n,k}\delta_{n,m} - Y_{n,m} + Y_{n,0}\delta_{n,m} \right) V_m \\ &=\, \sum_{m=1}^{N} \left(D_{n,m} - C_{n,m} + W_{n,m}\right) V_m \end{aligned} \tag{2.13}$$

According to the Green's function defining the inverse of a linear differential operator the inverse matrix of the grounded circuit Laplacian is called Green's matrix $\boldsymbol{G}$. Remember that a matrix $\boldsymbol{A}$ is invertible if and only if its determinant $\det \boldsymbol{A} \,=\, \prod_{i=1}^{n} \lambda_i$ is not zero, which corresponds to having only non-zero eigenvalues λ. The theoretical models we are investigating in this work are expected to host topological modes with eigenvalues equal to zero, making the Green's matrix non-invertible. Because of the finite size of our

experimental models, component tolerances and parasitics the eigenvalues will never be exactly zero, keeping the Green's matrix invertible.

2.1.3 Matrix properties of the grounded circuit Laplacian

The matrix representation of the circuit enables us not only to calculate the voltages caused by an external current or to figure out the impedances between two points in a compact way, but provides us with the tools of linear algebra to describe the circuit. We get a deep insight into the behavior of the circuit by calculating the eigendecomposition of the grounded circuit Laplacian. Therefore, the investigated square matrix $\boldsymbol{J}$ must be transformable into a diagonal matrix $\boldsymbol{\Lambda}$:

$$\boldsymbol{\Lambda} \;=\; \boldsymbol{R}^{-1}\boldsymbol{J}\boldsymbol{R} \tag{2.14}$$

To find the matrix $\boldsymbol{R}$ and its inverse $\boldsymbol{R}^{-1}$, which transform the grounded circuit Laplacian into a diagonal matrix, we think about the definition of left $\vec{\phi}_n^{\dagger}$ and right $\vec{\psi}_n$ eigenvectors

$$\vec{\phi}_n^{\dagger}\boldsymbol{J} \;=\; j_n\vec{\phi}_n^{\dagger} \qquad \boldsymbol{J}\vec{\psi}_n \;=\; j_n\vec{\psi}_n \;, \tag{2.15}$$

where j_n is the corresponding eigenvalue of matrix $\boldsymbol{J}$.
Therefore, a multiplication of $\boldsymbol{J}$ from the left (right) with a matrix $\boldsymbol{\Phi}$ ($\boldsymbol{\Psi}$) with rows (columns) made of left (right) eigenvectors produces a diagonal matrix containing the eigenvalues

$$\boldsymbol{\Phi}\boldsymbol{J} \;=\; \mathrm{diag}\,(j_1 \ldots j_N)\,\boldsymbol{\Phi} \qquad \boldsymbol{J}\boldsymbol{\Psi} \;=\; \boldsymbol{\Psi}\mathrm{diag}\,(j_1 \ldots j_N)\,. \tag{2.16}$$

By multiplying by $\boldsymbol{\Psi}$ ($\boldsymbol{\Phi}$) from the right (left)

$$\begin{aligned} &\boldsymbol{\Phi}\boldsymbol{J}\boldsymbol{\Psi} \;=\; \mathrm{diag}\,(j_1 \ldots j_N)\,\boldsymbol{\Phi}\boldsymbol{\Psi} \qquad \boldsymbol{\Phi}\boldsymbol{J}\boldsymbol{\Psi} \;=\; \boldsymbol{\Phi}\boldsymbol{\Psi}\mathrm{diag}\,(j_1 \ldots j_N) \\ &\Leftrightarrow \quad \mathrm{diag}\,(j_1 \ldots j_N)\,\boldsymbol{\Phi}\boldsymbol{\Psi} \;=\; \boldsymbol{\Phi}\boldsymbol{\Psi}\mathrm{diag}\,(j_1 \ldots j_N) \end{aligned} \tag{2.17}$$

it can be obtained that the product of the matrices made of left and right eigenvectors $\boldsymbol{\Phi}\boldsymbol{\Psi}$ commutes with the diagonal matrix of eigenvalues.
Furthermore it can be shown that every matrix $\boldsymbol{M}$ which commutes with a diagonal matrix $\boldsymbol{D}$ with *distinct* diagonal entries $d_{ii} \neq d_{jj}$, has to be a diagonal matrix, too. This can be seen by comparing the left and the right hand side of the commutator relation component-wise leading to

$$(\boldsymbol{M}\boldsymbol{D})_{ij} \;=\; \sum_{k=1}^{n} m_{ik}d_{kj} \;=\; m_{ij}d_{jj} \;=\; d_{ii}m_{ij} \;=\; \sum_{k=1}^{n} d_{ik}m_{kj} \;=\; (\boldsymbol{D}\boldsymbol{M})_{ij} \;, \tag{2.18}$$

which can be brought to the form

$$m_{ij}\,(d_{jj} - d_{ii}) \;=\; 0\,, \tag{2.19}$$

stating that as long as all entries of the diagonal matrix are different, every entry of matrix $\boldsymbol{M}$ with different indices i and j has to be zero.
Therefore, the product of the matrices built of left and right eigenvectors has to be

a diagonal matrix, which means that every left eigenvector is orthogonal to all right eigenvectors but the one corresponding to the same eigenvalue

$$\vec{\phi}_i^{\dagger}\vec{\psi}_j \;=\; 0 \quad \forall\, i \neq j \tag{2.20}$$

as long as all eigenvalues are distinct.
By normalizing the eigenvectors the product of corresponding left and right eigenvectors can always be made one and thus the matrix product $\boldsymbol{\Phi\Psi}$ has to be equal to the identity matrix, which means that $\boldsymbol{\Phi}$ and $\boldsymbol{\Psi}$ are inverse matrices.
With this in mind eq. 2.17 equals eq. 2.14 and we find the matrices of left and right eigenvectors to be the transformation matrices needed to get the Laplacian in its diagonal form:

$$\boldsymbol{\Lambda} \;=\; \mathrm{diag}\,(j_1 \ldots j_N) \;=\; \boldsymbol{\Phi J \psi} \tag{2.21}$$

It can be the case that some of the eigenvalues of $\boldsymbol{J}$ are degenerate. If the number m_i of different left or right eigenvectors, i.e. the geometric multiplicity, corresponding to the same eigenvalue j_i, equals to the number of occurrences of the eigenvalue (algebraic multiplicity), the corresponding eigenvectors can be made orthogonal by linear combination. When the geometric multiplicity is smaller than the algebraic multiplicity, the matrix is called defective and cannot be diagonalized by its eigenvectors.

When the eigendecomposition is applicable to the grounded circuit Laplacian $\boldsymbol{J}$, the matrix can be expressed by its eigenvalues and eigenvectors:

$$\boldsymbol{J} \;=\; \boldsymbol{\Psi\Lambda\Phi} \;=\; \sum_{n=1}^{N} \lambda_n \vec{\psi}_n \vec{\phi}_n^{\dagger} \tag{2.22}$$

By inverting this equation (no zero eigenvalues required) the Green's matrix is given by

$$\boldsymbol{G} \;=\; (\boldsymbol{\Psi\Lambda\Phi})^{-1} \;=\; \boldsymbol{\Phi}^{-1}\boldsymbol{\Lambda}^{-1}\boldsymbol{\Psi}^{-1} \;=\; \boldsymbol{\Psi\Lambda}^{-1}\boldsymbol{\Phi} \;=\; \sum_{n=1}^{N} \frac{1}{\lambda_n} \vec{\psi}_n \vec{\phi}_n^{\dagger}. \tag{2.23}$$

With these connections in mind, we see that each set of external currents $\vec{I}_{ext}$ caused by voltages $\vec{V}$ applied to the circuit and each voltage profile $\vec{V}$ induced by external currents $\vec{I}_{ext}$ can be expressed as linear combinations of the right eigenvectors weighted by the related eigenvalue and the scalar product of the applied voltage/current vector and the corresponding left eigenvector.

$$\vec{I}_{ext} \;=\; \boldsymbol{J}\vec{V} \;=\; \sum_{n=1}^{N} \lambda_n \vec{\psi}_n \left(\vec{\phi}_n^{\dagger}\vec{V}\right) \qquad \vec{V} \;=\; \boldsymbol{G}\vec{I}_{ext} \;=\; \sum_{n=1}^{N} \frac{1}{\lambda_n} \vec{\psi}_n \left(\vec{\phi}_n^{\dagger}\vec{I}_{ext}\right) \tag{2.24}$$

Thus we can draw conclusions on the eigenvectors of our circuit by probing it experimentally.
First of all, we have to think about the feasibility of the desired measurements. In practice most of the electrical measurements are traced back to measuring a voltage and most current measurements need additional components which convert the investigated

current into a voltage signal. Therefore, we prefer determining voltages in our circuits under test.
From equation 2.24 we see that there are two ways to investigate the circuit's eigenvectors. We can apply voltages to all circuit nodes and measure the resulting external currents determined by the circuit Laplacian, or we can drive external currents to all nodes and investigate the resulting voltages given by the Green's matrix of the circuit. The latter has one main advantage: To drive a zero external current no source is needed, while applying zero voltage needs a voltage source that provides a suitable current to keep the potential of the node at the ground level.
So applying a voltage profile to the circuit forces us to attach a separate voltage source to each node, whereas a non-trivial external current configuration can already be generated by only a single current source.
Therefore, for the sake of simplicity, most experiments performed in this work get along with one single external current provided by a voltage source feeding current through a series resistor which can be used for measuring the external input current as the voltage drop at the resistor.

By feeding one current to all nodes of the circuit one after another and simultaneously recording the voltages of all nodes the Green's matrix $\boldsymbol{G}$ of the system can be reconstructed. The example

$$\begin{pmatrix} V_1 \\ \vdots \\ V_n \end{pmatrix} = \begin{pmatrix} G_{11} I_1 \\ \vdots \\ G_{n1} I_1 \end{pmatrix} = \begin{pmatrix} G_{11} & \dots & G_{1n} \\ \vdots & \ddots & \vdots \\ G_{n1} & \dots & G_{nn} \end{pmatrix} \begin{pmatrix} I_1 \\ \vdots \\ 0 \end{pmatrix} \tag{2.25}$$

shows that a current input at node 1 leads to a voltage profile made of the entries of column 1 in the Green's matrix multiplied by the current value. So each entry can be calculated by dividing the voltage of node h by the associated input current I_k:

$$G_{h,k} = \frac{V_h}{I_k} \tag{2.26}$$

From equation 2.6 we know that impedances between nodes in the circuit can be expressed by the Green's matrix. This can be written in terms of eigenvectors and eigenvalues of the grounded circuit Laplacian, too.

$$\begin{aligned} Z_{AB} &= G_{AA} + G_{BB} - G_{AB} - G_{BA} \\ &= \sum_{n=1}^{N} \left[\frac{1}{\lambda_n} \left(\psi_{n,A} \phi^*_{n,A} + \psi_{n,B} \phi^*_{n,B} - \psi_{n,A} \phi^*_{n,B} - \psi_{n,B} \phi^*_{n,A} \right) \right] \\ &= \sum_{n=1}^{N} \frac{\left(\psi_{n,A} - \psi_{n,B} \right) \left(\phi^*_{n,A} - \phi^*_{n,B} \right)}{\lambda_n} \end{aligned} \tag{2.27}$$

The index n of the sum extends over all N eigenvectors/-values and the capitalized indices A, B indicate the A, Bth entry of the nth eigenvector.
As we can see from equations 2.23, 2.24 and 2.27, the contributions of eigenvectors to

the Green's matrix, as well as to the voltage profile induced by an input current and to the impedance readout are all scaled by the inverse of their eigenvalue. Consequently, the voltage profile or an impedance measurement will be dominated by the contribution of the eigenvector with smallest absolute eigenvalue. Vice versa, a measurement of the voltage profile or the impedance can provide information about eigenvectors having eigenvalues with small magnitude, which can be a powerful tool for the investigation of topological systems.

2.2 Translating a tight binding Hamiltonian into an electrical circuit

In solid state physics the tight binding model is used to describe an atomic lattice consisting of repeated unit cells. It can be used to derive the band structure and several essential material properties from the solid.
Some of the features of the considered lattices do not depend on the exact lattice structure or the values of the hopping strengths, but are determined only by the connectivity of the system. They can be investigated by the mathematical concept of topology describing properties of objects that do not change with continuous transformations of the underlying parameter space.
The appearance of topologically protected states in the energetic bulk band gap spatially located at the edges of an insulating material is an example of such topology driven effects. This leads to a division of the parameter space, e.g. defined by the hopping strengths in the tight binding model, in topologically distinct regions, which are classified by topological invariants corresponding to the number of topological edge states existing in the system due to bulk boundary correspondence in Hermitian systems. The number of edge states is fixed immutable in each topological region of parameter space and can only be changed by switching to another region. The transition between different topological regions by changing the system parameters adiabatically always comes along with closing and reopening the band gap of the insulating system (see chap. 1).
In the following paragraphs first a detailed description of the commonalities and differences between the tight binding Hamiltonian and the grounded circuit Laplacian will be given. After that, the one-dimensional Su-Schrieffer-Heeger model and its topological properties will be introduced. Therefore, its band structure, the eigenstates and their eigenvalues will be calculated for different parameter settings. Furthermore we will see how the (dis-)appearance of the edge states fall together with closing the band gap and can be described by the bulk winding number.
Finally an electrical circuit with admittance matrix similar to the tight binding Hamiltonian of the SSH model will be deduced. Thereby we pay attention to the ease of circuit implementation and the accessibility for electrical investigation of the admittance matrix eigensystem.

2.2.1 Commonalities and differences in the descriptions of solid state crystals and electrical circuits

To start the comparison between properties of the considered atomic and electric lattices we should first mention which assumptions are made for the description of the solid state crystal, i.e. which properties of the solid can be described by the tight binding approximation.

A full quantum-mechanical description of a solid would request a many-body Hamiltonian considering all kinetic and interacting terms for all electrons and nuclei in the solid. Due to the big difference in mass between electrons and nuclei we can use the Born-Oppenheimer approximation and concentrate on the treatment of electronic wave

functions only. Therefore, we will not be able to describe any type of lattice vibrations of the investigated solid.
The nuclei produce an effective periodic potential interacting with the electrons. When furthermore the different electrons do not interact with each other, the wave function of a single electron can be approximated by plane waves along the periodic potential (Bloch's theorem), i.e. the position of an electron is fully periodic along the atomic lattice.
In a next step the potential is treated by perturbation theory. This can be done in the two extreme cases, i.e. the potential only weakly alters the wave functions of the electrons or the electrons are tightly bound to the nuclei permitting only small interactions with the neighboring nuclei. The former describes the nearly free electron model mainly used to describe the band structures of metals, the latter is the tight binding method more likely for semiconductors or insulators which we will deal with.
Therefore, the orthonormal set of electronic wave functions (called Wannier states) can be assumed by the orbitals of isolated atoms or linear combinations of those. The transitions due to the lattice potential between the Wannier states can then be written in compact form as a matrix equation. This matrix, the single electron tight binding Hamiltonian, will be called Hamiltonian for short in the following. Its matrix entries, called hopping amplitudes, describe the probability of a single electron to hop between the Wannier states localized at the atomic positions.
This single particle tight binding approximation can be used to describe the location of one electron, i.e. the eigenstates of the Hamiltonian, induced by the lattice potential. Furthermore, the allowed electron energies in the lattice can be deduced by the electronic band structure of the crystal. The band structures of insulating material featuring a band gap can be classified from a topological point of view with important consequences such as topological protected in-gap states (see chap. 1).

The Hamiltonian is the point where the emulation of the crystal by an electric circuit aims at. Due to the conceptual similarity of the matrix representation of the Hamiltonian and the grounded circuit Laplacian properties of the solid can also be found in the electric circuit.
Accordingly, the hopping amplitudes of the Hamiltonian equal the admittances in the circuit network, and the voltage vectors applied to the Laplacian matrix correspond to the electron's wave function. The circuit nodes being the basis of the voltage vector consequently correspond to the basis of the Hamiltonian's Hilbert space, i.e. the Wannier states, reflecting the position of the electron in the crystalline lattice.
In contrast to the quantum mechanical wave function, the magnitude of which only could be measured, the node voltages can be determined exactly. Furthermore, it is much easier to define interaction between different lattice sites in an electrical circuit because the matrix entries are given by lumped elements and do not depend on the spatial arrangement of the nodes, as it is the case for the periodic lattice potential introduced by the atomic orbitals and positions in the solid.
Therefore, the grounded circuit Laplacian can be seen as a tool to investigate the stationary Schrödinger equation of the solid providing information about the eigenenergies and eigenstates of the electron. It cannot be used to address the time-dependent Schrödinger equation, where the Hamiltonian acts as the generator of the system's time evolution.
In the grounded circuit Laplacian the differential equations are Fourier transformed to

achieve algebraic equations connecting voltage and current, while assuming the system to be in a stationary state and disregarding the transient response of the circuit. This is why the external current input used to stimulate and investigate the circuit does not have an analogue in the quantum mechanical description of the solid: The Schrödinger equation does not have an external excitation, i.e. an inhomogeneity.
To find out more about the time evolution of the circuit's voltage another circuit description has to be used, called the Hamiltonian formalism [57, 70], which will not be introduced in detail in this work.

The band structure derived from the solid connecting energy and wave vector leads to a dispersion relation between the angular frequency and the wave vector of the electron wave and therefore provides information about the wave propagation in the solid. In contrast, the circuit analogue, the admittance band structure that can be derived by a measurement procedure described in section 2.3.4, connects only the admittance eigenvalues with spatial sinusoidal voltage contributions independent from the signal's angular frequency. The angular frequency ω in the electric circuit description is a free external parameter of the measurement signals, which only scales the admittances of frequency dependent components and can be set at will under experimental conditions. Finally it should be emphasized that an electrical circuit is a classical system, therefore topological features known of the emulated solid can only be transferred to the circuit analogue if they are not based on quantum mechanical properties like spin or the quantization of Hilbert space.

2.2.2 The Su-Schrieffer-Heeger model

In the following paragraphs we will introduce a simple tight binding model for the organic polymer trans-polyacetylene. It was first investigated by W.P. Su, J.R. Schrieffer and A.J. Heeger during their research on solitons in polyacetylene [58] and is nowadays called Su-Schrieffer-Heeger (SSH) model. The descriptions are based on the lecture notes of Asbóth, Oroszlány and Pályi [72]. Furthermore we recommend an instructive article [73] on the SSH model and its topological features.

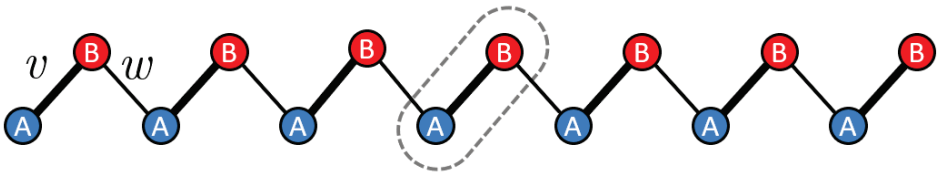

Figure 2.2: Schematic illustration of the polyacetylene chain. The colored circles represent the two different subgroups of carbon atoms (A,B) that are interlinked by weak w and strong hoppings v. A unit cell is defined by the dashed line and contains one atom of each type. After the choice of a unit cell (in this case A-B) the hoppings can be labeled intracell hopping v and intercell hopping w (from [66]).

The carbon atoms of the polymer are linked by alternating single and double bonds introduced by Peierls instability [74], which divides them into two distinguishable subgroups A and B forming unit cells (dashed line) shown in Fig. 2.2. The bonds are represented

by the intercell hopping v and the intracell hopping w. Its single particle tight binding Hamiltonian in Dirac notation is given by:

$$\hat{H}_{SSH} \;=\; v\sum_{m=1}^{N}\left(|m,B\rangle\langle m,A| \;+\; h.c.\right) + w\sum_{m=1}^{N-1}\left(|m+1,A\rangle\langle m,B| \;+\; h.c.\right) \tag{2.28}$$

The first index m of the states extends over all N unit cells while the second one displays the sublattice site of the state A, B. The abbreviation h.c. is indicating the Hermitian conjugated terms needed to enable hopping in both directions. The Hamiltonian can be written in matrix form, which we will prefer in the following. This form indicates the similarity to the admittance matrix of a circuit, which will be shown in the next section.

$$\left(\boldsymbol{H}_{SSH}\right)_{(m,\alpha),(n,\beta)} \;=\; \begin{pmatrix} 0 & v & 0 & 0 & \dots & 0 \\ v & 0 & w & 0 & \dots & 0 \\ 0 & w & 0 & v & \dots & 0 \\ 0 & 0 & v & 0 & \dots & 0 \\ \vdots & \vdots & \vdots & \vdots & \ddots & v \\ 0 & 0 & 0 & 0 & v & 0 \end{pmatrix} \tag{2.29}$$

The investigation of the chain's eigenstates can be split up into the contribution of the bulk (the inner part of the chain) and the edges (ends of the chain).
To consider the bulk eigenstates (Bloch states) in solid state physics it is common to think of a translation invariant chain of infinite length so that the ends of the chain do not play a significant role and choosing periodic boundary conditions (thinking of a translation invariant ring) is valid. Therefore, we can Fourier transform the local space of the unit cells depending only on relative distances r and keep the different sublattice sites as internal degrees of freedom.

$$\left(\boldsymbol{H}_{SSH}\right)_{\alpha,\beta}(k) \;=\; \sum_{r}\left(\boldsymbol{H}_{SSH}\right)_{\alpha,\beta}(r)\cdot e^{-ikr} \tag{2.30}$$

This leaves us with only two linear independent equations of the periodic Hamiltonian corresponding to the two sublattice sites, the so called bulk momentum-space Hamiltonian. By setting the distance r between two atoms to one it can be written as

$$\left(\boldsymbol{H}_{SSH}\right)_{\alpha,\beta}(k) \;=\; \begin{pmatrix} 0 & v \;+\; we^{-ik} \\ v \;+\; we^{ik} & 0 \end{pmatrix}, \tag{2.31}$$

and by calculating the eigensystem of the bulk momentum-space Hamiltonian $\boldsymbol{H}_{SSH}\,|\pm(k)\rangle = E_{SSH}(k)\,|\pm(k)\rangle$ the dispersion relation $E_{SSH}(k)$ and the eigenstates $|\pm(k)\rangle$

$$\begin{aligned} E_{SSH}(k) \;&=\; \pm\sqrt{v^2 \;+\; w^2 \;+\; 2vw\cos(k)} \\ |\pm(k)\rangle \;&=\; \begin{pmatrix} \pm\frac{v+we^{-ik}}{\sqrt{v^2+w^2+2vw\cos(k)}} \\ 1 \end{pmatrix} \;=\; \begin{pmatrix} \pm e^{-i\Phi(k)} \\ 1 \end{pmatrix} \\ \Phi(k) \;&=\; \arctan\left(\frac{w\sin(k)}{v+w\cos(k)}\right) \end{aligned} \tag{2.32}$$

can be found. The dispersion relation is shown in Fig. 2.3 for different combinations of hopping amplitudes. It can be noted that the system describes an insulator for unequal v and w due to the gap between the upper and lower band (Figs. 2.3 a),b),d),e)), but resembles a conducting material for $v = w$ because of the gap closing at the edges of the Brillouin zone (Fig. 2.3 c)).

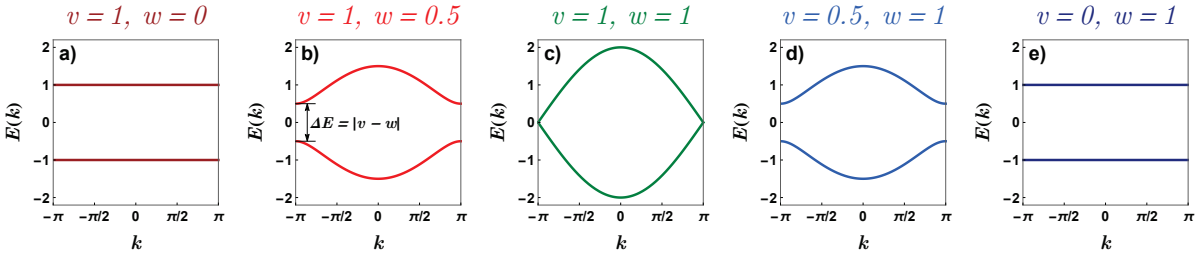

Figure 2.3: Dispersion relation of the SSH model (Eq. 2.32) for different sets of hoppings. a),b),d),e): For unequal hopping amplitudes $|v| \neq |w|$ a gap ΔE exists between the upper and lower band, i.e. the minimal difference of the two bands (indicated in b)). c): When $|v|$ equals $|w|$ the band gap closes at the edges of the Brillouin zone (adapted from [72]).

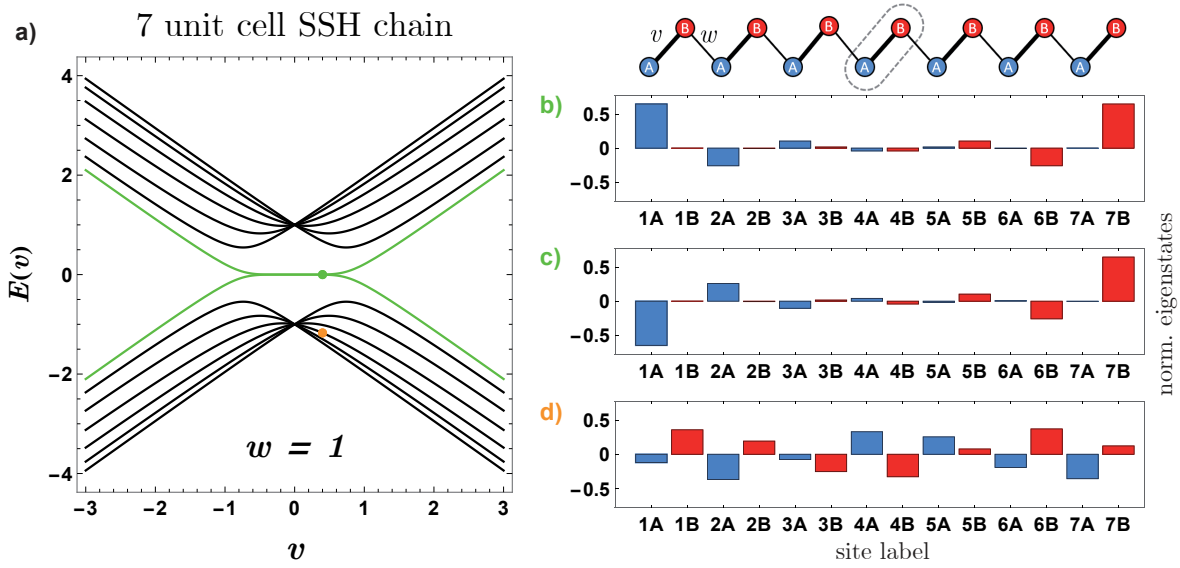

Figure 2.4: a): Energy eigenspectrum of a 7 unit cell SSH chain for fixed intercell hopping $w = 1$ and variable intracell hoppings v. The energy eigenvalues of the bulk states are painted in black, the ones of the edge states ($|v| < |w|$) are plotted in green. For $|v| > |w|$ the energies of the edge states split up towards those of the bulk states and the edge localization disappears. The green and orange dots at $v = 0.4, w = 1$ indicate the energies of the states shown in b)-d). b),c): Normalized eigenstates (hybridized edge states) for the energy values 0^+ in b) and 0^- in c). d): Bulk eigenstate with eigenvalue $E \approx -1.17$ (adapted from [72]).

The eigenstates occurring due to the edges of the chain differ significantly depending on the ratio of the two hopping strengths. When the hopping at the beginning/end

of the chain is smaller than the next/previous one, two zero energy modes exist in the band gap of the insulator (see Fig. 2.4 a), green lines for $|v| < |w|$). They represent exponentially localized topological edge states (hybridized due to the finite chain length, Fig. 2.4 b),c)) with localization length $\xi = 1/\log(|w|/|v|)$ depending on the ratio of the hopping strengths. For $|v| > |w|$ their eigenvalues split up towards the energies of the delocalized bulk states (e.g. Fig. 2.4 d)).

The origin of this transition between localized edge modes and delocalized bulk modes is a topological phase transition at $|v| = |w| = 1$ indicated by the gap closing of the SSH band structure (Fig. 2.3 c)). The topological invariant given by the number of edge states per edge changes from 1 for $|v| < |w|$ to 0 for $|v| > |w|$.
Another topological invariant, the so called bulk winding number, which equals the number of edge states, can be read of the bulk properties of the system. For the calculation of the bulk winding number the bulk momentum-space Hamiltonian 2.31 needs to be represented in the basis of the Pauli matrices $\boldsymbol{\sigma_i}$:

$$\begin{aligned}
\boldsymbol{H}_{SSH} &= \begin{pmatrix} 0 & v + w(\cos k - i \sin k) \\ v + w(\cos k + i \sin k) & 0 \end{pmatrix} \\
&= 0 \cdot \begin{pmatrix} 1 & 0 \\ 0 & 1 \end{pmatrix} + (v + w \cos k) \cdot \begin{pmatrix} 0 & 1 \\ 1 & 0 \end{pmatrix} + w \sin k \cdot \begin{pmatrix} 0 & -i \\ i & 0 \end{pmatrix} + 0 \cdot \begin{pmatrix} 1 & 0 \\ 0 & -1 \end{pmatrix} \\
&= 0 \cdot \boldsymbol{\sigma_0} + (v + w \cos k) \cdot \boldsymbol{\sigma_1} + (w \sin k) \cdot \boldsymbol{\sigma_2} + 0 \cdot \boldsymbol{\sigma_3} \\
&= d_0(k) \cdot \boldsymbol{\sigma_0} + \vec{d}(k)\, \vec{\boldsymbol{\sigma}}
\end{aligned} \tag{2.33}$$

The vector $\vec{d}(k)$ containing the contributions of the different Pauli matrices to the bulk momentum-space Hamiltonian carries a lot of information about the bulk system. Due to Hermiticity ($\boldsymbol{\sigma}_i = \boldsymbol{\sigma}_i^\dagger$) and unitarity ($\boldsymbol{\sigma}_i^\dagger \boldsymbol{\sigma}_i = 1$) of the Pauli matrices the eigenvalues end up to be representable by the length of $\vec{d}(k)$ plus the additional energy shift $d_0(k)$ proportional to the unit matrix σ_0:

$$\begin{aligned}
E_{SSH}(k) = d_0(k) \pm |\vec{d}(k)| &= \pm\sqrt{v^2 + 2vw\cos k + (w\cos k)^2 + (w \sin k)^2} \\
&= \pm\sqrt{v^2 + w^2 + 2vw\cos k}
\end{aligned} \tag{2.34}$$

The direction of $\vec{d}(k)$ contains information about the eigenvectors of the model. The phase $\Phi(k)$ used to parameterize the eigenvectors is set by the components of $\vec{d}(k)$ (see eq. 2.32). From the path of $\vec{d}(k)$ for $k = 0 \to 2\pi$ in the two dimensional parameter space ($\sigma_3 = 0$) the bulk winding number can be read off. Fig. 2.5 shows the circles formed by the endpoint of $\vec{d}(k)$ for different parameter settings.

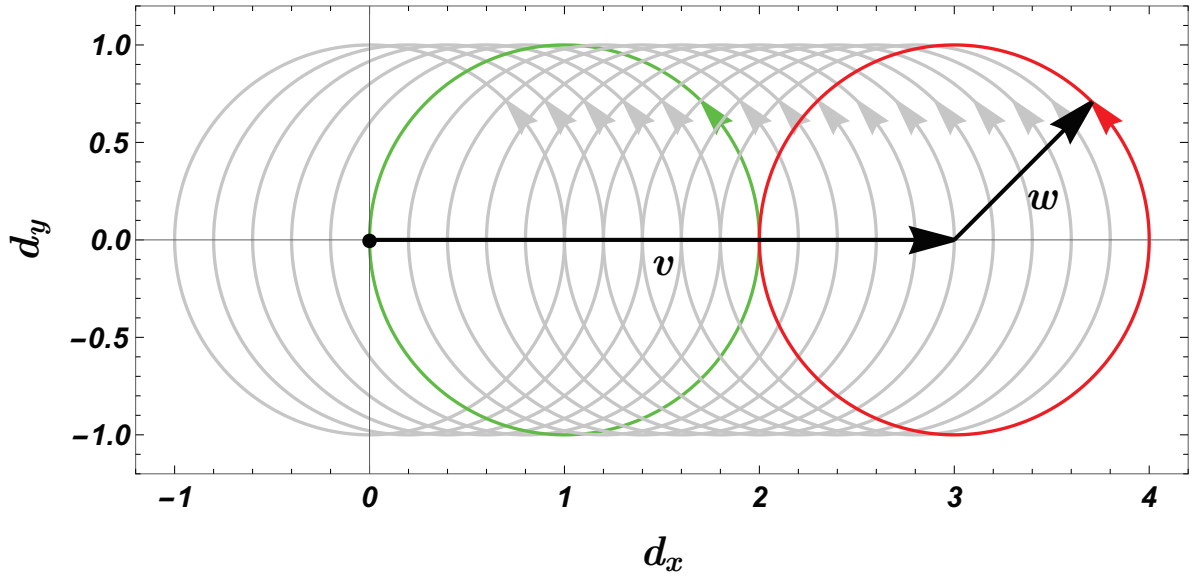

Figure 2.5: Courses of the end point of $\vec{d}(k)$ with fixed intercell hopping $w = 1$ and different intracell hoppings $0 \leq v \leq 3$ while sweeping through the Brillouin zone. The band gap equals the minimal length of $\vec{d}(k)$ for $k = 0 \to 2\pi$. The paths form circles with center fixed at $(v, 0)$ and radius w (shown for $v = 3$, $w = 1$, red circle). The green circle depicts the case $v = w = 1$ where the circle crosses the origin (black point) and the band gap closes (adapted from [72]).

The bulk winding number corresponds to how often these lines wrap around the origin while k runs through the Brillouin zone. As long as $|v| < |w|$ the circle contains the origin fixing the bulk winding number to 1. For $|v| = |w|$ the curve intersects the origin implying a closing of the band gap and a topological phase transition respectively. When $|v| > |w|$ the path no longer encircles the origin. The bulk winding number is 0 in this case and no topological edge modes appear in the non-periodic SSH chain. This fundamental connection between bulk properties and boundary effects (edge states) in Hermitian systems is known as the bulk-boundary or bulk-edge correspondence.
Not every insulator described by a tight binding Hamiltonian can host topological edge modes, instead topological properties are determined by certain discrete symmetries. In case of the SSH model this is ensured by the chiral or sublattice symmetry given by the fact that the lattice is bipartite (see section 2.4).

2.2.3 Electric circuit representation of the SSH model

From the explanations in section 2.2.2 we know that the hopping Hamiltonian of the SSH model has the form of equation 2.29

$$(\boldsymbol{H}_{SSH})_{(m,\alpha),(n,\beta)} = \begin{pmatrix} 0 & v & 0 & 0 & \dots & 0 \\ v & 0 & w & 0 & \dots & 0 \\ 0 & w & 0 & v & \dots & 0 \\ 0 & 0 & v & 0 & \dots & 0 \\ \vdots & \vdots & \vdots & \vdots & \ddots & v \\ 0 & 0 & 0 & 0 & v & 0 \end{pmatrix},$$

which can be emulated by a circuit of two repeated circuit elements with different admittances (Fig. 2.6) plus two extra grounding elements. It can be described by an admittance matrix of the form:

$$\boldsymbol{Y} = \begin{pmatrix} Y_1{+}Y_2 & -Y_1 & 0 & 0 & \dots & 0 \\ -Y_1 & Y_1+Y_2 & -Y_2 & 0 & \dots & 0 \\ 0 & -Y_2 & Y_1+Y_2 & -Y_1 & \dots & 0 \\ 0 & 0 & -Y_1 & Y_1+Y_2 & \dots & 0 \\ \vdots & \vdots & \vdots & \vdots & \ddots & -Y_1 \\ 0 & 0 & 0 & 0 & -Y_1 & Y_1{+}Y_2 \end{pmatrix} \tag{2.35}$$

Two additional circuit elements connected to ground are needed at the beginning/end of the chain to compensate for the missing second circuit element connected to the first/last node and to achieve a uniform diagonal in the admittance matrix.

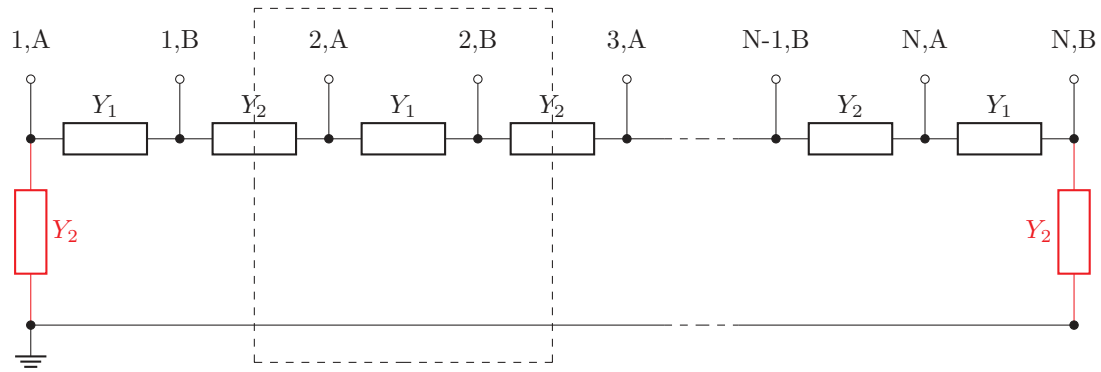

Figure 2.6: Schematic of a SSH-like circuit with N unit cells containing two sublattice sites A and B. The two repeated circuit elements (Y_1, Y_2) equal the alternated hopping caused by the single and double bounds in the SSH chain (Fig. 2.2). The two red elements (Y_2) connected to ground are used the get a uniform diagonal of the admittance matrix. A unit cell corresponding to the one defined in Fig. 2.2 is indicated by the dashed rectangle. The node indices are adapted in the same way.

For the choice of circuit elements used in the chain some additional thoughts should be made. To avoid voltage dependent admittances, additional power supplies, circuit instabilities etc. passive linear, reciprocal two terminal elements (resistors R, capacitors C, inductors L) are used.
This restriction leaves us with two sorts of admittances, purely real ($Y_R = 1/R$) and purely imaginary ($Y_C = i\omega C, Y_L = -i/(\omega L)$) ones. While ideal resistors have one fixed resistance value for all AC driving frequencies, the admittances of ideal capacitors and inductors vary with excitation frequency $f = \omega/(2\pi)$.
From fig. 2.4 we know that the eigenvalue spectrum of the SSH chain lies in the range $\pm(|v| + |w|)$ (fig. 2.7 a)) with topological edge modes for $|v| < |w|$. The admittance matrix of the circuit presented in fig. 2.6 can be split into two matrices, one equaling the SSH Hamiltonian and a diagonal matrix scaled with the sum of admittances connected to a unit cell:

$$\boldsymbol{Y} = \begin{pmatrix} 0 & -Y_1 & 0 & 0 & \dots & 0 \\ -Y_1 & 0 & -Y_2 & 0 & \dots & 0 \\ 0 & -Y_2 & 0 & -Y_1 & \dots & 0 \\ 0 & 0 & -Y_1 & 0 & \dots & 0 \\ \vdots & \vdots & \vdots & \vdots & \ddots & -Y_1 \\ 0 & 0 & 0 & 0 & -Y_1 & 0 \end{pmatrix} + (Y_1 + Y_2) \cdot \mathbb{1} \tag{2.36}$$

Therefore, the eigenvalue spectrum of the first matrix equaling the SSH Hamiltonian is shifted by $Y_1 + Y_2$.

When we use the same type of circuit elements to emulate both couplings, the admittance eigenvalue spectrum will be real when using resistors (fig. 2.7 b)) and purely imaginary when using capacitors or inductors (fig. 2.7 c),d)). In section 2.3.4 we will see that the eigenvectors with eigenvalue near zero dominate the circuit behaviour. When we want other eigenvectors than the ones with the lowest/highest eigenvalue to dominate the circuit response, a mechanism to tune the position of the spectrum in the complex admittance plane is needed.

There are two options to make the eigenvalue spectrum vary around zero admittance. We could use different frequency dependent circuit elements (fig. 2.7 e)) to represent the different hopping terms or introduce a frequency-induced admittance shift by adding suitable grounding elements.
Different frequency dependent circuit elements have several disadvantages, and we will only mention a few of them. For example, we cannot pair real and imaginary admittances as hopping elements because this could not be mapped back onto the non-complex SSH model any more. Therefore, the only chance would be using inductors and capacitors as hopping elements leading to purely imaginary eigenvalues.
In this combination zero is no longer located at an end of the spectrum and the position of the spectral range varies around zero with frequency (see fig. 2.7 e)). But for each frequency where an eigenvalue crosses zero and dominates the admittance matrix the ratio between the frequency dependent hopping elements are different. Therefore, the frequency dependence causes the hoppings of the electric SSH model to be different for each eigenvector which dominates the circuit's response. Consequently, each dominating eigenvector with eigenvalue near zero belongs to a different configuration of the SSH model.

The most practicable solution is given by using suitable grounding elements. When we add the same grounding element to each node the admittances are only added to the shifting term of the eigenvalues (see eq. 2.36). Moreover, using the same type of imaginaty circuit elements as hoppings means that they scale with frequency in the same way, keeping the SSH configuration the same for each measurement frequency because the model only depends on the ratio of the hoppings.

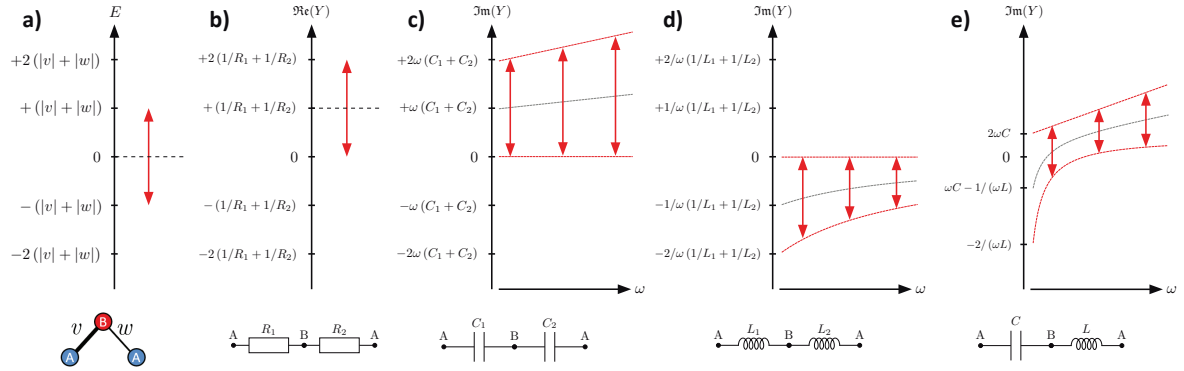

Figure 2.7: Eigenvalue ranges of the SSH model and of different electric configurations emulating the model. a): The eigenvalues of the SSH model lie symmetrically in the range (red span) of $\pm(|v|+|w|)$ with its center at the origin (dashed line). b): When resistors are used to emulate the hoppings, the admittance eigenvalues (red span) are real and positive due to the shifted center (dashed line) by the diagonal matrix. c): With capacitors used to mimic the hoppings the admittance eigenvalues (red span) are purely imaginary, but shifted upwards as it was the case in b). Furthermore, the center (gray dashed line) and the upper limit (upper red dashed line) of the spectral range is now increase with the angular frequency ω. The lower limit (lower red dashed line) is always at zero. d): When the hopping terms are made by inductors (negative imaginary admittances) the spectral range is negative. Due to the inverse dependency on ω the scaling behaviour is reversed compared to c). e): When capacitors and inductors are combined, the lower limit of the spectral range scales like double the inductive susceptance $-2/(\omega L)$ and the upper limit like double the capacitive susceptance $2\omega C$. For low ω the center scales at the inductive susceptance $-1/(\omega L)$, for high ω at the capacitive susceptance ωC.

If resistive hopping elements were used, variable negative resistances to ground would be needed to shift the admittance spectrum towards zero, which is in principle realizable by active circuitry, but the shift has to be set manually by changing the negative resistance and the circuit could get unstable due to the energy input by the active circuit elements.

Therefore, we use capacitors and inductors as hopping and grounding elements. The one type of admittances is used as hopping elements ensuring the same model configuration for all frequencies. The other type is used as grounding elements whose admittance only contributes to the eigenvalue shift and ensures that all eigenvalues pass through zero at a certain finite frequency due to the respective negative admittance compared to the hopping elements. This enables us to selectively investigate different eigenstates of the same SSH configuration at different AC frequency. As an example in fig. 2.13 the shifting of the spectrum with frequency and the impact on an impedance readout of eigenvalues crossing zero can be seen.

So finally, there are two possible settings left to implement the SSH circuit with capacitors and inductors. In Fig. 2.8 the two approaches of building an SSH circuit are shown. For our experimental investigation, which will be described briefly in the section 3.1, we

chose the capacitive hopping version fig. 2.8 b). An explanation of this choice can be found in section 2.3.1. Accordingly, the grounded circuit Laplacian will be written in this configuration.

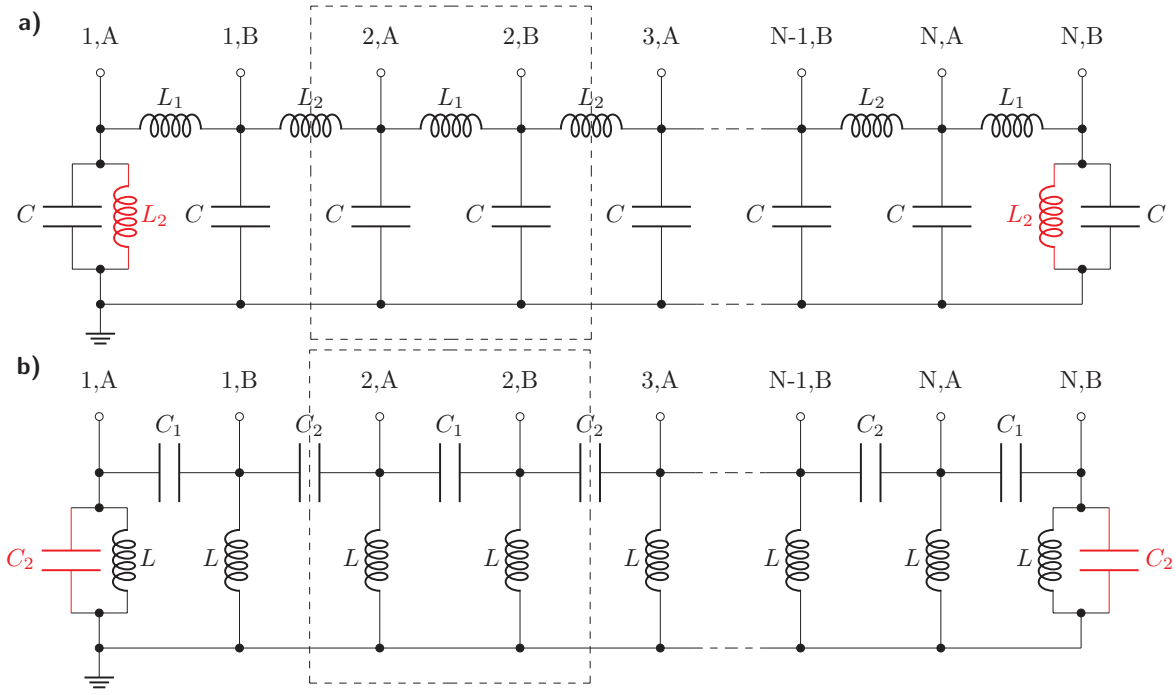

Figure 2.8: Schematic of two realizations of the SSH circuit with N unit cells containing two sublattice sites A and B. The alternated hopping is implemented by inductors in a) and capacitors in b). The red elements connected to ground are used to get a uniform diagonal of the admittance matrix. Additional grounding elements (capacitors a), inductors b)) are used to fix the zero value of the diagonal, i.e. form a resonant circuit. A unit cell corresponding to the one defined in fig. 2.2 is indicated by the dashed rectangle, and the node indices are also chosen according to fig. 2.2.

As described in section 2.1.2 the grounded circuit Laplacian ($\boldsymbol{J} = \boldsymbol{D} - \boldsymbol{C} + \boldsymbol{W}$) can be split up into three matrices, namely the adjacency matrix C, the total node conductance matrix D and the ground matrix W:

$$\boldsymbol{C} = i\omega \begin{pmatrix} 0 & C_1 & 0 & 0 & \dots & 0 \\ C_1 & 0 & C_2 & 0 & \dots & 0 \\ 0 & C_2 & 0 & C_1 & \dots & 0 \\ 0 & 0 & C_1 & 0 & \dots & 0 \\ \vdots & \vdots & \vdots & \vdots & \ddots & C_1 \\ 0 & 0 & 0 & 0 & C_1 & 0 \end{pmatrix} \tag{2.37}$$

$$\boldsymbol{D} = i\omega \begin{pmatrix} C_1 & 0 & 0 & 0 & \dots & 0 \\ 0 & C_1 + C_2 & 0 & 0 & \dots & 0 \\ 0 & 0 & C_1 + C_2 & 0 & \dots & 0 \\ 0 & 0 & 0 & C_1 + C_2 & \dots & 0 \\ \vdots & \vdots & \vdots & \vdots & \ddots & 0 \\ 0 & 0 & 0 & 0 & 0 & C_1 \end{pmatrix} \tag{2.38}$$

$$\boldsymbol{W} = i\omega \begin{pmatrix} C_2 - \frac{1}{\omega^2 L} & 0 & 0 & 0 & \dots & 0 \\ 0 & -\frac{1}{\omega^2 L} & 0 & 0 & \dots & 0 \\ 0 & 0 & -\frac{1}{\omega^2 L} & 0 & \dots & 0 \\ 0 & 0 & 0 & -\frac{1}{\omega^2 L} & \dots & 0 \\ \vdots & \vdots & \vdots & \vdots & \ddots & 0 \\ 0 & 0 & 0 & 0 & 0 & C_2 - \frac{1}{\omega^2 L} \end{pmatrix} \tag{2.39}$$

The equality to the tight binding Hamiltonian is set by the adjacency matrix while the ground matrix is used as a tool to vary all diagonal entries by frequency variation, which are given by the total node conductance matrix, i.e. to form a resonant circuit.

$$\boldsymbol{J}_{SSH} = i\omega \cdot \left[\begin{pmatrix} 0 & -C_1 & 0 & \dots & 0 \\ -C_1 & 0 & -C_2 & \dots & 0 \\ 0 & -C_2 & 0 & \dots & 0 \\ \vdots & \vdots & \vdots & \ddots & -C_1 \\ 0 & 0 & 0 & -C_1 & 0 \end{pmatrix} + \left((C_1 + C_2) - \frac{1}{\omega^2 L} \right) \cdot \mathbb{1} \right] \tag{2.40}$$

2.3 Experimental investigation of tight binding Hamiltonians in circuits

In this section we want to elaborate how the properties of tight binding Hamiltonians can be investigated in electric circuits. Therefore, we first think about parasitic effects that could appear in realistic circuits and their impact on measurement results. After that we shortly explain the Lock-in technique used for frequency selective phase sensitive detection of the voltage signals and the principles of AC impedance measurements. In the main part of this section we introduce different measurement routines used to investigate the eigenstates and eigenvalues of admittance matrix of the circuit and draw conclusions about the emulated solid state system. In the end, some options for speeding up the measurement process will be introduced.

2.3.1 Imperfections appearing in circuits and their impact on the grounded circuit Laplacian

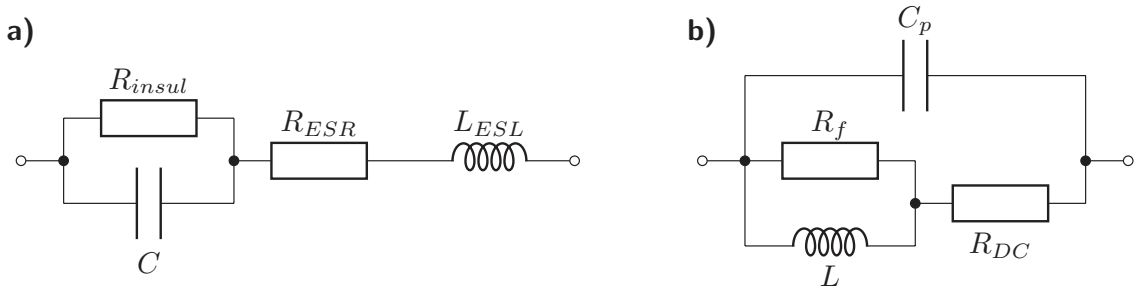

Figure 2.9: Exemplary equivalent circuits for realistic capacitors a) and inductors b). a): In addition to the capacitance C of a typical capacitor, insulation resistance R_{insul}, equivalent series resistance R_{ESL} and equivalent series inductance L_{ESL} should be taken into account. b): The behaviour of an inductor with inductance L can be interfered by parallel capacitance C_p, DC resistance R_{DC} and frequency dependent resistance R_f (adapted from [66]).

In reality, circuit elements are subject to a number of additional effects making them deviate from the suspected ideal behaviour. In Fig. 2.9 a) an equivalent circuit for a capacitor is shown. Its capacitive behaviour is affected by further properties resulting from leads, form, material etc. The insulation resistance R_{insul} is dictated by its dielectric material and specifies the leakage current and the ability to store electric charge over time. The equivalent series resistance R_{ESR} indicates ohmic losses due to leads and contacts. The equivalent series inductance describes the effective self-inductance of the capacitor introduced by the inductance of the leads and its internal structure, causing the circuit element to form a resonant circuit. As a result of this, the so called self-resonant frequency can be specified describing at which frequency the element changes its electrical behaviour from capacitive to inductive.
In Fig. 2.9 b) is shown how the parasitic effects of an inductor can be separated. The

ohmic losses are divided in DC R_{DC} and frequency dependent parts R_f. The DC resistance is determined by the material properties of the wire used to wind the inductor, while the frequency dependent resistance is driven by the skin effect and magnetic losses stemming from the core and/or the shielding of the inductor. Equivalent to capacitors, inductors can also act as resonant circuit, depending on the capacitance C_p introduced by the adjacent but isolated windings.
Consequently, the impedances Z of capacitors and inductors should be written as frequency dependent complex values and the ratio between resistance R and reactance X is given by the quality factor Q:

$$Z(f) = R(f) + iX(f) \quad Q(f) = \frac{|X(f)|}{R(f)} \tag{2.41}$$

In terms of admittances Y to be used in the grounded circuit Laplacian:

$$\begin{aligned} Y(f) &= G(f) + iB(f) := \frac{1}{Z} = \frac{R(f) - iX(f)}{[R(f)]^2 + [X(f)]^2} \\ Q(f) &= \frac{|B(f)|}{G(f)} = \frac{|X(f)|}{R(f)} \end{aligned} \tag{2.42}$$

To emulate the Hamiltonian the best way possible the quality factors of the used components should be as high as possible. In most cases capacitors can be found with higher quality factors than inductors, which guides us to the decision to use capacitors as hopping elements and inductors for grounding. When assuming all components used not to have any manufacturing tolerances, the parasitics of components used as hopping elements will modify both the first matrix in equation 2.40 mimicking the model Hamiltonian and the second matrix introducing the eigenvalue shift. On the other hand, the parasitics of the grounding elements just enter in the prefactor of the identity matrix modifying only the eigenvalue shift.
Unavoidable fabrication tolerances should be as small as possible to not affect the structure of the Laplacian, resulting in higher costs or the need for pre-characterization. Again, commercially available capacitors usually are specified with lower tolerances than inductors. Fortunately, the impact of tolerances can be studied beforehand by computer simulations by adding random deviations to the tight binding Hamiltonian or the circuit equivalent.

Additional care must be taken when selecting the type of inductors used referring to their magnetic field distributions. When using unshielded inductors their magnetic fields can induce parasitic signals in neighboring coils, which adds additional linkage between the nodes not described by the Laplacian. To avoid this problem physical distance between the inductors should be created and/or inductors with magnetic shielding should be used (at the expense of higher magnetization losses).
The wires and traces on the printed circuit board (PCB) itself can also introduce further couplings. To be able to use the lumped-element model as mentioned at the beginning of this work (section 2.1) the introduced parasitic resistances, inductances and capacitances of the connections between the circuit elements should be kept as small as possible, at least significantly smaller than the values of the components used. Again, a trade-off

between trace length, trace width, substrate thickness, signal routing etc. has to be made to minimize those kinds of parasitics.
Also the wavelengths of the signals applied to the circuit have to be sufficiently small in respect to the trace lengths/circuit board dimensions to avoid phase lags due to the signal traveling along the circuit.

2.3.2 Lock-in technique for phase sensitive detection of AC voltages

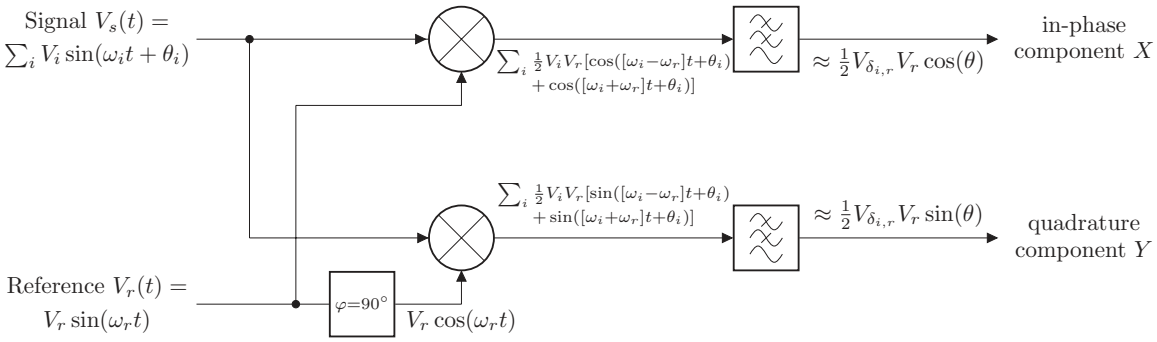

Figure 2.10: Basic operating principle of a dual-phase Lock-in amplifier. The signal is multiplied by a reference signal and its 90° phase shifted equivalent. The results are low-pass filtered to get the portions where the signal frequency ω_s approximately equals the reference frequency ω_r.

As indicated in section 2.2.3, the circuits dealt with in this work are made for AC signals. Being a complex quantity due to amplitude and phase turns the signals into suitable quantities, especially for the investigation of complex-valued Hamiltonians. However, from the measurement point of view the phase sensitive detection of these signals is more intricate than measuring DC signals.
AC signals could be recorded with an oscilloscope reading off the amplitude directly and could then be compared to a reference signal to figure out the phase shift. But as soon as the signal is composed by several frequency components because of noise or non-linear effects of the circuit the detection via oscilloscope reaches its limits.
In this regime so called lock-in amplifiers are widely used to measure a single frequency component at optimum, while the evaluation frequency is determined by a reference signal. A lot of educational introductions to lock-in amplifiers can be found describing the different measurement details and types of instruments (descriptions provided for the instruments used: [75] and [76]), which is why here only a short introduction to understand the basics of the technique is given.
A sketch of the operating principle is shown in fig. 2.10. The signal $V_s(t) = \sum_i V_i \sin(\omega_i t + \theta_i)$ is composed by sine waves with different frequencies ω_i, amplitudes V_i and phases θ_i. By multiplying with a reference signal $V_r(t) = V_r \sin(\omega_r t)$ and its 90° phase shifted equivalent, differences and sums of the frequencies arise. With an ideal low-pass filter that passes only DC signals the component where $\omega_i = \omega_r$ could be picked, resulting in

the in-phase component X and the quadrature component Y of the signal with respect to the reference signal.
A realistic filter will not be able to select the signal component of only one frequency, the damping of neighboring signal components depends on their distances in frequency instead (for an introduction to electrical filters see [77]). To lower the portion of frequency components passing the filter that do not match the reference frequency exactly two parameters can be tuned, the bandwidth and the filter roll-off.
The bandwidth of low-pass filters is defined by the intervall between zero and the cut-off frequency $f_{cut-off}$ or f_{-3dB}, describing where the transfer function of the filter exhibits an attenuation of 3 dB with respect to the DC component. The roll-off of a low-pass filter specifies how much the attenuation increases in a fixed frequency interval mostly given in decibels per octave. To get as close as possible to the ideal case the bandwidth should be as low as possible and the roll-off as high as possible. In experiment a trade-off has to be found because the improvement of both parameters results in slower filter settling. This means that the lower the bandwidth and the higher the roll-off of the filter is, the longer it takes the filter to reach the aimed measurement value, leading to longer measurement times.
Unless otherwise mentioned in this work the bandwidth is at least 10^4 times smaller than the measurement frequency and the roll-off is as high as possible. The waiting time for the filter to settle was chosen to have at least 99 % of the input voltage.
Additional attention during the circuit design has to be paid to the input impedances of the lock-in amplifiers so that the Laplacian is not affected by connecting the measurement devices. Typical values are resistances above 10 MΩ in parallel to a capacitor with several tens of picofarads.

2.3.3 AC impedance measurements

AC impedance measurement devices can be mainly split into two classes. For measurements of frequency dependent quantities like inductance or capacitance so called LCR meters can be used, which determine the inductance (L), capacitance (C) and resistance (R) of devices under test (DUT) at fixed frequencies. On the other hand, with an impedance analyzer impedances can be recorded while sweeping over freely selectable frequency ranges. These curves will be called impedance spectra in the following.
For the determination of impedances phase sensitive measurements of current and voltage similar to the lock-in technique (see sec. 2.3.2) are needed. These measurements can be carried out with a lot of different types of measurement methods, e.g. the I-V method or the auto-balancing bridge method, and various measurement setups, e.g. two- or four-terminal configuration.
Here we describe a typical shielded four-terminal impedance measurement (see fig. 2.11 a)). The instrument feeds a current through the DUT from H_{CUR} to L_{CUR} while the amplitude and phase of the current is measured at the L_{CUR} terminal, for example as a voltage drop across a current sensing resistor. The voltage measurement is performed with two separate leads to avoid measuring voltage drops caused by the current feeding lines. The connection between instrument and DUT is indicated by dashed coaxial cables signaling the variety of different connections and test fixtures. The two high (H) and low (L)

connection lines should be shielded, and the shields should be interconnected as near as possible to the DUT to omit residuals caused by test fixture or cabling.
To decrease residuals caused by the connections between the ports of the high/low terminals pairs and the DUT, correction routines can be used. The most commonly used method is the open/short compensation. Therefore, the test fixture can be seen as the equivalent circuit depicted in fig. 2.11 b). When the DUT (dashed symbol) is removed the impedance $1/(G_O + i\omega C_O)$ can be measured because it can be assumed to be much higher than $R_S + i\omega L_S$. By shortening the measurement terminals $1/(G_O + i\omega C_O)$ can be eliminated and the measured impedance equals $R_S + i\omega L_S$. Afterwards the measured residuals can be subtracted from the values achieved for the DUT. A detailed introduction in the different impedance measurement procedures, test fixtures, compensation methods, etc. can be found in reference [78].

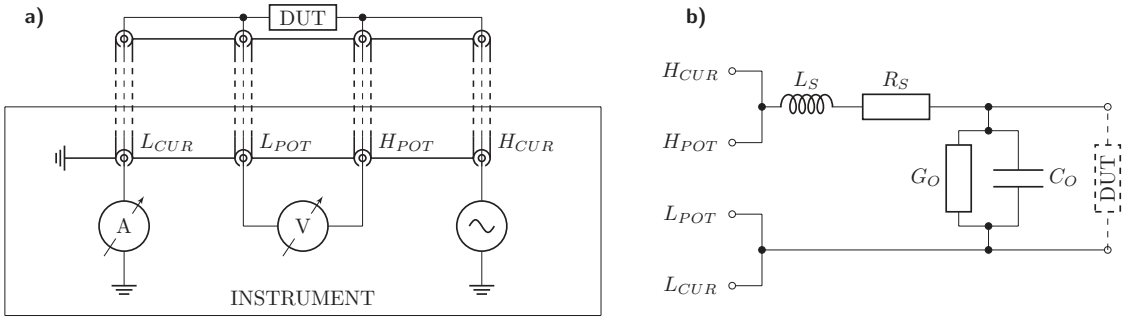

Figure 2.11: Impedance measurement and test fixture compensation. a): Schematic of a shielded four-terminal impedance measurement. The device under test (DUT) is fed by a current produced by the source at the H_{CUR} terminal and sensed via a current sensing unit at the L_{CUR} port. The voltage drop across the DUT is measured with the H_{POT} and L_{POT} terminals. b): Equivalent circuit for describing impedances of the test fixture. The lines between the connections of the high and low terminals and the DUT can be modeled by short inductance L_S, short resistance R_S, open conductance G_O and open capacitance C_O. They can be determined by measurements where the DUT is shortened or removed.

For the measurements performed in this thesis, we use both kinds of impedance measurement devices. We employ impedance analyzers to record impedance spectra of the circuit nodes to detect eigenvalues and eigenstates of the admittance matrix. And furthermore, LCR meters are used to pre-characterize circuit components that are available with high tolerances only to ensure the adequate reproduction of the tight binding model.
To pre-characterize a component its impedance is measured at a certain frequency and is converted into appropriate circuit model parameters afterwards. Consequently, all circuit models used to quantify the impedance are electrically equivalent and the choice of a specific model does not affect the measurement.
In general, capacitors and inductors can have serial and parallel resistances (see fig. 2.9) and the question is whether the serial or parallel circuit model should be chosen to represent the measured impedance.

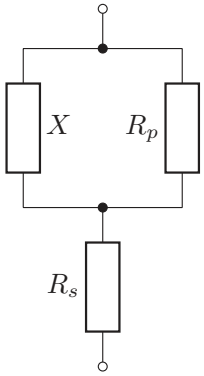

Figure 2.12: Equivalent circuit for a reactive circuit element X (capacitor/inductor) with parallel R_p and serial R_s parasitic resistances.

The overall impedance of a reactive circuit element X with parallel R_p and serial R_s resistances (fig. 2.12) is given by

$$Z = \frac{1}{\frac{1}{iX} + \frac{1}{R_p}} + R_s = \frac{R_p}{1 + \left(\frac{R_p}{X}\right)^2} + R_s + i\frac{X}{1 + \left(\frac{X}{R_p}\right)^2}. \tag{2.43}$$

Assuming that the impact of the parasitic resistances is small in respect to the reactance ($R_s < X < R_p$) leads to high values of R_p and low values of R_s. When now X is relatively high $X \lesssim R_p$, $(R_p/X)^2$ in the denominator of the parallel parasitic resistance contribution will be small compared to R_p in the nominator and the parallel contribution is much bigger than the serial one, making the serial resistance less relevant.
In contrast, if the reactance X is relatively low $R_s \lesssim X$, the quotient in the parallel parasitic resistance is small, and for sufficiently small reactances, the serial resistive contribution dominates. Therefore, as a rule of thumb for high reactances (capacitors at low frequencies, inductors at high frequencies) the parallel circuit models ($R_p - C_p$, $R_p - L_p$) and for low reactances (capacitors at high frequencies, inductors at low frequencies) the serial circuit models ($R_s - C_s$, $R_s - L_s$) should be chosen. The transition between parallel and serial circuit representation is recommended somewhere between reactances of $10\,\Omega$ (serial) and $10\,\mathrm{k}\Omega$ (parallel).
In any case, it should be mentioned that the parasitic resistances have a physical nature as they are described in section 2.2.1 and it is not given that the resistance is mostly serial/parallel just because the reactance is low/high. The rule of thumb for the choice of equivalent circuits only depends on which kind of parasitic resistance contributes more to the measurement result and does not decide which kind is more present in the DUT.

2.3.4 Electrical investigation methods and their insights

Of course, every electrical study of a circuit boils down to feeding current or applying voltage and measuring voltages and currents. Nevertheless, there are various investigation routines differing in position and number of excitation and measuring points in the circuit. As described in section 2.1 all electric properties of a circuit (as long as it meets the restriction of the lumped-port model) are given by the Laplacian or the Green's

matrix respectively. When the Laplacian has no zero eigenvalues, which is almost always the case in experiment due to parasitics and tolerances, it can be inverted into the Green's matrix with the same eigenvalues and left/right eigenvectors (see eq. 2.23).
In the following paragraphs we will describe the measurement routines used to investigate the eigenvalues and eigenvectors of the Green's matrix/grounded circuit Laplacian. When only a few restrictions are met, the existence and shape of topological edge states can be determined as well as an electric equivalent of the solid state band structure.

Zero eigenvalue detection via two-point impedance measurement

If only the information whether one or more modes with absolute value of the eigenvalue near to zero exist an impedance measurement between two points can bring insights

$$\begin{aligned} Z_{AB}(f) &= G_{AA}(f) + G_{BB}(f) - G_{AB}(f) - G_{BA}(f) \\ &= \sum_{n=1}^{N} \Bigg[\frac{1}{\lambda_n(f)} \big(\psi_{n,A}(f)\, \phi^*_{n,A}(f) + \psi_{n,B}(f)\, \phi^*_{n,B}(f) \\ &\qquad - \psi_{n,A}(f)\, \phi^*_{n,B}(f) - \psi_{n,B}(f)\, \phi^*_{n,A}(f) \big) \Bigg] \\ &= \sum_{n=1}^{N} \frac{\left(\psi_{n,A}(f) - \psi_{n,B}(f)\right) \left(\phi^*_{n,A}(f) - \phi^*_{n,B}(f)\right)}{\lambda_n(f)} \,, \end{aligned} \tag{2.44}$$

here written with frequency dependencies to call in mind that our circuits are built of frequency dependent components and that a change in frequency can change the response of the system.
Eigenvalues of magnitude zero result in a diverging impedance value due to the inverse proportionality. Because of the circuit board and the used components the circuit made of imaginary impedances will also contain parasitic resistances. Consequently, the eigenvalues cannot have an absolute value of exactly zero and the impedance cannot diverge. As explained for the SSH model in section 2.2.3 the position of the eigenvalues on the admittance axis can be shifted by the excitation frequency $f = \omega/(2\pi)$. In fig. 2.13 we see that every time an eigenvalue (blue curves) crosses zero (indicated by red vertical lines) a peak in the absolute value of the impedance (black curve) occurs. This provides us with a tool to investigate the relative positions of eigenvalues as long as they are not frequency dependent themselves. But there are a few further limitations.

First of all, the decision whether an impedance value is high or low can only be made in relation to other values (frequency sweep, theoretically estimated, etc.).
Second the impedance is not only determined by the eigenvalue but also by the entry of the eigenvectors corresponding to the nodes where the impedance is measured. For example assume a 1D SSH chain hosting only one edge mode with eigenvalue near zero localized at one edge and living on only one sublattice. If now an impedance measurement is performed at nodes near the other end of the chain or on the other sublattice, the impedance value will be low although a nearly zero eigenvalue state exists.

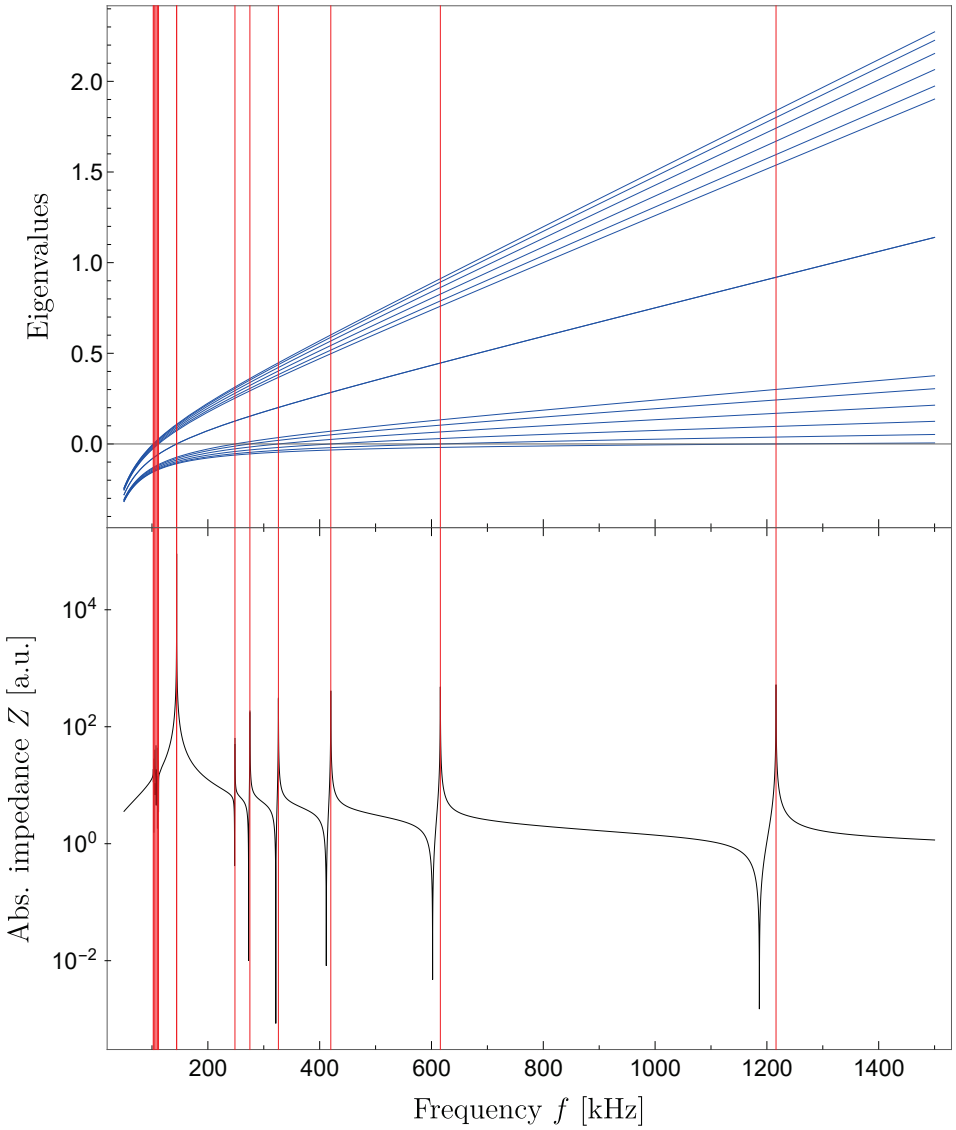

Figure 2.13: Eigenvalues and absolute value of the impedance at Node 1A to ground (equal to the first diagonal entry of the Green's matrix) of a 7 unit cell SSH circuit as a function of the frequency f. When an eigenvalue (blue curves) reaches 0 (red vertical lines) due to the shift caused by changing the frequency a resonance in the impedance (black curve) can be found.

Third, the fact that the impedance value is high does not distinguish (without any reference) whether one or more modes with eigenvalues near zero contribute to the impedance.
And fourth, the higher the resistive parasitics of the circuit are, the higher the minimum absolute value of the eigenvalue is, even if the imaginary part is tuned to exactly zero by shifting the frequency. So with higher resistive parasitics the height of the impedance peaks decreases, making the eigenvalue detection in the impedance spectrum in the worst case impossible due to low peak heights and overlapping contributions of neighboring eigenvalues.

Measuring the shape of eigenvectors

By definition, measuring the shape of an eigenvector would be like applying a voltage or current vector that is linear dependent to one left eigenvector under test and causes the current/voltage response to take the same form as the corresponding right eigenvector. In practice this procedure is unusable because the shape of the eigenvectors are not known beforehand, sources and measuring devices as much as circuit nodes would be needed and the tunable degrees of freedom would be as much as twice the number of existing circuit nodes due to magnitude and phase of the complex signals.
Hence, we need to use a similar approach as before to obtain information about the shape of an eigenvector, which again comes along with some limitations. As long as the absolute value of the corresponding eigenvalue is the value closest to zero and separated from the other eigenvalues, the Green's matrix will be dominated by the contribution of this eigenvalue λ_x and the corresponding right and left eigenvectors $\vec{\psi}_x\vec{\phi}_x^\dagger$:

$$\begin{aligned} \boldsymbol{G} &= \frac{1}{\lambda_1}\vec{\psi}_1\vec{\phi}_1^\dagger + \ldots + \frac{1}{\lambda_x}\vec{\psi}_x\vec{\phi}_x^\dagger + \ldots + \frac{1}{\lambda_n}\vec{\psi}_n\vec{\phi}_n^\dagger \\ &\approx \frac{1}{\lambda_x}\vec{\psi}_x\vec{\phi}_x^\dagger \quad \text{if} \quad |\lambda_x| \ll |\lambda_m| \quad \forall\, m \neq x \end{aligned} \tag{2.45}$$

This leaves us with the approximated Green's matrix

$$\boldsymbol{G}_{app} = \frac{1}{\lambda_x}\begin{pmatrix} \psi_{x,1}\phi_{x,1}^* & \psi_{x,1}\phi_{x,2}^* & \psi_{x,1}\phi_{x,3}^* & \cdots & \psi_{x,1}\phi_{x,N}^* \\ \psi_{x,2}\phi_{x,1}^* & \psi_{x,2}\phi_{x,2}^* & \psi_{x,2}\phi_{x,3}^* & \cdots & \psi_{x,2}\phi_{x,N}^* \\ \psi_{x,3}\phi_{x,1}^* & \psi_{x,3}\phi_{x,2}^* & \psi_{x,3}\phi_{x,3}^* & \cdots & \psi_{x,3}\phi_{x,N}^* \\ \vdots & \vdots & \vdots & \ddots & \vdots \\ \psi_{x,N}\phi_{x,1}^* & \psi_{x,N}\phi_{x,2}^* & \psi_{x,N}\phi_{x,3}^* & \cdots & \psi_{x,N}\phi_{x,N}^* \end{pmatrix} \tag{2.46}$$

which we can in principle investigate in two different ways, by measuring the voltage vector produced by a current input or by measuring different two-point impedance values. The easiest way to implement a current vector is to plug one current source between one node and ground:

$$\vec{v}_{I_k} = \boldsymbol{G}_{app}\begin{pmatrix} 0 \\ \vdots \\ I_k \\ \vdots \\ 0 \end{pmatrix} = \frac{1}{\lambda_x}\phi_{x,k}^* I_k \begin{pmatrix} \psi_{x,1} \\ \psi_{x,2} \\ \psi_{x,3} \\ \vdots \\ \psi_{x,N} \end{pmatrix} \tag{2.47}$$

So a single current at one node produces approximately a voltage vector in the shape of the right eigenvector if the eigenvalue is near zero $|\lambda_x| \approx 0$, separated from other eigenvalues $|\lambda_x| \ll |\lambda_m|$ and the corresponding left eigenvector has a non-vanishing contribution on the node where the current is fed in $\phi_{x,k}^* \neq 0$.
For a two-point impedance measurement the approximated Green's matrix leads to a result of the form of equation 2.6:

$$
\begin{aligned}
Z_{a,b} &= \frac{V_a - V_b}{I} = \frac{1}{\lambda_x} \frac{\left(\psi_{x,a}\phi^*_{x,a} - \psi_{x,a}\phi^*_{x,b}\right) I - \left(\psi_{x,b}\phi^*_{x,a} - \psi_{x,b}\phi^*_{x,b}\right) I}{I} \\
&= \frac{1}{\lambda_x} \left(\psi_{x,a} - \psi_{x,b}\right) \left(\phi^*_{x,a} - \phi^*_{x,b}\right)
\end{aligned}
\tag{2.48}
$$

By measuring the impedances of all nodes with respect to ground we can build a vector of impedances

$$
\vec{Z} = \frac{1}{\lambda_x} \begin{pmatrix} \psi_{x,1}\phi^*_{x,1} \\ \psi_{x,2}\phi^*_{x,2} \\ \psi_{x,3}\phi^*_{x,3} \\ \vdots \\ \psi_{x,N}\phi^*_{x,N} \end{pmatrix} \tag{2.49}
$$

and for normal Laplacian matrices ($\boldsymbol{J}\boldsymbol{J}^\dagger = \boldsymbol{J}^\dagger\boldsymbol{J}$), where left and right eigenvectors are the same

$$
\vec{Z}_{normal} = \frac{1}{\lambda_x} \begin{pmatrix} |\psi_{x,1}|^2 \\ |\psi_{x,2}|^2 \\ |\psi_{x,3}|^2 \\ \vdots \\ |\psi_{x,N}|^2 \end{pmatrix} \tag{2.50}
$$

we can read out the absolute square of the entries of the eigenvector weighted by the inverse of the eigenvalue.

Determination of the admittance band structure

The previous methods all contained the assumption that an eigenvalue is near zero to detect the existence of an eigenstate. The admittance band structure is independent from zero eigenvalues and is used to get insights into the bulk properties of the tested circuit. Equivalently to the energy band structure of a tight binding Hamiltonian for a crystalline system (see section 2.2) an admittance band structure for the circuit equivalent can be explored [59].
To investigate the eigenstates contributed by the bulk of the material in solid state physics a translation invariant crystal with infinite size can be assumed due to the high number of atoms in typical bulk material. In most meta-materials only a few unit cells can be built in a practical way, so that the periodic boundary conditions (PBC) of the system have to be implemented explicitly. In the lumped-element circuit model this can be done easily by just connecting the opposite ends of the circuits. In addition, to guarantee the translation symmetry of the circuit best possible the component tolerances should be kept small. This makes the Laplacian $\boldsymbol{J}$ depending only on differences of the unit cell indices

$$
\boldsymbol{J}_{(\vec{m},\alpha),(\vec{n},\beta)} = \boldsymbol{J}_{\alpha,\beta}\left(\vec{r} = \vec{m} - \vec{n}\right) \tag{2.51}
$$

with $(\vec{m}, \alpha)$ representing unit cell and sublattice site. A discretized version of Bloch's theorem can be applied using plane wave-like vectors for the basis of unit cells $\vec{r}$

$$\vec{V}_{(\vec{r},\alpha)} = \vec{V}_\alpha(\vec{k}) \cdot e^{i\vec{k}\cdot\vec{r}} \tag{2.52a}$$

$$\vec{I}_{(\vec{r},\alpha)} = \vec{I}_\alpha(\vec{k}) \cdot e^{i\vec{k}\cdot\vec{r}} \tag{2.52b}$$

The finite number of unit cells N_i in each direction leads to a discretization of reciprocal space and the total number of $\vec{k}$ values is given by the total number $N = \prod_i^D N_i$ of unit cells N_i per direction $i = 1, \ldots, D$:

$$\vec{k} = \begin{pmatrix} n_1 \frac{2\pi}{N_1} \\ \vdots \\ n_D \frac{2\pi}{N_D} \end{pmatrix} \quad \forall\, n_i \in [0, N_i[\tag{2.53}$$

This ansatz transforms the equations of the periodic grounded circuit Laplacian into decoupled quadratic blocks with sizes equaling the number of sublattice sites (greek indices) for every wave vector $\vec{k}$:

$$(\boldsymbol{J}_{per})_{(\alpha,\beta)} \left(\vec{k}\right) = \begin{pmatrix} J_{1,1}(\vec{k}) & \ldots & J_{1,\Omega}(\vec{k}) \\ \vdots & \ddots & \vdots \\ J_{\Omega,1}(\vec{k}) & \ldots & J_{\Omega,\Omega}(\vec{k}) \end{pmatrix} \tag{2.54}$$

The total number of sublattice sites is given by Ω. For the measurement process the unit cell information in voltage and current vectors is transformed by discrete Fourier transform:

$$\vec{V}_\alpha(\vec{k}) = \begin{pmatrix} \sum_{\vec{r}} V_1 e^{-i\vec{k}\cdot\vec{r}} \\ \vdots \\ \sum_{\vec{r}} V_\Omega e^{-i\vec{k}\cdot\vec{r}} \end{pmatrix} \qquad \vec{I}_\alpha(\vec{k}) = \begin{pmatrix} \sum_{\vec{r}} I_1 e^{-i\vec{k}\cdot\vec{r}} \\ \vdots \\ \sum_{\vec{r}} I_\Omega e^{-i\vec{k}\cdot\vec{r}} \end{pmatrix} \tag{2.55}$$

Here the sums extend over all unit cell positions $\vec{r}$. The fact that the circuit model describes a weighted graph, i.e. no physical length scales are needed, leads to the ability of choosing the the length scale at will. For simplicity we use tuples of integers representing the number of the unit cells in each direction. The measurement is performed by feeding currents and measuring voltages using the periodic Green's matrix $\boldsymbol{G}_{per}$:

$$\begin{pmatrix} V_1(\vec{k}) \\ \vdots \\ V_\Omega(\vec{k}) \end{pmatrix} = \begin{pmatrix} G_{1,1}(\vec{k}) & \ldots & G_{1,\Omega}(\vec{k}) \\ \vdots & \ddots & \vdots \\ G_{1,\Omega}(\vec{k}) & \ldots & G_{\Omega,\Omega}(\vec{k}) \end{pmatrix} \begin{pmatrix} I_1(\vec{k}) \\ \vdots \\ I_\Omega(\vec{k}) \end{pmatrix} \tag{2.56}$$

As long as current is fed one after another to each type of sublattice site the Fourier transformed current vectors contain only non-zero entries at the corresponding sublattice site. Consequently, measuring all voltages per current input enables us to calculate each entry of the periodic Green's matrix:

$$G_{\alpha,\beta} = \frac{V_\alpha(\vec{k})}{I_\beta(\vec{k})} \tag{2.57}$$

The Green's matrix can then be diagonalized for each value of $\vec{k}$, leading to the eigenvalues forming the admittance band structure and the corresponding eigenvectors.
Note that due to the graph nature of the circuit for computational ease we can choose a spatial basis of unit cells with orthogonal basis vectors of equal lengths to calculate the admittance band structure. When compared to a solid state model, where the spatial basis vectors do not meet these criteria, the admittance band structure can be mapped onto the solid state basis.
By appropriate choice of the working frequency the signal to noise ratio and thus the measurement results can be optimized. Each eigenstate's contribution to the Green's matrix is weighted with the inverse eigenvalue, i.e. the higher the eigenvalues are the lower is the state's contribution to the measurement signal. Therefore, the measurement frequency should be chosen to minimize the maximum of absolute values of the eigenvalues.

Reconstruction of the grounded circuit Laplacian

When it is necessary to analyze all eigenstates and eigenvalues, e.g. for a circuit with open boundary conditions (OBC), and no further symmetry arguments can be used to reduce the measurement effort, the measurement process from the previous paragraph can be extended to evaluate the complete grounded circuit Laplacian.
Again the Green's matrix can be measured and the structure of the grounded circuit Laplacian (eigenvalues/-vectors, matrix representation, etc.) can be determined numerically by diagonalization, matrix inversion etc. To measure all entries of the Green's matrix (see eqs. 2.25 and 2.26 in section 2.1.3) a current has to be fed in between each node and ground (independent of sublattice site or unit cell) while all voltages of all nodes have to be measured for each single current input. The measurement effort thus scales with the number of unit cells and sublattice sites per dimension. The total number of measurement M_{ges} that have to be carried out is given by:

$$M_{ges} = \left(\Omega \prod_{i=1}^{D} N_i\right)^2 + \Omega \prod_{i=1}^{D} N_i = \Sigma(\Sigma + 1) \tag{2.58}$$

Here Ω is the number of sublattice sites per unit cell, N_i specifies the number of unit cells in each of the D dimensions and $\Sigma = \Omega \prod_{i=1}^{D} N_i$ is the total number of nodes in the circuit. The first summand contains the number of voltage measurements that have to be taken for each of the current inputs. The second term adds the current measurements needed for every current input.
Here it can be seen that as soon as the circuit contains a large number of nodes (be it due to a huge amount of unit cells or higher dimensionality) the process to evaluate the total circuit system gets long and options to speed up the measurement routine are needed. A few possibilities that were considered during the work on this topic are listed in the next paragraph.

2.3.5 Speeding up the measurement process

To reduce the time needed to carry out the measurements for analyzing the circuit, various options can be taken into consideration. As explained in section 2.3.2 the accuracy

of the lock-in technique mainly depends on the bandwidth and roll-off of the low-pass filter, and increasing the accuracy leads to an increase of the measurement duration.
Therefore, the only way of reducing the individual measurement durations without decreasing accuracy is to increase the working frequency. This can only be done to some extents because the working frequency is limited by the measurement instruments and the circuit design. As soon as the wave length of the signals gets in the order of the physical dimensions of the investigated circuit the lumped-element model holds no longer true due to phase shifts of the traveling signals introduced by trace lengths, etc.
Furthermore, by increasing the working frequency, i.e. the resonance frequency f_r of the circuit, the capacitance and/or inductance values used to build the circuit have to be chosen smaller due to the inverse dependency of the resonance frequency $f_r = 1/(2\pi\sqrt{L_{\mathrm{p,ges}}C_{\mathrm{p,ges}}})$ of the total parallel capacitance $C_{\mathrm{p,res}}$ and the total parallel inductance $L_{\mathrm{p,res}}$ used in the circuit.
The smaller capacitances and/or inductances are chosen the closer they reach to the parasitic contributions of the circuit board, again leading to the breakdown of the lumped-element model.
Thus, we primarily considered ways to parallel or automate the measurement process. A few options and their advantages and disadvantages are presented in the following paragraphs.

Parallel measurements with multiple devices

The easiest way to speed up the measurement process can be implemented by using several devices to carry out multiple measurements simultaneously. As a result the measurement time can be reduced by a factor equal to the number of devices. Of course this can only be done to some extent, limited by the costs, required spaces, test lead lengths, etc.
But there are some additional limitations given by the measurement task itself. Several two-point impedance measurements (excluding variants using a common current source) cannot be carried out in parallel because the currents induced by devices used simultaneously would affect the other measurements. Therefore, only measurements with common current sources can use parallel voltage measurements, as it is the case for measuring the shape of eigenvectors or determining Green's matrices to evaluate the admittance band structure or reconstruct the Laplacian.
The main requirement is set by the phase sensitive measurement, leading to the need of synchronization. Depending on the type of lock-in amplifiers (used instruments: SR530 (Stanford Research Systems), 3961 (Ithaco, Inc.) and DSP7265 (AMETEK, Inc.)) this can be done, for example, by using the same external reference signal, which is in-phase with the current input, and adjusting all instruments in-phase to the reference signal. For our multi-device MFLI (Zurich Instruments AG) measurement setup the oscillators and measurements of the lock-in amplifiers were synchronized using their internal multi-device synchronization function. Here the 10 MHz clocks are synchronized and master/slave control is introduced.

Measurement automation by multiplexers

Another approach aims to automate the connection between the measurement devices and the circuit nodes. As long as more voltages/currents than the number of measurement instruments are measured the connections between circuit and lock-in amplifier have to be reassigned for each measurement cycle. This leads to waiting times, ties up human resources and can be the reason of assignment errors.
To overcome these problems, the use of electrical switching components like relays and multiplexers was considered. Multiplexer solutions were preferred over relay circuits due to less space requirements, power consumption, etc.

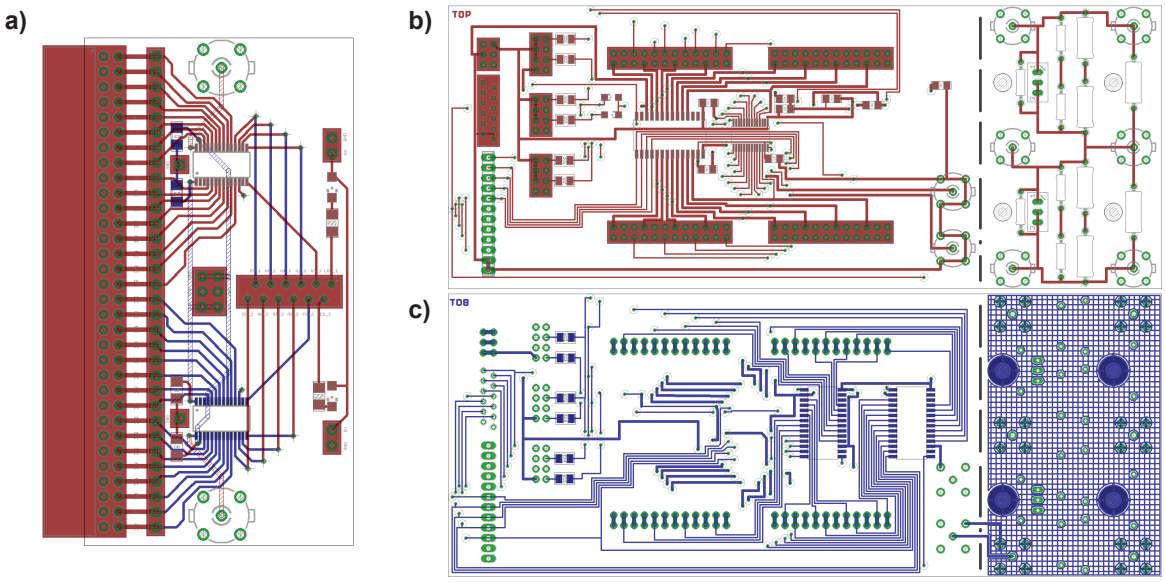

Figure 2.14: Circuit board designs of two multiplexer boards used to automate the instrument-circuit connection. a): Dual 16:1 voltage multiplexer board, the ground planes on the two inner layers are not shown. Circuit board connection via a right-angled 32x2 socket header [79] (red rectangle at the left) that is soldered and glued on the circuit board for mechanical stability. From left to right it is followed by a 32x1 pin header and two ground pins used for current input [80], two 16:1 analog multiplexer with TSSOP-28 package (MUX36S16IPW [81]), a 3x2 pin header [80] for positive and negative power supply for the mutliplexers (in the middle), two BNC sockets [82] (top and bottom) connected to the drain pin of the multiplexers, a WR-MM female connector[83] for digital communication and two 2x1 pin header [80] (5 V digital power supply) with LEDs [84],[85] indicating active multiplexers. b),c): Top and bottom side of a 16 port voltage and current multiplexer board with measurement state indication. The detailed description of this circuit board and the used components can be found in appendix A.2.

In figure 2.14 two developed multiplexer boards are shown. Depending on the size of the circuit and the number of measurement devices the process can be automated for the most part. But there are also a few problems coming along with the measurement

automation by multiplexers. Due to the small outline and the finite off-isolation of the multiplexers crosstalk between the different channels in the device and along the connecting traces can be introduced, the input/output capacitances (few tens of picofarads) can affect the grounded circuit Laplacian, etc.

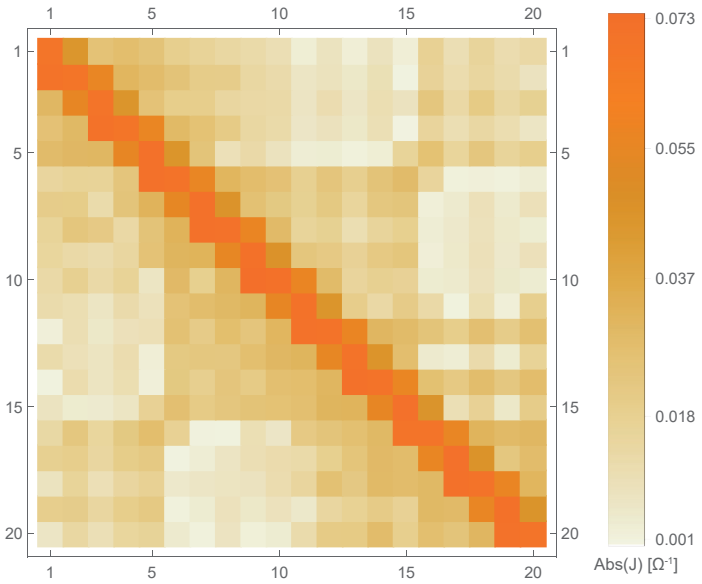

Figure 2.15: Measurement of the grounded circuit Laplacian of an open 1D chain (see section 4.2) performed with multiplexer boards depicted in 2.14 b),c). The nodes 1-5 & 16-20 and 6-15 are measured by using one multiplexer board each.

In fig. 2.15 a measurement of the grounded circuit Laplacian of a 1D chain (see section 4.2) using multiplexer boards as shown in fig. 2.14 b),c) is presented. The expected main features of the Laplacian (diagonal and upper and lower secondary diagonals) can be seen, but some additional structure on the other nodes that is in good agreement with the regions connected by different multiplexer boards can also be found.
Therefore, the automation with multiplexers should be used with caution, always evaluating whether the effects caused by the multiplexers distort the properties of the investigated model too much.

2.4 Symmetries and their impacts on grounded circuit Laplacians

For the theoretical investigation of condensed matter systems symmetries play an important role to describe the behaviour of the model without the need of precise knowledge of all model parameters.
They can be used to classify systems and restrict and predict their properties, e.g. ruling out which kind of systems can have topological non-trivial properties [16], [86]. In the following we briefly introduce the important symmetries appearing in the investigated models. Further information on circuit symmetries can be found in [57, 62, 63] and [69–71].

Hermiticity

In quantum mechanics an linear operator is called Hermitian when it equals to its conjugate transpose. As a consequence of this all eigenvalues of the Hermitian operator are real-valued, which leads to the conservation of energy in the quantum system. In the process of representing a tight binding Hamiltonian by a circuit we translate real-valued hopping terms into imaginary component admittances (see section 2.2). Therefore, a Hermitian Hamiltonian yields an anti-Hermitian grounded circuit Laplacian $\boldsymbol{J}$:

$$\boldsymbol{J} \;=\; -\boldsymbol{J}^{\dagger} \quad \Leftrightarrow \quad J_{(i,\alpha),(j,\beta)} \;=\; -J^{*}_{(j,\beta),(i,\alpha)} \tag{2.59}$$

Here, $J_{(i,\alpha),(j,\beta)}$ is an entry of the matrix $\boldsymbol{J}$ whose position in the matrix is determined by unit cells i and j and sublattice sites α and β. This means that the real part of $\boldsymbol{J}$ has to be skew-symmetric and the imaginary part has to by symmetric. The eigenvalues j_n of the grounded circuit Laplacian then have to be purely imaginary:

$$j_n \;=\; -j_n^{*} \quad \Leftrightarrow \quad \mathfrak{Re}\left[j_n\right] \;=\; 0 \tag{2.60}$$

When the Laplacian is transformed into reciprocal space $\boldsymbol{J}(\vec{k})$ the restrictions and implications for the Laplacian matrix stay the same:

$$\begin{aligned} \boldsymbol{J}(\vec{k}) \;&=\; -\boldsymbol{J}^{\dagger}(\vec{k}) \quad \Leftrightarrow \quad J_{\alpha,\beta}(\vec{k}) \;=\; -J^{*}_{\beta,\alpha}(\vec{k}) \\ j_m(\vec{k}) \;&=\; -j_m^{*}(\vec{k}) \quad \Leftrightarrow \quad \mathfrak{Re}\left[j_m(\vec{k})\right] \;=\; 0 \end{aligned} \tag{2.61}$$

Consequently, the conservation of energy can be transferred directly into a circuit representation. There is no dissipation in circuit systems that can be described by a Hermitian grounded circuit Laplacian. Purely imaginary eigenvalues for the Laplacian can only be obtained without the use of resistive elements that convert electrical energy into heat and as a result do not conserve the energy of the system.

Reciprocity

First of all, it has to be mentioned that different definitions of reciprocity exist. In this work we will deviate from the definition by the reciprocity theorem in electrical

engineering and use a more general statement. Here, the grounded circuit Laplacian is said to be reciprocal if every current I_{ij} running from one node i to another node j equals the negative of the current I_{ji} flowing in the reverse direction, i.e. charge is conserved and no current sinks or sources are present in the circuit elements used to build the Laplacian. Mathematically speaking this means that the real space Laplacian is equal to its transpose

$$\boldsymbol{J} = \boldsymbol{J}^\top \quad \Leftrightarrow \quad J_{(i,\alpha),(j,\beta)} = J_{(j,\beta),(i,\alpha)} \,. \tag{2.62}$$

The transposition of the unit cells ($i \leftrightarrow j$) leads to the reversion of the wave vector $\vec{k}$ in reciprocal space and the transposition of the sublattice sites ($\alpha \leftrightarrow \beta$) produces a transposition of the Laplacian in reciprocal space:

$$\boldsymbol{J}(\vec{k}) = \boldsymbol{J}^\top(-\vec{k}) \quad \Leftrightarrow \quad J_{\alpha,\beta}(\vec{k}) = J^\top_{\beta,\alpha}(-\vec{k}) \tag{2.63}$$

Because the determinants of a matrix and its transpose are the same we can derive further restrictions for the eigenvalues $j_m(\vec{k})$ of the grounded circuit Laplacian in $\vec{k}$-space:

$$j_m(\vec{k}) = j_m(-\vec{k}) \tag{2.64}$$

Consequently, the spectrum in reciprocal space is symmetric about $\vec{k} = 0$ and the admittance eigenvalues are two-fold degenerate. As an example, every circuit made of only capacitors, inductors and resistors is reciprocal by this definition.
Deviating from the reciprocity theorem circuits made of, for instance, passive non-linear elements such as diodes can have a reciprocal Laplacian, too, because the current going from left to right and vice versa is the same and the orientation and magnitude of the applied voltage is not taken into account in this definition. To avoid confusion we will state reciprocity of the grounded circuit Laplacian, not of the circuit which is described.

Chirality

An operator $\hat{H}$ is said to be chiral symmetric, sublattice symmetric or bipartite if it satisfies the equation

$$\hat{\Sigma}_z \hat{H} \hat{\Sigma}_z^\dagger = -\hat{H} \,, \tag{2.65}$$

i.e. it anti-commutes with the sublattice operator $\hat{\Sigma}_z$. The sublattice operator has to be unitary and Hermitian $\hat{\Sigma}_z^\dagger \hat{\Sigma}_z = \hat{\Sigma}_z^2 = 1$, it needs to be local, i.e. it must not act between different unit cells. Furthermore, the symmetry also has to be robust, i.e. equation 2.65 has to be fulfilled for disorder on the parameters. It can be written in terms of the two sublattice projectors $\hat{P}_A$ and $\hat{P}_B$:

$$\hat{\Sigma}_z = \hat{P}_A - \hat{P}_B \tag{2.66}$$

This symmetry leads to some implications for the energy spectrum and eigenstates of the Hamiltonian. First of all, the spectrum has to be symmetric because every eigenstate with eigenvalue E has a chiral symmetric partner with eigenvalue $-E$. Chiral symmetric non-zero energy eigenstates $(|\psi_n\rangle \,, \hat{\Sigma}_Z |\psi_n\rangle)$ are orthogonal and therefore, have to have equal support on both sublattices:

$$0 = \langle \Psi_n | \hat{\Sigma}_z | \Psi_n \rangle = \langle \Psi_n | \hat{P}_A | \Psi_n \rangle - \langle \Psi_n | \hat{P}_B | \Psi_n \rangle \tag{2.67}$$

Zero energy eigenstates ($\hat{H}\,|\Psi_n\rangle = 0$) satisfy the equation

$$\hat{H}\hat{P}_{A/B}\,|\Psi_n\rangle \;=\; \frac{1}{2}\hat{H}\left(|\Psi_n\rangle \pm \hat{\Sigma}_z\,|\Psi_n\rangle\right) \;=\; 0 \tag{2.68}$$

because $\hat{P}_{A/B} = 1/2 \cdot (\hat{\mathbb{I}} \pm \hat{\Sigma}_z)$ and thus can be chosen to have non-zero contributions only on one sublattice and are chiral symmetric partners of themselves [72]. Because chirality also holds true for complex entries of the matrix $\boldsymbol{H}$ it directly translates to the grounded circuit Laplacian.

Parity

A parity transformation $\hat{\mathcal{P}}$ can be expressed by a unitary operator introducing a flip in sign in one spatial coordinate, but in three dimensions it can also be achieved by flipping all coordinates. An operator $\hat{H}$ is said to be invariant under parity transformation when it commutes with the hermitian ($\hat{\mathcal{P}}^\dagger\hat{\mathcal{P}} = 1$) and unitary ($\hat{\mathcal{P}}^2 = 1$) parity operator $\hat{\mathcal{P}}$:

$$\left[\hat{\mathcal{P}}, \hat{H}\right] \;=\; 0 \tag{2.69}$$

The eigenstates of this operator are then eigenstates of the parity operator, too. Due to the unitarity of the parity operator the eigenvalues of it can only be ± 1 corresponding to even ($+1$) or odd (-1) parity. Therefore, the eigenstates of $\hat{H}$ can only be purely even or odd.
Again there are no further restrictions on the operator making the symmetry directly applicable to the grounded circuit Laplacian either.

Time-reversal symmetry $\hat{\mathcal{T}}$

A process is time-reversal symmetric if it works the same for time running forward and backward. Hence the transformation of the describing quantities under time-reversal have to be taken into account. Voltage V and charge Q do not depend on the direction of time and therefore are even under time-reversion $t \to -t$, whereas the current as the flow rate of electrically charged particles is odd $I \to -I$ under time-reversion $t \to -t$ because the charged particles reverse their traveling direction if time is reversed.
Capacitors and inductors connect the time-reversal symmetric quantities charge Q and voltage V in an even way because of the even numbers (0 and 2) of time derivatives:

$$Q_C(t) \;=\; CV_C(t) \qquad V_L(t) \;=\; L\frac{\mathrm{d}^2 Q_L(t)}{\mathrm{d}t^2} \tag{2.70}$$

Resistors instead break time-reversal symmetry due to the connection of odd and even time-reversal quantities:

$$V_R(t) \;=\; RI_R(t) \tag{2.71}$$

For the grounded circuit Laplacian formalism time-reversal symmetry translates into the condition that it needs to be a purely imaginary matrix:

$$\boldsymbol{J} \;=\; -\boldsymbol{J}^* \quad \Leftrightarrow \quad J_{(i,\alpha),(j,\beta)} \;=\; -J^*_{(i,\alpha),(j,\beta)} \tag{2.72}$$

For real matrices we know that the eigenvalues are real or occur in complex conjugated pairs. Therefore, for purely imaginary matrices the eigenvalues have to be purely imaginary or come in pairs with positive and negative real part. In reciprocal space these pairs belong to the positive and negative wave vector $\vec{k}$ because the wave vector is odd under time-reversion, making the spectrum symmetric about the real axis in the complex plane:

$$\begin{aligned} \boldsymbol{J}(\vec{k}) \;=\; -\boldsymbol{J}^*(-\vec{k}) \quad \Leftrightarrow \quad J_{\alpha,\beta}(\vec{k}) \;=\; -J^*_{\alpha,\beta}(-\vec{k}) \\ j_m(\vec{k}) \;=\; -j^*_m(-\vec{k})\,. \end{aligned} \tag{2.73}$$

3 Topological phenomena in Hermitian systems

In this part we are going to briefly discuss three projects that have been investigated in the author's master thesis [66] (written in German). They serve as prime examples to experimentally demonstrate the connections between solid state materials and electrical circuit lattices [68] and show the opportunities and limitations of the electric metamaterial platform. Based on these findings, design rules and investigation techniques are deduced for the investigation of circuits describing topological phenomena stemming from system beyond the linear Hermitian regime. Those will be elaborated in the main part of this work in chapter 4. The single particle tight binding Hamiltonian describing the solids are translated into coupled electrical resonator networks whose grounded circuit Laplacians, i.e. the circuit admittances, obey the same coupling structure as the tight binding Hamiltonians (as explained in sec. 2.2). Consequently, the electrical investigation methods introduced in section 2.3.4 are used to analyze eigenvectors and eigenvalues given by the admittance matrix of the circuit, which can be traced back to solid state properties.
We will see how a two-point impedance measurement can be used to detect the existence of topological edge modes, how a measurement of the circuit node voltages provides information about the spatial profile of the edge modes and how a current-voltage measurement procedure applied to a periodic circuit lattice can emulate the band structure of the solid.
Therefore, topological edge states in the SSH lattice introduced in section 2.2.2 as an example for the circuit-solid equivalence (sec. 2.2.3), and its band structure are analyzed (sec. 3.1). Subsequently, the two dimensional band structure of the honeycomb lattice with its Dirac cone feature is investigated (sec. 3.2). And finally, the topological edge mode detection is used to verify a theoretically predicted second-order 2D topological insulator, also known as a quadrupolar topological insulator (sec. 3.3).

3.1 Edge states and band structure of the SSH model

The one-dimensional SSH model is often used as an pedagogical starting point when introducing topology in condensed matter physics (e.g. see [72]). Its properties have already been explained in section 2.2.2 where it was used to explain the translation from the tight binding model into an electrical circuit (section 2.2.3).
The measurements described here originate from the author's master thesis [66] (chapter 4, written in German) and are explained in technical detail there. Some of the results are also published in [58].
Due to the real symmetric Hamiltonian (eq. 2.29) it is a time-reversal symmetric and Her-

mitian model conserving energy and having purely real eigenvalues. Consequently, the grounded circuit Laplacian of the ideal circuit representation has to be anti-Hermitian with imaginary eigenvalues. As explained in section 2.2.3 it is built of capacitors and inductors and therefore, preserves reciprocity, i.e. has a symmetric spectrum $j(k) = j(-k)$. Sublattice (chiral) symmetry adds equal support of the eigenvectors on both sublattices, makes the eigenvalue spectrum symmetric and opens the opportunity for eigenstates with zero eigenvalues to have only non-zero contributions on one sublattice site. In addition, parity is also preserved, resulting in purely even or odd eigenstates. Illustratively, the chain could be flipped, which just leads to an interchange of sublattice labels. This holds true as long as the chain is made of whole unit cells, i.e. an even number of nodes. Therefore, in an ideal symmetric model topological edge states can only appear in an even or odd combination of left and right edge mode (see fig. 2.4). In experiment we will see that parity is broken due to component tolerances and the linear combinations fall apart in a mainly left and a mainly right localized edge mode.

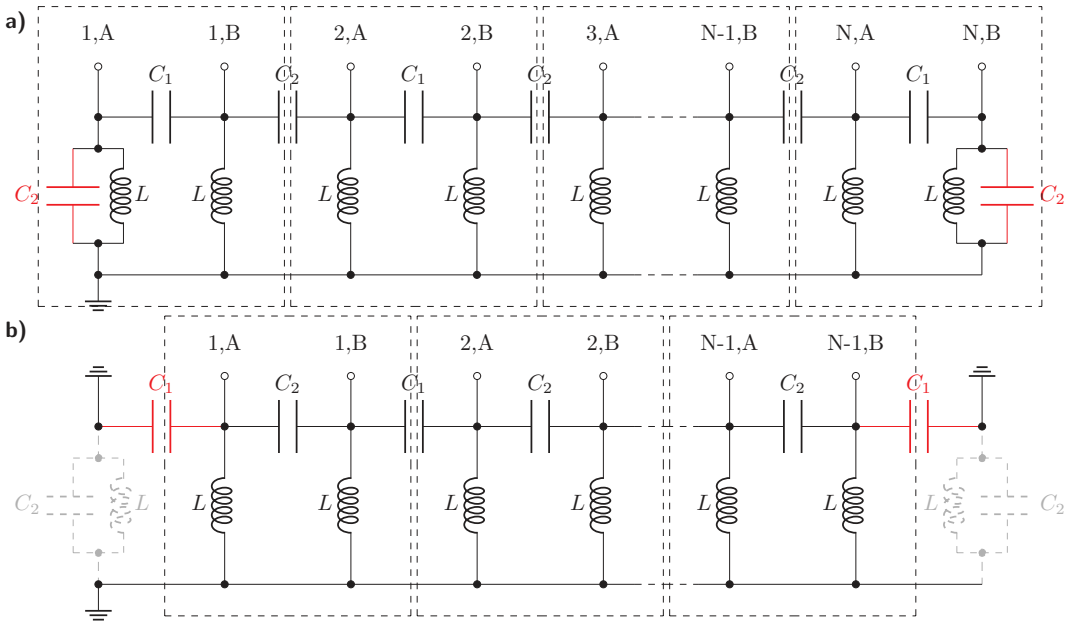

Figure 3.1: Switching topological regimes of SSH circuit by grounding the first and last node of the chain. a): SSH chain of N unit cells, the topological regime is determined by $t = \frac{C_1}{C_2}$. An additional capacitor to ground (red) is needed to fix the total node conductance of the first and last node. b): By grounding the first and last node of the chain shown in a) the first and last hopping capacitor (red) takes the role of the additional circuit element fixing the total node conductance. The capacitors C_1 and C_2 are interchanged, leading to a N-1 unit cell chain in the opposite topological regime (adapted from [66]).

3.1.1 10 unit cell SSH circuit

The SSH circuit was built in two versions with different components and working frequencies. The first version of the SSH circuit was built of class 1 ceramic SMD (surface-mounted device) capacitors ($C_1 = 22\,\mathrm{nF} \pm 1\,\%$, $C_2 = 100\,\mathrm{nF} \pm 1\,\%$) and toroidal inductors

($L = 10\,\mu\text{H} \pm 10\,\%$). As already explained in section 2.3.1 the capacitors were chosen as hopping elements due to the lower tolerances and higher quality factors; the inductors were used as grounding elements. The 10 unit cell circuit with a resonance frequency, i.e. a working frequency tuning the diagonal of the grounded circuit Laplacian to zero, of $f_r \approx 144.1\,\text{kHz}$ was arranged in a U shape on the PCB (see ref. [66] appendix A.1).

As long as C_1 is not equal to C_2, the model should have an energetic gap between the two bands in which the the edge states are energetically located when the system is in the topological phase ($C_1 < C_2$, see sec. 2.2.2). When the working frequency is chosen near the resonance frequency the topological edge states should have eigenvalues with magnitude nearly zero and therefore dominate the two-point impedance (see sec. 2.3.4). To compare the circuit in both topological regimes no changes of the hopping capacitors need to be done. By grounding the ends of the chain the capacitor used to couple the first/last node of the chain to the neighboring node plays the role of the additional capacitor needed to fix the resonance frequency at the edges of the lattice (fig. 3.1) and the topological regime is switched, which can be seen by a redefinition of the unit cell.

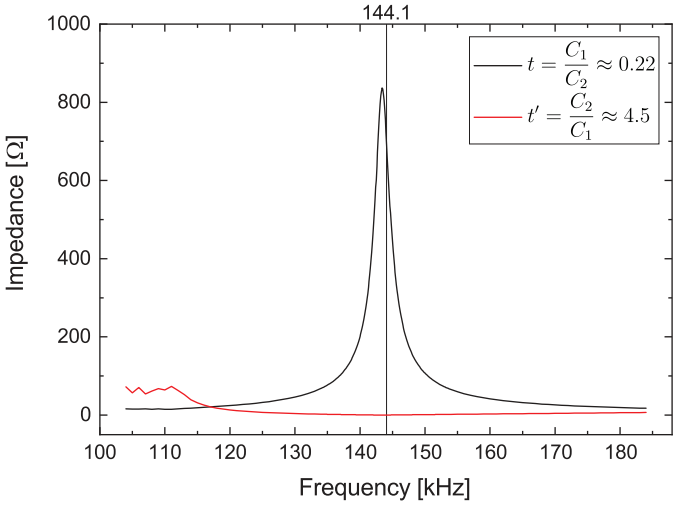

Figure 3.2: Impedance spectra of the left edge node recorded from the first version of the SSH circuit. Black: $t < 1$, 10 unit cells, topological regime, red: $t' > 1$, 9 unit cells, topologically trivial regime. The vertical line indicates the theoretically expected resonance frequency $f_r = \frac{1}{2\pi\sqrt{(C_1+C_2)L}}$ (adapted from [66]).

In figure 3.2 the impedance spectra from the left edge node near the resonance $f_r = 144.1\,\text{kHz}$ are shown. In the topological regime $t < 1$ (black curve) a peak in impedance near f_r can be found, indicating that modes with eigenvalue near zero and contributions at the left edge exist. Furthermore, this peak vanishes when the the configuration is switched to the topologically trivial regime $t' > 1$ (red curve). The slight deviation of the resonance frequency from the theoretically expected value is caused by the component tolerances and the finite peak height results from finite quality factors, tolerances and parasitic resistances of the PCB.

To check whether the shape of the eigenvector that is present in the topological regime equals an exponentially decaying topological edge mode a current was fed into the left-most node and the voltage profile of the whole chain was measured (see fig. 3.3).
A topological edge mode should have exponentially decaying entries only on one sublattice that alternate in sign. As mentioned in the beginning of this section the hybridization of the edge states brakes down due to component tolerances and finite size effects leading to an eigenvector that is dominated by one of the two edge modes (for details see [66]).The data points 1A-6A on sublattice A in fig. 3.3 are consistent with the theoretically expected exponential decay, while the absolute values of the voltages at the other end of the chain increase again independently of their sublattice type.
The fact that the voltage signal does not further decrease could stem from reaching the noise floor of the measurement device, but on the other hand the voltage increases again at the other end of the chain, which could be a result of inductive coupling between the toroidal coils located at the ends of the chain due to their spatial proximity because of the U shaped geometry.

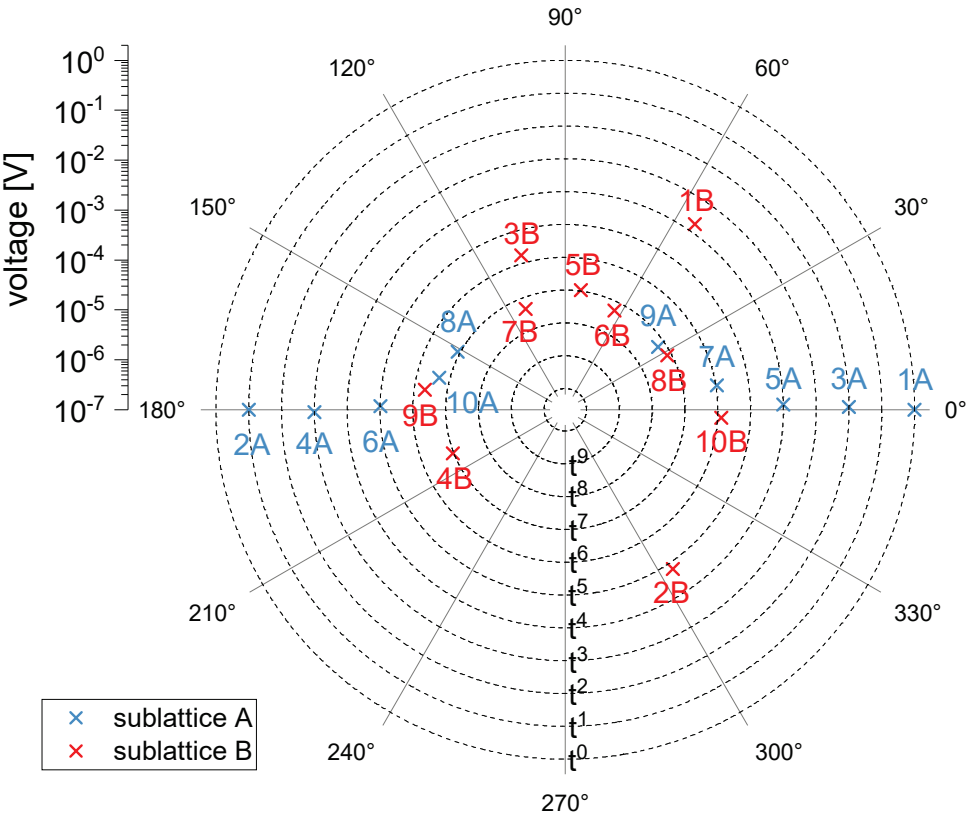

Figure 3.3: Normalized voltages measured at the SSH circuit version 1 for current input ($f = 144.15\,\text{kHz}$) at node 1A. Note that the radial direction has a logarithmic scale and the phase is measured in relation to the voltage at node 1A. The dashed rings indicate powers of $t = 0.22$ to compare with the theoretical decay length of a topological edge mode (adapted from [66]).

3.1.2 20 unit cell SSH circuit

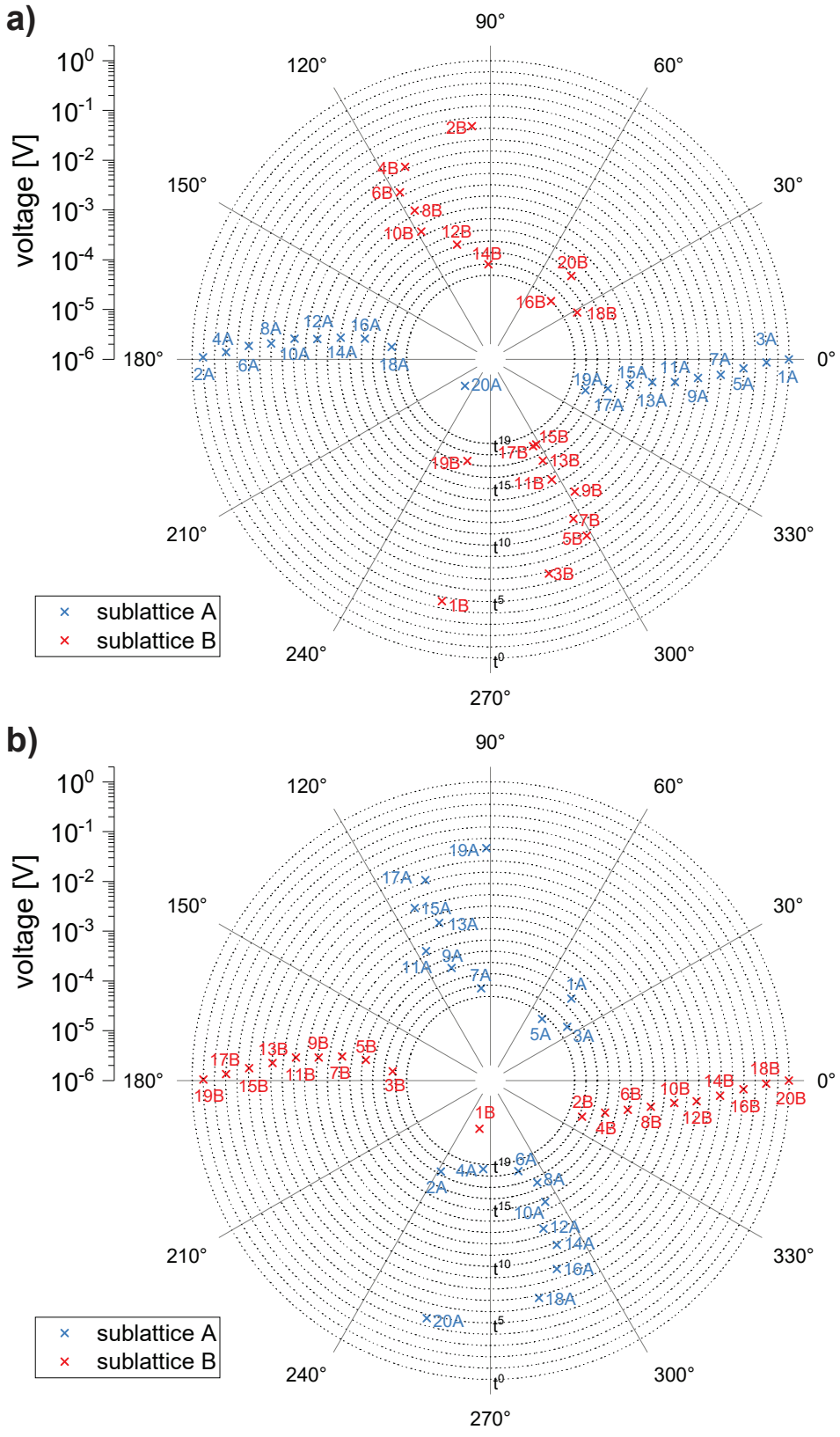

Figure 3.4: Normalized voltage profiles of the 20 unit cell SSH circuit version 2 at $f = 14.3\,\mathrm{kHz}$. The radial direction has a logarithmic scale, the phase is measured in relation to the current input node. Dashed rings indicate powers of $t = 0.59$ to compare with the theoretical decay length of the corresponding topological edge modes. a): Current input at node 1A (left end), b): current input at node 20B (right end) (adapted from [66]).

To get a better understanding of the phenomena observed in the circuit, a second version of the SSH model was designed (see ref. [66] appendix A.2). Here, the capacitance ratio $t = 0.59$ was chosen to ensure a slower decay to be able to build a longer chain without falling below the minimum voltage measured before. Additionally, magnetic shielded inductors $L = 10\,\mu\text{H} \pm 20\,\%$ were selected to avoid inductive coupling.
To keep magnetization losses small a low working frequency was aspired, leading to the need of higher capacitance values, which could be achieved by using SMD capacitors of class 2 (higher permittivity, but lower accuracy and long-term stability). Due to the high tolerances of the shielded inductors and the variation of capacitance caused by the properties of the class 2 ceramic capacitors a pre-characterization of the circuit components was done to reduce tolerances ($L = (10.59 \pm 0.01)\,\mu\text{H}$) and find out the actual values of the capacitors near the working frequency ($C_1 = (4.33 \pm 0.01)\,\mu\text{F}$, $C_2 = (7.30 \pm 0.02)\,\mu\text{F}$ for $f = 11\,\text{kHz}$). In figure 3.4 the voltage profiles for current input at the left and right end of the chain are shown together with dashed circles indicating powers of $t = C_1/C_2 = 0.59$. The expected exponentially decaying behaviour with 180° phase shift of topological edge modes can be found for both ends of the chain. An additional clockwise phase shift that increases uniformly with the decay of the edge modes exists. But here the effect can be explained precisely with the finite quality factor of the class 2 ceramic capacitors having non-zero resistive contributions in impedance. The deviations from the expected decay at the last sites (opposite end of the chain with respect to the current input) is due to the finite system size and can be found in simulations as well. The exact exponential decaying edge state is a solution only for the infinite lattice (for details see [66]).

To study the transition between the topologically distinct regimes, impedance spectra and admittance band structures have been measured. Therefore, an additional circuit board with $t = 1$ ($C_1 = C_2 = (4.33 \pm 0.01)\,\mu\text{F}$) probing the transition point has been assembled. In fig. 3.5 a) the impedance spectra at the end of the chains in different topological regimes are shown. For $t < 1$ an impedance peak due to the topological edge mode occurs, whereas for $t > 1$ (first and last node grounded) a minimum corresponding to the band gap of the insulator can be found. At the transition point $t = 1$ a continuous sequence of peaks that do not differ significantly in amplitude can be found, indicating the gap closing in the solid-state equivalent.
To analyze the electronic equivalent of the band structure the ends of the chain were connected and the procedure to measure the admittance band structure (as described in section 2.3.4) was executed. Due to the imaginary admittances used to build the real valued hoppings of the SSH model the admittance band structure is expected to be purely imaginary. Consequently, the imaginary parts of the eigenvalues calculated from the spatially Fourier transformed signals are plotted in fig. 3.5 b) in agreement with the theoretically expected curves. As already indicated by the impedance spectra the band structure of the circuit with $t = 1$ shows a gap closing for $k = \pm\pi$ while the $t = 0.59\,/\,t = 1.7$ circuit features a band gap in the Brillouin zone.
Parasitic resistances in the non-ideal circuit elements can affect the admittance eigenvalues in various ways. Assuming no component tolerances, a real part in the admittance of the grounding elements (here: inductors) would only produce a shift in the real part of the eigenvalues (grounding elements contribute only on the diagonal entries of the Laplacian matrix).

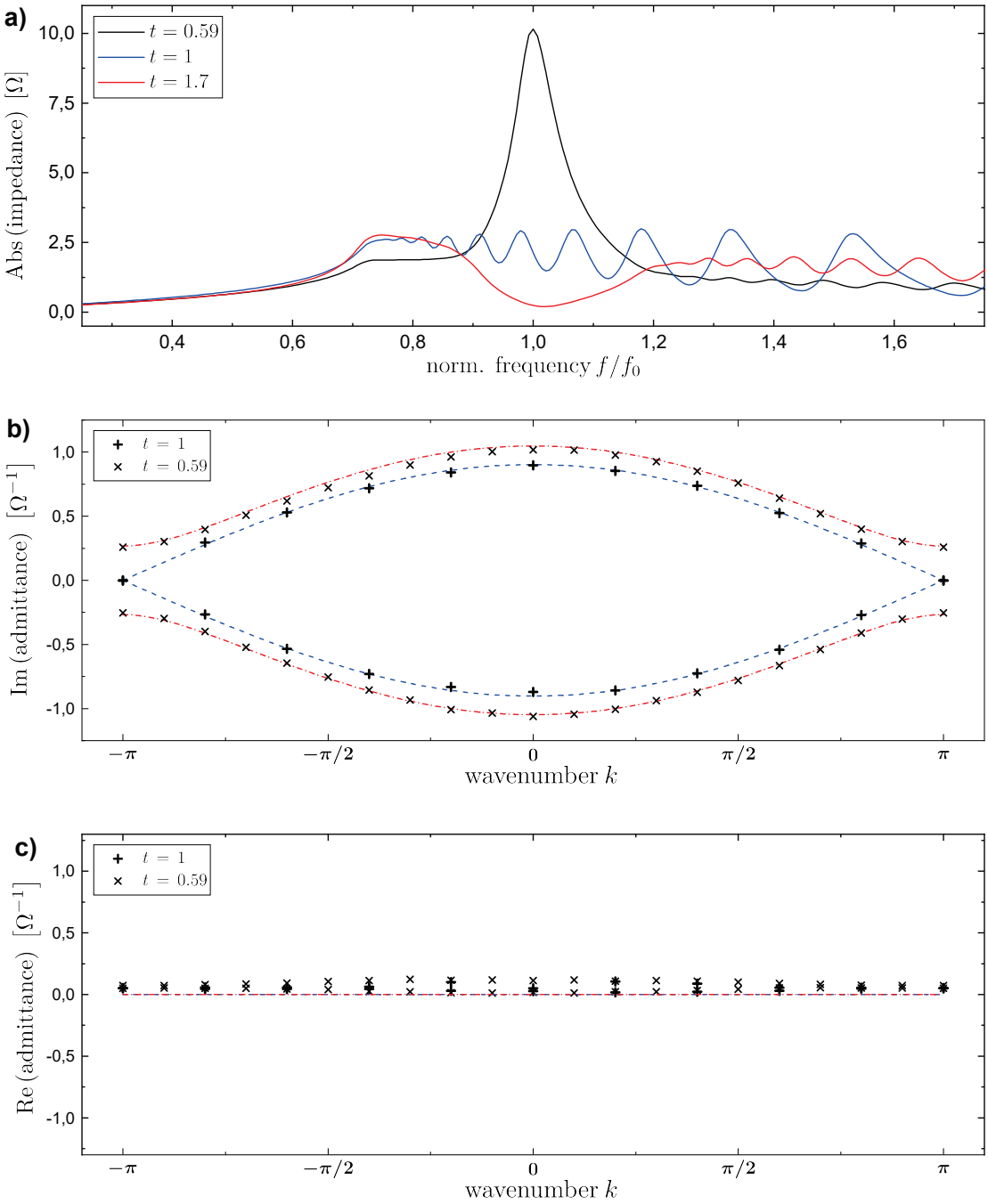

Figure 3.5: Impedance spectra and admittance band structures of SSH circuits with different hopping ratios t. a): Impedance spectra with normalized working frequencies at the left edges of the circuits: 20 unit cells $t = 0.59$ (blue, $f_0 = 14.3\,\text{kHz}$), 10 unit cells $t = 1$ (black, $f_0 = 16.45\,\text{kHz}$) and 19 unit cells $t = 1.7$ (red, $f_0 = 14.3\,\text{kHz}$). b),c): Imaginary and real part of the admittance band structure of the circuits described in a) measured at f_o. Due to the periodicity the circuits for $t = 0.59$ and $t = 1.7$ are the same. Here, 20 unit cells are used. The dashed lines are theoretically proposed curves (adapted from [59]).

Resistive contributions to the hopping elements (here: capacitors) will be added to both the overall shift in real part and also to the admittances mimicking the tight binding model and therefore, can produce variations of the ideal band structure (imaginary part of the eigenvalues) and additional k-dependent terms of the real part of the eigenvalues. As soon as components from the same type differ due to component tolerances, the exact translation invariance of the chain is violated and the measured eigenvalues do not need to be purely imaginary any more. Therefore, the measured admittance band structure can deviate from the ideal band structure in arbitrary ways, which should be prevented best possible by minimizing component tolerances.
The real part of the measured band structure can be seen in fig. 3.5 c). In comparison to the imaginary part in b) the values of the real parts are small. We can identify a slight positive shift due to resistive parasitics of the components and in addition, a k-dependent variation due to the resistive contributions of the hopping elements and component tolerances.

3.1.3 Conclusions

The results from the investigation of the SSH model can essentially be divided into two parts. One part is the validation of the Laplacian formalism to map the properties of a tight binding Hamiltonian onto an electric circuit. An impedance measurement can be used to get a first guess whether an eigenstate with eigenvalue near zero exists and its shape can be investigated by the voltage profile of the circuit as long as it can be assured that no further eigenvectors with eigenvalues near zero feature additional non-vanishing contributions at the current input node. For the bulk of the system - equivalently to a solid state system - an admittance band structure can be defined and studied by measurement.
The other part of the results can be summarized as design rules for the solid state emulating circuit development. We learned that unwanted inductive couplings between circuit elements should be avoided best possible because their effects can be various and are difficult to prove. When using inductors containing magnetic material (as a core or for magnetic shielding) magnetization losses have to be taken into account which increase with frequency. To keep the working frequency small without increasing the inductance values, the capacitances have to be chosen higher, which can lead to the need of ceramic material with higher permittivity. Capacitors with higher capacitance tend to have higher ohmic losses, which again affect the circuit model. Therefore, a compromise must be found between the properties of the components used, the working frequency (also limited by the measurement devices) and the circuit board layout. The component tolerances should be kept as small as possible to minimize random deviations from the solid state model and to be able to rule out the impact of non-ideal components more accurate.

3.2 Band structure studies of the honeycomb lattice

For further investigation of the admittance band structure concept an electrical circuit implementing a honeycomb lattice was designed. The measurements described here originate from the author's master thesis [66] (chapter 5, written in German) and are explained in technical detail there. Some of the results are also published in [59]. The derivation of the theoretical formalism is explained in [70].
Its Bravais lattice is described by a hexagonal lattice with two-atom basis (see fig. 3.6 a)). One of its most famous appearances in nature is the two-dimensional honeycomb lattice of graphene formed by carbon atoms.
The connection between the linear dispersion relation, i.e. the Dirac cone in the band structure, and the Dirac equation describing massless particles was published independently by G.W. Semenoff [87] and D.P. DiVincenzo together with E.J. Mele [88] in 1984. The corresponding experimental investigation of a two-dimensional graphene sheet by K. Novoselov and A. Geim [89] could be accomplished 20 years later, leading to the Nobel Prize in Physics in 2010. The appearance of such carbon lattices is not limited to a 3D bulk crystal or a 2D graphene sheet. A lot of other forms exist, like fullerenes ball, bi- and multilayer graphene systems and carbon nanotubes. The latter will also be investigated by using the implemented circuit.

3.2.1 Graphene-like admittance band structure

The fact that these kinds of materials are extensively studied and host various solid state properties led us to use them for further investigation of the opportunities given by the circuit platform. Our electric circuit was built to show the properties of a hexagonal lattice with nearest neighbor hoppings (see fig. 3.6) as it can be used to describe the energetic properties of the delocalized π electrons of the carbon atoms in graphene. Because all distances between the carbon atoms are the same size, the hoppings are set to be the same in each direction. Again, due to the graph nature of a lumped element electrical circuit the spatial arrangement does not affect the properties determined by the admittances of the connecting elements. Therefore, the unit cells were arranged in a rectangular fashion and the lattice vectors were chosen to be perpendicular to each other and to have the same length. The honeycomb lattice shown in fig. 3.6 a) can be converted into the brick wall lattice (fig. 3.6 b)) by the transformation

$$\begin{aligned} \boldsymbol{\mathcal{R}} &: \vec{a}' \to \vec{a} = \boldsymbol{\mathcal{R}}\vec{a}' \\ \boldsymbol{\mathcal{R}} &= \begin{pmatrix} 1/3 & -1/\sqrt{3} \\ 1/3 & 1/\sqrt{3} \end{pmatrix} . \end{aligned} \tag{3.1}$$

Due to the definition $\vec{a}_i^{\top}\vec{b}_j = 2\pi\delta_{i,j}$ of reciprocal lattice vectors $\vec{b}_i$ the Brillouin zone of the brick wall lattice has the same square shape as the unit cell spanned by the primitive lattice vectors $\vec{a}_i$. The band structure of the honeycomb lattice can be calculated from the brick wall band structure by using $\vec{k} \to \boldsymbol{\mathcal{R}}^{\top}\vec{k}$.

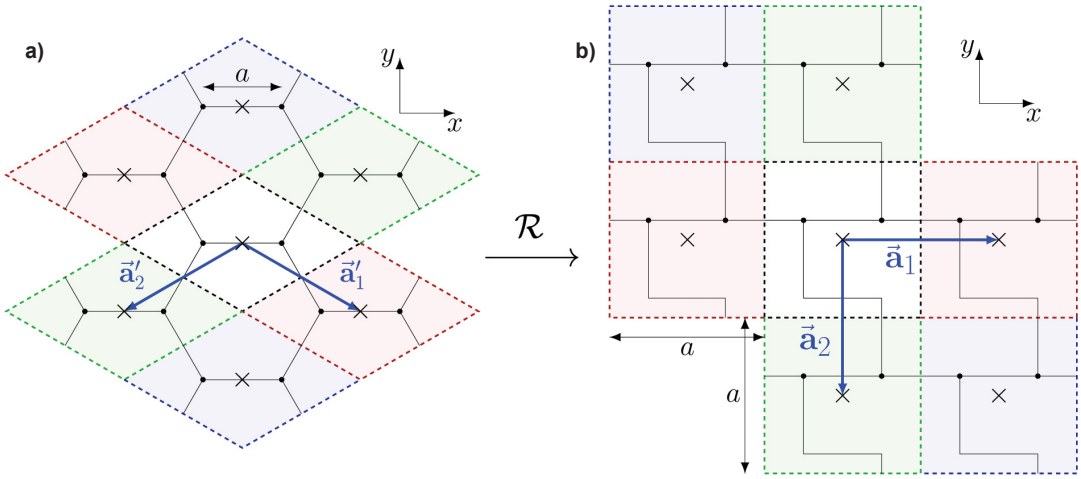

Figure 3.6: Spatial configuration of a): a honeycomb lattice with nearest neighbor hoppings (straight lines), b): a brick wall-like arrangement of the same lattice. Coloring and dashed lines are guides to eye and represent the different unit cells. Each unit cell consists of two atoms/nodes, one from each sublattice A and B. Primitive lattice vectors ($\vec{a}'_1, \vec{a}'_2$ and $\vec{a}_1, \vec{a}_2$) are shown for both configurations. They are connected via $\vec{a} = \boldsymbol{\mathcal{R}}\,\vec{a}'$ (adapted from [59]).

With the design rules found during the SSH circuit project (see section 3.1) taken into account the circuit was made of class 1 ceramic SMD capacitors ($C = 100\,\mathrm{nF} \pm 1\,\%$) as hopping elements and pre-selected shielded inductors ($L = 10.1\,\mu\mathrm{H} \pm 1\,\%$ at $80\,\mathrm{kHz}$) as groundings. The PCBs where designed to host 6×6 unit cells each with the option to link several boards in both directions (see reference [66] appendix A.3). To measure the band structure the ends of the circuit in each direction were connected to introduce periodicity and form a torus.
The reciprocal Laplacian can be written as

$$\begin{aligned}(\boldsymbol{J}_{honey})_{(\alpha,\beta)}\,(\vec{k}) \;&=\; i\omega \begin{pmatrix} 3C - \frac{1}{\omega^2 L} & -C\left(1 + e^{-i\vec{k}\vec{a}_1} + e^{-i\vec{k}\vec{a}_2}\right) \\ -C\left(1 + e^{i\vec{k}\vec{a}_1} + e^{i\vec{k}\vec{a}_2}\right) & 3C - \frac{1}{\omega^2 L} \end{pmatrix} \\ &=\; i\omega \left[\left(3C - \frac{1}{\omega^2 L}\right) \boldsymbol{\sigma_0} - C\left(1 + \cos(k_x) + \cos(k_y)\right) \boldsymbol{\sigma_1} - C\left(\sin(k_x) + \sin(k_y)\right) \boldsymbol{\sigma_2} \right] \end{aligned} \tag{3.2}$$

with the length of lattice vectors set to 1. The resulting admittance band structure reads

$$j_{honey}(\vec{k}) \;=\; i\omega \left[\left(3C - \frac{1}{\omega^2 L}\right) \pm C\sqrt{3 + 2\cos(k_x) + 2\cos(k_x - k_y) + 2\cos(k_y)} \right], \tag{3.3}$$

featuring band touching points when all cosine terms equal -0.5, which is the case when their arguments are $\pm\frac{2}{3}\pi + 2\pi z$ with $z \in \mathbb{Z}$. In the quadratic first Brillouin zone ($k_x, k_y = [-\pi, \pi[$) this is the case for $k_x = -k_y = \pm\frac{2}{3}\pi$. Therefore, the number of unit cells in each direction should be chosen as multiples of six to be able to guarantee that the discrete admittance band structure has data points exactly at the proposed band touchings.

Consequently, 3×3 PCBs were stacked together, hosting 18×18 unit cells. The admittance band structure was measured as described in section 2.3.4 with current input in the middle of the circuit.

In fig. 3.7 a) the measured imaginary parts of the admittances along paths between high symmetry points of the hexagonal lattice are shown. They match the theory curve (dashed line) in good agreement, proving that a circuit can be used to achieve band structures of crystals with higher dimensionality as well. As already explained in section 2.3.4 the states with admittance eigenvalues further away from the reference level (set by the working frequency) are stimulated more weakly and therefore are more sensitive for deviations due to component tolerances and noise.

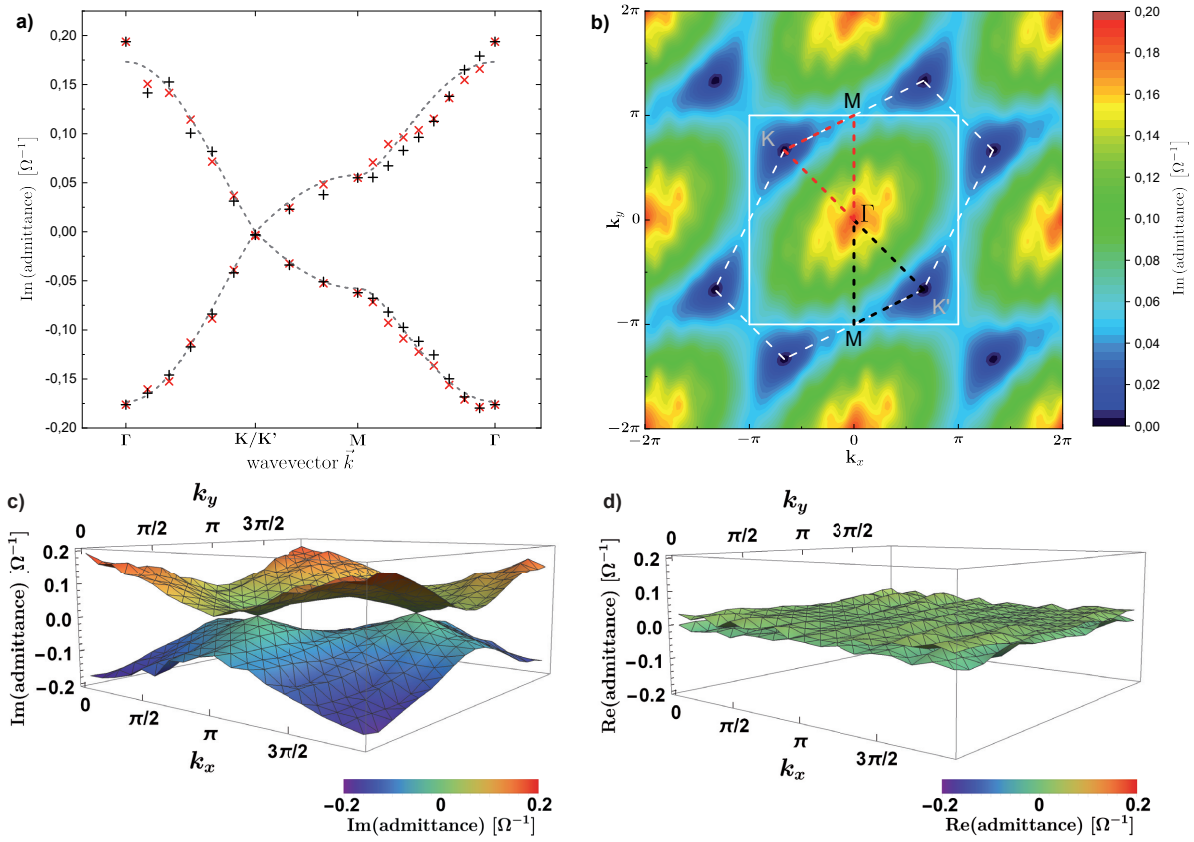

Figure 3.7: Admittance band structure of the periodic 18×18 unit cell circuit. a): Measured points along paths through the Brillouin zone between high symmetry points depicted in b) as dashed red/black lines, the colors of the points coincide with those of the paths. The theoretical proposal is shown by the dashed black curves. b): Interpolated color plot of the admittances of the upper band. The white square shows the Brillouin used to analyze the measurement, the distorted dashed white hexagon indicates the Brillouin zone as it would be expected from the hexagonal lattice. The black and red dashed lines depict paths between high symmetry points of the hexagonal Brillouin zone. c), d): Imaginary/real parts of the admittance eigenvalues plotted, depending on the position in reciprocal space. The coloring is used as a guide to the eye and does not contain additional information (adapted from [59]).

The interpolated color plot of the upper band (fig. 3.7 b)) allows us to recognize the symmetries of the hexagonal lattice, which can be restored by inverse transformation $\mathcal{R}^\top$ of the reciprocal space (fig. 3.8). At the corners (K, K' points) of the hexagonal Brillouin zone (dashed white lines) linear band touchings which are called Dirac cones in electronic band structures can be found (see fig. 3.7 a)-c)).
In the real part of admittances (fig. 3.7 d)) a small positive shift due to parasitic resistances of all circuit elements and additional random spreadings higher than the positive offset because of the coupling capacitors parasitics and tolerances of all circuit components are present.

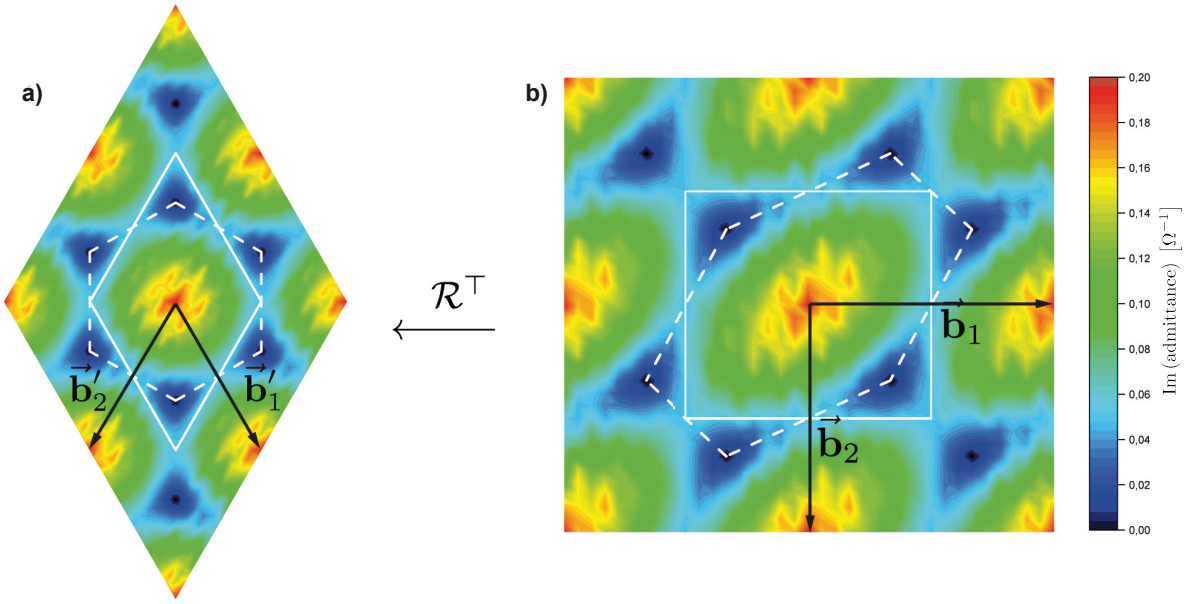

Figure 3.8: By applying $\mathcal{R}^\top$ to the reciprocal vectors of the measured admittance band structure the typical hexagonal Brillouin zone can be restored. a): Transformed color plot of the upper band. The hexagonal Brillouin zone is restored (dashed white line), whereas the quadratic Brillouin zone is transformed into a rhombus (solid white line). The reciprocal lattice vectors are shown by $\vec{b}'_1$ and $\vec{b}'_2$. b): Color plot of the upper band in the chosen quadratic geometry. The Brillouin zone is given by the white square, the distorted dashed white hexagon indicates the Brillouin zone of the hexagonal lattice. The reciprocal lattice vectors of the quadratic lattice $\vec{b}_1$ and $\vec{b}_2$ are also shown (adapted from [59]).

3.2.2 Carbon nanotube-like admittance band structure

A part of the two dimensional honeycomb circuit was further used to build circuit equivalents of carbon nanotubes. Therefore, 6×18 unit cells were connected periodically only in one direction while the other direction was terminated in different ways. In the nomenclature of [90] we built equivalents to $18(1, 0)$ GNRs (graphene nanoribbons). Because the circuit platform has its strengths in detecting admittance bands near zero the termination was made to implement zigzag ends, which are known to show zero energy bands [90]. In fig. 3.9 three tubes with different types of zigzag ends and their measured admittance band structures together with the dashed numerically predicted curves can

be seen. Fig. 3.9 a) has two zigzag ends and therefore two flat bands for $k > |2/3\pi|$. In fig. 3.9 b),c) both/one edge(s) are equipped with so called Klein defects [91] referred to as bearded zigzag or bearded edges. The bearded edges in fig. 3.9 b) introduce an additional pair of flat zero energy bands for all k that hybridize with the flat zigzag bands at $k > |2/3\pi|$ and split them up towards the bulk bands, leaving us with flat bands only at $k < |2/3\pi|$. The mixture of zigzag and bearded edge in fig. 3.9 c) adds one non-degenerated flat band and splits up the bands introduced due to the zigzag edge. For a detailed description see reference [90].

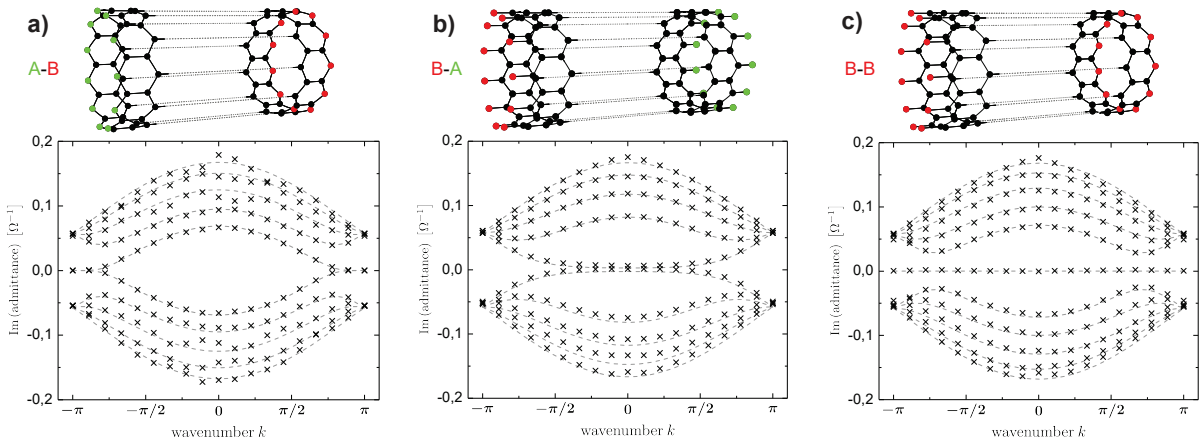

Figure 3.9: Admittance band structures of carbon nanotube-like circuit implementations with different edge terminations. The lattices are drawn schematically at the top of the pictures with highlighted sublattice nodes (A green, B red) at the edges. The models correspond to a simplified description of carbon nanotubes (see ref. [90]). The edge terminations are: Zigzag-zigzag edges at a), bearded-bearded edges at b) and bearded-zigzag edges at c) (adapted from [59]).

3.2.3 Conclusions

For the applicability of electric circuit lattices as tight binding model investigation platform we see that they can also be used to build and describe arbitrary tight binding models with higher dimensions and more complex admittance band structures that cannot be determined in an easy analytical way. Eigenvalues near the reference level determined by the working frequency match the predicted theoretical curves best, while the eigenvalues with bigger absolute value further away from the reference level differ more from the theoretical description due to less excitation, component tolerances and parasitics. When the design principles from the previous section are considered the real parts of the eigenvalues are small in comparison to the imaginary parts with slight positive shift and small variations and do not significantly modify the admittance band structures expected for the Hermitian models.

3.3 Quadrupolar topological insulator

To show that the electric circuit platform can also be used to investigate phenomena of present research interest a two-dimensional model describing a so called quadrupolar topological insulator was implemented. In 2017 Benalcazar, Bernevig and Hughes [60] extended a theoretical concept, which connects the polarization of a crystal with its Berry phase [5] to higher electrical multipole moments.
They proposed a two-dimensional lattice with vanishing dipole but non-zero quadrupole moments leading to topological corner states in the gap of the insulating bulk. Although the concept of crystal polarization cannot be transferred directly to the electric circuit platform, the spatial and spectral symmetries required to generate such corner states can be directly implemented in an electrical circuit. The measurements described here originate from the author's master thesis [66] (chapter 6, written in German) and are explained in technical detail there. Some of the results are also published in [61].

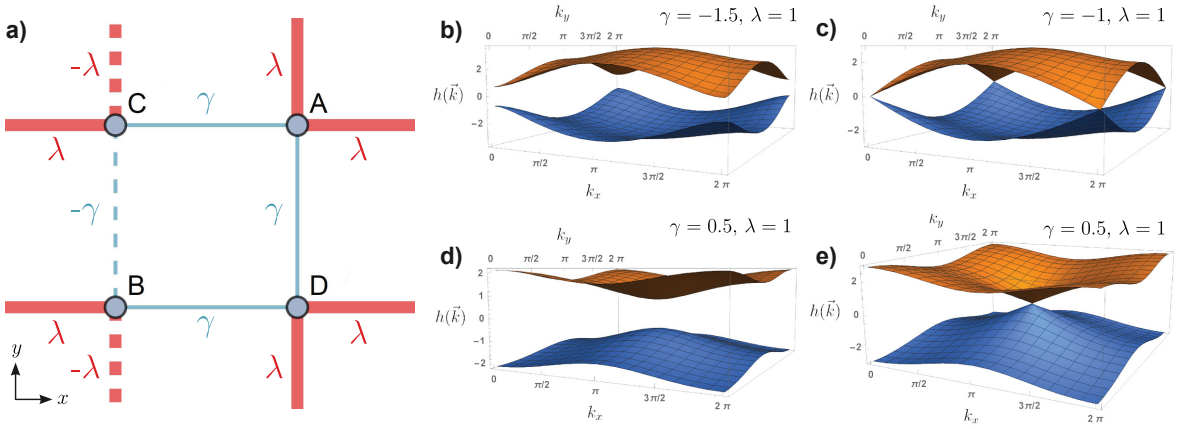

Figure 3.10: Lattice of the quadrupolar topological insulator model. a): 4-side unit cell of the square lattice with intracell hopping $\pm\gamma$ (blue) and intercell hopping $\pm\lambda$ (red) introducing a π flux per plaquette. The negative hoppings are indicated by dashed lines. The sublattice labels are chosen in accordance to the matrix representation used. b)-e): Band structure of the model for different parameter sets γ, λ. Both the upper (orange) and lower band (blue) are twofold degenerated. The model describes an insulator for $\gamma \neq \lambda$ (b),e)) and has band touchings for $\gamma = -\lambda$ (c)) at the Γ point and for $\gamma = \lambda$ (e)) at the M point of the Brillouin zone.

3.3.1 Hopping model of the quadrupolar topological insulator

To define a system with vanishing dipole and non-zero quadrupole moment a two-dimensional lattice with four-node unit cell and additional reflection symmetries that do not commute are needed [60]. In fig. 3.10 a) the unit cell of the lattice can be seen. Three connections between the nearest neighbors are made of the intracell hopping $+\gamma$, and the fourth connection has opposite sign $-\gamma$ causing a π flux in the square plaquette. The connections to neighboring unit cells are made by the intercell hoppings $\pm\lambda$. The two-dimensional lattice can be thought of as intertwined one-dimensional SSH chains

where the coupling/grounding elements are swapped in the chains with negative couplings $-\gamma$, $-\lambda$.
The structure of the periodic hopping Hamiltonian $\boldsymbol{H}_{quad}$ in reciprocal space can be described by 4×4 matrices represented by Kronecker products of Pauli matrices $\boldsymbol{\sigma_i}$, $\boldsymbol{\tau_i}$

$$\boldsymbol{H}_{quad} = [\gamma + \lambda \cos(k_x)]\, \boldsymbol{\Gamma_4} + \lambda \sin(k_x) \boldsymbol{\Gamma_3} + [\gamma + \lambda \cos(k_y)]\, \boldsymbol{\Gamma_2} + \lambda \sin(k_y) \boldsymbol{\Gamma_1} \tag{3.4}$$

with $\boldsymbol{\Gamma_i} = -\boldsymbol{\sigma_2 \tau_i}$ for $i = 1, \ldots, 3$ and $\boldsymbol{\Gamma_4} = \boldsymbol{\sigma_1 \tau_0}$. It satisfies the symmetries

$$\begin{aligned} \boldsymbol{M_x} \boldsymbol{H}_{quad}(k_x, k_y) \boldsymbol{M_x^{-1}} &= \boldsymbol{H}_{quad}(-k_x, k_y) \\ \boldsymbol{M_y} \boldsymbol{H}_{quad}(k_x, k_y) \boldsymbol{M_y^{-1}} &= \boldsymbol{H}_{quad}(k_x, -k_y) \\ \boldsymbol{C_4} \boldsymbol{H}_{quad}(k_x, k_y) \boldsymbol{C_4^{-1}} &= \boldsymbol{H}_{quad}(k_y, -k_x) \\ \boldsymbol{C} \boldsymbol{H}_{quad}(k_x, k_y) \boldsymbol{C^{-1}} &= -\boldsymbol{H}_{quad}(k_x, k_y) \end{aligned} \tag{3.5}$$

and the combined symmetries $\boldsymbol{M_{x\bar{y}}} = \boldsymbol{C_4 M_y}$ and $\boldsymbol{M_{xy}} = \boldsymbol{C_4 M_x}$

$$\begin{aligned} \boldsymbol{M_{x\bar{y}}} \boldsymbol{H}_{quad}(k_x, k_y) \boldsymbol{M_{x\bar{y}}^{-1}} &= \boldsymbol{H}_{quad}(-k_y, -k_x) \\ \boldsymbol{M_{xy}} \boldsymbol{H}_{quad}(k_x, k_y) \boldsymbol{M_{xy}^{-1}} &= \boldsymbol{H}_{quad}(k_y, k_x)\,. \end{aligned} \tag{3.6}$$

Here the anti-commuting reflection symmetries ($\boldsymbol{M_x M_y} = -\boldsymbol{M_y M_x}$) can be written as $\boldsymbol{M_x} = \boldsymbol{\sigma_1 \tau_3}$ and $\boldsymbol{M_y} = \boldsymbol{\sigma_1 \tau_1}$, the fourfold rotational symmetry as $\boldsymbol{C_4} = [(\boldsymbol{\sigma_1} + i\boldsymbol{\sigma_2})\, \boldsymbol{\tau_0} - (\boldsymbol{\sigma_1} - i\boldsymbol{\sigma_2})\, (i\boldsymbol{\tau_2})]\, /2$ and the chiral symmetry as $\boldsymbol{C} = \boldsymbol{\sigma_3 \tau_0}$. Note that the rotational symmetry turns the system clockwise in this representation, the combined mirror symmetries anti-commute ($\boldsymbol{M_{x\bar{y}} M_{xy}} = -\boldsymbol{M_{xy} M_{x\bar{y}}}$) as well and their indices define the mirror axis, e.g. $\boldsymbol{M_{x\bar{y}}}$ stands for mirroring at the diagonal from the top left to the low right corner corresponding to the coordinate system shown in fig. 3.10 a).
Due to the involution property of the $\boldsymbol{\Gamma}$ matrices the band structure can be calculated to

$$\pm \sqrt{2\left[\lambda^2 + \gamma^2 + \lambda\gamma\left(\cos(k_x) + \cos(k_y)\right)\right]}\,, \tag{3.7}$$

which can be seen in fig. 3.10 b)-e) for different sets of γ and λ. Each of the two bands are twofold degenerated. The spatial ($\boldsymbol{M_x}$, $\boldsymbol{M_y}$, $\boldsymbol{C_4}$,$\boldsymbol{M_{x\bar{y}}}$,$\boldsymbol{M_{xy}}$) and spectral ($\boldsymbol{C}$) symmetries and the gap closing for $|\gamma/\lambda| = 1$ indicating a topological phase transition can also be traced by the band structure plots.
When investigating simulations of a finite, non-periodic lattice topological corner modes occur. In fig. 3.11 a) the eigenvalues of the Hamiltonian for different parameter sets of γ, λ are plotted hosting two doubly degenerated zero modes for $|\gamma/\lambda| < 1$. Their shapes (fig. 3.11 b)-e)) can be identified with hybridized exponentially localized topological corner modes. Note that the coordinate basis used for the OBC simulations and the circuit implementation differs from the one chosen for the description of the periodic circuit (compare fig. 3.10 a) and fig. 3.12 a)).

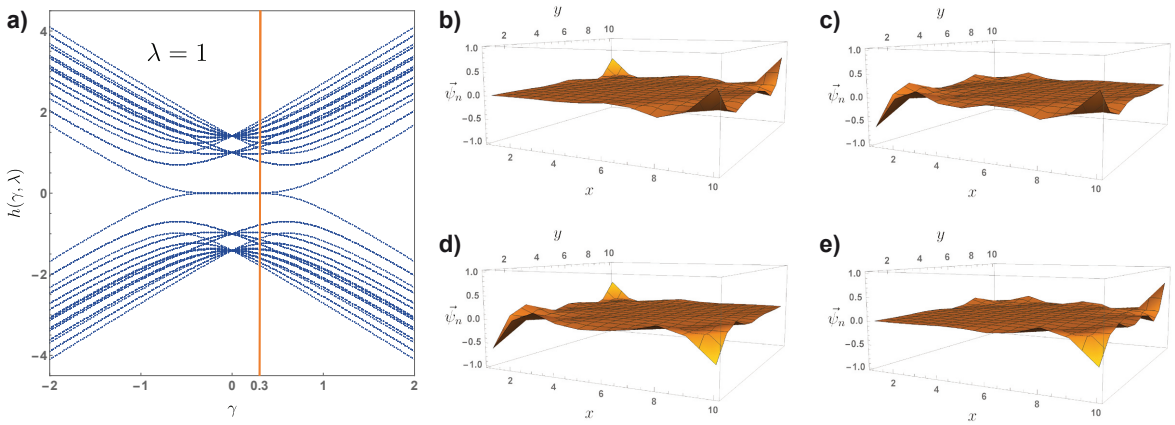

Figure 3.11: Simulation of a finite quadrupolar lattice with 5×5 unit cells. a): Eigenvalues of the finite lattice for different intracell hoppings γ and fixed intercell hopping $\lambda = 1$. The parameter set used to calculate the corner modes b)-e) is indicated by an orange line ($\gamma = 1/3.3, \lambda = 1$). b)-e): Eigenstates of the 5×5 unit cell Hamiltonian containing different hybridizations of corner modes.

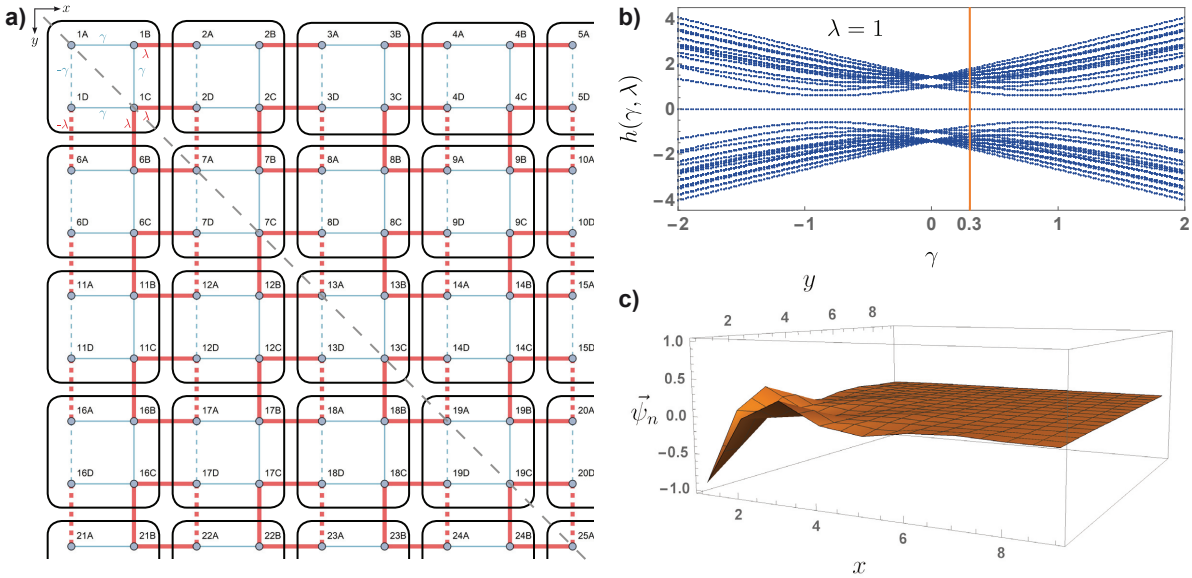

Figure 3.12: Finite quadrupolar lattice with 4.5×4.5 unit cells. a): Schematic drawing of the lattice made of unit cells like depicted in fig. 3.10 a). The unit cells (black squares) are cut at the right and bottom edge leading to symmetry breaking except of the mirror symmetry along the gray dashed diagonal line. b): Simulated eigenvalues of the lattice for different intracell hoppings γ and fixed intercell hopping $\lambda = 1$. The settings used for the simulation in c) and the circuit implementation are marked by an orange line ($\gamma = 1/3.3, \lambda = 1$). c): Simulated corner mode of the 4.5×4.5 unit cell lattice.

3.3.2 Circuit implementation and measurement results

To proof the topological and symmetry protection of the corner modes a lattice with 4.5×4.5 unit cells (see fig. 3.12 a)) was investigated. The half unit cell terminations break all spatial symmetries but the mirror symmetry along the gray dashed line. Therefore, topological modes should only appear at the corners lying on this line.

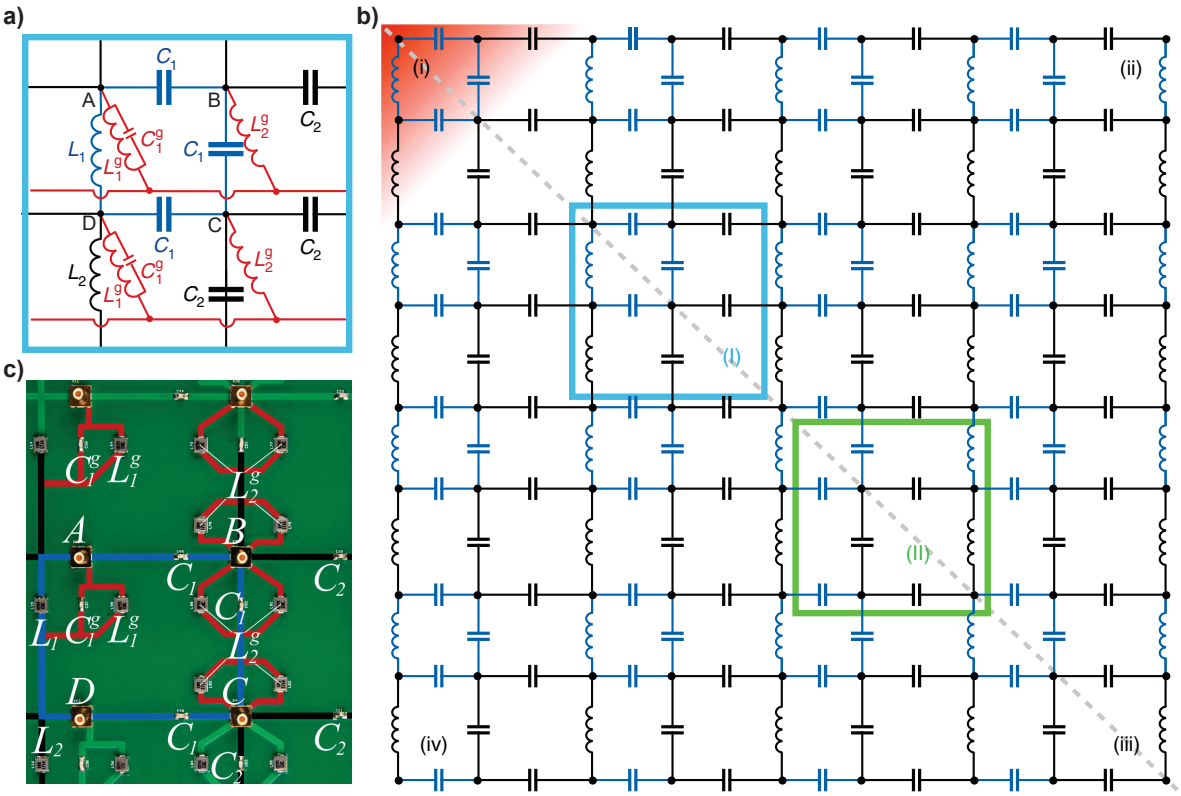

Figure 3.13: Quadrupolar topological circuit implementation. a): Sketch of the electrical unit cell used to build the circuit. Blue ($\pm\gamma = \pm 1/3.3$) and black ($\pm\lambda = \pm 1$) circuit elements indicate intra- and intercell hoppings. Positive hoppings are implemented by capacitors, negative hoppings are built by inductors ($\mathrm{sgn}(Z_C) = -\mathrm{sgn}(Z_L)$). Grounding elements used to set the total node conductance to zero are marked red. The resonance frequencies are chosen to match ($\omega_0 = 1/\sqrt{L_1 C_1} = 1/\sqrt{L_2 C_2} = 1/\sqrt{L_1^g C_1^g}$). b): Layout of the 4.5×4.5 unit cells circuit. Grounding elements are not shown in this picture. The symmetry axis is indicated by the gray dashed line, the blue (I) and green boxes (II) display the two possible choices of unit cells beginning from the upper left or lower right side. A topological corner mode is therefore expected in the upper left corner (i) (marked by the shaded red region), whereas it should lie in the lower right corner (iii) for interchanging γ and λ. No corner modes can appear at (ii) and (iv) due to the symmetry breaking. c): Unit cell of the experimental circuit board equaling the schematic unit cell in a) and the blue box in b). The coloring and labeling is in accordance to a) (adapted from [61]).

The circuit implementation is depicted in fig. 3.13 with $C_1 = 1\,\mathrm{nF} \pm 2\,\%, C_2 = \lambda/\gamma C_1 = 3.3\,\mathrm{nF} \pm 2\,\%, L_1 = 3.3\,\mu\mathrm{H} \pm 2\,\%, L_2 = \gamma/\lambda L_1 = 1\,\mu\mathrm{H} \pm 2\,\%$, the grounding elements are chosen to set the total node conductance to zero at the resonance frequency ω_0. The built circuit is explained in detail in [61] and the author's master thesis [66].
Due to the two possible choices of unit cells (see fig. 3.13 b), blue and green boxes) the two possible bulk circuit Laplacians provide that when the Laplacian of the unit cell in upper left corner $\boldsymbol{J}^{(I)}(\omega_0, \vec{k})$ is in a topological phase, the one matching the unit cell in the lower right corner is in the trivial phase $\boldsymbol{J}^{(II)}(\omega_0, \vec{k})$ and vice versa, satisfying the equation $\boldsymbol{J}^{(II)}_{\lambda/\gamma}(\omega_0, \vec{k}) = \lambda/\gamma \boldsymbol{J}^{(I)}_{\gamma/\lambda}(\omega_0, \vec{k})$ and therefore guaranteeing that only one of the two corners hosts a topological mode.
The circuit with the parameters γ=1/3.3 and λ=1 (see fig. 3.13) was investigated by two-point impedance measurements with respect to the topological trivial bottom right corner $(9, 9)$ (fig. 3.14). Due to the position of the topological corner mode in the band gap of the 4-band insulator the impedance profile should be dominated by its shape.

The normalized predicted and measured impedances are in good agreement (fig. 3.14 a)) and the exponential decay of the topological corner mode can be verified in the logarithmic plot of the points near the corner (fig. 3.14 b)). Note that the impedance profile is proportional to the absolute square of the eigenstate (see section 2.3.4) and therefore has the squared decay length $(\lambda/\gamma)^2$. Furthermore the topological corner state exists only on the sublattice of the topological corner and thus has contributions only on the odd node numbers in fig. 3.14.

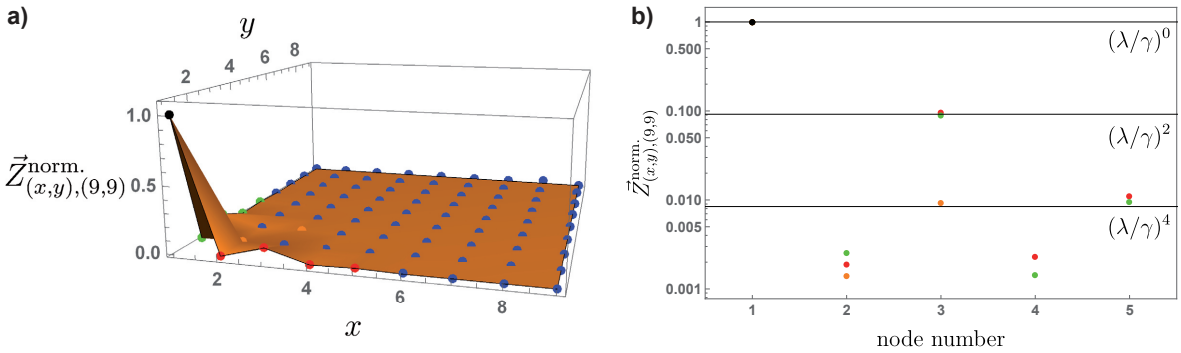

Figure 3.14: Normalized two-point impedances of the 4.5 × 4.5 unit cell circuit with respect to the topological trivial corner (9,9) at the resonance frequency ($f = 2.77\,\mathrm{MHz}$). a): Theoretically predicted (interpolated orange surface) and measured (colored dots) normalized impedances plotted against the node position. The impedance of the trivial corner (9,9) is set to zero. b): Logarithmic plot of the points at the topological corner. The exponential decay of the corner mode along the x (red) and y (green) edge can be seen for the odd node numbers (sublattice sites where the state lives on). Along the diagonal (orange dots) the state decays twice as fast due to the overlap of the decays along both directions. Note that the impedance profile decreases with the squared decay length of the eigenstate ($(\lambda/\gamma)^2$) because of the impedance measurement (see section 2.3.4).

3.3.3 Conclusions

The obtained results demonstrate that a two dimensional system having π-flux per plaquette and the necessary symmetries exhibits the predicted zero dimensional topological corner modes, which opens a new route of potential applications in metamaterial and solid state systems.
Again, we see that the circuit platform is an ideal examination method for (not necessarily) topological phenomena in tight binding systems due to the use of common techniques to build and analyze electrical circuits in the low frequency regime where they can be treated as lumped element systems. Because of affordable measurement devices and the variety of available circuit components, electric circuits provide a flexible platform to investigate theoretical concepts that do not rely on quantum phenomena. Furthermore, metamaterials in general and the versatile electric circuit platform in detail are perfectly suited to transfer the conceptual knowledge of solid state physics to other fields of application and can therefore act as a driver of innovation.

4 Topological phenomena beyond linear Hermitian systems

The main part of this work considers the investigation of topological phenomena present in translation invariant systems away from the linear Hermitian regime. Leaving the extensively investigated field of Hermitian physics a variety of questions concerning the applicability of known concepts and the emergence of new interrelationships describing topological phenomena arise.
In this chapter, we study the field of linear, but non-Hermitian systems and prove the concept of bulk-boundary correspondence in $\mathcal{PT}$ symmetrical and non-reciprocal models. Furthermore, we will see the different behaviours of topological edge and defect states in the $\mathcal{PT}$ symmetrical model [62, 69] and the extensive change of eigenstates by switching between an open and periodic non-reciprocal chain [63].
Non-Hermitian models require real (imaginary) entries in the grounded circuit Laplacians (tight binding Hamiltonians) that can be inserted quite naturally by resistive circuit elements due to their $\pm 90°$ phase difference in impedance with respect to capacitors or inductors and could already be found as parasitic contributions in the Hermitian systems (see chapter 3).
To be able to also implement negative imaginary entries the concept of negative resistance is needed, which can be achieved by active circuitry, i.e. pumping additional energy in the system and thus endangering the stability of the circuit. For advanced stability analysis of the investigated models the time evolution of the eigenstates has to be considered. This can be done by calculating the complex frequencies for which the eigenstates are solutions of the homogeneous equation $\boldsymbol{J}(\omega)\vec{V}(\omega) = 0$ and determining whether these solutions are stable. Therefore, the so called Hamilton formalism [57] describing the time evolution of the circuit in the style of a quantum mechanical system can be used. A negative imaginary part of the found frequencies which would correspond to exponentially increasing, unstable modes $\propto e^{i\mathfrak{Re}(\omega)t}e^{-\mathfrak{Im}(\omega)t}$ leads to non-converging integrals in the Fourier transform, resulting in a break down of the formalism and the prediction of non-causal behaviour. Note that the expansion of the Fourier transform to complex frequencies made in this formalism is similar to the two-sided Laplace transform used in electrical engineering.
A second way to go beyond linear Hermitian systems is to abandon the linearity of the underlying mathematics. By adding non-linearity to a system we will not be able to transform the underlying differential equations into simple algebraic equations in frequency space any more and the superposition principle will get lost. In this context, the grounded circuit Laplacian describing the linkage between current and voltage also loses its applicability and we have to investigate whether the circuit behaviour can be divided into features that appear due to the non-linearity and properties that can be traced back to the topological character of the underlying lattice.

Therefore, we will build well understood SSH lattices endowed with additional active, non-linear resistive grounding. The description of the resulting self-excited and self sustained oscillatory circuit will be lead back to the solutions of the non-linear differential van der Pol equation and the topological character of the underlying coupling network [65].

4.1 $\mathcal{PT}$-SSH model

We will take a first step towards the exploration of non-Hermitian Hamiltonians in electrical circuits by the extension of the SSH model to a non-Hermitian version that obeys $\mathcal{PT}$ symmetry and can have purely real eigenvalues although Hermiticity is broken. An implementation of the $\mathcal{PT}$-SSH model in electrical circuits is described from theory in [69]. The main contributions of the author of this thesis were in the experimental implementation, investigation and interpretation of the acquired data. The results have been published in [62].
In 1998 Bender and Boettcher [92] proposed that Hamiltonians being symmetric under combined parity symmetry $\mathcal{P}$ ($p \to -p$, $x \to -x$ in a one dimensional system) and time reversal symmetry $\mathcal{T}$ ($t \to -t$, $p \to -p$), have a real and positive spectrum although they are non-Hermitian. The class of non-Hermitian Hamiltonians with real spectrum was later generalized by the concept of pseudo-Hermitian Hamiltonians ($\hat{H}^\dagger = \hat{\eta}\,\hat{H}\,\hat{\eta}^{-1}$, with $\hat{\eta}$ being a Hermitian linear automorphism) by Mostafazadeh [93].

4.1.1 Consequences of $\mathcal{PT}$ symmetry in the SSH model

First of all, we will describe the role of $\mathcal{PT}$ symmetry in terms of physical systems connected to their environment based on the explanations of Carl M. Bender in his book *PT Symmetry In Quantum and Classical Physics* [94]. In conventional quantum mechanics a system is described by a Hermitian Hamiltonian leading to real eigenvalues (observables) and the conservation of energy and probability in time, i.e. an isolated system. From an experimental point of view an isolated system is an idealized assumption that can be realized in a experimental setup only up to a certain extent. Every contact between the system and its environment can increase or reduce the probability leading to a net flow of probability between the environment and the system which is not isolated anymore. We now treat the non-isolated system as a subsystem, add a second copy of the subsystem with reversed net flow of probability (gain $\leftrightarrow$ loss) and interconnect the two subsystems in such a way that the parity operator just interchanges the two subsystems. If the interconnection strength is large enough compared to gain and loss the system can be in dynamic equilibrium, i.e. gain and loss can compensate each other. In dynamic equilibrium it resembles a closed system and has purely real eigenvalues although the system has external in- and outflow and is therefore not isolated. When a dynamic equilibrium can be established the system is said to be in an unbroken $\mathcal{PT}$-symmetric phase, otherwise the $\mathcal{PT}$ symmetry is broken.
To introduce these properties in the already discussed SSH model, we will point out the differences of the grounded circuit Laplacians of the SSH and $\mathcal{PT}$-SSH model. The

Laplacian of the Hermitian SSH model at its resonance frequency ω_0 dealt with in sections 2.2.2, 2.2.3 and 3.1 can be written as:

$$\widetilde{\boldsymbol{J}}_{\text{SSH}} = \frac{\boldsymbol{J}_{\text{SSH}}}{i\omega_0 C_0} = \begin{pmatrix} 0 & -t_1 & 0 & \dots & 0 \\ -t_1 & 0 & -t_2 & \dots & 0 \\ 0 & -t_2 & 0 & \dots & 0 \\ \vdots & \vdots & \vdots & \ddots & -t_1 \\ 0 & 0 & 0 & -t_1 & 0 \end{pmatrix} \tag{4.1}$$

Here the hopping strengths are given by the unitless and real values t_1, t_2 in reference to the admittance scale $i\omega_0 C_0$. The factor $i\omega_0 C_0$ is scaled out in $\widetilde{\boldsymbol{J}}_{\text{SSH}}$ to avoid confusion while comparing the real-valued hopping Hamiltonians and complex-valued grounded circuit Laplacians.
To extend this model we should first gain intuition about the matrix representation of parity $\boldsymbol{\mathcal{P}}$ and time reversal $\boldsymbol{\mathcal{T}}$ symmetry. A parity transformation $\boldsymbol{\mathcal{P}}$ can be expressed in the present case as

$$\boldsymbol{\mathcal{P}} = \begin{pmatrix} 0 & \dots & 0 & 0 & 1 \\ 0 & \dots & 0 & 1 & 0 \\ 0 & \dots & 1 & 0 & 0 \\ \vdots & \iddots & \vdots & \vdots & \vdots \\ 1 & \dots & 0 & 0 & 0 \end{pmatrix}, \tag{4.2}$$

while time reversal symmetry $\boldsymbol{\mathcal{T}}$ is anti-unitary and is represented here by a complex conjugation $\boldsymbol{\mathcal{T}} = \boldsymbol{K}$. With this in mind it can easily be checked that the Hermitian SSH model is time reversal symmetric due to its real entries and parity symmetric as long as it is built of full unit cells, i.e. being mirror symmetric with respect to the middle of the chain. In addition, it is also symmetric under the combined space-time-reflection symmetry $\boldsymbol{\mathcal{PT}}$.

To break Hermiticity,parity and time reversal symmetry, the model can be extended by alternating positive and negative imaginary on-site potentials. In terms of the pictorial description given at the beginning of this section we add gain and loss to the different sublattice sites, which are connected by the SSH chain leading to:

$$\widetilde{\boldsymbol{J}}_{\text{PT-SSH}} = \frac{\boldsymbol{J}_{\text{PT-SSH}}}{i\omega_0 C_0} = \begin{pmatrix} -i\gamma & -t_1 & 0 & \dots & 0 \\ -t_1 & i\gamma & -t_2 & \dots & 0 \\ 0 & -t_2 & -i\gamma & \dots & 0 \\ \vdots & \vdots & \vdots & \ddots & -t_1 \\ 0 & 0 & 0 & -t_1 & i\gamma \end{pmatrix} \tag{4.3}$$

Hermiticity ($H = H^{\top *}$) is broken due to the imaginary entries along the diagonal, spatial inversion and complex conjugation change sign of the on-site terms and therefore $\boldsymbol{\mathcal{P}}$ and $\boldsymbol{\mathcal{T}}$ are also broken. On the other hand, the combined anti-unitary space-time-reflection symmetry $\boldsymbol{\mathcal{PT}}$, which includes a sign change of the imaginary diagonal elements twice, is still present and commutes with the $\mathcal{PT}$-SSH Laplacian $\left[\boldsymbol{\mathcal{PT}}, \widetilde{\boldsymbol{J}}_{\text{PT-SSH}}\right] = 0$.

Moreover, the chiral symmetry $\boldsymbol{\Sigma_z}$ represented by

$$\boldsymbol{\Sigma_z} = \begin{pmatrix} 1 & 0 & 0 & \dots & 0 \\ 0 & -1 & 0 & \dots & 0 \\ 0 & 0 & 1 & \dots & 0 \\ \vdots & \vdots & \vdots & \ddots & \vdots \\ 0 & 0 & 0 & \dots & -1 \end{pmatrix}, \tag{4.4}$$

which leads to a symmetric spectrum and the sublattice character of the topological edge states in the Hermitian case, is violated in the $\mathcal{PT}$ symmetric SSH chain. Combined with time-reversal symmetry $\boldsymbol{\mathcal{T}}$ it describes another anti-unitary symmetry of the $\mathcal{PT}$-SSH model, the so called anti-$\mathcal{PT}$ symmetry $\boldsymbol{\mathcal{APT}}$, which anti-commutes with the Laplacian $\left\{\boldsymbol{\mathcal{APT}}, \widetilde{\boldsymbol{J}}_{\text{PT-SSH}}\right\} = 0$.

Due to the non-linearity of the complex conjugation $\mathcal{K}$ [$\mathcal{K}(\alpha x) = \alpha^* \mathcal{K}(x) \neq \alpha \mathcal{K}(x)$ for $\alpha \in \mathbb{C}$] commuting/anti-commuting operators do not necessarily mean that they have a common eigenbasis. With this in mind we can determine a condition for the $\mathcal{PT}$ symmetry to be unbroken. When $\vec{\psi}$ is an eigenstate of the Hamiltonian $\boldsymbol{H}$ with eigenvalue E and the Hamiltonian commutes with the $\boldsymbol{\mathcal{PT}}$ operator

$$\boldsymbol{H}\vec{\psi} = E\vec{\psi} \tag{4.5}$$

$$[\boldsymbol{\mathcal{PT}}, \boldsymbol{H}] = 0 \tag{4.6}$$

we can apply the $\boldsymbol{\mathcal{PT}}$ operator to the eigenvalue equation 4.5

$$\boldsymbol{H}(\boldsymbol{\mathcal{PT}}\vec{\psi}) \overset{(4.6)}{=} \boldsymbol{\mathcal{PT}}\boldsymbol{H}\vec{\psi} = \boldsymbol{\mathcal{PT}}E\vec{\psi} = \boldsymbol{\mathcal{PT}}E(\boldsymbol{\mathcal{PT}})^2\vec{\psi} = E^*(\boldsymbol{\mathcal{PT}}\vec{\psi}) \tag{4.7}$$

and see that an eigenstate $(\boldsymbol{\mathcal{PT}}\vec{\psi})$ exists with eigenvalue E^*. If $\vec{\psi}$ is $\mathcal{PT}$ symmetric, then $\vec{\psi}$ and $(\boldsymbol{\mathcal{PT}}\vec{\psi})$ are the same states and the corresponding eigenvalue has to be real ($E = E^*$). Otherwise, when E is complex the two states differ and transform into each other by applying $\boldsymbol{\mathcal{PT}}$.
Similar conclusions can be made by considering the anti-unitary $\mathcal{APT}$ symmetry. With

$$\{\boldsymbol{\mathcal{APT}}, \boldsymbol{H}\} = 0 \tag{4.8}$$

we achieve:

$$\boldsymbol{H}(\boldsymbol{\mathcal{APT}}\vec{\psi}) \overset{(4.8)}{=} -\boldsymbol{\mathcal{APT}}\boldsymbol{H}\vec{\psi} = -\boldsymbol{\mathcal{APT}}E\vec{\psi} = -E^*(\boldsymbol{\mathcal{APT}}\vec{\psi}) \tag{4.9}$$

So for every state $\vec{\psi}$ an additional eigenstate $(\boldsymbol{\mathcal{APT}}\vec{\psi})$ exists with eigenvalue $-E^*$. Therefore, when $\vec{\psi}$ is $\mathcal{APT}$ symmetric the eigenvalue has to be complex ($E = -E^*$). If the eigenvalue is not complex, the states transform into each other under $\boldsymbol{\mathcal{APT}}$.
Because of the commutation/anti-commutation of the $\mathcal{PT}$-SSH Laplacian with both the $\boldsymbol{\mathcal{PT}}$ and the $\boldsymbol{\mathcal{APT}}$ operator we can conclude that the eigenstates, as long as their eigenvalues are not zero, only appear in pairs with $\mathcal{PT}/\mathcal{APT}$ symmetric partners with purely real or purely imaginary eigenvalues (see also the Supplemental Material of [62]).

To investigate the consequences for the band structure we can extend our theoretical considerations that we made for the hermitian-SSH model in section 2.2.2. The band structure calculation for a the periodic lattice can again be done in Bloch form in terms of Pauli matrices:

$$\widetilde{\boldsymbol{J}}_{\text{PT-SSH}}(k) \;=\; (-t_1 - t_2\cos(k))\,\boldsymbol{\sigma_1} - t_2\sin(k)\boldsymbol{\sigma_2} + i\gamma\boldsymbol{\sigma_3} \tag{4.10}$$

The band structure is thus given by

$$\widetilde{j}_{\text{PT-SSH}}(k) \;=\; \pm\sqrt{t_1^2 + t_2^2 + 2t_1t_2\cos(k) - \gamma^2}\,. \tag{4.11}$$

The on-site potentials add the term $-\gamma^2$ to the radicand of the SSH band structure, enabling negative results and therefore imaginary solutions of the square root. At this point we can already see that the band structure should only be exclusively real or imaginary for a given k value due to the square root behaviour corresponding to the $\mathcal{PT}/\mathcal{APT}$ symmetric restrictions.

Based on the maximum and minimum values of the cosine term (±1) the maximum and minimum values of the band structure can be written as:

$$\left(\widetilde{j}_{\text{PT-SSH}}\right)_{\text{max/min}} \;=\; \sqrt{(t_1 \pm t_2)^2 - \gamma^2} \tag{4.12}$$

The corresponding phase diagram is shown in fig. 4.2 a) for the gain/loss parameter γ with respect to the dimerization $|t_1 - t_2|$ both scaled in terms of the total hopping $|t_1 + t_2|$. As long as $|\gamma| < |t_1 - t_2|$ the radicand is positive for all k values leading to an exclusively real $\mathcal{PT}$ symmetric band structure. When $|t_1 - t_2| < |\gamma| < |t_1 + t_2|$, positive and negative values can be achieved depending on k, and the symmetry is broken. For $|\gamma| > |t_1 + t_2|$ the radicand is negative for all values of k and the band structure is purely imaginary, so the model is in the $\mathcal{APT}$ symmetric phase.

Following our figurative explanation introduced at the beginning the hopping strengths in relation to the imaginary on-site potentials decide if the system can be in dynamic equilibrium or not and determine whether we achieve imaginary eigenvalues, i.e. break $\mathcal{PT}$ symmetry.

4.1.2 Circuit implementation

To implement this model in an electrical circuit we extend our SSH circuit introduced in section 2.2.3. To add imaginary on-site potentials to the diagonal we need circuit elements whose current-voltage relation has an additional 90° phase shift with respect to capacitors/inductors leading to negative/positive exclusively real admittances for the representation of gain and loss.
Positive real admittances can be realized by ohmic resistors, whereas negative real admittances would need active circuit components to introduce gain to the circuit, i.e. pump current into the circuit against the direction of the voltage difference. To avoid the need

of negative resistance and possible stability issues we design our circuit with passive circuit components only and therefore have an offset in the imaginary part of the eigenvalues. The considered hopping model and the circuit diagram can be seen in fig. 4.1 a) and c).

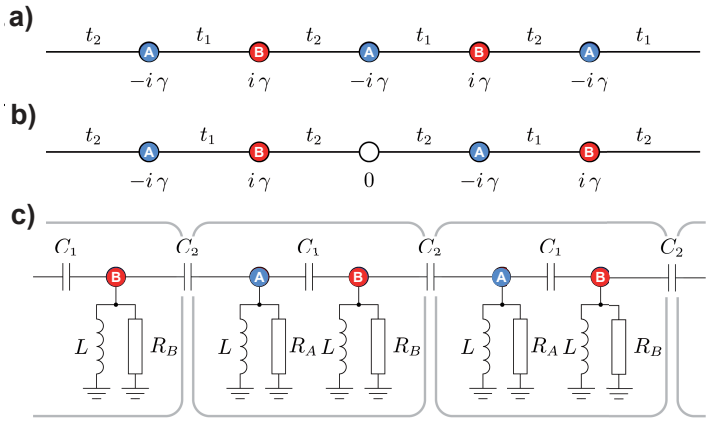

Figure 4.1: $\mathcal{PT}$-SSH hopping model without/with defect and circuit implementation. a): SSH-like chain (compare fig. 2.2) with imaginary on-site terms $\pm i\gamma$, b): $\mathcal{PT}$-SSH chain with defect point (no on-site term), c): circuit diagram of the $\mathcal{PT}$-SSH chain, the hopping is implemented by capacitors ($C_1 = 2 \times 100\,\mathrm{nF} \pm 1\,\%, C_2 = 100\,\mathrm{nF} \pm 1\,\%$), the grounding needed to set the resonance frequency $\omega_0 = 90.6\,\mathrm{kHz}$ is made by inductors ($L = 9.96\,\mu\mathrm{H} - 9.98\,\mu\mathrm{H}$, pre-characterized at 80 kHz). The on-site imaginary terms are built of additional resistors to ground. The 20 unit cell chain investigated here is made of two concatenated circuit boards (see appendix A.1) (adapted from [62], note that the nomenclature is adjusted to the labeling used on the circuit board shown in appendix A.1 differing from [62]).

With

$$g = \frac{1}{R_A} + \frac{1}{R_B} = \frac{R_A + R_B}{R_A R_B} \quad \Delta g = \frac{1}{R_A} - \frac{1}{R_B} = \frac{R_A - R_B}{R_A R_B} \tag{4.13}$$

$$\frac{1}{R_A} = \frac{g + \Delta g}{2} \qquad \frac{1}{R_B} = \frac{g - \Delta g}{2} \tag{4.14}$$

the scaled Laplacian of the model at resonance can then be written as

$$\widetilde{\boldsymbol{J}}_{\text{PT-SSH}} = \begin{pmatrix} -i\frac{\Delta g}{2\omega_0 C_0} & -t_1 & 0 & \dots & 0 \\ -t_1 & i\frac{\Delta g}{2\omega_0 C_0} & -t_2 & \dots & 0 \\ 0 & -t_2 & -i\frac{\Delta g}{2\omega_0 C_0} & \dots & 0 \\ \vdots & \vdots & \vdots & \ddots & -t_1 \\ 0 & 0 & 0 & -t_1 & i\frac{\Delta g}{2\omega_0 C_0} \end{pmatrix} - i\frac{g}{2\omega_0 C_0} \cdot \mathbb{1} \tag{4.15}$$

where we can identify $\gamma = \frac{\Delta g}{2\omega_0 C_0}$. Due to the admittance scaling $i\omega_0 C$ the term $-i\gamma$ represents loss, $i\gamma$ corresponds to gain. The imaginary offset is given by the term $-i\frac{g}{2\omega_0 C_0}$ proportional to the unit matrix. For the sake of simplicity the resistors of sublattice B are left out, leading to $g = \Delta g = 1/R_A$.

4.1.3 Experimental investigation

The investigation of this circuit will start with the admittance band structure of the 20 unit cell non-Hermitian $\mathcal{PT}$-SSH model for different resistor values analyzed by the measurement process described in section 2.3.4. The resistances are set by trimmer resistors. To minimize the deviations due to component tolerances in the regime where the band structure should have steep changes due to the switching between real and imaginary part along the k-axis, the trimmer resistors were replaced by fixed metal film resistors ($R_A = 5\,\Omega \pm 0.1\,\%$).
In fig. 4.2 three different offset corrected band structures can be seen, indicating three different types of symmetry phases. For low imaginary on-site potentials γ (high resistances) the band structure is real only (fig. 4.2 b)) as it is expected for $\mathcal{PT}$ symmetric systems. With increasing on-site potentials (decreasing resistances) the band structure is purely real/imaginary for different parts of the Brillouin zone (fig. 4.2 c)) indicating the symmetry broken regime. The points in k-space where the real and imaginary parts of the band structure are simultaneously zero are called exceptional points and differ significantly from degeneracies found in Hermitian systems. For a Hermitian degeneracy at least two eigenvalues match while their eigenvectors are still orthogonal. At an exceptional point the eigenvalues are the same and the eigenvectors are parallel, making the Hamiltonian non-diagonalizable [95],[96]. A further increase leads to an exclusively imaginary band structure (fig. 4.2 d)).

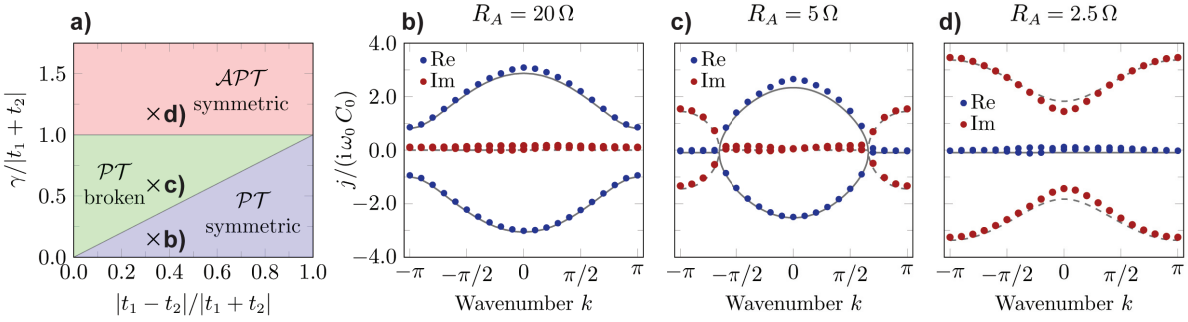

Figure 4.2: Complex admittance band structure j of a 20 unit cell long $\mathcal{PT}$-SSH circuit with different grounding resistors. a): Predicted phase diagram of the built circuit, the position of the different measurements is marked by crosses. b)-d): Theory curves (black lines) and measured values (real part: blue dots, imaginary parts: red dots) of the admittance band structures j at the resonance frequency $\omega_0 = 90.6\,\mathrm{kHz}$. The shifts in the imaginary parts due to the resistive offsets $-i/(2\omega_0 C R_B)$ are subtracted. The dimerization $|t_1 - t_2|$ is the same for all settings ($|t_1 - t_2|/|t_1 + t_2| \approx 0.33$). b): $\mathcal{PT}$ symmetric phase, $|\gamma|/|t_1 + t_2| \approx 0.15$, c): $\mathcal{PT}$ broken phase,$|\gamma|/|t_1 + t_2| \approx 0.59$. d): $\mathcal{APT}$ symmetric phase, $|\gamma|/|t_1 + t_2| \approx 1.2$ (adapted from [62]).

The match between experimental data and theoretical prediction indicates the validity of our circuit to implement the $\mathcal{PT}$-SSH in all three symmetry phases. The slight deviation of the data points from the theory curve around $k = 0$ could stem from the tolerances of the resistors used. The smaller the resistance, the larger the impact of the deviations is

due to trimming mismatch of the potentiometers or the manufacturing tolerances of fixed resistors. Nevertheless, the features of the phase transitions like the switching between real and imaginary eigenvalues and the closing and reopening at exceptional points can be observed.

4.1.4 Topological protected localized states

To study the behavior of topological states in these non-Hermitian $\mathcal{PT}$-symmetric systems we apply open boundary conditions and ground the first/last node of the chain (see appendix A.1) to have the intercell hopping bigger than the intracell hopping (equivalent to the topological regime for the Hermitian SSH chain, see section 2.2.2). Furthermore, we add a defect state in the middle of our chain not violating the symmetries of the system as suggested by Poli *et al.* [97] and Weimann *et al.* [98] to give rise to a topological midgap state. Note that different kinds of topological and trivial defect states can be implemented in the non-Hermitian/Hermitian SSH model that do not necessarily have a counterpart in the respective other model. A general discussion can be found in [99]. In our case the defect is implemented in the circuit by adding an auxiliary node between two unit cells in the middle of the chain coupled by hopping t_2 in both directions (see fig. 4.1 b)), forming a symmetry center. To introduce a zero mode it has to have neither gain nor loss, which is why in our case only the resistive offset $g/2 = 1/(2R_A) =: 1/R_{\text{def}}$ has to be added. The corresponding scaled circuit Laplacian is:

$$\widetilde{\boldsymbol{J}}_{\text{PT-SSH,def}} = \begin{pmatrix} i\gamma & -t_2 & 0 & \dots & 0 & 0 & 0 & 0 & 0 \\ -t2 & -i\gamma & \ddots & \dots & 0 & 0 & 0 & 0 & 0 \\ 0 & \ddots & \ddots & -t_1 & 0 & 0 & 0 & 0 & 0 \\ \vdots & \vdots & -t_1 & i\gamma & -t_2 & 0 & 0 & 0 & 0 \\ 0 & 0 & 0 & -t_2 & 0 & -t_2 & 0 & 0 & 0 \\ 0 & 0 & 0 & 0 & -t_2 & -i\gamma & -t_1 & \vdots & \vdots \\ 0 & 0 & 0 & 0 & 0 & -t_1 & \ddots & \ddots & 0 \\ 0 & 0 & 0 & 0 & 0 & \dots & \ddots & i\gamma & -t_2 \\ 0 & 0 & 0 & 0 & 0 & \dots & 0 & -t_2 & -i\gamma \end{pmatrix} \tag{4.16}$$

Due to the non-periodicity of the circuit we reconstruct the Green's matrix of the whole system under test (see section 2.3.4) with the same three resistor settings used for the band structure measurements to be able to calculate the eigenvalues and right eigenvectors (left and right eigenvectors are not equal because $\widetilde{\boldsymbol{J}}_{\text{PT-SSH}}$ is a non-normal matrix) in the non-periodic system with defect.
The results are shown in fig. 4.3. The bulk eigenvalues (fig. 4.3 d)-f), gray crosses) match the symmetry restrictions described earlier. In the $\mathcal{PT}$ symmetric phase (fig. 4.3 a),d)) the bulk eigenvalues are all purely real due to the $\mathcal{PT}$ symmetry, whereas in the symmetry-broken regime there are some eigenvalues lying on the real axis corresponding to $\mathcal{PT}$ symmetric states, whereas some other eigenvalues lie on the imaginary axis belonging to $\mathcal{APT}$ symmetric states. Nearby the origin of the complex plane the eigenvalues show slight deviations from the real/imaginary axis. In the $\mathcal{APT}$ symmetric phase all bulk

eigenvalues are localized on the imaginary axis, but there is a systematic bending the closer the eigenvalues are to the origin.

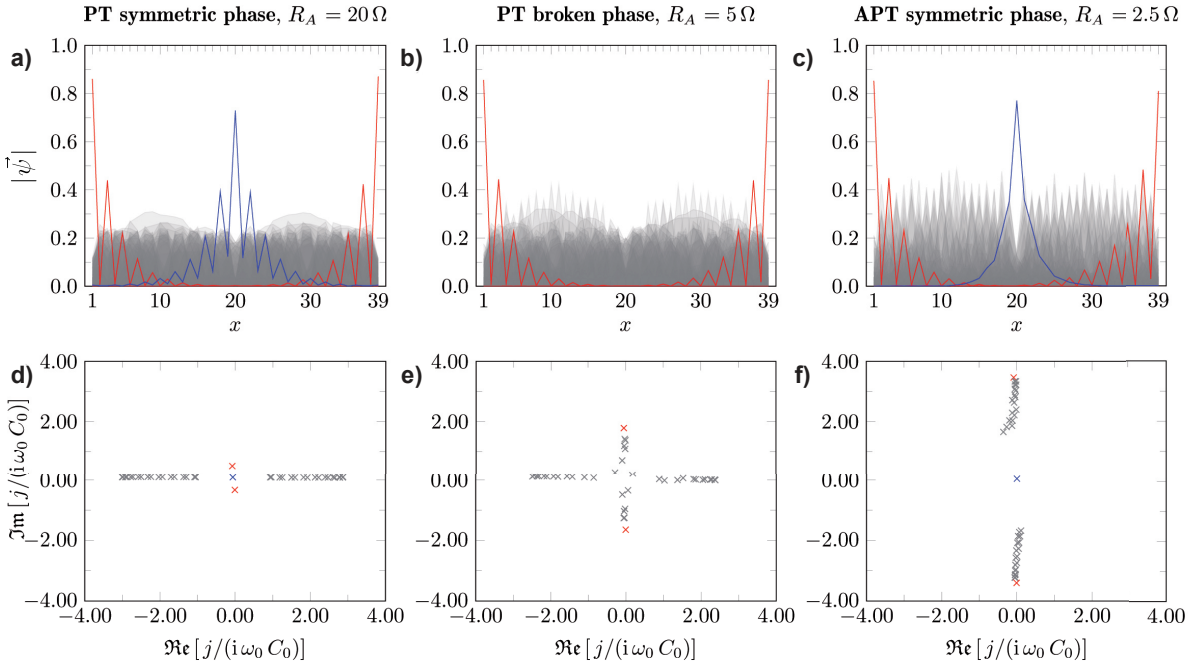

Figure 4.3: Offset corrected eigensystem evaluation of the non-periodic $\mathcal{PT}$-SSH circuit with defect and edge modes tuned to three different symmetry phases already investigated in fig. 4.2. a)-c): Absolute values of the eigenstates $\vec{\psi}$, edge modes are colored red, the defect mode is blue and the bulk modes are depicted with semi-transparent gray lines. d)-f): Imaginary offset corrected admittance eigenvalues j plotted in the complex plane. The colors of the markers correspond to the shown eigenstates (adapted from [62]).

To check if this could be an effect caused due to component tolerances we run simulations with every non-zero entry of the Laplacian randomly varied in different tolerance ranges. In fig. 4.4 the eigenvalues of the three symmetry phases with different tolerances r can be seen. We find that the $\mathcal{PT}/\mathcal{APT}$ symmetric regimes are much more robust against disorder than the $\mathcal{PT}$ broken one. Especially in the transition region between real and imaginary eigenvalues the points can be spread away from the origin due to intermixing of the states as it can be found in the measurement (fig. 4.3 e)).
In addition no systematic bending in the $\mathcal{APT}$ symmetric regime caused by disorder can be seen, which excludes component tolerances as an origin of the bending seen in fig. 4.3 f). Another impact on the eigenvalues could be given by parasitic admittances of the circuit elements, which are simulated in fig. 4.5. In the plots fig. 4.5 a)-c) the eigenvalues for additional inductive (real, positive) admittance ($s = 5\,\%$ of the resistive admittance γ) added to the positive/negative imaginary on-site potential of the simulation model are shown. This causes only a shift in the real part of the eigenvalues and affects the position of the zero eigenvalue because the added values are the same on every node except for the defect which carries zero on-site potential.

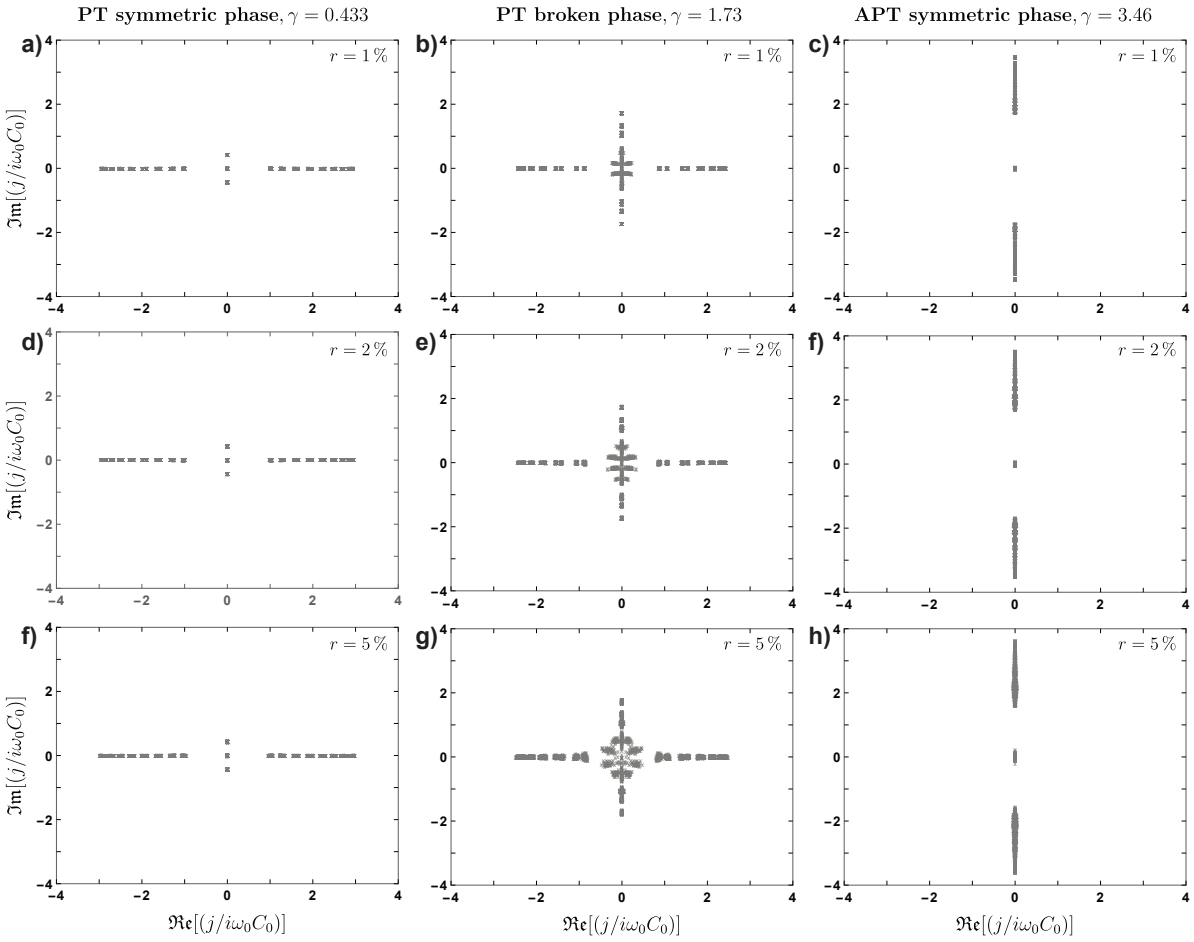

Figure 4.4: Simulated eigenvalues j of the non-periodic $\mathcal{PT}$-SSH circuit with defect and edge modes in the three symmetry phases with disorder. All SSH parameters are chosen the same as in fig. 4.3, the imaginary on-site terms are chosen symmetrically around zero. Every plot contains the eigenvalues of 100 different sets where each non-zero entry of the Laplacian at resonance is multiplied by a random variable x with $1 - r \leq x \leq 1 + r$. a),d),f): $\mathcal{PT}$ symmetric phase. b),e),g): $\mathcal{PT}$ broken phase. c),f),h): $\mathcal{APT}$ symmetric phase.

To represent the actual circuit implementation better the simulation model is extended to have only positive resistive contribution (negative on-site potential) and no negative resistances as it is the case in the circuit, and again 5 % inductive parasitics are added. From the results shown in fig. 4.5 d)-f) it can be determined that besides the already mentioned imaginary offset due to the not present negative resistance additional inductive parasitics lead to a bending of the eigenvalue position as they get closer to the origin, equaling the effect seen in the measured data in fig. 4.3 f). Hence, it can be ascertained that this is a phenomenon that can be traced back to the parasitics of the resistive elements in the used loss-only configuration.

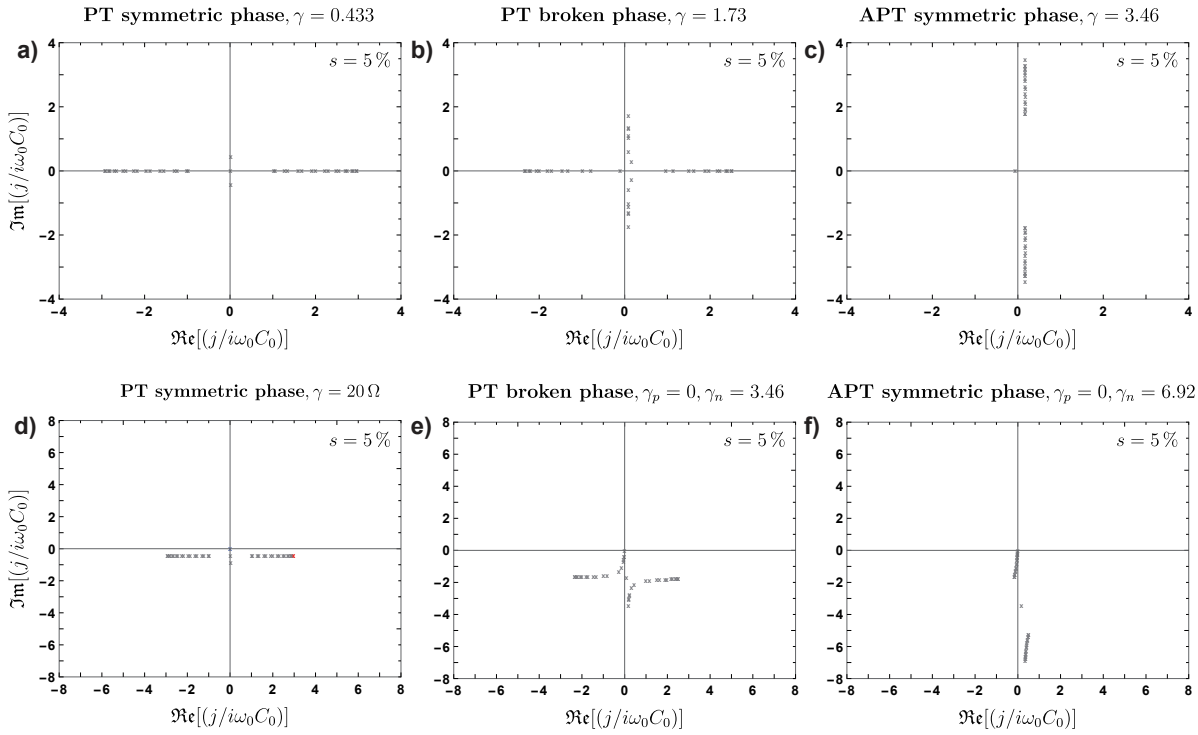

Figure 4.5: Simulated eigenvalues j of the non-periodic $\mathcal{PT}$-SSH circuit with defect and edge modes in the three symmetry phases with inductive parasitics at the grounding resistors. The values of the inductive admittance added are $s = 5\,\%$ of their resistive admittance. All system parameters are chosen the same as in fig. 4.3. a),b),c): Simulated systems with positive and negative resistance. d),e),f): Simulated systems with positive γ_n and no negative resistance $\gamma_p = 0$.

Moreover, the re-entrant behaviour of the defect mode will be discussed. In the measured data (fig.4.3) a defect mode localized in the middle of the chain can be found in the $\mathcal{PT}$ symmetric phase, which seems to be absent in the $\mathcal{PT}$ broken phase, but occurs again in the $\mathcal{APT}$ symmetric case. From the fact that the Laplacian commutes/anti-commutes with both, the $\mathcal{PT}$ and $\mathcal{APT}$ operator, combined with the odd number of lattice sites, a zero mode should exist. Under $\mathcal{PT}/\mathcal{APT}$ symmetry eigenstates can only exist in pairs with opposite sign. A system with an uneven number of states that still preserves both symmetries therefore has to have one mode with zero eigenvalue. From the measurements (fig. 4.3) it can be confirmed that there is a localized defect mode with eigenvalue near zero in the $\mathcal{PT}$ and $\mathcal{APT}$ symmetric phase (blue lines/crosses), but no such can be found in the symmetry broken phase. As discussed earlier the position of the zero eigenvalue could be shifted due to disorder and parasitics, but the eigenstates of the system (fig. 4.3 b)) do not show any localized state in the middle of the chain either.

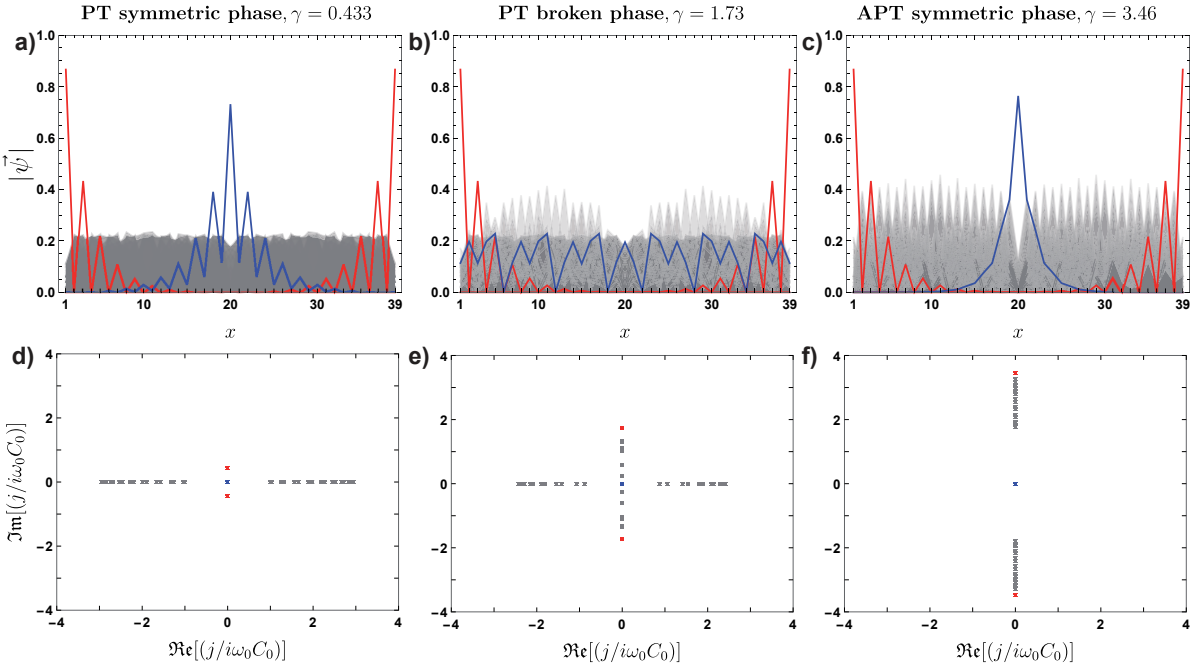

Figure 4.6: Absolute values of the simulated eigenstates $\vec{\psi}$ a)-c) and eigenvalues j d)-f) of the non-periodic $\mathcal{PT}$-SSH circuit with defect and edge modes in the three symmetry phases. All SSH parameters are chosen the same as in fig. 4.3, the imaginary on-site terms are chosen symmetrically around zero. a),d): $\mathcal{PT}$ symmetric phase. b),e): $\mathcal{PT}$ broken phase. c),f): $\mathcal{APT}$ symmetric phase.

In the simulated model without disorder for the symmetry broken phase (fig. 4.6 b)) the eigenstate with eigenvalue zero is also delocalized, in contrast to the exponentially localized defect states in the other regimes.

4.1.5 Theoretical description of the topological states

Consequently, a theoretical explanation for the re-entrant behaviour of the defect state should be found. We present two different approaches to describe this topological midgap state. A mathematical rigorous approach can be found by a closed-form solution for a zero defect mode in an infinite chain (see [98],[69]). A guess for the solution can be achieved by considering the scaled Laplacian $\widetilde{\boldsymbol{J}}_{\text{PT-SSH,def}}$ line by line. For a zero mode $(\widetilde{\boldsymbol{J}}_{\text{PT-SSH,def}})\vec{\psi}_{\text{def}} = 0$ leads to:

$$
\begin{aligned}
&\vdots \\
-t_2\psi_{d-3} - i\gamma\psi_{d-2} - t_1\psi_{d-1} &= 0 \\
-t_1\psi_{d-2} + i\gamma\psi_{d-1} - t_2\psi_d &= 0 \\
-t_2\psi_{d-1} + 0\cdot\psi_d - t_2\psi_{d+1} &= 0 \\
-t_2\psi_d - i\gamma\psi_{d+1} - t_1\psi_{d+2} &= 0 \\
-t_1\psi_{d+1} + i\gamma\psi_{d+2} - t_2\psi_{d+3} &= 0 \\
&\vdots
\end{aligned}
\tag{4.17}
$$

Here d labels the position of the defect and $\vec{\psi}_{\text{def}}$ is zero mode. Repeated insertion of the equations shows the structure of $\vec{\psi}_{\text{def}}$:

$$\begin{aligned} \psi_{d-o} &= -\psi_{d+o} \\ \psi_{d-e} &= \psi_{d+e} \end{aligned} \tag{4.18}$$

The entries with an odd node distance o to the defect point are arranged symmetrically, whereas the even distances e are arranged in an anti-symmetric way. With the additional restrictions due to $\mathcal{PT}$ symmetry (real part of $\vec{\psi}_{\text{def}}$ has to be symmetric around the inversion point, imaginary part has to be anti-symmetric) the entries of $\vec{\psi}_{\text{def}}$ with odd distance have to be purely imaginary and anti-symmetric and for even distances purely real and symmetric. Together with the requirement of an exponential decay these conditions lead to the ansatz

$$\psi_n = \frac{i^{n-d}}{2}\nu^{|n-d|}\left[E(1-(-1)^{n-d+1}) + O(1-(-1)^{n-d})\right] , \tag{4.19}$$

where n is the node number, $\frac{i^{n-d}}{2}$ produces the alternating real and imaginary entries, $\nu^{|n-d|}$ guarantees the exponential decay for $|\nu| < 1$, and O and E stand for the amplitudes with odd and even distance from the defect.By inserting this ansatz in the scaled Laplacian only two independent equations can be retrieved

$$\begin{aligned} -t_2\nu^2 O + \gamma\nu E + t_1 O &= 0 \\ t_1\nu^2 E + \gamma\nu O - t_2 E &= 0\,, \end{aligned} \tag{4.20}$$

which can be rearranged to:

$$O = -\frac{\gamma\nu}{-t_2\nu^2 + t_1}E \tag{4.21}$$

$$\nu^4 + 2\omega\nu^2 + 1 = 0 \qquad \text{with} \quad \omega = \frac{\gamma^2 - t_1^2 - t_2^2}{2t_1 t_2} \tag{4.22}$$

To meet the requirement $|\nu| < 1$ for an exponentially localized state the solutions of equation 4.22

$$\nu = \pm_1\sqrt{\pm_2\sqrt{\omega^2-1} - \omega} \tag{4.23}$$

have to be analyzed and $|\nu| < 1$ translates into the conditions

$$\omega < -1 \Leftrightarrow |\gamma| < |t_1 - t_2| \;\cup\; \omega > 1 \Leftrightarrow |\gamma| > |t_1 + t_2|\,. \tag{4.24}$$

A detailed analysis of all possible cases can be found in the supplement of [98]. With these solutions an exponentially localized defect state can only exist in the $\mathcal{PT}$ and $\mathcal{APT}$ symmetric regime, but not in the symmetry broken phase. Instead it can be shown that for $|\omega| < 1$ the radicand of $\sqrt{\omega^2-1}$ gets negative, which can be re-expressed by $i\sqrt{1-\omega^2}$, and consequently the absolute value of the radicand of $\nu = \sqrt{(\omega)^2 + (\sqrt{1-\omega^2})^2}$ is 1 in the symmetry broken regime. So the state is maximum delocalized.
A more general way to describe exponentially localized modes in systems with translation invariance (for detailed explanation see [100]) is to take the wave vectors k of the periodic Bloch states as a complex quantity $k \to \widetilde{k} = k + i\kappa$. In periodic systems

only states with real wave vectors meet the conditions of normalizability and periodicity, whereas for periodicity-broken configurations such as open boundary conditions or defect points exponentially localized states can occur and still have to be solutions to the translation invariant part of system, too, and therefore have to obey the eigenvalue equation with complex wave vectors. To find the corresponding eigenvalues the calculated band structure can be analytically continued to the complex numbers and the complex wave vector $\widetilde{k}$ of a zero mode can be found by solving

$$\pm\sqrt{t_1^2+t_2^2+2t_1t_2\cos(\widetilde{k})-\gamma^2}\;=\;0\,, \tag{4.25}$$

leading to

$$\widetilde{k}^{\pm}\;=\;\pm\arccos\left(\frac{\gamma^2-t_1^2-t_2^2}{2t_1t_2}\right)\;=\;\pm i\ln\left(\omega\pm\sqrt{\omega^2-1}\right)\,. \tag{4.26}$$

The absolute value of the imaginary part of the complex wave vector $|\mathfrak{Im}(\widetilde{k})|$ then defines to the localization length $\xi=|\mathfrak{Im}(\widetilde{k})|^{-1}$ of the localized state $\vec{\psi}\propto e^{-\frac{m}{\xi}}$, with m defining the number of unit cells away from the defect point. When we take into account that ν determines the localization length via $\xi=\ln(|\nu^2|)$ because the predicted defect state $\vec{\psi}_{\text{def}}$ decreases per unit cell by the factor $|\nu^2|$, the two approaches lead to the same localization lengths in the three different regimes and therefore consistently predict the localization/delocalization of the midgap state for the same sets of parameters.

The localized edge states (marked red in fig. 4.3) on the other hand show another behaviour. From the eigenvalue spectra (fig. 4.3 a)-c)) it can be seen that their eigenvalues are shifted away from zero to positive/negative imaginary values in all symmetry phases hence being $\mathcal{APT}$ symmetric and thus break $\mathcal{PT}$ symmetry.
This behaviour can be understood with a few qualitative thoughts starting with a Hermitian SSH model. A Hermitian SSH model in the topological non-trivial phase (intracell hopping smaller than intercell hopping) would host exponentially localized topological zero modes at the edges, each of them living on one sublattice only. We will not consider the defect at this point because it can be assumed to not affect the exponentially localized edge modes as long as our chain is long enough, i.e. the defect is far away from the edges. If we now introduce alternating imaginary gain/loss terms in our model, each sublattice will host *either* gain *or* loss. The edge states that live on only one sublattice will be affected by only one type of imaginary on-site potential acting as a uniform shift on their subspace, which only shifts their eigenvalues. For this reason the former zero modes are symmetrically shifted to $\pm\gamma$. Because this argument does not depend on the strengths of the on-site potentials, it holds true for all symmetry phases of the $\mathcal{PT}$-SSH model as it can be seen in fig. 4.3.
By using complex wave vectors again

$$\pm\sqrt{t_1^2+t_2^2+2t_1t_2\cos(\widetilde{k})-\gamma^2}\;\overset{!}{=}\;\pm i\gamma \tag{4.27}$$

we see that eigenvectors for eigenvalues $\pm i\gamma$ can be found with

$$\widetilde{k}^{\pm}\;=\;\pm\arccos\left(\frac{-t_1^2-t_2^2}{2t_1t_2}\right)\;=\;\pm i\ln\left(-\frac{t_2}{t_1}\right) \tag{4.28}$$

for $t_2 < t_1$ leading to localization lengths

$$\xi \;=\; |\mathfrak{Im}(\widetilde{k}^{\pm})|^{-1} \;=\; \ln\left(\frac{t_2}{t_1}\right)\,, \tag{4.29}$$

which is equal to the localization length of the Hermitian SSH model [72] and confirms our qualitative argument.

For the sake of completeness, we compare the absolute values of the measured localized states with their theoretical counterparts. Therefore, the absolute value of the theory curve's amplitude at the edge/defect node was set to be the same as the experimentally achieved value.
For the defect state the theoretical model (eq. 4.19) and the experiment agree in both symmetry phases in localization length and sublattice behaviour near the defect point (see fig. 4.7). In the $\mathcal{APT}$ symmetric regime the measurement values deviate more from theory than in the $\mathcal{PT}$ symmetric phase, which can be due to the higher imaginary on-site potentials/lower resistive contributions giving rise to higher localization of the eigenstate and stronger voltage localization at the current input during the measurement and therefore a higher signal to noise level in combination with the higher impact of the parasitics of the circuit already seen in the band structure of the $\mathcal{APT}$ symmetric phase (fig. 4.3 c)). At the ends of the chain the measured values differ significantly from the predicted curves. Here finite size effects can limit the match of theory and measurement.

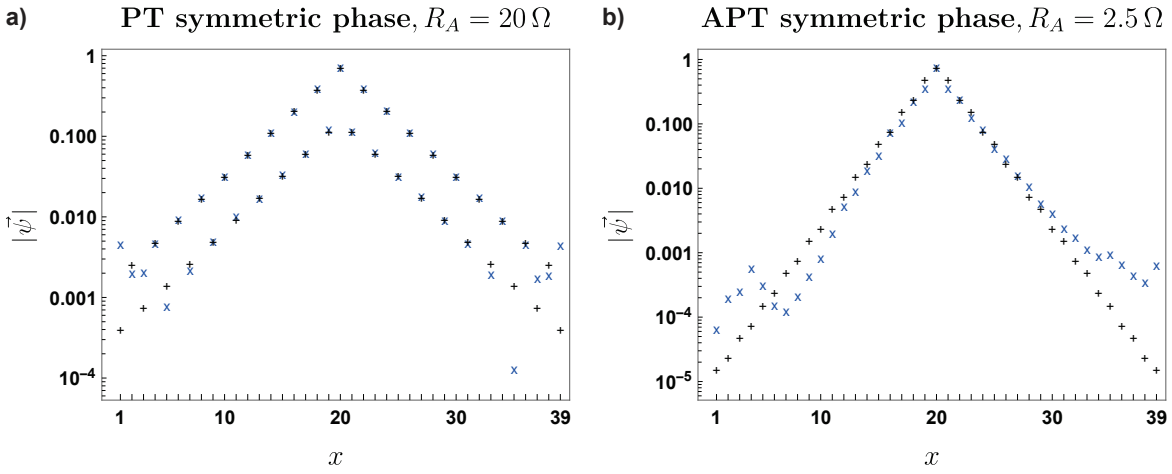

Figure 4.7: Logarithmic plot of the absolute value of the measured (blue) and theoretically predicted (black, see equation 4.19) defect mode $\vec{\psi}_{\text{def}}$. The theory curve is chosen to fit the experimental curve at the defect point (node 20). a): $\mathcal{PT}$ symmetric regime, parameters: $t_1 = 2$, $t_2 = 1$, $\gamma = 0.433$ and $|\psi_{20}| = 0.729\,185$. b): $\mathcal{APT}$ symmetric regime, parameters: $t_1 = 2$, $t_2 = 1$, $\gamma = 3.46$ and $|\psi_{20}| = 0.770\,431$.

The same comparison for the localized edge states can be found in fig. 4.8. In theory these modes are exponentially localized edge states with contributions only on one sublattice as they would be expected for the Hermitian SSH model.

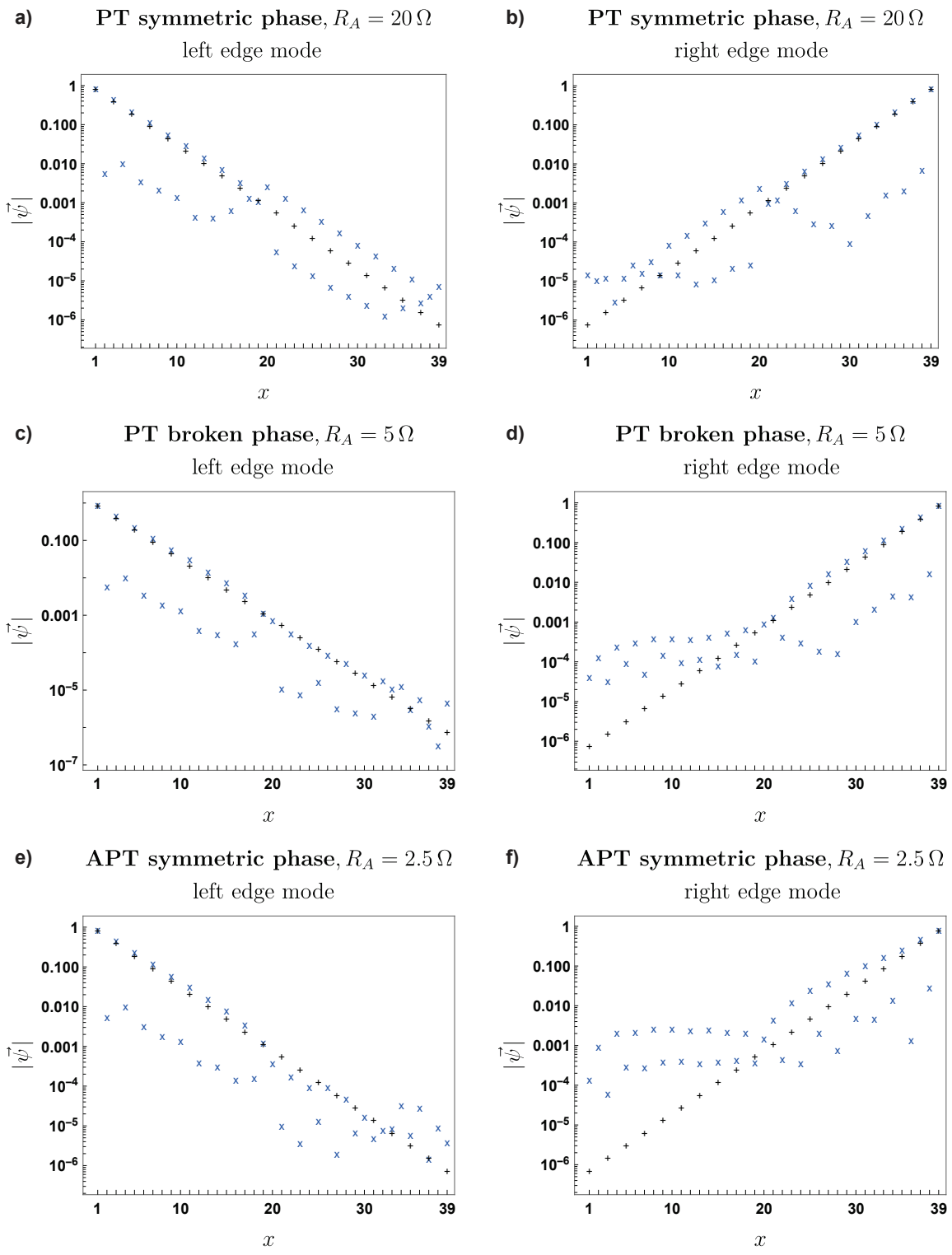

Figure 4.8: Logarithmic plot of the absolute value of the measured (blue) and theoretically predicted (black) edge modes $\vec{\psi}_{\text{edge}}$. The theory curves ($\xi = 2$) are chosen to fit the experimental data at the edge nodes (node 1 for left edge modes, node 39 for right edge modes). a): Left edge mode in the $\mathcal{PT}$ symmetric regime, $|\psi_1| = 0.860\,65$. b): Right edge mode in the $\mathcal{PT}$ symmetric regime, $|\psi_{39}| = 0.870\,633$. c): Left edge mode in the $\mathcal{PT}$ broken regime, $|\psi_1| = 0.856\,495$. d): Right edge mode in the $\mathcal{PT}$ broken regime, $|\psi_{39}| = 0.856\,236$. e): Left edge mode in the $\mathcal{APT}$ symmetric regime, $|\psi_1| = 0.852\,508$. f):Right edge mode in the $\mathcal{APT}$ symmetric regime, $|\psi_{39}| = 0.810\,002$.

Between the localization edge and the defect point (1-19 or 21-39 respectively) the points on the sublattices (odd nodes) on which the edge states reside show the same decaying behaviour as the theory model, the measurement points on the other sublattices (even nodes) are significantly lower as it can be found for the Hermitian case (see fig. 3.3, fig. 3.4 or [66]). The measured localization length seems to be slightly longer than the theory value ($\xi = 2$) because the measurement points are lying above the theory curve in this region in all symmetry phases. The lower the resistive grounding elements get the higher the deviation between theory and experiment is, suggesting that this could be an effect of the higher impact of the circuit's parasitics for lower resistances and also of the resistor tolerances as explained earlier. Another observation that reinforces this assertion is that for higher on-site potential/lower resistances the edge states which exist on the sublattice where the resistors are soldered to (the right edge mode on sublattice A) differ much more from the theoretical points than on the other sublattice where no grounding resistors/on site potentials are added.
The defect point influences the edge modes because of the breaking of translation invariance. In the $\mathcal{PT}$ symmetric phase (fig. 4.8 a),b)) the defect does not seem to affect the fundamental structure of the edge state because only a shift in the absolute value of the eigenvector is induced at node 20 and the same decay as before can now be seen on the even nodes. Keep in mind that the added defect node causes a switching in the assignment between the sublattices and odd/even node numbers.
In the $\mathcal{PT}$ broken and $\mathcal{APT}$ symmetric phases the left edge mode seems to be much less influenced by the defect point than the right edge mode. It cannot be verified conclusively if this assertion is valid because of the loss-only configuration the additional parasitics are just added on the nodes with grounding resistors and due to the so introduced imaginary shift the eigenvalue of the right edge mode is significantly further away from the origin (see fig. 4.5 d)-f)). Therefore, the eigenvector has much less contribution to the Laplacian (scaling with the inverse of the eigenvalue, see section 2.3.4) and its signal to noise ration is significantly lower than the one of the left edge state.

4.1.6 Conclusions

Based on these observations we are able to draw some broader conclusions for the $\mathcal{PT}$-SSH model. In contrast to a Hermitian topological phase transition the localized edge states receive non-zero imaginary eigenvalues and can be found in all three symmetry regimes although a gap closing in the complex band structure takes place. Modes with zero eigenvalue would delocalize in the $\mathcal{PT}$ broken regime, which can be seen from the consideration of complex wave vectors. Therefore, this effect is due to the imaginary eigenvalues, which are solely a consequence of the non-Hermiticity of the model. To describe this phenomenon the topological classification of the $\mathcal{PT}$-SSH model can be extended to all symmetry regimes. In the Hermitian case the quantized Zak phase [101] is used as topological invariant to distinguish between topological and trivial phase. Calculated from our measurements of the $\mathcal{PT}$-SSH model it can be found that it is quantized only in the $\mathcal{PT}$ symmetric regime and thus does not serve as topological invariant in the other symmetry phases. To compensate for this flaw, another topological invariant, the $\mathcal{PT}$ winding number, can be introduced, which is equal to the Zak phase in the $\mathcal{PT}$

symmetric regime and also quantized in the other symmetry regimes (described in detail in [62]). Therefore, we are able to predict the presence of topologically protected edge states from the bulk properties as it is the case in the Hermitian model.
In contrast to this, we saw the absence of the topological defect state in the $\mathcal{PT}$ broken regime, which cannot be described by the before mentioned bulk-boundary correspondence. The localization/delocalization of the topological midgap state in this case matches the gap closing which can be predicted by the use of complex wave vectors and goes along with the symmetry phase transitions in the $\mathcal{PT}$-SSH model.
Consequently, we can conclude that the concept of bulk-boundary correspondence as it is known from Hermitian physics is not able to describe all topological aspects of this non-Hermitian model. Furthermore, topological defect states in non-Hermitian models can open a broader field of tuning and controlling topological states that are inaccessible to topological edge states.

4.2 Non-Hermitian, non-reciprocal SSH model

In the last section 4.1 we saw that the topological properties of models containing non-Hermiticity can differ from the established concepts derived from isolated Hermitian systems. In this section we want to investigate a model that breaks Hermiticity and additionally reciprocity for which *all* existing modes in a periodic configuration are predicted to become edge states for a finite open chain [100],[102]. This phenomenon of extensive bulk mode localization has been termed the non-Hermitian skin effect [102] due to its conceptual similarity to the electronic skin effect where the current density of alternating currents gets exponentially localized at the surface of the conducting material.
This research project was initiated by C.H. Lee and R. Thomale based on their findings about the anatomy of skin modes described in [100] together with T. Helbig, T. Hofmann and M. Greiter. The main contributions of the author of this thesis were in the experimental implementation, investigation and interpretation of the acquired data. The theoretical descriptions of the observed effects as well as the numerical simulations (included in the sections 4.2.2 - 4.2.5) were elaborated by T. Helbig, T. Hofmann, C.H. Lee, A. Szameit, M. Greiter and R. Thomale. The results of these investigations have been published in [63].

4.2.1 Circuit implementation

To be able to prove the predicted non-Hermitian skin effect experimentally on the circuit platform we first introduce a non-Hermitian, non-reciprocal hopping model and show how this can be translated into an electric circuit. In fig. 4.12 a) the structure of a one-dimensional 2 base hopping model is presented. The intercell hopping $r \in \mathbb{R}$ is made of a single capacitor, while the intracell hopping is formed by two parts $v(\omega)$ and $\pm\gamma$ with $v(\omega), \gamma \in \mathbb{R}$. The hopping $v(\omega) = (C_1 - 1/(\omega^2 L_1))$, tunable by frequency due to its implementation via a parallel LC resonator circuit, is reciprocal, whereas the direction-dependent hopping $\pm\gamma$ breaks reciprocity. Therefore, our system consists of a Hermitian SSH chain with frequency dependent intracell hopping $v(\omega)$ and an additional non-reciprocal, Hermiticity breaking intracell hopping $\pm\gamma$.
A change in sign of the hopping γ, as it is required for the non-reciprocal hopping, could be implemented easily as explained at the beginning (sec. 2.2.3) by the 180° phase difference using inductive and capacitive impedance. The difficulty here is the ability to change the sign depending on the hopping direction. Another artificial way exists to create the effectively negative of an impedance, a concept which can be traced back to the beginnings of the 19th century mainly used for resistance neutralization [103]. With the development of various amplifier circuits general descriptions of so called negative impedance converters arose [104]. For our purpose we use a negative impedance converter with current inversion (INIC) formed by an operational amplifier (OpAmp) circuit as it was first proposed for electronic metamaterials in [57] and is shown in fig. 4.9.

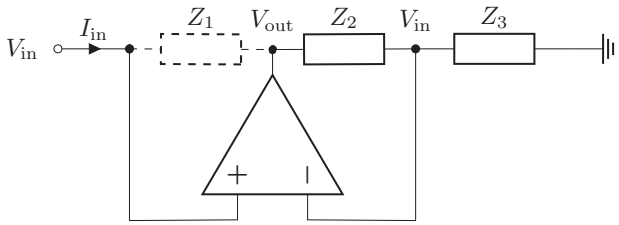

Figure 4.9: Non-inverting amplifier circuit ($\frac{V_{\text{out}}}{V_{\text{in}}} = 1 + \frac{Z_2}{Z_3}$) with impedance ($Z_3$, dashed) added between input and output.

An ideal non-inverting amplifier circuit due to its negative feedback network formed by Z_2 and Z_3 regulates the output voltage so that the voltage at the inverting input ($-$) equals the voltage at the non-inverting input ($+$) which is the input voltage V_{in}. Therefore, the amplification is set by the voltage divider formed by Z_2 and Z_3:

$$V_{\text{in}} = \frac{Z_3}{Z_2 + Z_3} \quad \Leftrightarrow \quad \frac{V_{\text{out}}}{V_{\text{in}}} = 1 + \frac{Z_2}{Z_3} \tag{4.30}$$

When an impedance is added between input and output (Z_1, dashed in fig. 4.9) the current flowing into the circuit is

$$I_{\text{in}} = \frac{V_{\text{in}} - V_{\text{out}}}{Z_1} = -\frac{Z_2}{Z_1 Z_3} V_{\text{in}} \tag{4.31}$$

or by looking at the impedance seen from the input:

$$Z_{\text{INIC}} = \frac{V_{\text{in}}}{I_{\text{in}}} = -\frac{Z_1 Z_3}{Z_2} \tag{4.32}$$

If now Z_1 or Z_3 equals Z_2, the respective other impedance would represent a negative impedance. When the circuit is used in floating configuration (see fig. 4.10 a)), again assuming ideal OpAmp behaviour, the currents flowing into the circuit are described by

$$I_{\text{right}} = \frac{1}{Z_3}(V_{\text{right}} - V_{\text{left}}) = \frac{1}{Z_2}(V_{\text{left}} - V_{\text{out}}) \tag{4.33a}$$

$$I_{\text{left}} = \frac{1}{Z_1}(V_{\text{left}} - V_{\text{out}}) \overset{(4.33a)}{=} \frac{1}{Z_3}\frac{Z_2}{Z_1}(V_{\text{right}} - V_{\text{left}})\,, \tag{4.33b}$$

which can be written as compact matrix equation:

$$\begin{pmatrix} I_{\text{left}} \\ I_{\text{right}} \end{pmatrix} = \frac{1}{Z_3} \cdot \begin{pmatrix} -\frac{Z_2}{Z_1} & \frac{Z_2}{Z_1} \\ -1 & 1 \end{pmatrix} \cdot \begin{pmatrix} V_{\text{left}} \\ V_{\text{right}} \end{pmatrix} \tag{4.34}$$

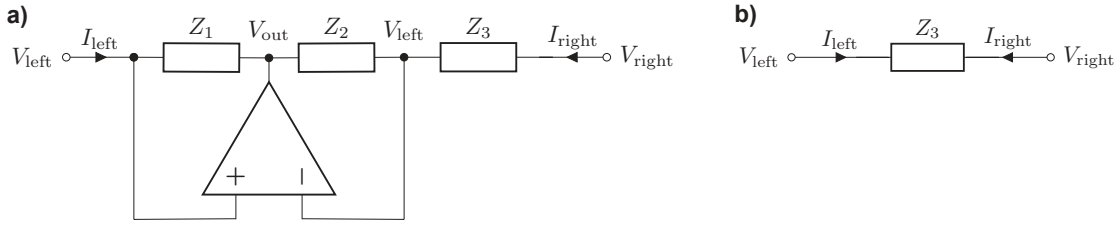

Figure 4.10: Comparing INIC and impedance. a): Circuit diagram of a floating INIC circuit, b): Voltages and currents at an impedance Z_3.

With $Z_1 = Z_2$ the current voltage relations are

$$\begin{pmatrix} I_{\text{left}} \\ I_{\text{right}} \end{pmatrix} = \frac{1}{Z_3} \cdot \begin{pmatrix} -1 & 1 \\ -1 & 1 \end{pmatrix} \cdot \begin{pmatrix} V_{\text{left}} \\ V_{\text{right}} \end{pmatrix} , \tag{4.35}$$

whereas for a passive impedance Z_3 (see fig. 4.10 b)) they are:

$$\begin{pmatrix} I_{\text{left}} \\ I_{\text{right}} \end{pmatrix} = \frac{1}{Z_3} \cdot \begin{pmatrix} 1 & -1 \\ -1 & 1 \end{pmatrix} \cdot \begin{pmatrix} V_{\text{left}} \\ V_{\text{right}} \end{pmatrix} \tag{4.36}$$

The left current I_{left} of the INIC flows in the reversed direction in comparison to the passive impedance, but the right current is the same as for a passive impedance. Therefore, the floating INIC circuit acts as a negative impedance seen from the left side and a positive impedance seen from the right, which breaks our definition of reciprocity ($\boldsymbol{J} \neq \boldsymbol{J}^\top$, see section 2.4).
Note that the applications of the INIC are not limited to single-ended or floating non-reciprocal impedance converters, there are many more variations/extensions of the INIC circuit with further possible applications. One feedback resistor could be replaced by a potentiometer to create a variable negative impedance (fig. 4.11 a)), negative inductances can be formed by capacitances that have much smaller outlines and are less prone to parasitics (fig. 4.11 b)) or a floating reciprocal negative impedance (fig. 4.11 c)) can be formed by the combination of two floating INICs (fig. 4.10 a)), to give just a few examples.

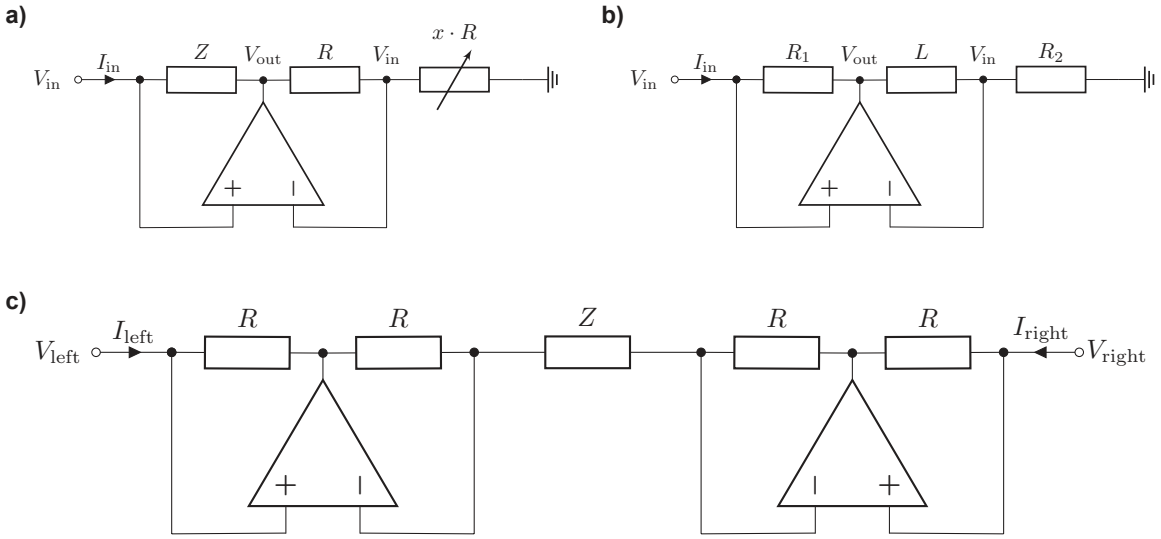

Figure 4.11: Several more INIC implementations. a): Grounded variable negative impedance $Z_{\text{var}} = -xZ$, b): Grounded negative artificial inductance $Z_{\text{-L}} = -i\omega C R_1 R_2$, c): Floating negative impedance $Z_{\text{float}} = -Z$.

Furthermore, the additional components connecting the nodes to ground (see fig. 4.12 c)) will be explained. The inductors L_0 are used to set the working frequency of the circuit, i.e. the frequency where the imaginary part of the diagonal of the grounded circuit Laplacian vanishes. Extra capacitors C_0 at the A sublattice twice as high as the non-reciprocal capacitors $\pm C_3$ from the INIC circuit are needed to compensate for the -1 entry on the diagonal of the INICs voltage-current relations (see eq. 4.35).
In contrast to the $\mathcal{PT}$-SSH circuit (see section 4.1) we are not able to eliminate the total need of active circuitry by an imaginary shift in our circuit model, but we are going to use the same concept (introduced by R_0 in fig. 4.12 c)) to ensure the stability of our circuit.

To be able to drive the circuit as expected we have to understand the nature of the circuit instabilities, how they manifest in the voltage response of the circuit and how they can be removed. In the following we will distinguish two different kinds of instabilities, instabilities caused by the non-ideal properties of the OpAmp circuits and instabilities introduced by diverging eigenmodes.

To describe the behaviour of a realistic OpAmp by its ideal model, several constrains of external parameters have to be met and the following elaborations do not reflect all of them. We will focus on those that have been explicitly considered during circuit design or had to be adjusted to achieve the expected circuit operation.

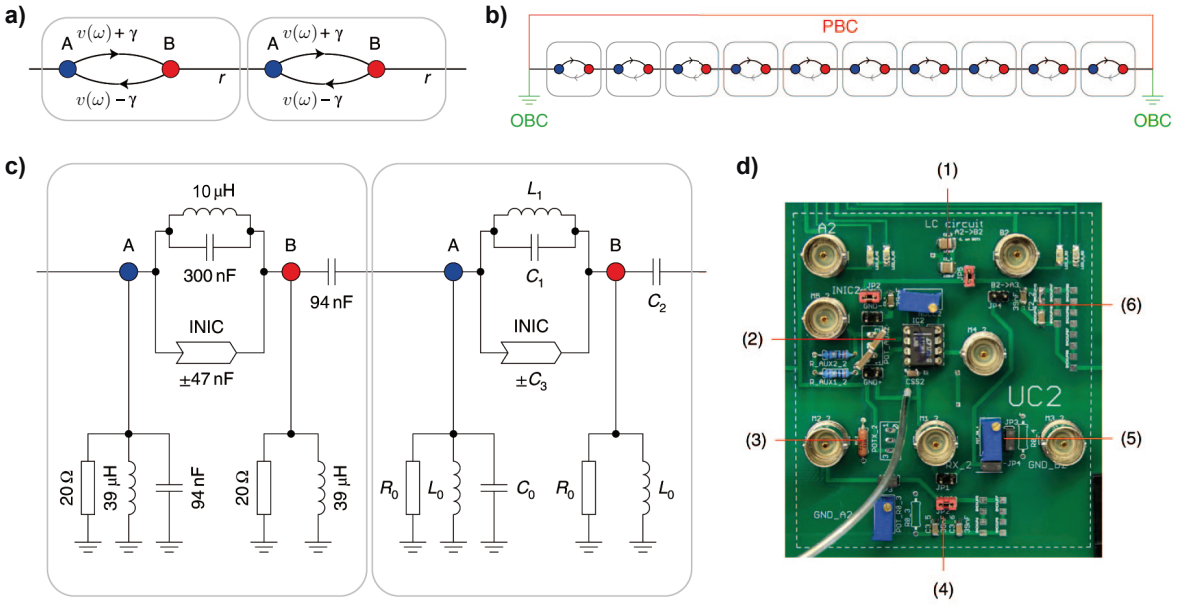

Figure 4.12: One-dimensional non-Hermitian and non-reciprocal circuit model. a): Hopping model of the one-dimensional chain. The intracell hopping is divided into a reciprocal frequency dependent part $v(\omega)$ and a non-reciprocal asymmetric part $\pm\gamma$. The intercell hopping is given by r. b): The investigated chain consists of 10 unit cells which can be used in periodic (PBC, red) and open configuration (OBC, green), the transition between PBC and OBC can be passed trough by adjusting the connection of the first and last node and the grounding elements at the edges. c): Circuit diagram of two unit cells of the implemented circuit labeled with nominal component values (left) and their designations in the theoretical model (right, see eq. 4.41). d): Cut out of a unit cell on the circuit board (see A.2 b)), each labeled building block can be added/subtracted by jumpers. (1): LC circuit to implement $v(\omega)$ formed by two parallel SMD capacitors (2×150 nF) and a high-current SMD inductor (on the backside); (2): INIC circuit (see fig. 4.10 a)) to implement the non-reciprocal hopping $\pm\gamma$ made of an OpAmp (LT1393, Analog Devices) powered by ±15 V DC with bypass capacitors (one can be seen below the LT1363, the other one is mounted on the backside), the positive and negative feedback is formed by parallel metal film resistors ($R_{\mathrm{INIC}} = 20\,\Omega$) and SMD capacitors ($C_{\mathrm{INIC}} = 470\,\mathrm{nF}$), the positive/negative impedance is set by a SMD capacitor ($C_3 = 47\,\mathrm{nF}$), for nulling the OpAmp circuit slots for additional jumpers to ground the inputs and a 5 kΩ nulling potentiometer are added; (3): Additional intracell resistor ($R_x = 10\,\Omega$, not used); (4): Grounding elements of sublattice A: A trimmer resistor to set R_0, a shielded wire wound inductor L_0 (backside), two parallel SMD capacitors (2x47 nF) for C_0; (5): Grounding elements of sublattice B: Same as (4) except of additional SMD capacitors; (6): Intercell hopping r built of two parallel SMD capacitors (2×47 nF) (adapted from [63]).

First of all the output of a realistic OpAmp is limited by the power supplies and its internal design. For the used setup the LT1363 OpAmp was powered with ±15 V. In

the data sheet we see that its output current should not exceed 50 mA [105]. From our INIC configuration we know that the output has to be able to provide a current that is twice the current flowing through the same but passive impedance with the same voltage applied as to the INIC circuit. To estimate the maximum output current we assume a capacitance of $C_3 = 47\,\mathrm{nF}$ at a maximum frequency of $f = 100\,\mathrm{kHz}$ and a maximum voltage of $V = 0.5\,\mathrm{V}$ and calculate the estimated maximum output current to $I_{max} = 2 \cdot 0.5\,\mathrm{V} \cdot 2\pi \cdot 100\,\mathrm{kHz} \cdot 47\,\mathrm{nF} \approx 30\,\mathrm{mA}$. The feedback resistors Z_1 and Z_2 have to carry the same current as the passive impedance and their resistance value determines the needed output voltage to drive this current. Therefore, the resistance should not exceed the maximum output voltage divided by the output current $R_{max} = 15\,\mathrm{V}/15\,\mathrm{mA} = 1\,000\,\Omega$. We chose significantly lower metal film resistors with low tolerance ($20\,\Omega \pm 0.1\,\%$) to not introduce problems due to the finite slew rate of the OpAmp by keeping the output voltage low. Meeting the elaborated requirements no unwanted saturation effects should obstruct the non-reciprocal capacitor to work as expected.
But beside saturation, the OpAmp operation can be disrupted by overshoot, ringing or oscillation effects, which is the case when the feedback signal is delayed. Reasons for this can be phase lags of the OpAmp's output signal due to the internal circuitry or phase shifts introduced by the feedback network. During the circuit board design we took care that the selected LT1363 OpAmp is unity gain stable (approximately 40° phase margin), but the feedback determined by the floating INIC converter configuration

$$\frac{V_{\mathrm{fb}}}{V_{\mathrm{out}}} = \frac{\frac{1}{i\omega C_3}}{\frac{1}{i\omega C_3} + R} = \frac{1}{1 + i\omega R C_3} \tag{4.37}$$

adds an additional amount of phase shift φ given by

$$\varphi = \arctan(-\omega R C_3)\,, \tag{4.38}$$

which equals $-45°$ at $f = 1/(2\pi R C_3) \approx 169\,\mathrm{kHz}$ and goes to $-90°$ for increasing frequencies. The phase shift due to the amplification process in the OpAmp is lower than $-90°$ for $f \gtrsim 1\,\mathrm{MHz}$ and led to an oscillation at approximately 1.4 MHz because the combined phase shifts get $-180°$ at this frequency and the negative feedback turns into an effective positive one due to the inverting input, which drives the system unstable. To compensate for this flaw, we added equal capacitors in parallel to the positive and negative feedback resistors Z_1 and Z_2 to make sure that they do not affect the INIC functionality, but remove the phase shift in the feedback loop (see 4.13).

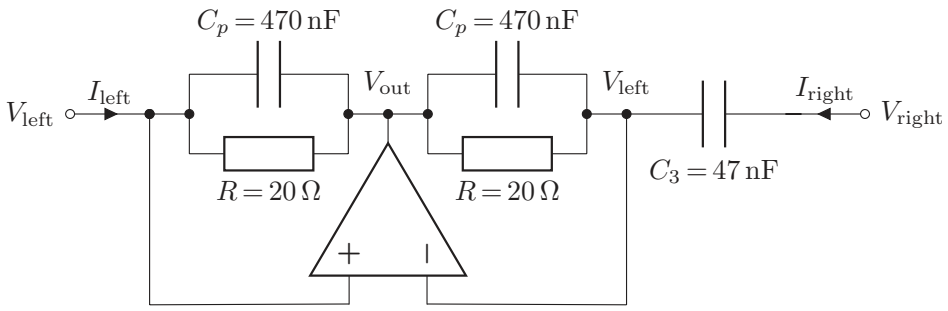

Figure 4.13: Non-reciprocal INIC implementation with improved feedback impedance to eliminate high frequency oscillations.

The added capacitors change the transfer function of the feedback loop to

$$\frac{V_{\mathrm{fb}}}{V_{\mathrm{out}}} = \frac{\frac{1}{i\omega C_3}}{\frac{1}{i\omega C_p + \frac{1}{R}} + \frac{1}{i\omega C_3}} = \frac{1 + i\omega R C_p}{1 + i\omega R(C_3 + C_p)}\,. \tag{4.39}$$

If $C_p \gg C_3$ the transfer function is approximately 1 and does not add any phase shift. The impedance magnitude of the feedback impedances is lowered by the parallel capacitors, but the output current is still determined only by C_3. Therefore, we do not exceed the maximum output current and the output voltage is further reduced due to the lower impedance.

The second kind of instability is introduced due to eigenmodes of the circuit having negative imaginary resonance frequencies, i.e homogeneous solutions of the set of differential equations increasing without any limit. Resistors connecting the nodes to ground can be used to add an imaginary shift to the eigenvalues of the grounded circuit Laplacian and eventually shift the resonance frequencies, too. It can be determined numerically for which complex frequencies the eigenvalues are zero and if they have negative imaginary parts.
For this purpose we set up the theoretical grounded circuit Laplacian in reciprocal space for the PBC circuit described in fig. 4.12 and calculate the admittance band structure. With the grounding capacitor C_0 chosen to compensate for the diagonal of the INIC configuration $C_0 = 2C_3$ and $\omega_0 = 1/\sqrt{C_1 L_1}$ we get:

$$\begin{aligned} \boldsymbol{J}_{\mathrm{skin}}(k,\omega) = i\omega \Bigg[& \left(C_1 + C_2 + C_3 - \frac{1}{\omega^2}\left(\frac{1}{L_0} + \frac{1}{L_1}\right) - \frac{i}{\omega R_0} \right) \mathbb{1} \\ & - \begin{pmatrix} 0 & C_1\left(1 - \frac{\omega_0^2}{\omega^2}\right) + C_2 e^{-ik} - C_3 \\ C_1\left(1 - \frac{\omega_0^2}{\omega^2}\right) + C_2 e^{ik} + C_3 & 0 \end{pmatrix} \Bigg], \end{aligned} \tag{4.40}$$

or in terms of Pauli matrices

$$\begin{aligned} \boldsymbol{J}_{\mathrm{skin}}(k,\omega) = i\omega \Bigg[& \left(C_1\left(1 - \frac{\omega_0^2}{\omega^2}\right) + C_2 + C_3 - \frac{1}{\omega^2 L_0} - \frac{i}{\omega R_0} \right) \boldsymbol{\sigma_0} \\ & - \left(C_1\left(1 - \frac{\omega_0^2}{\omega^2}\right) + C_2\cos(k) \right) \boldsymbol{\sigma_1} - \left(C_2 \sin(k) - iC_3 \right) \boldsymbol{\sigma_2} \Bigg], \end{aligned} \tag{4.41}$$

The admittance band structure is then given by:

$$j_{\text{skin}}(k,\omega) = i\omega\Bigg[\left(C_1\left(1-\frac{\omega_0^2}{\omega^2}\right)+C_2+C_3-\frac{1}{\omega^2 L_0}-\frac{i}{\omega R_0}\right) \pm\sqrt{\left(C_1\left(1-\frac{\omega_0^2}{\omega^2}\right)+C_2\cos(k)\right)^2+\left(C_2\sin(k)-iC_3\right)^2}\Bigg] \tag{4.42}$$

The term in front of the square root shifts the center in the complex plane and the square root term forms the complex admittance band structure. The resonance frequencies can be found either using the Hamilton formalism [57],[70] or searching for complex frequencies for which the eigenvalues are zero. By numerical simulations using the Hamilton formalism we find that for $R_0 \leq 45.0\,\Omega$ in the PBC configuration and for $R_0 \leq 66.8\,\Omega$ with OBC termination all eigenfrequencies do not have negative imaginary parts (as explained in the beginning of chapter 4) and therefore the circuit should be stable.
With these extended stability considerations and an additional circuit board optimization (for details see appendix A.2) the circuit could be investigated in open and periodic configuration.

4.2.2 Non-local voltage response as an indicator of mode localization

To check if an extensive edge localization of modes can be found we investigate the voltage response to a local current excitation of the circuit. As explained in section 2.3.4 the relation between current input and voltage response is determined by the Green's matrix, which can be put together by the normalized left ($\vec{\phi}_n^\dagger$) and right eigenvectors ($\vec{\psi}_n$) forming a complete basis as long as no degeneracies occur (degeneracies could be found for example for an exact system at exceptional points) weighted by the inverse eigenvalues $1/\lambda_n$ (eq. 2.45). In PBC configuration all eigenvectors are delocalized along the chain (Bloch states) and therefore the voltage response can only be delocalized (in a system without parasitic resistances) or localized at the input node due to parasitic resistive damping. The eigenvalues can be approximated by $\lambda_n \propto \frac{1}{\rho}+\epsilon_n$ with ρ representing damping resistances present in the circuit and ϵ_n describing the original eigenvalue without resistive contributions. Expanding this in $\rho\epsilon_n$ for $1/\rho \gg |\epsilon_n|$ leads to

$$\boldsymbol{G} = \rho\underbrace{\sum_n \vec{\psi}_n\vec{\phi}_n^\dagger}_{\mathbb{1}} - \sum_n(\rho^2\epsilon_n)\vec{\psi}_n\vec{\phi}_n^\dagger + \mathcal{O}(\rho^3\epsilon_n^2)\,, \tag{4.43}$$

which shows that the voltage response for large damping resistances is localized at the current input due to its proportionality to the local input current in 0-th order.
In OBC configuration localized modes are not forbidden anymore because periodicity is broken. For eigenstates (right eigenvectors) with sublattice independent exponentially localization at one edge of the chain (here: right edge), the entries of the right eigenvectors are proportional to $\psi_{n,x} \sim |\alpha|^{x-N}$ regardless of the sublattice position A, B with

$|\alpha| > 1$ and the variable x counting the N unit cells from left to right. The entries of the left eigenvectors $\vec{\phi}_n^\dagger$ are proportional to $\phi_{n,x} \sim |\alpha|^{-x}$ (eigenvectors of the transposed Laplacian, therefore localized at the other edge).
Assuming that the Greens matrix is dominated by the eigenmode with smallest eigenvalue λ_1 (resistive damping has to be sufficiently small) the voltage response to a current input $I \sim \delta_{x,a}$ at a node in unit cell a

$$\vec{V} \sim \frac{1}{\lambda_1} \frac{\vec{\psi}_1 \vec{\phi}_1^\dagger}{(\vec{\phi}_1^\dagger \vec{\psi}_1)} \vec{I} = \frac{1}{\lambda_1} \frac{\phi_{1,a}^*}{(\vec{\phi}_1^\dagger \vec{\psi}_1)} \vec{\psi}_1 \tag{4.44}$$

is proportional to the stimulated right eigenvector $\vec{\psi}_1$. $\phi_{1,a}$ is the entry of the left eigenvector at the current input node and $(\vec{\phi}_1^\dagger \vec{\psi}_1) \sim 2N\,|\alpha|^{-N}$ guarantees the normalization. Consequently, the voltages at the different unit cells x should be

$$V_x \sim \frac{1}{\lambda_1} \frac{|\alpha|^{-a}}{2N\,|\alpha|^{-N}} |\alpha|^{x-N} = \frac{1}{2N\,\lambda_1} |\alpha|^{x-a} \tag{4.45}$$

leading to an increasing voltage towards the right edge where the eigenstate is localized. With the assumption that all modes of the model are localized at the same edge the circuit should exhibit a non-local voltage response without any fine tuning for mode selection.

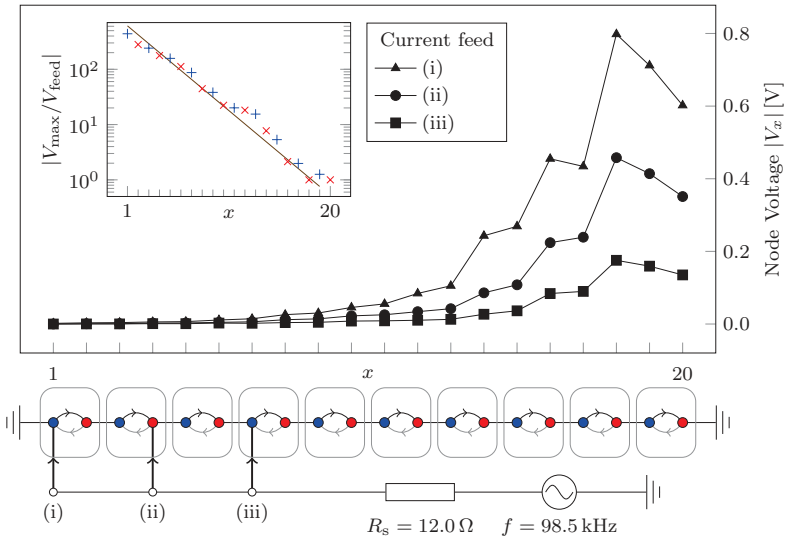

Figure 4.14: Measured node voltages for current inputs on nodes 1 (i, triangles), 4 (ii, circles) and 7 (iii, squares) by a voltage source with series resistor ($R_s = 12.0\,\Omega$) at $f = 98.5\,\text{kHz}$. The grounding resistance of the circuit is set to $R_0 = 120\,\Omega$. The inset shows the maximum amplification for current input at each node. It is calculated by the quotient of the maximum voltage magnitude measured in the voltage response divided by the voltage measured at the current input. Blue pluses (A) and red crosses (B) indicate the different sublattices, the black line shows the maximum amplification expected from the localization factor $\alpha = (2.2 \pm 0.3)$ (same fitting procedure as in tab. 4.2) calculated from the bulk eigenvectors (from [63]).

To minimize the localization effect due to resistive damping we chose $R_0 = 120\,\Omega$, a value near the experimental limit of circuit stability. This value is almost twice as high as the theoretically predicted maximum value for OBC $R_0 \leq 66.8\,\Omega$ and only stable due to parasitic resistive terms having a positive impact on the circuit stability.
In fig. 4.14 the voltage profiles for three different current input positions near the left edge of the circuit are shown. The further away the input is from the right edge, the higher the maximum voltage is at the other side of the chain indicating a localization of the dominant mode for this configuration. The position of the voltage maximum slightly away from the edge depends on the explicit form of the dominant mode and in the further course of the investigations we will see that eigenstates with maximum at this position exist in this circuit configuration (see fig. 4.15 e)).
In the inset of fig. 4.14 the measured maximum amplification of the input voltage $|V_{\text{max}}|/|V_{\text{feed}}|$ for current input at every single node of the circuit is plotted with a logarithmic vertical axis confirming the exponential localization.

4.2.3 Extended circuit investigation

After this first indication of edge localization present in the circuit under test we perform several measurements in OBC and PBC configuration to find the eigenvalue spectra and analyze all (right) eigenvectors in the open chain for different sets of parameters (for investigation methods see section 2.3.4). In order guarantee circuit stability the grounding resistors are set to $R_0 = 20\,\Omega$.

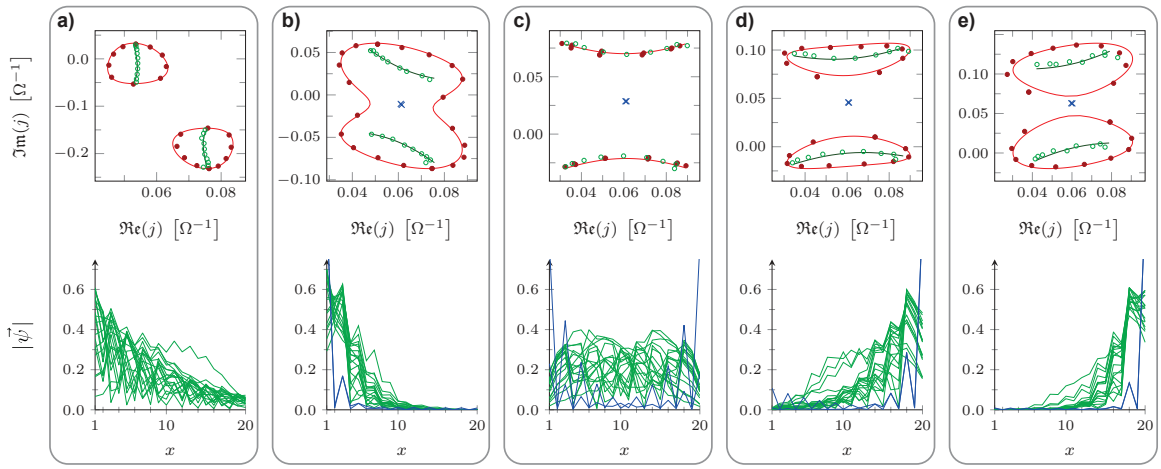

Figure 4.15: Analysis of the measured grounded circuit Laplacian of the periodic (PBC) and open (OBC) 10 unit cell chain. The upper plots show the PBC (red points) and OBC (green points/blue crosses) eigenvalues j, solid lines correspond to the fitted theory models (see eq. 4.48). The lower plots depict the absolute value of the eigenvectors $\vec{\psi}$ in the OBC case. The blue curves correspond to topological edge modes as they would be expected for a SSH chain with eigenvalue in the middle of the band gap and single sublattice supply, the green curves are the bulk eigenvectors. a): $f = 70.0\,\text{kHz}$, b): $f = 84.2\,\text{kHz}$, c): $f = 91.5\,\text{kHz}$, d): $f = 95.0\,\text{kHz}$, e): $f = 98.5\,\text{kHz}$ (adapted from [63]).

In the upper half of fig. 4.15 measured eigenvalues (solid points) for different measurement frequencies for PBC (red) and OBC (green/blue) configuration are shown. The theory curves are achieved by fitting the theoretical circuit model (eq. 4.48) to the different data sets by varying the inductances with added serial resistance (see tab. 4.1). A slight variation of the serial inductances of the coils with frequency could also be found during the pre-characterization process, as well as an increase in the serial resistance.

Frequency f [kHz]	70.0	80.0	84.2	91.5	95.0	98.5
Serial inductance L_0 [µH]	33.0	32.0	31.7	30.3	30.1	30.0
Serial resistance R_{L_0} [mΩ]	660	700	750	780	780	780
Serial inductance L_1 [µH]	10.1	10.1	10.1	10.1	10.1	10.1
Serial resistance R_{L_1} [mΩ]	220	230	250	280	300	320

Table 4.1: Fit of the theoretical Laplacian (see eq. 4.48) to the different data sets by variation of the circuit serial inductances with parasitic serial resistance (adapted from [63]).

The frequency dependence of the inductance could stem from the magnetic properties of the core and shielding material, the main cause for the increasing serial resistance is the electrical skin effect. But the non-idealities of the other circuit components as well as parasitics introduced due to the circuit board can be reflected in these fitting parameters, too.
In figs. 4.15 a),b),d),e) we find that the eigenvalues for PBC lie on one or two *closed* curves (red), which is dictated due to the periodicity of the circuit which results in periodicity of the admittance band structure. In OBC, where no periodicity is present, the eigenvalues (green) lie on open arcs encircled by the PBC curves with some additional isolated points (blue). Note that this is in stark contrast to the findings for Hermitian systems, as well as to our results for the $\mathcal{PT}$-SSH circuit where the eigenvalues in periodic and open configuration do not differ significantly except for some localized edge or defect modes. For the measurement at $f = 91.5\,\mathrm{kHz}$ in fig. 4.15 c) where the reciprocal hopping should be approximately zero the OBC and PBC eigenvalues lie on the same open arc except for two OBC eigenvalues in the gap between the two arcs.
In this case the eigenvectors plotted in the lower half of fig. 4.15 show the same delocalized behaviour as for Hermitian Bloch states. The eigenvectors with eigenvalues in the gap (blue, figs. 4.15 b)-e)) show a different localization behaviour than the other modes and single sublattice support, as it is the case for topological edge modes in a Hermitian system.
The eigenvectors in the other measurements where OBC and PBC spectra differ exhibit edge localization for all OBC eigenvectors independent from the position of their eigenvalues (figs. 4.15 a),b),d),e)), an unknown feature in Hermitian systems. Furthermore, the localization position and strength depends on the reciprocal hopping and can be found to show a maximum at figs. 4.15 b),d), which can be comprehended on the basis of the plots for the left edge localization due to increasing and weakening afterwards for decreasing $v(\omega)$, starting at $v(\omega) \approx 0$ for fig. 4.15 $c) \to b) \to a)$.

4.2.4 Bulk mode localization: The non-Hermitian skin effect

The effect of localization of all bulk modes is known in theory as the non-Hermitian skin effect. The concept can be understood by the thought experiment of threading a complex magnetic flux through a periodic atomic chain [106–108]. A magnetic flux ϕ flowing through a periodic N unit cell chain introduces a constant phase factor $e^{i\frac{\phi}{N}}$ added to the hoppings, which can be denoted as a shift of the wave vector by $k \to k + \frac{\phi}{N}$. When we now think about a complex flux $\mathfrak{Re}(\phi) + i\mathfrak{Im}(\phi)$ our shifted wave vector can be treated as a complex variable as we did in the previous section 4.1

$$k \;\to\; k + \frac{1}{N}\mathfrak{Re}(\phi) + i\frac{1}{N}\mathfrak{Im}(\phi) \;=:\; \widetilde{k} + i\kappa\,. \tag{4.46}$$

In this picture the real part of the adiabatically pumped flux shifts the permitted discrete wave vectors in the finite chain. For every $\phi \to \phi_0 + 2\pi$ this causes a new assignment between the eigenvectors and eigenvalues. In a finite lattice k takes N equidistant values $\frac{2\pi}{N}$ in $[0, 2\pi[$ and is shifted by one of these steps for every $\phi \to \phi_0 + 2\pi$.
The imaginary part of the flux adds an exponential damping $e^{-\frac{\mathfrak{Im}(\phi)}{N}}$ to the hoppings, which decreases their contribution to the PBC eigenvalues. *All* eigenvectors are also altered and decrease exponentially along the chain due to the damping.
By gauge transformation $\boldsymbol{V^{-1}JV}$ with $V = \mathrm{diag}(e^{i\phi/N}, e^{2i\phi/N}, \ldots, e^{i\phi})$ the accumulated phase shift can be assigned to the single intercell hopping at the connection of the two ends of the periodic ring [100, 102, 109]. Therefore, the impact of the threaded flux can also be seen as an exponential weakening $e^{-|\mathfrak{Im}(\phi)|}$ and a phase shift $e^{\pm i\mathfrak{Re}(\phi)}$ of this single hopping term, which are experimentally accessible parameters.
When the imaginary part of the flux is increased until the hopping is suppressed to zero, this corresponds to a transition from a periodic to an open chain. Of course the limit $\mathfrak{Im}(\phi) \to \infty$ does not represent the OBC limit because it would mean that every hopping along the chain would be suppressed and so the chain would fall apart. It can be shown mathematically [100, 109] that in the limit of long chains $N \to \infty$ a necessary condition for reaching the OBC limit is the degeneracy of the spectrum $j(\widetilde{k} + i\kappa)$, i.e. the OBC limit is reached for the smallest value of κ for which two eigenvalues with different real parts of the wave vector $\widetilde{k}, \widetilde{k}'$ conincide:

$$j(\widetilde{k} + i\kappa) \stackrel{!}{=} j(\widetilde{k}' + i\kappa) \quad \text{for } \widetilde{k}' \neq \widetilde{k} \text{ with } \widetilde{k}', \widetilde{k} \in \mathbb{R}. \tag{4.47}$$

To investigate this phenomenon experimentally, the hopping between the ends of the chain was gradually reduced until the OBC configuration was reached. Additionally, the grounding of the two end nodes was adjusted accordingly to do not change the diagonal term of the grounded circuit Laplacian at these nodes.
The sketched hopping model of this process is shown in fig. 4.16 a) and the measured eigenvalues (black dots) and -vectors (gray lines) are given in fig. 4.16 b),d). For the admittance spectra fig. 4.16 b) we find that they evolve from one closed loop for the periodic chain ($\eta = 1$) to two open arcs in the open configuration ($\eta = 0$), which also coincides with the computed spectral flow of a 32 site chain depicted in fig. 4.16 c). This process equals the geometrical interpretation of the condition established in eq. 4.47. Due to the periodicity $j(k + 2\pi) = j(k)$ in PBC, the spectrum forms a periodic curve in

complex admittance space. When κ is increased, the area inside the closed loop shrinks to zero (see [109] for an illustrative explanation) until the degeneracy forced by eq. 4.47 is reached on open arcs or isolated points.
This geometrical interpretation furthermore explains why the non-Hermitian skin effect cannot be found in Hermitian models as well as in the non-Hermitian $\mathcal{PT}$-SSH model. A Hermitian model in the grounded circuit Laplacian formalism forces a purly imaginary admittance spectrum $j_m(\vec{k}) = -j_m^*(\vec{k})$ (see section 2.4). This spectrum already lies on open arcs, i.e. the imaginary admittance axis, for PBC and therefore needs not to be further shrunk to reach the OBC constrains. Also the PBC spectrum of the non-Hermitian $\mathcal{PT}$-SSH model is restricted to open arcs, which lie on the real and imaginary axes due to $\mathcal{PT}$ and $\mathcal{APT}$ symmetry (see section 4.1). Even the spectrum of a non-Hermitian system exhibiting reciprocity would not form a closed loop with non-zero inner area in the complex plane because the eigenvalues retract themselves due to $j(k) = j(-k)$ (see section 2.3.4).
In summary the spectrum of a periodic system must lie on closed loops with non-zero area inside, so that a shrinking to open arcs/isolated points is needed to reach the OBC spectrum and a complex wave vector is must be introduced to fulfill eq. 4.47 leading to a localization of all eigenstates. In terms of system symmetries this can only be achieved by a combined breaking of Hermiticity and reciprocity.

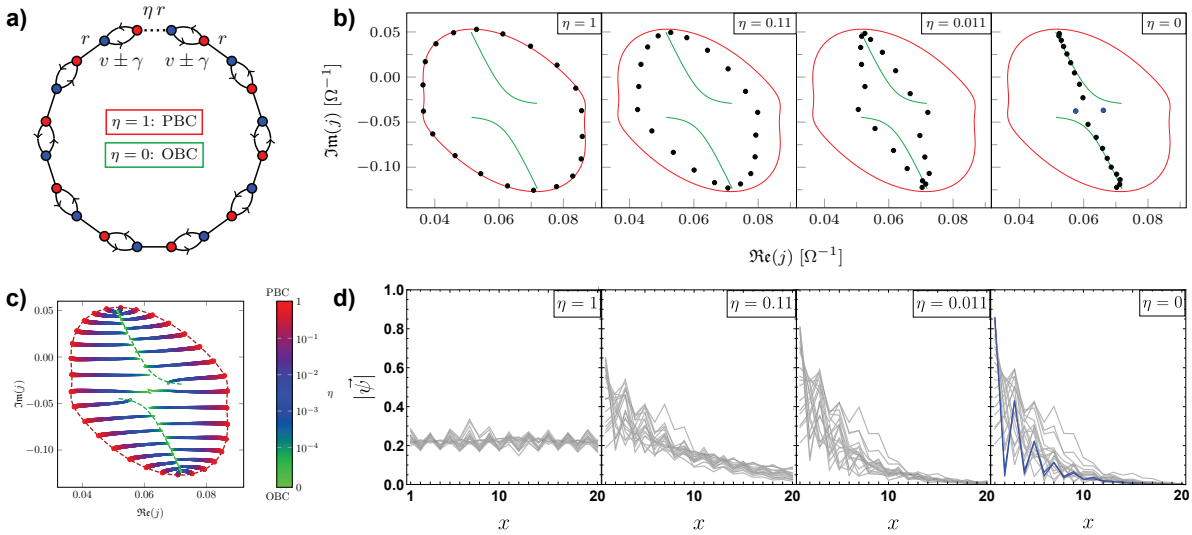

Figure 4.16: Spectral flow from PBC ($\eta = 1$) to OBC ($\eta = 0$). a): Hopping model with variable (η) hopping term connecting both ends of the chain. b): Measured admittance eigenvalues j (black points) for decreasing boundary hopping $\eta\, r$ together with the computed spectra for a periodic (red) and open (green) long chain at $f = 80.0\,\mathrm{kHz}$ (see eq. 4.48, parameters can be found in fig. 4.12 and tab. 4.1 respectively). c): Computed spectral flow (dots) for a 32 site chain from PBC ($\eta = 1$, red dashed loop for long chain) to OBC ($\eta = 0$, green dashed arcs for long chain). d): Eigenvectors $\vec{\psi}$ corresponding to the measured eigenvalues in b), for $\eta = 0$ (OBC) the vectors of the eigenvalues in the middle are highlighted in blue due to their characteristic topological edge state like form (adapted from [63]).

In addition to the spectral flow of the eigenvectors from PBC to OBC the localization of all eigenstates can directly be seen in fig. 4.16 d). While all eigenvectors are delocalized over the whole periodic chain for $\eta = 1$, they get localized at the left edge for decreasing η and show a finite localization length in the OBC configuration ($\eta = 0$).

To prove the concept of complex wave vectors again and gain more insights about the qualitative localization we recast our grounded circuit Laplacian from equation 4.40 by extending the inductors with parasitic serial resistances $L_j \to L_j + R_{L_j}/(i\omega)$:

$$\begin{aligned}
\boldsymbol{J}_{\text{skin}}(k,\omega) \;=\; & i\omega \Bigg[\left(C_1 + C_2 + C_3 - \frac{1}{\omega^2(L_1 + R_{L_1}/(i\omega))} - \frac{1}{\omega^2(L_0 + R_{L_0}/(i\omega))} - \frac{i}{\omega R_0} \right) \boldsymbol{\sigma_0} \\
& - \left(C_1 - \frac{1}{\omega^2(L_1 + R_{L_1}/(i\omega))} + C_2\cos(k) \right) \boldsymbol{\sigma_1} - \left(C_2 \sin(k) - iC_3 \right) \boldsymbol{\sigma_2} \Bigg] \\
= \; & i\omega \Bigg[\underbrace{\left(C_1 + C_2 + C_3 - \frac{1}{\omega^2 L_1 + i\omega R_{L_1}} - \frac{1}{\omega^2 L_0 + i\omega R_{L_0}} - \frac{i}{\omega R_0} \right)}_{\epsilon_0(\omega)} \boldsymbol{\sigma_0} \\
& - \Bigg(\underbrace{C_1 - \frac{L_1}{\omega^2 L_1^2 + R_{L_1}^2}}_{v_R(\omega)} + i \underbrace{\left(-\frac{1}{\omega} \cdot \frac{R_{L_1}}{\omega^2 L_1^2 + R_{L_1}^2} \right)}_{v_I(\omega)} + \underbrace{C_2}_{r} \cos(k) \Bigg) \boldsymbol{\sigma_1} \\
& - \Big(\underbrace{C_2}_{r} \sin(k) - i \underbrace{C_3}_{\gamma} \Big) \boldsymbol{\sigma_2} \Bigg] \\
= \; & i\omega\epsilon_0(\omega)\boldsymbol{\sigma_0} - i\omega \left[\left(v_R(\omega) + iv_I(\omega) + r\cos(k) \right) \boldsymbol{\sigma_1} + \left(r\sin(k) - i\gamma \right) \boldsymbol{\sigma_2} \right] \\
= \; & i\omega\epsilon_0(\omega)\boldsymbol{\sigma_0} - \omega \bar{\boldsymbol{J}}(k,\omega)
\end{aligned} \tag{4.48}$$

Here, $\bar{\boldsymbol{J}}(k,\omega)$ is the effective Laplacian without the complex shift $\epsilon_0(\omega)$. Therefore, the effective Laplacian can be written as

$$\bar{\boldsymbol{J}}(k) \;=\; i \left[\left(\underbrace{v_R(\omega) + r\cos(k)}_{h_x(k,\omega)} + iv_I(\omega) \right) \boldsymbol{\sigma_1} + \left(\underbrace{r\sin(k)}_{h_y(k)} - i\gamma \right) \boldsymbol{\sigma_2} \right] \;=\; i \cdot \vec{d}(k,\omega)\vec{\boldsymbol{\sigma}} \tag{4.49}$$

and its spectrum is given by

$$\bar{j}(k,\omega) \;=\; \pm i \sqrt{\left(h_x(k,\omega) + iv_I(\omega) \right)^2 + \left(h_y(k) - i\gamma \right)^2} \,. \tag{4.50}$$

To be able to calculate the imaginary part κ of the wave vector sufficiently to reach the OBC limit of the bulk spectrum and determining the localization of the bulk modes we consider a Bloch ansatz $(\psi_{x,A}, \psi_{x,B}) = \alpha^x (u_A, u_B)$ with complex factor $\alpha \in \mathbb{C}$ and x denoting the unit cell to solve the eigenvalue equations for the periodic chain:

$$i \left(\alpha^{-1} r + \left(v_R + iv_I - \gamma \right) \right) u_B \;=\; \lambda\, u_A \tag{4.51a}$$

$$i \left(\left(v_R + iv_I + \gamma \right) + \alpha r \right) u_A \;=\; \lambda\, u_B \tag{4.51b}$$

This leads to the equation

$$\begin{aligned} \lambda^2 &= -\left(\alpha^{-1}r + (v_R + iv_I - \gamma)\right) \cdot ((v_R + iv_I + \gamma) + \alpha r) \\ \Leftrightarrow\ 0 &= \underbrace{r\,(v_R + iv_I - \gamma)}_{a}\,\alpha^2 + \underbrace{(v_R + iv_I)^2 - \gamma^2 + \lambda^2 + r^2}_{b}\,\alpha + \underbrace{r\,(v_R + iv_I + \gamma)}_{c} \end{aligned} \tag{4.52}$$

for the Bloch factor α with the eigenvalue λ treated as a parameter. Note that this reproduces the effective spectrum in eq. 4.50 for purely real wave vectors $\alpha \to e^{ik}$. Taking the boundary conditions of the open chain into account [100],[102] it can be found that a necessary condition for non-topological bulk or skin modes to exist is that the absolute values of the Bloch factors α_1, α_2 coincide. Therefore, the quadratic equation eq. 4.52 in α has to be solved, which in general has two distinct solutions $\alpha_{1,2} \in \mathbb{C}$ in the form of

$$\alpha_{1,2} = \frac{-b \pm \sqrt{b^2 - 4ac}}{2a}\,. \tag{4.53}$$

Because of $|\alpha_1 \cdot \alpha_2| = |\alpha_1| \cdot |\alpha_2|$ and $|\alpha_1| \overset{!}{=} |\alpha_2| =: |\alpha|$ we can use

$$|\alpha| = \sqrt{|\alpha_1 \cdot \alpha_2|} = \sqrt{|-\frac{c}{a}|} = \sqrt{\left|\frac{v_R + iv_I + \gamma}{v_R + iv_I - \gamma}\right|} = \sqrt[4]{\frac{(v_R + \gamma)^2 + v_I^2}{(v_R - \gamma)^2 + v_I^2}} \tag{4.54}$$

to determine the magnitude of the Bloch factor α independently from the eigenvalue λ. Note that the imaginary part of the wave vector κ, which is needed to reach the spectrum in OBC, belongs to $|\alpha|$. Furthermore, the absolute value of the Bloch factor can be translated into the decay length ξ that the bulk modes obtain due to the non-Hermitian skin effect:

$$\xi = \frac{1}{\kappa} = -\frac{1}{\ln(|\alpha|)} = \left[\frac{1}{4}\ln\left(\frac{(v_R - \gamma)^2 + v_I^2}{(v_R + \gamma)^2 + v_I^2}\right)\right]^{-1} \tag{4.55}$$

The magnitude of α and therefore the localization length of the bulk modes is not affected by the intercell hopping r, only the sublattice coefficients u_A, u_B can be changed by r. To examine the consistency of κ between theoretical prediction and our experimental outcomes we calculate the imaginary wave vector from the parameters given in fig. 4.12 and tab. 4.1 and determine the measured values by fitting the exponential decay for the measurements shown in fig. 4.15. The results are summarized in tab. 4.2. Theory and experiment agree within the scope of the experimental standard deviations, which shows that the model describes localization behaviour of our circuit correctly within the whole experimentally investigated frequency range. The standard deviations of the decays show that the decay length of the bulk modes differ up to approximately 20 % (excluding the point ($f = 91.5\,\mathrm{kHz}$) where no decay can be found), which might be rooted in component tolerances and additional parasitics introduced by circuit board and components altering the translation invariance of the chain.

Frequency f [kHz]	70.0	84.2	91.5	95.0	98.5
Theory (fit): κ_{theo}	0.22	0.87	-0.02	-0.47	-0.93
Experiment: κ_{exp}	0.24 ± 0.04	0.87 ± 0.08	0.0 ± 0.1	-0.5 ± 0.1	-1.0 ± 0.1

Table 4.2: Calculated κ_{theo} and experimentally determined κ_{exp} imaginary wave vectors for different frequencies f. κ_{theo} is calculated by inserting the model parameters given in fig. 4.12 and the fitted values for the inductors from tab. 4.1 in eq. 4.55. The experimental values κ_{exp} are obtained as mean value of the fitted decay of all bulk eigenmodes, the error is given by the standard deviation and represents a measure of the agreement of the fitted localization lengths (adapted from [63]).

After the validation of our fitting model describing the localization of the modes, we can use it to describe the frequency dependence of the imaginary part of the wave vector corresponding to the inverse localization length $\kappa = 1/\xi$. Therefore, we start with the idealized model ($R_{L_1} = 0, v_I = 0$) leading to

$$\kappa_{\text{ideal}}(\omega) \;=\; \frac{1}{2} \ln \left| \frac{v_R(\omega) - \gamma}{v_R(\omega) + \gamma} \right|, \tag{4.56}$$

recalling the frequency dependence of $v_R(\omega)$. For $v_R(\omega) = 0$ the inverse localization length is zero, leading to delocalized modes in chain, whereas for $v_R(\omega) = \pm\gamma$ the inverse localization length diverges resulting in maximally localized states.
At the points in parameter space where the bulk eigenvectors are maximally localized the problem can be solved analytically. Here, the reciprocal hopping balances one direction of the non-reciprocal hopping so that the asymmetry between left and right hopping is at maximum. From the characteristic polynomials of these OBC Laplacians only three distinct eigenvalues can be figured out (for detailed calculation see the supplementary material of [63]):

$$\det(\lambda \mathbb{1} - \bar{\boldsymbol{J}}_{\text{OBC}}) \;=\; \lambda^2 \cdot \left(\lambda^2 - (ir)^2\right)^{N-1} \tag{4.57}$$

Thus the OBC spectrum consists of the two-fold degenerated eigenvalue $\lambda_1 = 0$ and the $(N-1)$-fold degenerate eigenvalues $\lambda_{2,3} = \pm ir$ corresponding to the three different eigenvectors (here: left edge localization, $v_R(\omega) = -\gamma$)

$$\begin{array}{rcl} \vec{\psi}_0 & = & (1, \quad 0, \quad\quad 0, \quad 0, \quad 0, \quad \dots)^\top \\ \vec{\psi}_{ir} & = & (1, \quad -\frac{r}{2\gamma}, \quad -\frac{r}{2\gamma}, \quad 0, \quad 0, \quad \dots)^\top \\ \vec{\psi}_{-ir} & = & (1, \quad \frac{r}{2\gamma}, \quad -\frac{r}{2\gamma}, \quad 0, \quad 0, \quad \dots)^\top . \end{array} \tag{4.58}$$

From our measurements (fig. 4.15 b),e)) we see that small serial resistances of the inductor L_1 as well as component tolerances remove the degeneration of eigenvalues and coincidence of the eigenvectors, but they still can be found maximally localized.

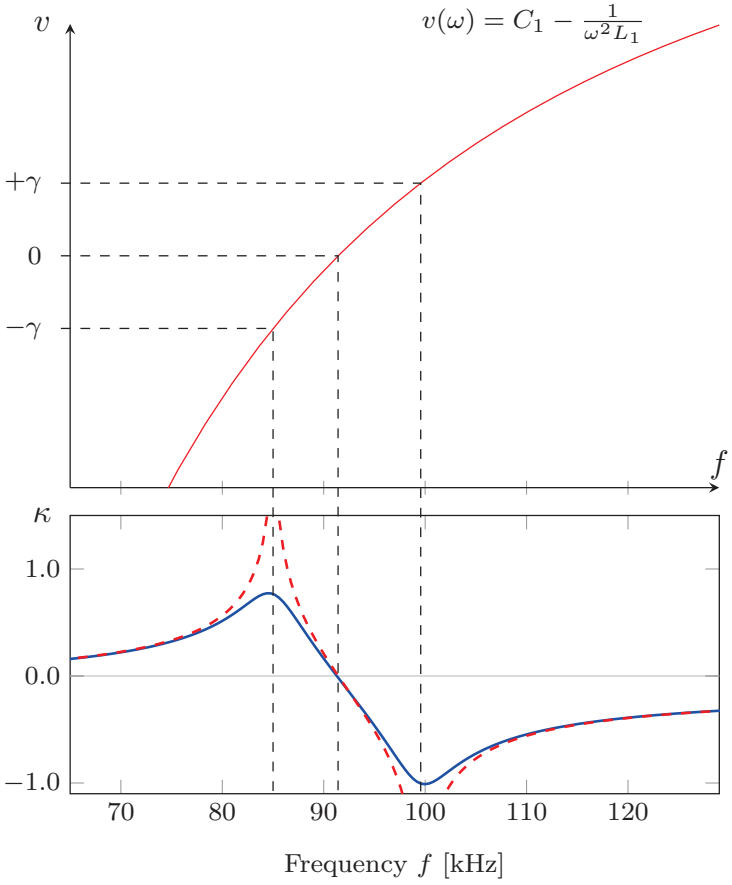

Figure 4.17: Frequency dependence of the inverse localization length κ. Top: Plot of the idealized ($R_{L_1} = 0, v_I = 0$) reciprocal intracell hopping $v_R(\omega) = v(\omega)$ (red curve) as a function of frequency $f = \omega/(2\pi)$. Bottom: Inverse localization length κ of the idealized model ($R_{L_1} = 0, v_I = 0$, dashed red curve) and of the fit model eq. 4.48 with serial resistance of L_1 fixed to $R_{L_1} = 320\,\mathrm{m\Omega}$ (blue curve). The frequencies/hoppings for the localization/delocalization maximum in the idealized model are marked with dashed black lines (from the supplementary material of [63]).

The points $\kappa = 0, \pm\gamma$ are marked by dashed black lines in fig. 4.17 where the idealized inverse localization length $\kappa_{\mathrm{ideal}}(\omega)$ (red dashed curve) and the inverse localization length of the fitting model $\kappa(\omega)$ (blue curve) are shown (bottom) together with the idealized reciprocal intracell hopping $v_R(\omega) = v(\omega)$ (top). The parasitic serial resistance of the inductor L_1 in the reciprocal intracell hopping causes the inverse localization length κ (eq. 4.55) to be damped to finite values for $v_R(\omega) = \pm\gamma$. Furthermore, due to the different frequency dependencies of the real and imaginary part of the non-idealized hopping $v_R(\omega) + iv_I(\omega)$, the maximum localization points are slightly shifted away from $v(\omega) = \pm\gamma$ and differ in localization lengths. On the contrary, the point of delocalization $\kappa = 0$ is not affected by the parasitics. The measurements shown in fig. 4.15 b),c),e) are performed at the frequencies where we find the maximum left localization (b)), delocalization (c)) and maximum right localization (e)).

At the delocalization point $\kappa = 0$ we find the PBC spectrum forming an open arc although Hermiticity and reciprocity are broken. This can be explained by an extended reciprocity condition. The PBC spectrum retraces itself not only if $j(k) = j(-k)$, but also for

$$j(k_s + k) = j(ks - k) \quad \text{with } k_s \in [0, 2\pi[\,. \tag{4.59}$$

Thus in our case at $v_R(\omega) = 0$, the PBC spectrum in eq. 4.42 fulfills the condition for

$$v_I \sin(k_s) = -\gamma \cos(k_s) \quad \Leftrightarrow \quad k_s = -\arctan(\frac{\gamma}{v_I}) \approx 0.4\,\pi\,. \tag{4.60}$$

Therefore, bulk-boundary correspondence is restored because of the bulk eigenmodes and spectra being the same for PBC and OBC and no localization of all eigenstates is present.

4.2.5 Distorted topological phase transitions

In our measurements (figs. 4.15 and 4.16) we find states in the gap of the complex admittance spectra for some frequencies/reciprocal intracell hoppings with different localization length than the other states and single sublattice support like the topological edge states in the SSH model (see section 3.1).
For Hermitian systems we know that the number of topologically protected edge states can be predicted by a closing and reopening of the gap in the eigenvalue spectrum. Therefore, we have to compare the gap closings in the PBC and OBC bulk spectra to check whether topological phase transitions can still be derived from the periodic spectrum.
To figure out where band touchings of the complex bulk bands, i.e. degeneracies of the eigenvalues at an exceptional point, in the PBC configuration are located in the parameter space we consider our effective model (eq. 4.48) again. The conditions for complex band closings in PBC configuration are given by the absolute value of the complex vector $\vec{d}(k)$ defined in eq. 4.50 to be zero:

$$\begin{aligned}
&\mathfrak{Re}(\vec{d}(k,\omega)) \cdot \mathfrak{Im}(\vec{d}(k,\omega)) = 0 \quad \wedge \quad |\mathfrak{Re}(\vec{d}(k,\omega))| = |\mathfrak{Im}(\vec{d}(k,\omega))| \\
\Leftrightarrow \quad &h_x(k,\omega)v_I(\omega) - h_y(k)\gamma = 0 \quad \wedge \quad (h_x(k,\omega))^2 + (h_y(k))^2 = (v_I(\omega))^2 + \gamma^2 \\
\Leftrightarrow \quad &h_x(k,\omega) = v_R(\omega) + r\cos(k) = \pm\gamma \quad \wedge \quad h_y(k) = r\sin(k) = \pm v_I(\omega)
\end{aligned} \tag{4.61}$$

A visual representation is given in fig. 4.18. Due to $r \geq \gamma$ and $r \geq v_I(\omega)$ four solutions exist in our model which correspond to each intersection of the left/right side of the circle with $\pm(\gamma, v_I(\omega))^\top$. With our fitted parameters for serial inductance and resistance of inductor L_1 we can estimate the positions numerically to $f_1 \approx 75.5\,\text{kHz}$, $f_2 \approx 85.0\,\text{kHz}$, $f_3 \approx 100\,\text{kHz}$ and $f_4 \approx 125\,\text{kHz}$. For the idealized case ($R_{L_1} = 0, v_I = 0$) they can be found analytically to be at

$$|v_R(\omega)| = \gamma \pm r\,. \tag{4.62}$$

Note that with our choice of $r = 2\gamma$ two of the PBC exceptional points $v_R(\omega) = \pm\gamma, \pm 3\gamma$ coincide with maximum localization points $v_R(\omega) = \pm\gamma$, which does not mean a general connection of the PBC exceptional points and the maximum localization.

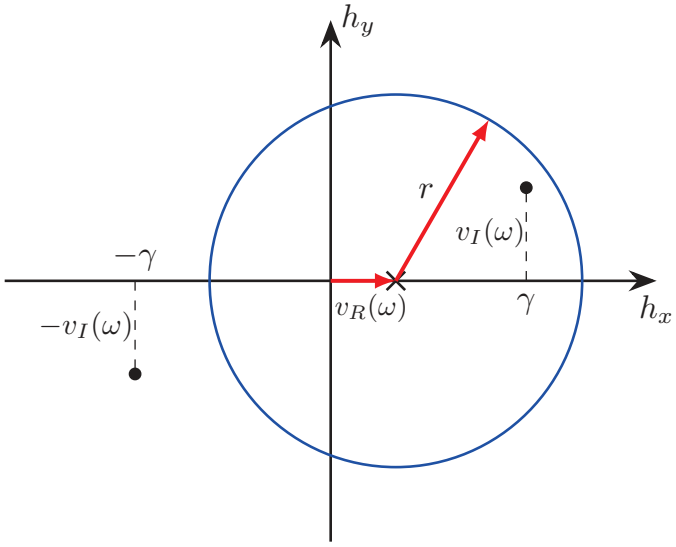

Figure 4.18: Visualization of the conditions for exceptional points derived in eq. 4.61 in the h_x-h_y plane. $h_x(k,\omega)$ and $h_y(k)$ form a circle (blue) with radius r for $k = 0 \to 2\pi$ and its center is shifted frequency dependent to $(v_R(\omega), 0)^\top$. An exceptional point exists if the circle intersects $(\pm\gamma, \pm v_I(\omega))^\top$, which can be reduced to $\pm(\gamma, v_I(\omega))^\top$ (black points) due to the symmetry (adapted from the supplementary material of [63]).

From our presented measurements in figs. 4.15 and 4.16 we can find no SSH-like edge modes for $f_I = 70.0\,\text{kHz}$ and two SSH-like edge modes for $f_{II} = 80.0\,\text{kHz}$, $f_{III} = 84.2\,\text{kHz}$, $f_{IV} = 91.5\,\text{kHz}$, $f_V = 95.0\,\text{kHz}$ and $f_{VI} = 98.5\,\text{kHz}$. If the exceptional points in the PBC spectrum would refer to the number of edge states, we would expect that the numbers differ between the groups $\{f_I\}$, $\{f_{II}, f_{III}\}$ and $\{f_{IV}, f_V, f_{VI}\}$, which is not the case.
Therefore we compare the PBC band touching points with those of the OBC bulk spectrum. We already showed that the PBC bulk spectrum can be transformed in the OBC counterpart considering a complex wave vector leading to localized modes with the Bloch factor α. Its magnitude was determined independent of the eigenvalues λ [100],[102]. Now we are searching for gap closings where some eigenvalues evolve to zero. Combining the solutions $\alpha_{1,2}$ for $\lambda = 0$

$$\alpha_{1,\lambda=0} = \frac{r}{v_R(\omega) + iv_I(\omega) - \gamma} \qquad \alpha_{2,\lambda=0} = \frac{v_R(\omega) + iv_I(\omega) + \gamma}{r} \tag{4.63}$$

with the restriction of $|\alpha| := |\alpha_1| = |\alpha_2|$ for OBC modes, we find the conditions for the idealized model ($R_{L_1} = 0, v_I = 0$)

$$|v_R(\omega)| = \sqrt{\pm r^2 + \gamma^2} \overset{r \geq \gamma}{\Rightarrow} |v_R(\omega)| = \sqrt{r^2 + \gamma^2} \tag{4.64}$$

and for the effective model with serial resistance

$$\begin{aligned} |v_R(\omega)| &= \sqrt{\gamma^2 - (v_I(\omega))^2 \pm \sqrt{r^4 - (2v_I(\omega)\gamma)^2}} \\ \overset{r>\gamma \gg v_I(\omega)}{\Rightarrow} \quad |v_R(\omega)| &= \sqrt{\gamma^2 - (v_I(\omega))^2 + \sqrt{r^4 - (2v_I(\omega)\gamma)^2}}\,, \end{aligned} \tag{4.65}$$

which are located in the present case at $f_L \approx 78.8\,\mathrm{kHz}$ and $f_H \approx 113.0\,\mathrm{kHz}$. This matches our observations that the number of edge modes differ for $f < f_L$ and $f_L < f < f_H$.
Another way to get insights of the topological character of the chain is given by mapping the OBC Laplacian to an effective reciprocal SSH-like model where bulk-boundary correspondence is restored. We use a similarity transformation of the OBC Laplacian suggested in [102] to get rid of the non-reciprocal hoppings.
The OBC Laplacian

$$\bar{\boldsymbol{J}}_{\mathrm{OBC}} = i \begin{pmatrix} 0 & v_R + iv_I - \gamma & 0 & \dots & 0 \\ v_R + iv_I + \gamma & 0 & r & \dots & 0 \\ 0 & r & 0 & \dots & 0 \\ \vdots & \vdots & \vdots & \ddots & v_R + iv_I - \gamma \\ 0 & 0 & 0 & v_R + iv_I + \gamma & 0 \end{pmatrix} \tag{4.66}$$

can be transformed by $\boldsymbol{S}_l = \mathrm{diag}(1, \alpha, \alpha, \alpha^2, \dots, \alpha^N)$ or $\boldsymbol{S}_r = \mathrm{diag}(\alpha^N, \dots, \alpha^2, \alpha, \alpha, 1)$ with the number of unit cells N and the Bloch factor

$$\alpha = \sqrt{\frac{v_R + iv_I + \gamma}{v_R + iv_I - \gamma}} \tag{4.67}$$

into the effective reciprocal Laplacian $\bar{\boldsymbol{J}}'_{\mathrm{OBC}} = \boldsymbol{S}_{l,r}^{-1} \bar{\boldsymbol{J}}_{\mathrm{OBC}} \boldsymbol{S}_{l,r}$

$$\bar{\boldsymbol{J}}'_{\mathrm{OBC}} = i \begin{pmatrix} 0 & \sqrt{(v_R + iv_I)^2 - \gamma^2} & 0 & \dots & 0 \\ \sqrt{(v_R + iv_I)^2 - \gamma^2} & 0 & r & \dots & 0 \\ 0 & r & 0 & \dots & 0 \\ \vdots & \vdots & \vdots & \ddots & \sqrt{(v_R + iv_I)^2 - \gamma^2} \\ 0 & 0 & 0 & \sqrt{(v_R + iv_I)^2 - \gamma^2} & 0 \end{pmatrix}. \tag{4.68}$$

The effective Laplacian takes the same form as for a reciprocal SSH model (see section 2.2.3) with complex coefficients, therefore its admittance band structure is given by

$$\bar{j}' = \pm i \sqrt{t_0^2 + r^2 + 2rt_0 \cos(k)} \tag{4.69}$$

with $t_0 = \sqrt{(v_R + iv_I)^2 - \gamma^2}$.
The bulk eigenstates of the transformed Laplacian $\bar{\boldsymbol{J}}'_{\mathrm{OBC}}$ are delocalized due to the transformation und thus bulk-boundary correspondence is restored enabling the prediction of topological phase transitions from the band closings calculated from the bulk. This is confirmed by the eigenvalue equation transformed back to the original non-reciprocal model:

$$\bar{\boldsymbol{J}}'_{\mathrm{OBC}} \psi'_{\mathrm{OBC}} = \bar{j}'_{\mathrm{OBC}} \psi'_{\mathrm{OBC}} \tag{4.70}$$

translates to

$$\bar{\boldsymbol{J}}_{\mathrm{OBC}} \left(\boldsymbol{S}_{l,r} \psi'_{\mathrm{OBC}} \right) = \bar{j}'_{\mathrm{OBC}} \left(\boldsymbol{S}_{l,r} \psi'_{\mathrm{OBC}} \right), \tag{4.71}$$

where the eigenvalues are the same for $\bar{\boldsymbol{J}}'_{\mathrm{OBC}}$ and $\bar{\boldsymbol{J}}_{\mathrm{OBC}}$ but the eigenvectors are transformed by $\boldsymbol{S}_{l,r}$ leading to a localization with localization length $\xi = -1/\ln|\alpha|$ at the left or right edge.

From the SSH chain we know that topological edge states exist for $|t_0| < |r|$, which translates to $|v_R(\omega)| < \sqrt{\gamma^2 - (v_I(\omega))^2 + \sqrt{r^4 - (2v_I(\omega)\gamma)^2}}$. The gap closing points match the ones predicted with the help of complex wave vectors in eq. 4.65 and the numbers of edge states found in the effective reciprocal model also agree with the topological modes found in our measurements.
The localization edge in the investigated circuit cannot be predicted by the similarity transformed model because $\boldsymbol{S_l}$ and $\boldsymbol{S_r}$ provide the same results due to the symmetry of the SSH model. Furthermore, we find that the localization properties of the topological edge states cannot be found by simply transforming the approximated edge states of SSH edge states. Here the asymmetry of the non-reciprocal model together with finite-size effects need to be taken into account.

4.2.6 Conclusions

Due to the non-local voltage response of the circuit found in fig. 4.14 mode localization at the edges of the system is expected, which could be verified for all eigenstates by determining the eigenvectors from the measured grounded circuit Laplacian (fig. 4.15). Therefore, the findings for topological edge states due to bulk-boundary correspondence in Hermitian systems based on the fact that the transition between PBC and OBC can be treated as a small perturbative effect cannot be applied in the present case. Instead we find the bulk admittance spectra from PBC and OBC differing when the edge localization of all modes, i.e. the non-Hermitian skin effect, is present. As requirements to the symmetries of the system to have different PBC and OBC bulk spectra the combined breaking of Hermiticity and reciprocity can be figured out.
The localization length shows a minimum for the maximum asymmetry between left and right hopping, which is the case when the reciprocal and the non-reciprocal hopping possess the same magnitude. From the ideal model we find that in this case the bulk eigenvectors degenerate to only two distinct vectors with corresponding two distinct eigenvalues, i.e. an exceptional point in the OBC spectrum.
With the concept of complex wave vectors the PBC spectrum (closed loops) can be transformed into the OBC bulk spectrum (open arcs) by fulfilling the condition of spectral degeneracy eq. 4.47 and respecting the boundary conditions, which means that the magnitude of the Bloch factors have to be the same (eq. 4.54). The localization parameters predicted by this technique meet the measured ones in the range of the experimental standard deviations (tab. 4.2).
For the transition point between left and right edge localization where the reciprocal hopping is zero we find delocalized bulk modes and the restoration of bulk-boundary correspondence due to extended reciprocity (eq. 4.59) of the model for this set of parameters.
We furthermore see that topological edge modes with localization lengths differing from the localized bulk modes exist, which cannot be predicted by gap closings in the PBC spectrum due to the break down of bulk-boundary correspondence. In fig. 4.19 the admittance spectra for the idealized fitting model (eq. 4.49) for the open (blue) and periodic (red) chain are plotted, where the discrepancy between gap closings in PBC and OBC case can be retraced.

To figure out the correct topological phase transition, i.e. the OBC gap closings, complex wave vectors with zero eigenvalues have to be figured out (eq. 4.63) or a similarity transformation of the system to an effectively reciprocal SSH model (eq. 4.68) has to be used.

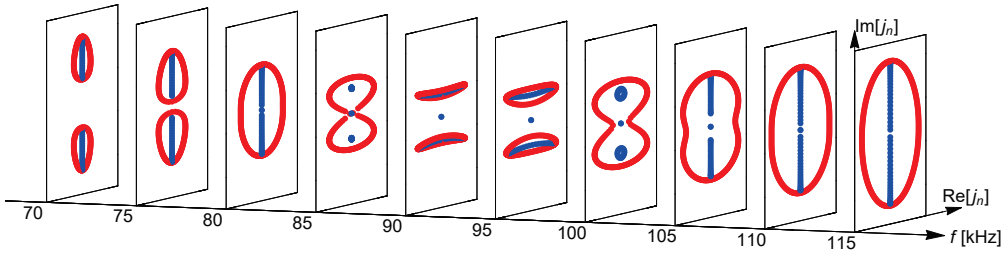

Figure 4.19: Calculated admittance spectra of the idealized ($R_{L_0} = R_{L_1} = 0, v_I = 0$) fitting model eq. 4.48 for PBC (red) and OBC configuration (blue) stacked for different frequencies. Parameters: System size OBC: 50 nodes, system size PBC 300 nodes, $C_1 = 300\,\mathrm{nF}$, $L_1 = 10.1\,\mu\mathrm{H}$, $C_2 = 94\,\mathrm{nF}$, $C_3 = 47\,\mathrm{nF}$, $L_0 = 31\,\mu\mathrm{H}$, $R_0 = 20\,\Omega$ (from supplementary material of [63]).

4.3 Non-linear SSH model

All systems studied previously were described by a set of linear differential equations, which could be transformed into a set of algebraic equations using Fourier transformation. For an electric circuit this translates into linear circuits made of ideal resistors, capacitors, inductors or more complicated subcircuits with linear differential equations connecting voltage and current.
In this project we are going to demonstrate that topological signatures can also be found in suitably designed coupled systems obeying non-linear differential equations. We derive design principles for self-organized and self-sustained circuit systems possessing topological protected features that could contribute new routes and understandings in a variety of research topics from autonomous device engineering [110] to neuronal network investigation [111].
The project was initiated by R. Thomale, H. Ronellenfitsch and J. Dunkel. The author's main contributions were in the experimental implementation, investigation and interpretation of the acquired data. The results were published in [65].

While non-linearity often occurs as natural deviation from the idealized components like voltage dependent capacitances due to ferroelectric effects in the dielectric materials of capacitors or current dependent inductances due to magnetic saturation of the inductor core material, a lot of circuit elements are indented to show non-linear behaviour such as diodes made of doped semiconductor junctions or vacuum tubes, voltage dependent resistors (varistors) or capacitors (varicaps) and others. When the non-linearity needs to obey predefined properties this can be accomplished by parallel/serial combination of different linear/non-linear circuit elements or by modeling the current-voltage relation directly by the use of integrated circuits like analog multipliers.

4.3.1 Non-linear van der Pol differential equation

Self-excitation can be achieved by a device that adds energy to the system like a negative impedance studied in the previous section 4.2. Each non-zero initial condition of the system leads to amplification and thus the standby position at zero voltage and current gets unstable. But a system with unlimited amplification would be driven out of bounds, therefore for higher voltages damping that exceeds the energy input is needed to reach a finite and self-sustained steady state.
Consequently, we would need a non-linear resistance with a current-voltage $(I - V)$ relation like for example

$$I = -\alpha V + \gamma V^3 \tag{4.72}$$

with constants α and γ, which leads to the following non-linear differential equation when it is used in a parallel resonant circuit

$$C \frac{\mathrm{d}^2 V(t)}{\mathrm{d}t^2} - (\alpha - 3\gamma (V(t))^2) \frac{\mathrm{d}V(t)}{\mathrm{d}t} + \frac{1}{L} V(t) = 0 \,. \tag{4.73}$$

The theoretical description of this kind of a self-excited, self-sustained oscillator was given by Van der Pol in 1926 [64] and is nowadays termed van der Pol oscillator. Rescaling

time by multiples of the undampend period $t = \sqrt{LC}\hat{t}$ and voltage by $V = \sqrt{\alpha/3\gamma}x$ leads to the more general non-linear differential equation

$$\ddot{x} - \underbrace{\alpha\sqrt{\frac{L}{C}}}_{\varepsilon}\left(1 - x^2\right)\dot{x} + x = 0 \tag{4.74}$$

with dots representing the derivative by rescaled time $\hat{t}$ and ε standing for the magnitude of the non-linearity. By expanding the second-order differential equation into two first-order differential equations

$$\dot{x} = y =: f(x, y) \tag{4.75a}$$
$$\dot{y} = \varepsilon\left(1 - x^2\right)y - x =: g(x, y) \tag{4.75b}$$

and searching for parameter sets where $\dot{x} = \dot{y} = 0$ we can find fixed points of the equations. This is the case for $(x, y) = (0, 0)$ independent from the value of ε. Linearization at the fixed point leads to the Jacobian matrix

$$\boldsymbol{J}_{(0,0)} := \begin{pmatrix} \frac{\partial f(0,0)}{\partial x} & \frac{\partial f(0,0)}{\partial y} \\ \frac{\partial g(0,0)}{\partial x} & \frac{\partial g(0,0)}{\partial y} \end{pmatrix} = \begin{pmatrix} 0 & 1 \\ -2\varepsilon xy - 1 & \varepsilon(1 - x^2) \end{pmatrix}_{(0,0)} = \begin{pmatrix} 0 & 1 \\ -1 & \varepsilon \end{pmatrix}, \tag{4.76}$$

which has eigenvalues

$$\lambda_{1,2} = \frac{1}{2}\left(\tau \pm \sqrt{\tau^2 - 4\Delta}\right) = \frac{1}{2}\left(\varepsilon \pm \sqrt{\varepsilon^2 - 4}\right). \tag{4.77}$$

In our case τ, which can be associated with the trace of the Jacobian/sum of the eigenvalues, equals to ε and Δ, which belongs to the determinant of the Jacobian/product of the eigenvalues, is 1 (vertical line in fig. 4.20). Therefore, the parameter ε directly determines the stability of the fixed point at the origin.

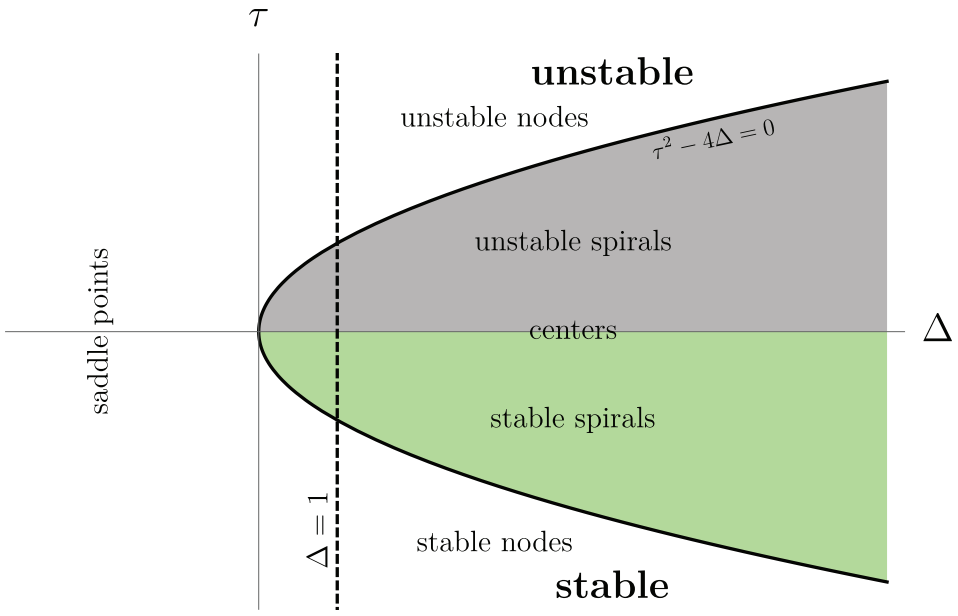

Figure 4.20: Stability of fixed points classified by the eigenvalues of the Jacobian matrices given by the linearization at the fixed points. If $\Delta < 0$ the eigenvalues indicate saddle points, when $\Delta > 0$ it can be distinguished between stable ($\tau < 0$) and unstable ($\tau > 0$) fixed points. If $\tau > 4\Delta$ the fixed point is a node and trajectories in phase space approach/leave the fixed point from/in a given direction. For $\tau < 4\Delta$ the fixed point is called a spiral and the spiroidal trajectories approach/leave the fixed point (adapted from [112]).

In fig. 4.21 phase portraits, i.e. vector fields illustrating the vector of derivatives $(\dot{x}, \dot{y})^\top$ in the $x - y$ plane, with trajectories of the evolution of points with given initial conditions and numerical solutions of the van der Pol equation 4.74 are shown for different magnitudes of non-linearity ε.
For negative ε the origin is a stable fixed point (fourth quadrant of fig. 4.20) and we can see in fig. 4.21 a),b),d),e) the trajectories in phase space evolving to the origin, i.e. the initial excitation $x(0)$ is damped out to zero. The non-/oscillatory behaviour of the $x(t) - t$ curve depends on the value of ε. For $-2 < \varepsilon < 0$ the origin is a stable spiral and initiated points in the surroundings of the origin in phase space flow on a spiral towards zero, which corresponds to a damped oscillatory solution (fig. 4.21 d),e)). For $\varepsilon < -2$ the fixed point is a stable node and the damped solution goes to zero without oscillation (not shown in fig. 4.21).
When $\varepsilon = 0$ the differential equation describes the ideal undamped harmonic oscillator, the fixed point is a center and each initial point in phase space flows around it on circles with constant radius, i.e. the solutions oscillate without any damping (fig. 4.21 c),f)).
In the region $\varepsilon > 0$, where we are going to operate, the fixed point at the origin turns unstable (fig. 4.21 g)-l)) and initial conditions near the origin increase towards a stable, unique limit cycle, which it plausible because $\varepsilon\,(1 - x^2)\,\dot{x}$ acts like negative damping for $|x| < 1$, but like positive damping $|x| > 1$ independent from ε and can be proofed by Liénard's theorem (for details see [112],[113]).

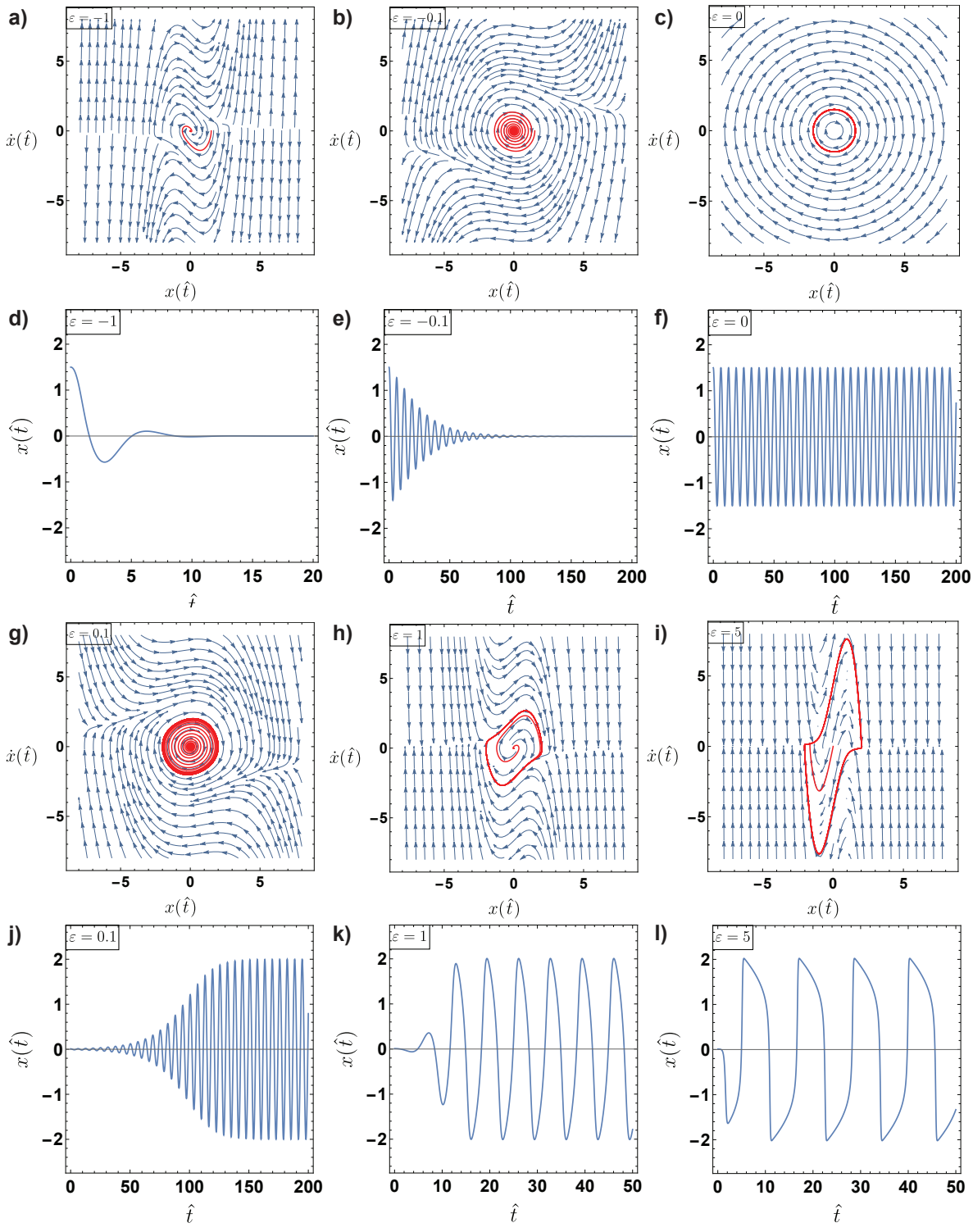

Figure 4.21: Phase portraits and numerical solutions of the van der Pol equation 4.74 for different magnitudes of non-linearity $\varepsilon = -1, -0.1, 0, 0.1, 1, 5$. Phase portraits (blue) with trajectories (red) a)-c) and numerical solutions d)-e) of van der Pol equations for $\varepsilon \leq 0$ (initial conditions: $x(0) = 1.5$, $\dot{x}(0) = 0$). Phase portraits with trajectories (red) g)-i) and numerical solutions j)-l) of van der Pol equations for $\varepsilon > 0$ (initial conditions: $x(0) = 0.01$, $\dot{x}(0) = 0$).

For weakly non-linear oscillators $0 \leq \varepsilon \ll 1$ (fig. 4.21 g),j)) the origin is an unstable spiral and the limit cycle in fig. 4.21 g) is nearly circular with radius 2. The numerical solution fig. 4.21 j) shows a slowly increasing approximately sinusoidal solution with amplitude converging to the radius of the limit cycle.
When $\varepsilon > 2$ the fixed point is an unstable node (fig. 4.20) and the trajectories approach the limit cycle before a full rotation in phase space is completed (4.21 i)). The higher the non-linearity gets the more is the sinusoidal shape of the solution distorted towards the shape of so called relaxation oscillations for $\varepsilon \gg 1$ (compare fig. 4.21 j)-l)).
The transition in the stability of the fixed point, when ε crosses zero with stable solutions for $\varepsilon < 0$ to unstable solutions with surrounding stable limit cycle for $\varepsilon > 0$, is called a supercritical Andronov-Hopf bifurcation and the eigenvalues of the Jacobian matrix $\lambda_{1,2} = \frac{1}{2}\left(\varepsilon \pm i\sqrt{4-\varepsilon^2}\right)$ cross the imaginary axis [112]. From linear differential equations we know that the oscillation frequencies of the solutions in the linearized case can be approximated by the imaginary part of the Jacobian's eigenvalues.

4.3.2 Circuit implementation

A subcircuit, in the following called van der Pol (vdP) element, obeying the voltage current relation proposed in eq. 4.72 can be designed in various ways. We will shortly explain the two variants used for our investigations [65].
In fig. 4.22 a vdP element made of diodes and a negative resistor [114] added to a SSH unit cell is shown. The part of the current-voltage relation eq. 4.72 proportional to V^3 is approximated by the diodes part (yellow) of the vdP element. Its current-voltage curve is central symmetric due to the anti-parallel diodes. The diodes are chosen to be of Schottky type to show a low forward voltage drop.

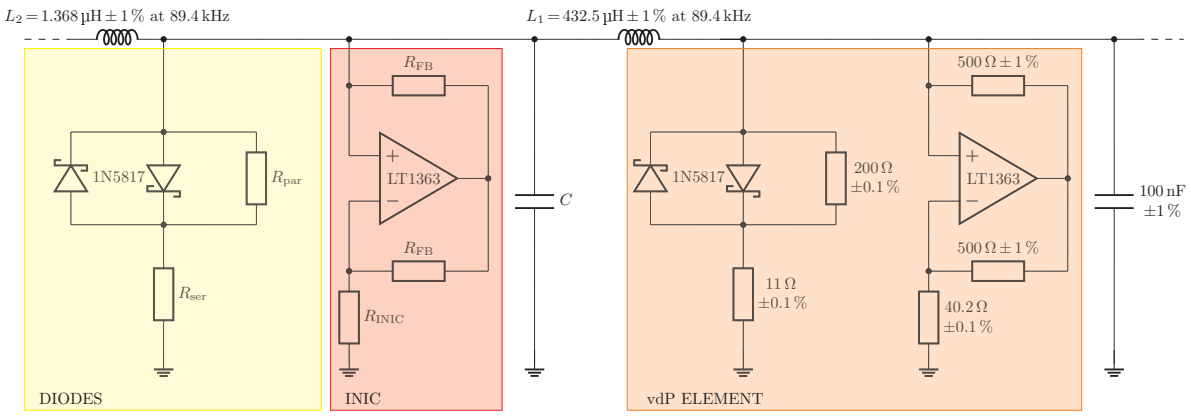

Figure 4.22: Unit cell of a one dimensional SSH chain (inductive coupling, capacitive grounding) with additional non-linear resistive vdP-element (orange) connected to ground. The vdP element is made of two parallel parts. The diodes (yellow) part made of anti-parallel Schottky diodes (1N5817) together with a serial (R_{ser}) and a parallel resistor (R_{par}) is used for the $I \sim V^3$ part of the required current-voltage relation eq. 4.72, while the linear negative part is made of an INIC (red) already explained in sec. 4.2.

The serial (R_{ser}) and parallel resistor (R_{par}) determine the current-voltage curve for

very low and very high voltage magnitudes. When the voltage magnitude is below the forward voltage drop of the diodes the current flows mainly through the two resistors connected in series, where the parallel resistor R_{par} with higher resistance mainly dictates the current-voltage profile. For voltage magnitudes above the forward voltage drop the parallel resistor is shortened by the now highly conductive diodes and the current-voltage relation is limited by the resistance of the series resistor R_{ser}.
The current-voltage relation of the INIC $I \approx 1/R_{\text{INIC}} \cdot V$ can be added to the one of the diodes part due to their parallel connection, leading to a curve that approximates eq. 4.72 in a certain voltage range.
In fig. 4.23 $I - V$ curves of an assembled vdP element are illustrated. The negative resistance of the INIC is proven in fig. 4.23 a). The sine voltage input is driven by a function generator (Keysight 33512B) at different frequencies, current (voltage drop at series resistor) and voltage are measured with an 8 channel digital oscilloscope (Picoscope 4824). The whole circuit is shunted with a resistor (10 Ω) smaller than the negative resistance of the INIC to keep the overall resistance positive. At 500 kHz the straight line is significantly split into an ellipse along the period of the input sine voltage due to the phase lag of the OpAmp at higher frequencies (discussed in the previous sec. 4.2).

In fig. 4.23 b) the current-voltage relation of the whole vdP element can be seen. Again, at higher frequencies the described hysteresis effect due to the OpAmp phase lag can be found. For small voltage magnitudes the curve can be approximated as a parallel circuit of R_{par} and $-R_{\text{INIC}}$ by a linear $I - V$ curve with slope $\frac{-R_{\text{INIC}} \cdot R_{\text{par}}}{R_{\text{par}} - R_{\text{INIC}}} \approx -0.02\,\Omega^{-1} \approx -\alpha$ and for high voltages the asymptotic behaviour of the current-voltage relation can be described by a parallel circuit of R_{ser} and $-R_{\text{INIC}}$.

Due to this limit the slope of the measured curve is lower than the desired V^3 dependency at higher voltages, which can be seen in fig. 4.23 c). Therefore, the fitting interval was chosen to be between −0.3 V and 0.3 V.

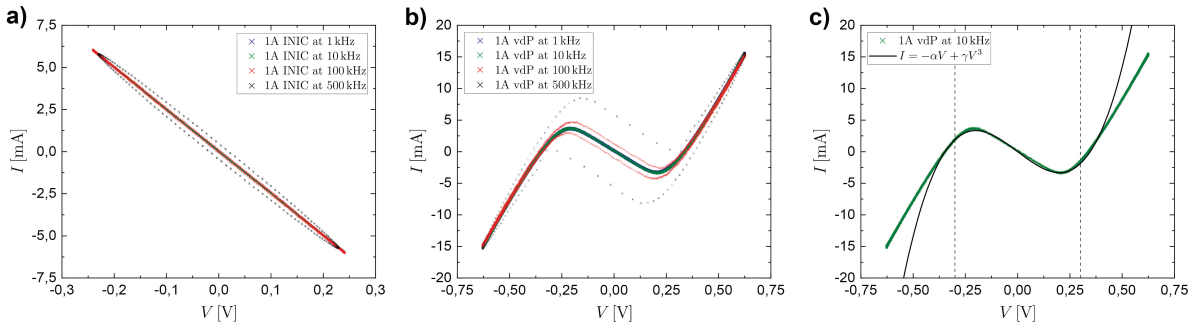

Figure 4.23: Characterization of the non-linear resistive elements. a): Current-voltage curve of an INIC for different frequencies. b): Current-voltage relation of the complete vdP-element for the same frequencies as in a) (adapted from [65]). c): $I - V$ curve (green crosses) from b) for 10 kHz fitted with eq. 4.72 ($\alpha = 0.024\,94\,\Omega^{-1}$, $\gamma = 0.206\,89\,\Omega^{-1}\,\text{V}^{-2}$, solid black line) in the interval (indicated by dashed vertical lines) between −0.3 V and 0.3 V.

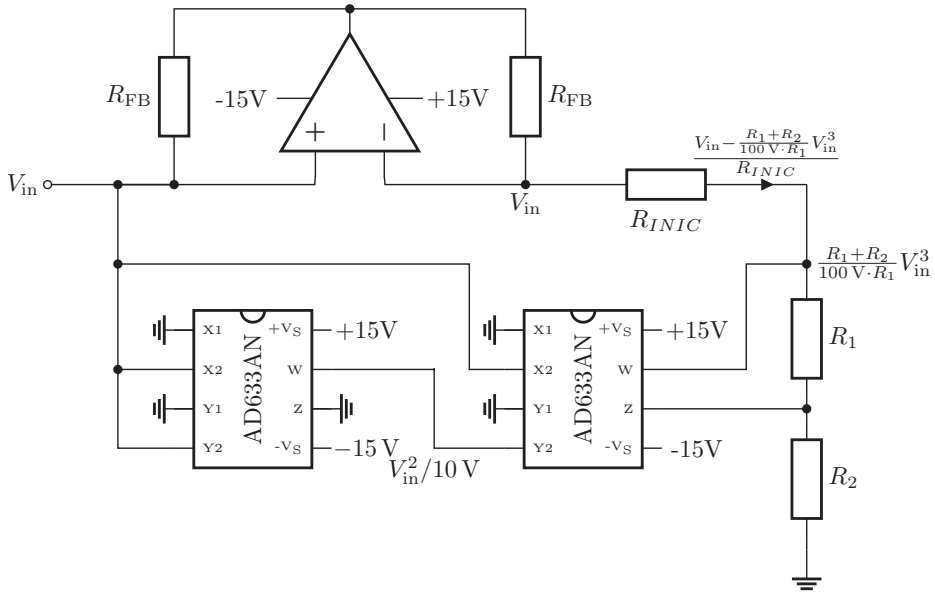

Figure 4.24: Non-linear resistive element with current-voltage relation eq. 4.72 made of an INIC (top) and two analog multipliers (AD633) (bottom) [115]. The multipliers are used to produce a V^3 voltage dependence, the INIC produces the output current which is the inverted current flowing through R_{INIC} (adapted from [65]).

A second way to achieve the non-linear current voltage relation eq. 4.72 is made of analog multipliers and an INIC circuit [115] as it is shown in fig. 4.24 (experimentally implemented and investigated by F. Moseley [65]). The analog multipliers internal circuitry is made of two differential inputs $(X1, X2,\ Y1, Y2)$ that are multiplied. The result is scaled with $1/10\,\mathrm{V}$ and an additional signal Z can be added to the result W. The transfer function is given by

$$W \;=\; \frac{(X1 - X2)(Y1 - Y2)}{10\,\mathrm{V}} + Z\,. \tag{4.78}$$

To produce a tunable voltage proportional to V^3 the first multiplier is used to square the input signal (note that connecting the signals to the pair of non-inverting/inverting inputs lead to the same result) and the second one raises the signal to the power of three. The voltage divider (R_1, R_2) at the output/summing input is used to scale the output voltage. This voltage is applied at the right side of an INIC like in fig. 4.10 a) where the current flowing through R_{INIC} is the inverted input current. Therefore, the $I - V$ curve is given by

$$I \;=\; -\underbrace{\frac{1}{R_{\mathrm{INIC}}}}_{\alpha}\cdot V_{\mathrm{in}} + \underbrace{\frac{R_1 + R_2}{100\,\mathrm{V}\cdot R_1 R_{\mathrm{INIC}}}}_{\gamma}\cdot V_{\mathrm{in}}^3\,, \tag{4.79}$$

which meets the V^3 dependence better than the non-linear resistance made of diodes and an INIC, but a phase lag is present for both multipliers and the OpAmp.

4.3.3 1D non-linear topological lattice

In this work we will concentrate on the experiments done with the vdP elements made of INIC and diodes (fig. 4.22). The modular circuit board (see figs. A.5,A.6) designed to build SSH-like (see section 3.1) lattices can be found in appendix A.4. The nodes are coupled by inductors L_1, L_2 and connected to ground by capacitors C. Therefore, we achieve a set of coupled non-linear differential equations

$$C\,\frac{\mathrm{d}^2V_i(t)}{\mathrm{d}t^2}\;-\;(\alpha-3\gamma(V_i(t))^2)\,\frac{\mathrm{d}V_i(t)}{\mathrm{d}t}\;+\;\frac{1}{L_0}\sum_{j=1}\frac{L_0}{L_{ij}}(V_i(t)-V_j(t))=0 \tag{4.80}$$

with j running through all nodes of the circuit and ground and the inductances are scaled by L_0, here chosen to be the smallest inductance in the circuit. Again, the equations can be rescaled with time by multiples of the undampend period $t=\sqrt{L_0C}\hat{t}$ and voltage by $V_i(t)=\sqrt{\alpha/3\gamma}x_i$, which leads to

$$\ddot{x}_i\;-\;\underbrace{\alpha\sqrt{\frac{L_0}{C}}}_{\varepsilon}\left(1-x_i^2\right)\dot{x}_i\;+\;\sum_{j=1}\beta_{ij}x_j\;=\;0\,. \tag{4.81}$$

The coupling matrix can be written as

$$\begin{aligned}\boldsymbol{\beta}\;&=\;L_0\begin{pmatrix}L_1^{-1}+L_2^{-1} & -L_1^{-1} & 0 & \dots & 0\\ -L_1^{-1} & L_1^{-1}+L_2^{-1} & -L_2^{-1} & \dots & 0\\ 0 & -L_2^{-1} & L_1^{-1}+L_2^{-1} & \dots & 0\\ \vdots & \vdots & \vdots & \ddots & -L_1^{-1}\\ 0 & 0 & 0 & -L_1^{-1} & L_1^{-1}+L_2^{-1}\end{pmatrix}\\ &=:\;\begin{pmatrix}g & -w & 0 & \dots & 0\\ -w & g & -s & \dots & 0\\ 0 & -s & g & \dots & 0\\ \vdots & \vdots & \vdots & \ddots & -w\\ 0 & 0 & 0 & -w & g\end{pmatrix}.\end{aligned} \tag{4.82}$$

Here, g corresponds to the sum of all inverted and scaled inductances connected to the node $\beta_{ii}=\sum_j L_0/L_{ij}$ and w, s indicate the weak and strong couplings between the nodes introduced by the inductances. Note that higher inductances represent lower coupling strengths and $s>w>0$ or $L_0/L_2>L_0/L_1>0$.
So in this configuration we have a chain of coupled van der Pol oscillators and the coupling matrix is similar to the hopping matrix describing the SSH model. To be able to distinguish between features existing due to the topological nature of the underlying SSH like coupling and characteristics found due to the non-linear resistive term we work in the nearly dimerized topological regime with $s\gg w$ or $L_2\gg L_1$ where topological edge states are highly localized.

For the investigation two circuit boards (see fig. A.6) were connected to host four unit cells of the 1D non-linear topological circuit. As shown in fig. 4.23 c) all non-linear resistive elements were fitted in the range between $\pm 300\,\mathrm{mV}$. The means of the parameters

are $\alpha = 0.024\,9\,\Omega^{-1}$ with variation smaller than 1 % and $\gamma = 0.207\,\Omega^{-1}\,\mathrm{V}^{-2}$, which varies less than 2.5 %. With the smallest inductances $L_0 = L_2 = 1.368\,\mu\mathrm{H}$ and the grounding capacitance $C = 100\,\mathrm{nF}$ the magnitude of non-linearity is $\varepsilon \approx 0.092$.
The power supplies of the OpAmps were synchronously activated by computer-controlled switching of two MOSFETs (metal-oxide-semiconductor field-effect transistor) that activate the supply lines. The activation was used to trigger the 8 channel digital oscilloscope sampling the eight nodes simultaneously with 20 MHz. In fig.4.25 a) we see that there is approximately a 3 µs offset between the instantaneous oscillation of the unstable nodes due to the vdP element and the trigger event. This does not impede the measurement since the synchronicity of the measurements is given and the real starting point is also sampled due to a small pre-trigger period.
All nodes start to oscillate with small amplitude at relatively high frequencies, the edge nodes (1A,4B) in fig. 4.25 a),i with approximately 381 kHz and the bulk nodes (1B-4A) in fig. 4.25 a),ii/iii with even higher frequencies at about 510 kHz. While the oscillations on the edge nodes are slowly increasing, the fast bulk oscillations decrease rapidly. Furthermore, it has to be mentioned that the fast oscillations of each two neighboring nodes connected by strong coupling are synchronized anti-phase and the edge nodes oscillation frequency slightly differ, which is recognizable from the slowly increasing phase difference.

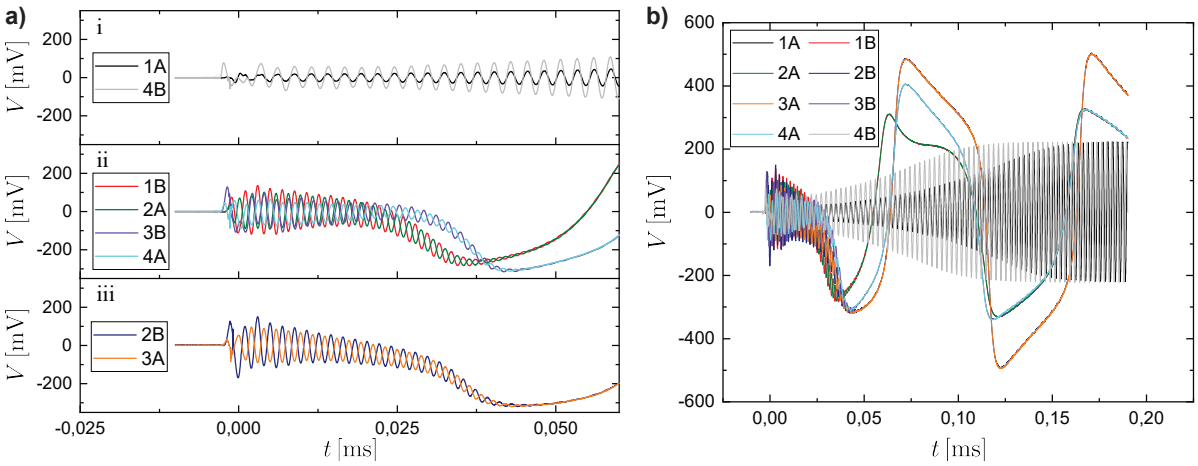

Figure 4.25: Transient response of the four unit cell 1D non-linear topological circuit. a): Cut out of the first 60 µs of b), nodes showing the same oscillatory behaviour after the transient are grouped in different plot planes (i-iii). b): Transient response of all nodes plotted together.

After the fast oscillations in the bulk have subsided the strongly coupled pairs show slow relaxation oscillations (fig. 4.25 b)) although the non-linearity of all single vdP elements is low (compare fig. 4.21). The increase of the edge oscillation's amplitude on the left side (1A) is slower than that of its symmetric partner on the right side (4B). Accordingly, the amplitude of the first cycle of the leftmost strongly coupled pair's relaxation oscillation (1B-2A) is also lower than that at the right side although the fast oscillations subsided faster. After one period the relaxation oscillations of the left- and rightmost strongly coupled pair show the same amplitude and frequency and the fast oscillations at both edge nodes have settled at a constant amplitude. Furthermore, it should be

mentioned that the amplitude of the relaxation oscillation of all strongly coupled bulk pairs is higher than that of the fast edge oscillations. The highest amplitude is found at the center pair, which has no symmetric partner in the chain.
From fig. 4.26 a) (insets) we see that the relaxation oscillations are also superimposed by the signal of the edge nodes with small amplitude, which is confirmed by the peak near 380 kHz in the Fourier transformed signal of node $1B$ (fig. 4.26 b)). For lower frequencies the spectrum is dominated by the odd multiples of the relaxation oscillation's base frequency $f_0 = 10.3\,\text{kHz}$. This is valid because the signal could be approximated by a sum of a square and a triangular wave, which both can be expressed by oly non-zero coefficients for odd multiples of the base frequency in the Fourier series.

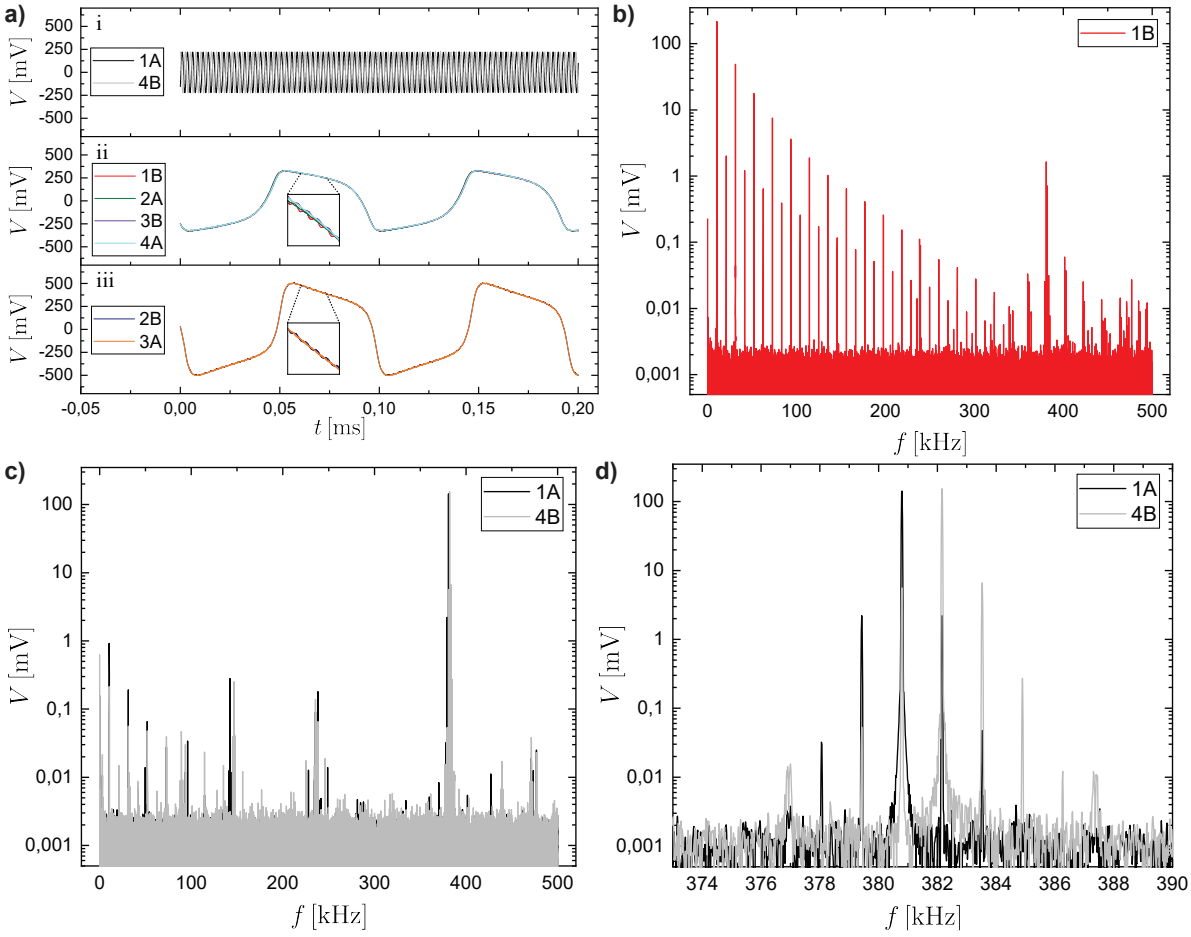

Figure 4.26: Stationary self-excited signal of the four unit cell 1D non-linear topological chain. a): Time domain signals at the edges (i), the left and right strongly coupled pair of nodes (II) and the center node pair (iii). b): Logarithmic plot of the Fourier transformed signal of the relaxation oscillation at node 1B. c): Logarithmic plot of the Fourier transformed signal of the edge nodes (1A,4B). d): Cut out of the edge nodes Fourier transform given in c) near their oscillation frequency.

The edge nodes Fourier transforms (fig. 4.26 c,d)) have a main peak at the resonance frequency at about 380 kHz because of the sinusoidal shape of the signal fig. 4.26 a),i. By zooming into the region of the resonance we can confirm that the left and right resonance frequencies are slightly different, which we already found at the investigation of the transient response (fig. 4.25 a),i). But each main resonance is accompanied by symmetrically arranged secondary peaks in multiples of the difference of the resonance frequencies. With sufficient high frequency difference the impact of the opposite edge's resonance frequency can be found as a beat of the two different frequency components manifested in a variation of the oscillation's amplitude with a low frequency sinusoidal.

From these experimental studies we find that in the non-linear active version a nearly sinusoidal mode exists at the edges of the circuit, which is present due to the topological properties of the coupling matrix (intracell coupling smaller than intercell coupling). In the bulk of the system phase locked relaxation oscillations are formed at each strongly coupled node pair, with amplitudes even higher than the localized edge mode, which is in stark contrast to the response known from a linear system.
This behaviour can be qualitatively understood with the approximation of the fully dimerized limit $w \to 0$. The coupling matrix eq. 4.82 then has two eigenvalues at g corresponding to eigenvectors located at the edges and two $n-2$-fold degenerate eigenvalues at $g \pm s$ corresponding to eigenvectors (1,$\pm$1) localized at each strongly coupled dimer. Furthermore, it is known in literature [116] that strongly coupled vdP oscillators that do not differ in resonance frequency are expected two show in-/anti-phase phase-locked solutions.

Due to the low magnitude of non-linearity ($\varepsilon \approx 0.092$) the system is near to the Andronov-Hopf bifurcation (discussed above for a single vdP oscillator) and therefore the frequencies of the system's limit cycles can be approximated by the imaginary parts of the eigenvalues of the Jacobian

$$\begin{pmatrix} \dot{\vec{x}} \\ \dot{\vec{y}} \end{pmatrix} = \begin{pmatrix} 0 & \mathbb{1} \\ -\boldsymbol{\beta} & \varepsilon\mathbb{1} \end{pmatrix} \begin{pmatrix} \vec{x} \\ \vec{y} \end{pmatrix} . \tag{4.83}$$

Because of the block structure of the Jacobian for each eigenvalue of $\boldsymbol{\beta}$ a pair of eigenvalues is given by

$$\lambda_{k,\pm} = \frac{1}{2}\left(\varepsilon \pm \sqrt{\varepsilon^2 - 4\mu_k}\right) . \tag{4.84}$$

The most unstable states, which will be activated most likely, are given by the eigenvalues with the highest magnitude, therefore the smallest μ_k correspond to the most unstable modes. In our case $\varepsilon \ll \mu_k$ the eigenvalues can be approximated to zeroth order by

$$\lambda_{k,\pm} = \pm\sqrt{-\mu_k} + \mathcal{O}(\varepsilon) \tag{4.85}$$

leading to the frequencies of the limit cycles $f = |\mathfrak{Im}(\lambda)|$

$$
\begin{aligned}
f_e &= \sqrt{g} \cdot \frac{1}{2\pi\sqrt{L_0 C}} = \sqrt{L_0 \left(\frac{1}{L_1} + \frac{1}{L_2}\right)} \cdot \frac{1}{2\pi\sqrt{L_0 C}} = 431\,\mathrm{kHz} \\
f_{b,-} &= \sqrt{g - s} \cdot \frac{1}{2\pi\sqrt{L_0 C}} = \sqrt{L_0 \frac{1}{L_1}} \cdot \frac{1}{2\pi\sqrt{L_0 C}} = 24.2\,\mathrm{kHz} \\
f_{b,+} &= \sqrt{g + s} \cdot \frac{1}{2\pi\sqrt{L_0 C}} = \sqrt{L_0 \left(\frac{1}{L_1} + \frac{2}{L_2}\right)} \cdot \frac{1}{2\pi\sqrt{L_0 C}} = 609\,\mathrm{kHz}\,.
\end{aligned}
\tag{4.86}
$$

f_e, which is predicted for the edge modes, is in the same order as the measured frequencies $f \approx 381\,\mathrm{kHz}$ with a deviation of approximately 13 %. The frequency of the in-phase bulk limit cycles is 10.3 kHz, which is less than half of the predicted frequency for the most unstable mode of the dimers oscillations $f_{b,-}$.
Therefore, the linearization in the fully dimerized limit can be used for qualitative predictions of the circuit behaviour, but remarkable quantitative discrepancies exist. In the linearized theoretical descriptions parasitic effects caused by the circuit board or the inductors resistances are not taken into account, and an additional reason for deviation could also stem from the experimental deviations of the ideal vdP equation.

The fact that the $I-V$ fit of the vdP elements only holds true in the $\pm 300\,\mathrm{mV}$ range can affect the amplitude of the limit cycle, which could be especially the case in the middle of the chain (iii, nodes 2B,3A) where the amplitude significantly exceeds this range.
For the high frequency boundary oscillation the hysteresis of the INIC circuits cannot be neglected anymore, which may influence the frequency of the limit cycle. Furthermore, it should be checked if the higher amplitude in the middle of the chain might be introduced due to deviations of the connection in between the dimer induced by the connection of the two circuit boards, which lies between the two nodes.
Therefore, several experimental setups with different chain lengths were fabricated and investigated. In fig. 4.27 the measured signals for the different chain lengths are shown. First of all, an increase of the strongly coupled bulk pair frequency with decreasing chain length can be seen a): 6.3 kHz → b): 10.4 kHz → c): 13.5 kHz → d): 21.1 kHz. Second we see in fig. 4.27 a),b) that the higher voltage of the middle pair, which has no symmetric partner due to the even number of unit cells, is indeed a feature of the circuit and not induced by the connection of two circuit boards. When the chain is longer than 8 nodes(fig. 4.27 a)), the signals of the strongly coupled pairs get distorted and differ from the shapes of single vdP oscillators with high non-linearity.

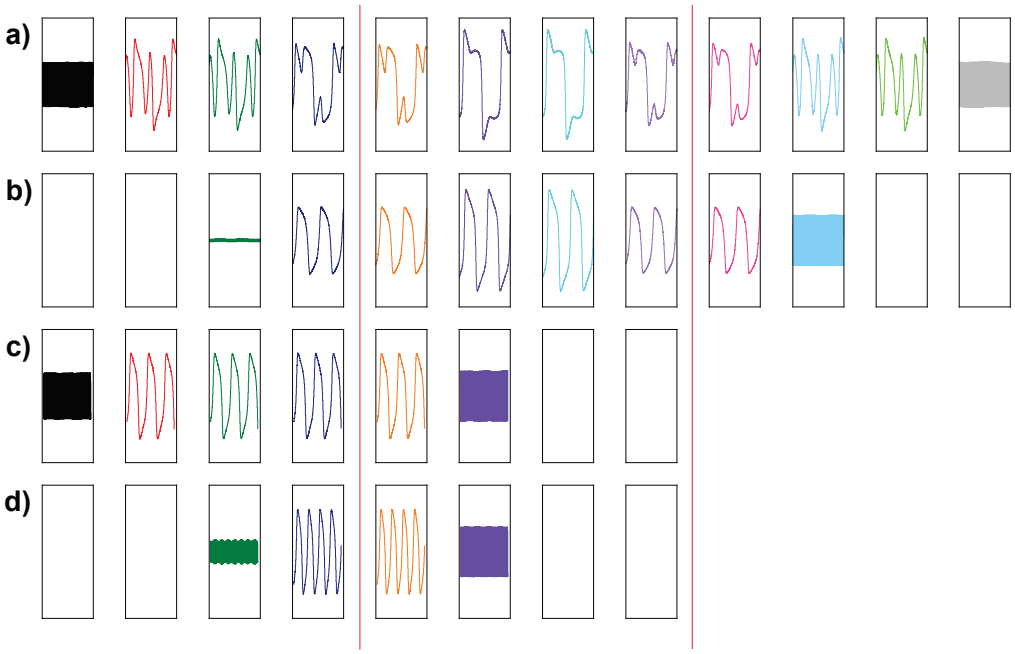

Figure 4.27: Qualitative signals of different sets of one dimensional topological non-linear chains. The x-axis of each plot corresponds to 215 ms, the y-axis to ±620 mV. The red vertical lines show where the circuit boards are connected. A blank plot indicates that the node is grounded. a): 12 node chain, b): 8 node chain, c): 6 node chain, d): 4 node chain.

The relative variation of the edge mode frequencies is much less compared to the significant increase of the bulk frequencies and lies in the range of approximately 10 %. The amplitude of the edge oscillations seems to be limited to approximately 200 mV, but is sometimes decreased when the end of the chain does not lie at the ends of the circuit board. We take this as a feature of parasitic resistance, which seems to be more prominent on the A sublattice and was found to be reduced when the circuit board parasitics are optimized (e.g. bridging long signal traces with short wires).

4.3.4 2D non-linear topological lattice

To investigate the interplay between topology and non-linearity in a bigger circuit and at higher dimension eight one-dimensional eight node chains are interconnected to form a 8×8 node two dimensional lattice. Both fitting parameters of the non-linear $I - V$ curve were ensured to lie in the region approximately 1 % around their mean values $\alpha = 0.024\,7\,\Omega^{-1}$ and $\gamma = 0.195\,\Omega^{-1}\,\mathrm{V}^{-2}$ for the ±300 mV fitting range. The values of the capacitors and inductors are kept the same as for the one dimensional lattice (see fig. 4.22).

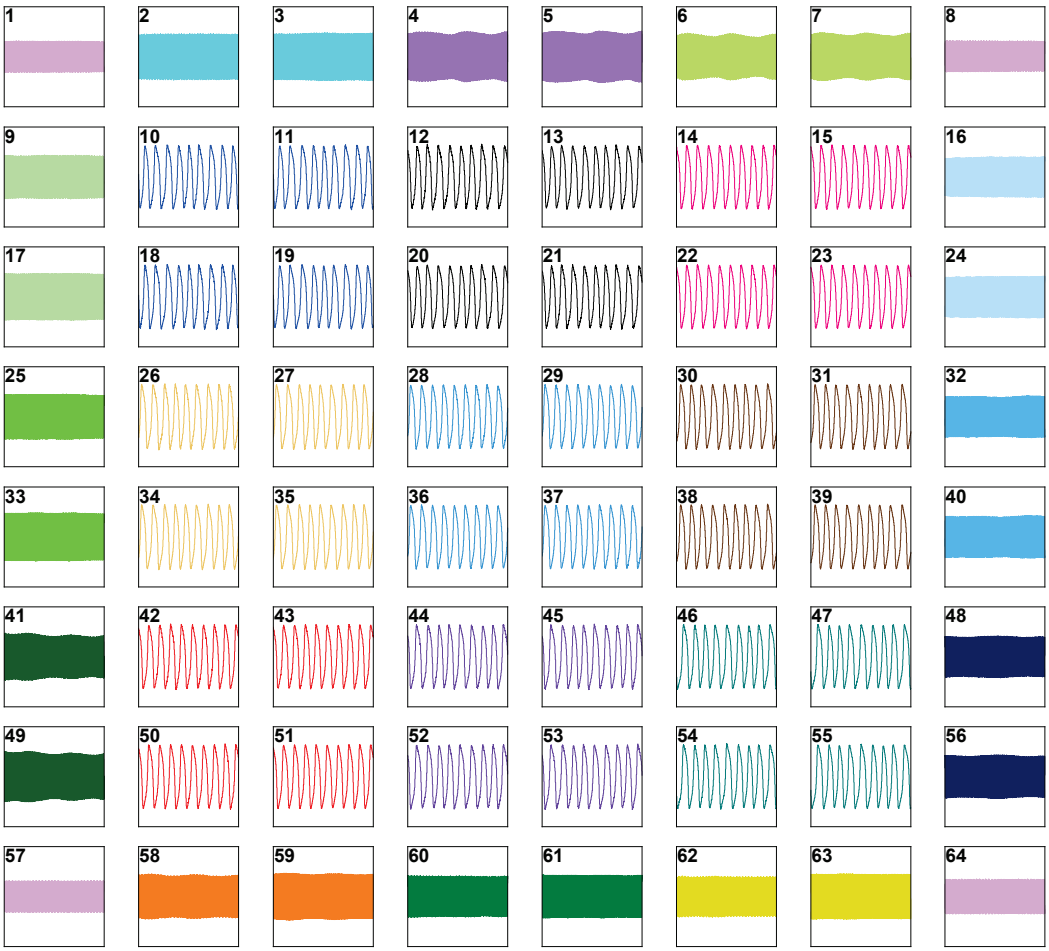

Figure 4.28: Voltage signals of the two-dimensional 8×8 non-linear circuit. Strongly coupled nodes have the same color and the four edges are colored the same. The x-axis of each plot corresponds to 200 µs, the y-axis to ±650 mV. All signals are synchronously measured, therefore node 36 is measured by nine 8 channel oscilloscopes (Picoscope 4824) and used to trigger the measurements. The other 63 channels are used to record the remaining node voltages.

First measurements showed that the fast topologically protected oscillations at the corners and edges of the circuit were significantly damped in relation to the amplitudes measured in the one dimensional chain. Improved parasitic resistances by reducing the trace length to the grounding inductors L_2 at the boundaries together with a decrease of the grounding capacitance to $C = 39\,\mathrm{nF}$ led to approximately the same amplitude of all corner/edge oscillation.
In fig. 4.28 the voltage signals of each node of the circuit are displayed. The oscillation frequencies at the edges (617 kHz ± 2 %) and corners (790 kHz ± 2.3 %) are significantly

higher than in the bulk (45.8 kHz ± 0.25 %). Each strongly coupled pair at the edges and quartets in the bulk (same colors) oscillates in-phase with approximately the same amplitudes.
Equivalently to the one-dimensional chain, the high frequency corner/edge oscillations are of sinusoidal type, whereas the low frequency bulk oscillations are of strong relaxation type (see fig. 4.29).

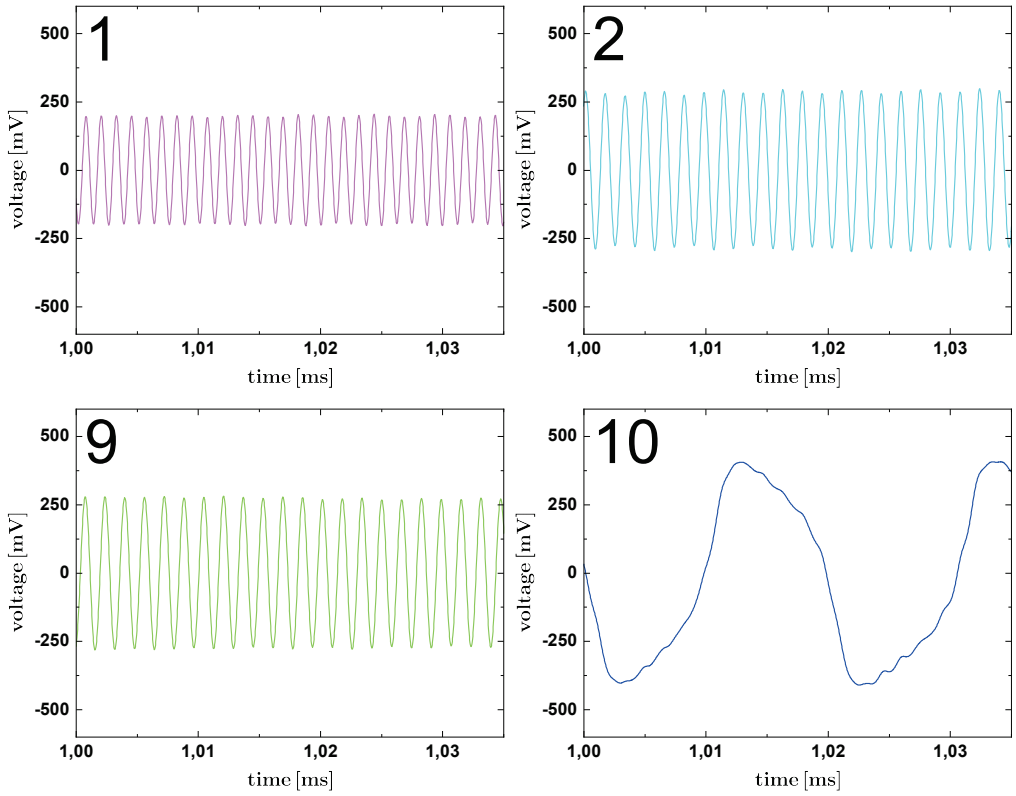

Figure 4.29: Voltage signals at the upper left edge of the 8×8 non-linear circuit (see fig. 4.28). Node 1 corresponds to an edge node high frequency sinusoidal oscillation ($f_1 = 806.0\,\text{kHz}$), Node 2 and 9 belong to two different strongly coupled edge pairs with sinusoidal oscillation and slightly lower frequency ($f_2 = 618.7\,\text{kHz}$, $f_9 = 616.9\,\text{kHz}$) and Node 10 is part of a strongly coupled bulk quartet showing low frequency relaxation oscillations ($f_{10} = 45.87\,\text{kHz}$).

Furthermore, the measured voltage data is numerically differentiated by calculating the central difference quotient, the voltage and its numerical derivative are normalized and the angle ϕ between them in phase space is calculated. The mean angular frequency ω is achieved by the mean value of the numerical derivative of the unwrapped phase angle ϕ. In this representation we are able to inspect the frequency and phase relations in a more accessible way than in fig. 4.28.
The results are shown in fig. 4.30 together with other circuit configurations. a) is the

representation of the data set displayed in fig. 4.28. The three different frequencies for corners, edge pairs and bulk quartets are indicated by the background color. In addition we see clearly that the oscillations of each strongly coupled nodes are in-phase. In contrast to results from simulations of similar, but ideal two dimensional circuits (see fig. S3 in the supplemental material of [65]) the phases of all bulk quartets are not synchronized due to the component tolerances resulting in slightly different frequencies of the the bulk oscillations.

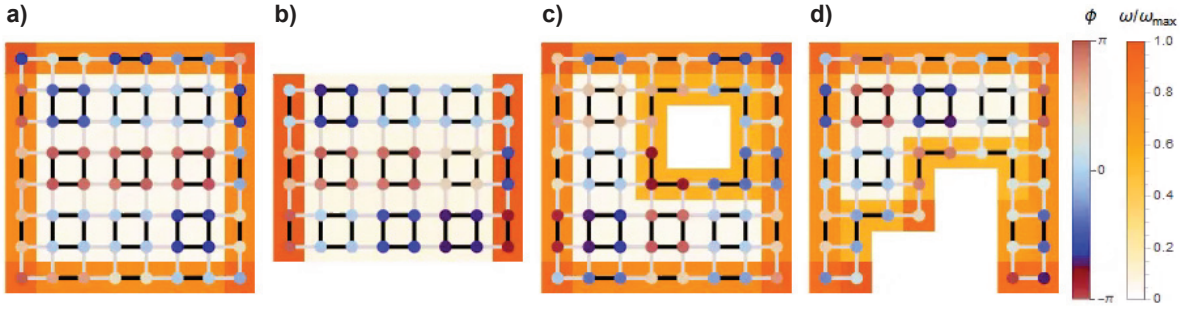

Figure 4.30: Phase angle ϕ (node color) and normalized mean angular frequency $\omega/\omega_{\max}$ (background color) of the two dimensional non-linear circuit lattice in different configurations, black/gray bars indicate strong/weak coupling. a): Corner mode regime, b): Edge mode regime, c): bulk defect configuration, d): edge defect configuration (adapted from [65]).

When the edges in one dimension are terminated to be in the topologically trivial regime (fig. 4.28 b)) the fast edge oscillations only appear in the perpendicular direction as it would be expected from passive topological circuits. Also lattice defects introduced by removing unit cells from the bulk or edge of the circuit (fig. 4.28 c),d)) do not alter the topological protection of the localized edge state, which wraps around the defects.
A new type of fast oscillating phase-synchronous triplets can be found. They emerge due to the cutout of one node of a bulk quartet and have lower oscillation frequencies than the edge pairs. From the four triplets in the circuit with bulk defect we can compute that the AC root mean square amplitudes of the nodes with two strong couplings are circa 1.38 times higher than the amplitudes of the nodes with only one coupling.
As in the one-dimensional case the system's oscillation frequencies can be approximated by the imaginary parts of the Jacobian eigenvalues (see eq. 4.84) with vanishing weak couplings. There are four possible building blocks in the investigated two dimensional circuits, which are isolated nodes (index i), dimers (index d), triplets (index d) and quartets (index q). Their corresponding eigenvalues in the coupling matrix are $\mu_i = g$, $\mu_d = g \pm s$, $\mu_t = g, g \pm \sqrt{2}s$ and $\mu_q = g \pm s \pm s$. Again the eigenvalues with lowest magnitude are preferred, which belong to in-phase oscillations. While for isolated nodes, dimers and quartets all entries of the corresponding eigenvectors are of equal size, in the triplet states the magnitude for the node with double coupling is $\sqrt{2}$ times higher than the two other entries, which explains the observations in the previous paragraph.
The approximated frequencies of the in-phase states achieved from the linearized model

are given by

$$\begin{aligned}
f_i &= \sqrt{g}\cdot\frac{1}{2\pi\sqrt{L_0C}} = \sqrt{L_0\left(\frac{2}{L_1}+\frac{2}{L_2}\right)}\cdot\frac{1}{2\pi\sqrt{L_0C}} = 976\,\mathrm{kHz}\\
f_d &= \sqrt{g-s}\cdot\frac{1}{2\pi\sqrt{L_0C}} = \sqrt{L_0\left(\frac{2}{L_1}+\frac{1}{L_2}\right)}\cdot\frac{1}{2\pi\sqrt{L_0C}} = 691\,\mathrm{kHz}\\
f_t &= \sqrt{g-\sqrt{2}s}\cdot\frac{1}{2\pi\sqrt{L_0C}} = \sqrt{L_0\left(\frac{2}{L_1}+\frac{2-\sqrt{2}}{L_2}\right)}\cdot\frac{1}{2\pi\sqrt{L_0C}} = 530\,\mathrm{kHz}\\
f_q &= \sqrt{g-2s}\cdot\frac{1}{2\pi\sqrt{L_0C}} = \sqrt{L_0\frac{2}{L_1}}\cdot\frac{1}{2\pi\sqrt{L_0C}} = 54.8\,\mathrm{kHz}\,,
\end{aligned} \tag{4.87}$$

which are up to 24 % higher than the measured frequencies, but the relative positions in approximation and experiment differ less than 7 %

$$\begin{aligned}
\frac{f_i}{f_q} &= 17.8 & \frac{f_i}{f_{q\,\mathrm{exp}}} &= 17.2\\
\frac{f_d}{f_q} &= 12.6 & \frac{f_d}{f_{q\,\mathrm{exp}}} &= 13.5\\
\frac{f_t}{f_q} &= 9.67 & \frac{f_t}{f_{q\,\mathrm{exp}}} &= 9.82\,.
\end{aligned} \tag{4.88}$$

Therefore, the approximation can also be used for quantitative statements about relative frequency positions in more complex circuits and higher dimensions.

4.3.5 Conclusions

A non-linear current-voltage relation was implemented by a subcircuit essentially made of anti-parallel diodes and a negative impedance converter (see fig. 4.22), which was included into topological LC networks with highly different intra- and intercell couplings representing the nearly dimerized limit. The resulting set of coupled differential equations resembles the non-linear van der Pol differential equation, which has an unstable rest state for positive non-linearity (fig. 4.21).
This leads to self-activated and self-sustained oscillations with different frequencies for edges and the bulk of the circuit. At the edges high frequency sinusoidal oscillations, which would be expected for a single weakly non-linear van der Pol oscillator, occur. In the bulk low frequency synchronous relaxation oscillations of the strongly coupled pairs can be found [116]. An explanation of this behaviour can be assumed by a linearization of the system at the rest state approximating the oscillation frequencies by the imaginary parts of the Jacobian eigenvalues (eq. 4.84) in the limit of vanishing intracell coupling. The frequencies are approximately determined by the most unstable states, which posses the smallest eigenvalue in the linear coupling matrix $\boldsymbol{\beta}$ with eigenvector located at the considered nodes.
The high frequency oscillations can be traced back to the topological edge modes of the

linear coupling matrix $\boldsymbol{\beta}$ formed by the inductive couplings of the nodes. It could be experimentally validated that they are present not only in a one-dimensional system, but also in two-dimensional lattices and are robust against edge or bulk defects (fig. 4.30). Furthermore, it was shown that the predicted frequencies obtained from the linearized and disconnected ($w \to 0$) network can be used to describe the relative positions of the different limit cycles frequencies as well as the relative amplitude and phase relations of the strongly coupled sets.

By combining insights from previous studies about the type [114,117–119] and strength [120, 121] of non-linearity with the results obtained from our investigations we can state general design rules for self-excited and self-sustained active circuitry with topologically protected edge modes.

When working with sufficiently low activity introduced by a non-linearity of Rayleigh type [122] the attractors of the circuit's nodes reflect those eigenstates of the underlying linear coupling of the system, which leads to the most unstable modes in the active circuit. The non-linearity defines the amplitude of the self-excited oscillation, while the frequencies of the modes are set by the coupling strengths. If the coupling structure of the network host topologically protected edge modes they can be found in the the response of the circuit also in the presence of lattice defects.

5 Conclusion and outlook

In this thesis we presented the grounded circuit Laplacian formalism to translate single particle tight binding Hamiltonians from solid state theory into electric circuits, where not only topological properties of the solid state models can be implemented and experimentally investigated on an easily accessible and macroscopic platform.
The electrical measurement routines can be performed with standard measuring equipment, whereby equivalents to the electronic wave functions in a solid, can be found by simple voltage measurements providing information about the eigenstates in the circuit. The allowed energies for electrons in the solid are given by the band structure, i.e. the energies associated with the electronic wave functions due to the crystalline environment and with respect to their wave vectors. It is based on the assumption of an infinite crystal and can be calculated theoretically by introducing periodic boundary conditions to the system. When these crystals are emulated on other platforms the system sizes are finite and not periodic, making it difficult to directly evaluate the band structure.
However, in lumped element electric circuits periodicity can be implemented easily by interconnecting the opposite ends of the finite sample, thus a discretized version of the solid state band structure, the admittance band structure, can be directly analyzed. Furthermore, for implementations with only capacitive or inductive circuit elements the measurement frequency can be used as an external parameter to probe the artificial solid state system at different energetic positions without restrictions like the chemical potential in solids.
This is an important benefit for the investigation of topological phenomena, where the bulk-boundary correspondence relates gap closings in the band structure with the existence of topological edge modes and thus the bulk band structure as well as boundary effects have to be investigated.

Applications of the above mentioned techniques have been tested in chapter 3 for Hermitian model systems and it was shown that we are able to experimentally prove the existence and characteristic profile of topological edge modes as well as the associated gap closing in the admittance band structure of the SSH model (sec. 3.1). In addition, we demonstrated that the band structure measurement can be carried out on bigger systems (18×18 unit cell honeycomb lattice) and also for more complicated sets of bands (carbon nanotube models) (sec. 3.2). Furthermore, we were able to experimentally verify a present theoretical proposal [60] and found higher order topological states in an electrical circuit (sec. 3.3).
Regarding these experimental realizations it has to be mentioned that simply working in the low frequency regime does not guarantee that the lumped element picture of a circuit holds without further limitations. Care has to be taken that parasitic couplings between adjacent conductive paths or circuit components, especially couplings between inductive circuit elements, do not alter the intended connectivity. Precisely when exponentially

localized topological edge modes should be measured, even small couplings can affect the exponentially decreasing signals towards the bulk.
In addition, each circuit element, even if it is intended to be purely reactive, shows albeit small resistive behaviour. Therefore, when Hermitian models are considered, additional efforts are required to keep parasitic resistive contributions small in comparison to the scheduled reactive impedances.

But resistive impedances can also be used to make a virtue of necessity, when they are intentionally implemented in topolectrical circuits to investigate non-Hermitian systems (chapter 4). Non-Hermiticity in translation invariant systems is a present research subject with links to topics like open quantum systems [48], photonics [49–53] and biological processes [55, 56] to name a few examples. Therefore, we used the complex nature of electric impedance and the phase sensitive determination of voltage and current to study non-Hermitian phenomena.

Starting with a phenomenon known from quantum mechanics, lattices obeying $\mathcal{PT}$ symmetry were shown to possess eigenstates with purely real energies although Hermiticity is explicitly broken. We consequently extended the SSH model with staggered on site resistances and were able to demonstrate the proposed real energies in the PT symmetric model (sec. 4.1). Thanks to the flexibility of the circuit platform we could use tunable resistors to investigate the $\mathcal{PT}$ symmetric, the $\mathcal{PT}$ broken and even the anti-$\mathcal{PT}$ symmetric regime in one circuit. In other emulating platforms such as optical wave guide systems it has not been possible to study the anti-$\mathcal{PT}$ symmetric regime before because the high amount of loss needed to reach this regime rendered the investigation impossible [62].
We found the bulk eigenvalues to change from purely real to purely imaginary and spontaneous $\mathcal{PT}$ symmetry-braking topological edge states with purely imaginary eigenvalues could be verified in all symmetry regimes, although the complex band structure of the system closes at exceptional points. In contrast, a localized topological defect state with zero eigenvalue could be implemented which changes its spacial profile during the change of symmetry regimes and was found delocalized when exceptional points where present in the band structure.
Therefore, the Hermitian concept of bulk-boundary correspondence cannot be transferred directly to those kinds of non-Hermitian systems for edge and defect states, although a quantized topological invariant could be found predicting topological modes in all three symmetry regimes [62].
With our experimental investigation we were able to deduce new insights about systems obeying $\mathcal{PT}$ symmetry, especially topological defects prove promising to engineer localized zero modes in $\mathcal{PT}$ symmetric lattices. Therefore, we hope to open new fields of application for $\mathcal{PT}$ symmetric materials, which are already predicted to be able to host a lot of novel phenomena such as non-reciprocal light propagation [52, 123], unidirectional invisibility [49, 124] and arbitrarily fast state evolution although the bandwidth of the system is limited [125, 126].

In a next step besides Hermiticity also reciprocity was broken in an extended SSH model to investigate a novel theoretical prediction in non-Hermitian systems about extensive

mode localization at the system edges [100, 102], termed the non-Hermitian skin effect (sec. 4.2). To break reciprocity a direction-dependent hopping element, i.e. an active subcircuit (INIC) with positive capacitance in one direction and negative capacitance in the other, was used. Due to an additional parallel resonant circuit as reciprocal hopping element the strength and side of the localization could be tuned by the measurement frequency.
For the experimental investigation of such non-Hermitian, non-reciprocal systems it should be mentioned that care has to be taken for not driving the circuit unstable and saturation effects occur or in the worst case the circuit gets damaged. Furthermore, when an extensive localization effect is present in an electrical circuit, parasitic couplings should be avoided best possible. We found that even small couplings due to the supply lines of the active circuitry or connection of several nodes to the same multiplexer showed non-negligible impact on the measured values, so that the circuit board had to be refined and the envisaged measurement automation could not be used.
Despite this, a significant change between the PBC and OBC eigenvalue spectrum could be found and visualized by measuring the spectrum while successively reducing the strength of a single hopping element to switch between PBC and OBC. The measurement results confirmed the theoretical framework using complex wave vectors to describe the spectral flow between the PBC and OBC bulk eigenvalues accompanied by the edge localization of all bulk modes. Additionally, it could be determined that an edge localization only takes place when the PBC spectrum has non-zero internal area, i.e. forms closed loops that shrink to lie on open arcs during the transition.
In addition to localized bulk modes, the system also hosts topologically protected edge modes with localization lengths differing from those of the bulk modes. By tuning the measurement frequency band touching points of the PBC spectrum could be found which do not match the changes in the number of edge modes. Instead, a gap closing in the OBC spectra is needed to change the number of edge states, which does not necessarily match the PBC band touching. Furthermore, we showed that a transformation to an effectively reciprocal model can be used to correctly predict this change. Therefore, the Hermitian concept of bulk-boundary correspondence, based on the fact that the PBC and OBC spectrum do not differ significantly, has to be generalized.
Possible applications of the investigated non-Hermitian skin effect with great potential are given in every scenario where a selective unidirectional energy transport is needed, e.g. for shock/vibration damping or energy harvesting in mechanical metamaterials [127] or as an optical funnel for enhanced sensitivity [123].

In the last project we enriched a topological SSH system with non-Hermitian, non-linear on-site resistance to produce self-activated and self-sustained topological circuits (sec. 4.3). We implemented active subcircuits with a current-voltage equation having a negative linear and positive cubic voltage term, so that the non-linear subcircuit acts as a negative resistor for small voltages, but as a non-linear positive resistor for large voltages. Consequently, the rest state at zero voltage and current is unstable and the circuit nodes are driven to non-zero voltages without external input. Mathematically speaking, we chose a weak van der Pol-like non-linearity [64] in such a way that the fixed point at the origin is unstable and stable limit cycles exist. Due to the non-linearity the Laplacian formalism based on linear algebra cannot be used anymore and the non-linear

differential equations describing the circuit have to be analyzed in the time domain.
In the limit of weak non-linearity and highly differing intra-/ intercell hoppings we found the phenomena introduced by topology and non-linearity to coexist. At the weakly coupled edges high frequency sinusoidal topological edge modes exist, whereas in the bulk low frequency relaxation oscillations can be found. Each strongly coupled set exhibits synchronous in-phase oscillation, so that the bulk is made of plaquettes with synchronous relaxation oscillations, while these plaquettes are truncated at the edges and perform high frequent in-phase sinusoidal oscillations. This behaviour could be verified in one and two dimensions and was found to hold true even with lattice defects at the edges or in the bulk of the system. The theoretical predictions for the oscillation frequencies stemming from linearized and isolated sets of nodes were found to differ from the measured values quantitatively, but the relative relations between the oscillation frequencies in the circuit agree well in theory and experiment.
With these investigations we derived design rules showing how to set up the interplay between topologically protected edge modes and self-activated and self-sustained oscillation due to non-linearity to combine the two phenomena in such a way that both features coexist in the circuit and can be described by straightforward theoretical models. Hereby we hope to contribute new insights for the design of autonomous devices [110] with topologically protected functionalities, which can be used for example for solitary signal transport [128] or for the understanding and utilization of biological functions and neuronal networks [111].

In summary it could be said that electric circuits serve as an extremely versatile platform for the investigation of not necessarily topological phenomena in translation invariant lattices. Due to the direct accessibility of each node, the huge commercial availability of different circuit components, the possibility of industrial production, the complex nature of admittance, the possible hoppings of arbitrary range and complexity, the unlimited dimensionality and the switching capability between periodic and open boundary conditions electrical circuits exceed most of the other metamaterial platforms dealing with topological phenomena, such as ultra cold atomic gases, photonic, acoustic or mechanical metamaterials.
In less than ten years a wide field of topological systems was studied with the help of electrical circuits, e.g. Chern insulators [57, 129–131], higher-order topological insulators [61, 132–134], topological semimetals [58, 135–138], topological states in more than three dimensions [58, 139], non-Hermitian and non-reciprocal topological effects [62, 63, 140–144], non-linear topological systems [65], etc.
But there are many more topics to be tackled with the help of topolectrical circuits. A few examples are given by time-dependent Floquet systems [145, 146], which can be investigated by varying component admittances with time, non-linear systems, where chaos can be introduced [147, 148], non-linear transmission lines obeying solitonic wave transport [149, 150] or systems in non-Euclidean space such as hyperbolic lattices [151, 152].
A direct technical application of topolectrical circuits is not in prospect at the moment because for matching with the commercially used highly integrated circuits a miniaturization of the topolectrical circuits has to take place to provide topological effects on a technically useful length and frequency scale. But with miniaturization the lumped element description of the circuit breaks down and line constants, couplings and production

tolerances are of crucial importance, which makes manufacturing of such circuits much more difficult.
Therefore, in near future topolectrical circuits may serve for example as an experimental test bench for novel theoretical predictions, where promising ideas can be transferred to other metamaterial or solid state platforms, as a simulator for complex non-linear systems, which may outperform classical computer simulations, or as an easy accessible demonstration experiment showing the impact of topological phenomena on translation invariant lattices.
The very active ongoing research on topolectrical circuits will show which impact those circuits will have on teaching topological phenomena, which novel theories can be investigated and which technical applications can be reached in the future.

A Circuit diagrams, board designs and parts lists

A.1 $\mathcal{PT}$-SSH circuit

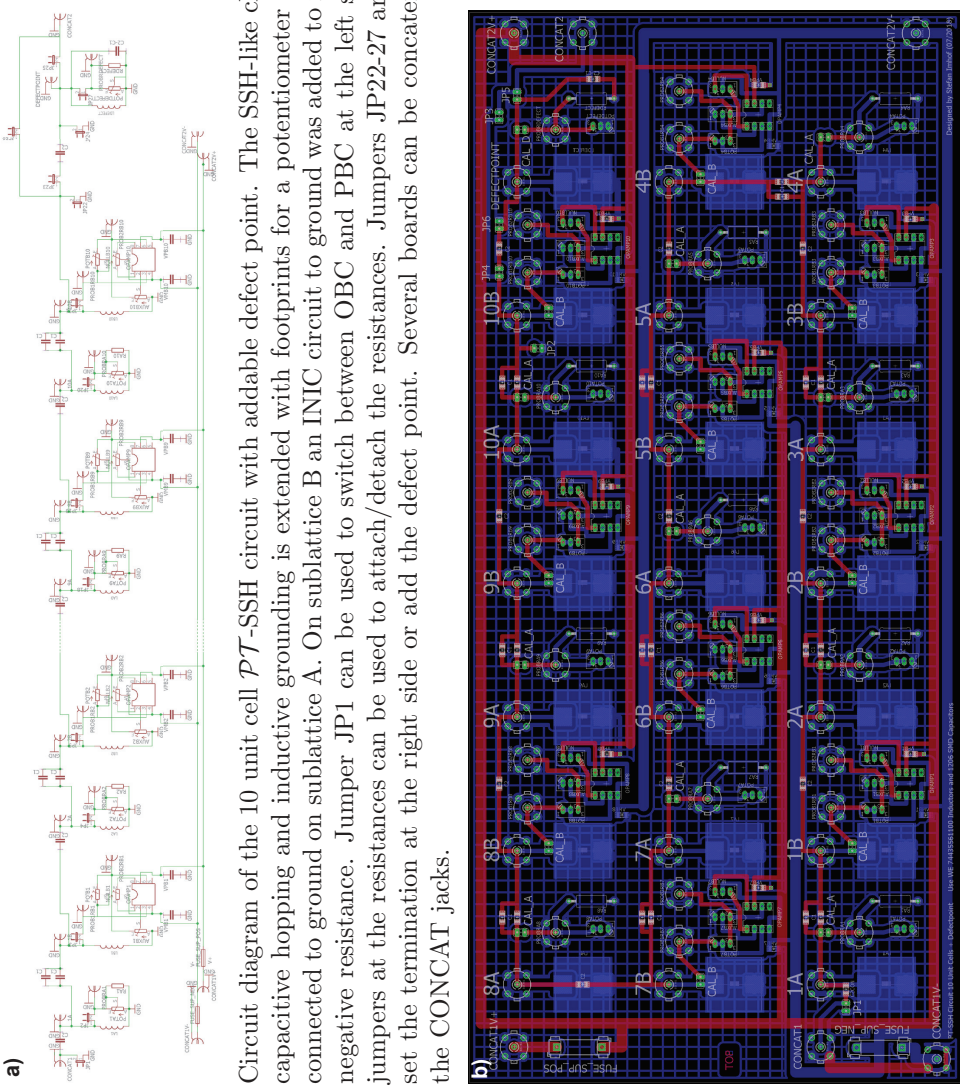

Circuit diagram of the 10 unit cell $\mathcal{PT}$-SSH circuit with addable defect point. The SSH-like chain with capacitive hopping and inductive grounding is extended with footprints for a potentiometer or resitor connected to ground on sublattice A. On sublattice B an INIC circuit to ground was added to introduce negative resistance. Jumper JP1 can be used to switch between OBC and PBC at the left side. The jumpers at the resistances can be used to attach/detach the resistances. Jumpers JP22-27 are used to set the termination at the right side or add the defect point. Several boards can be concatenated via the CONCAT jacks.

Circuit board of the $\mathcal{PT}$-SSH circuit (360 mm × 165 mm, FR4 1.55 mm, 105 µm copper). The nodes are arranged s-shaped to achive a equal spacing between the shielded flat wire inductors (bottom). For the hopping elements footprints for SMD 1206 capacitors are used. The supply lines for the operational amplifiers (INICs) can be fused and are arranged as stub lines. The signal lines are routed on the top, the ground plane is located at the bottom side.

Figure A.1: Circuit diagram a) and printed circuit board design b) of the $\mathcal{PT}$-SSH circuit.

Circuit position	Component label	Specifications
L	WE-HCI SMT High Current Inductor 74435561100 [153]	Inductance $L = 10\,\mu\text{H} \pm 20\,\%$ at 100 kHz/10 mA, range $9.96\,\mu\text{H} - 9.98\,\mu\text{H}$ pre-characterized at 80 kHz, DC resistance $R_{DC} = 6.9\,\text{m}\Omega \pm 8\,\%$, saturation current $I_{sat,10\%} = 10\,\text{A}$
C_1, C_2	Multilayer Ceramic Capacitor (MLCC) C1206C104F3GACTU [154]	Capacity $C = 100\,\text{nF} \pm 1\,\%$, nominal DC voltage: 25 V, dielectric: C0G (NP0), case code: 1206
Bypass capacitor	MLCC C1206C104F3GACTU [154]	Capacity $C = 100\,\text{nF} \pm 1\,\%$, nominal DC voltage: 25 V, dielectric: C0G (NP0), case code: 1206
R_A	Trimmer Resistor 3296W-1-500LF [155]	Resistance $R = 50\,\Omega \pm 10\,\%$, number of turns: 25, power rating: 500 mW
R_{def}	Trimmer Resistor 3296W-1-501LF [155]	Resistance $R = 500\,\Omega \pm 10\,\%$, number of turns: 25, power rating: 500 mW
R_A	Metal Film Resistor CPF15R0000BEE14 [156]	Resistance $R = 5\,\Omega \pm 0.1\,\%$, power rating: 1 W, temperature coefficient: 25 ppm/K
R_{def}	Metal Film Resistor CMF5510R000BHEA [157]	Resistance $R = 10\,\Omega \pm 0.1\,\%$, power rating: 0.5 W, temperature coefficient: 50 ppm/K
Node connector	BNC straight low profile PCB socket 5-1634503-1 [82]	Impedance: $50\,\Omega$, maximum frequency: 4 GHz

Table A.1: Parts list of the $\mathcal{PT}$-SSH circuit.

A.2 Non-Hermitian, non-reciprocal SSH circuit

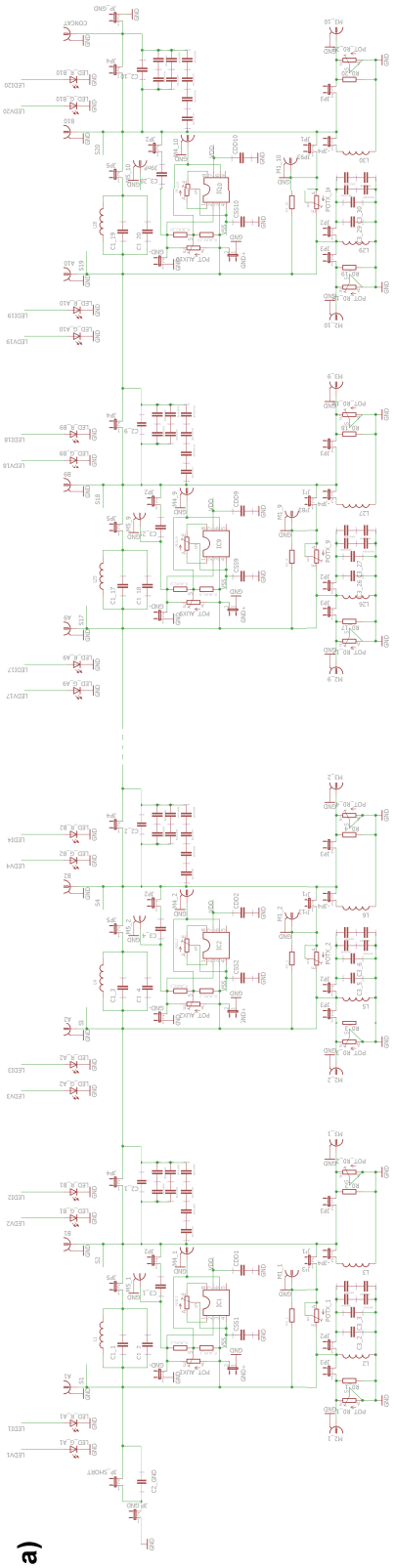

Circuit diagram of the 10 unit cell non-Hermitian, non-reciprocal SSH circuit. A detailed description of the components of each single unit cell can be found at fig. 4.12. The jumpers are used to add/subtract/calibrate single blocks of the unit cell, JP1: Additional intracell resistor (not used), JP2: INIC circuit and grounding capacitors on sublattice A, JP3: Grounding resistors, JP4: Removes grounding inductor on sublattice B and shorts intercell hopping (single sublattice cain), JP5: Intracell LC resonator, GND±: Short OpAmp inputs for nulling purposes, JP_SHORT/JP_GND: Set OBC terminations. The additional BNC sockets M1-5 can be used for calibrating/nulling. The circuit can be made periodic by connecting node A1 with CONCAT, several boards can be used in series by connecting CONCAT of the previous with A1 of the next board. The LEDs at each node are used for automized measurements to indicate where the current is fed in (green, LED_G) and the voltage is measured (red, LED_R).

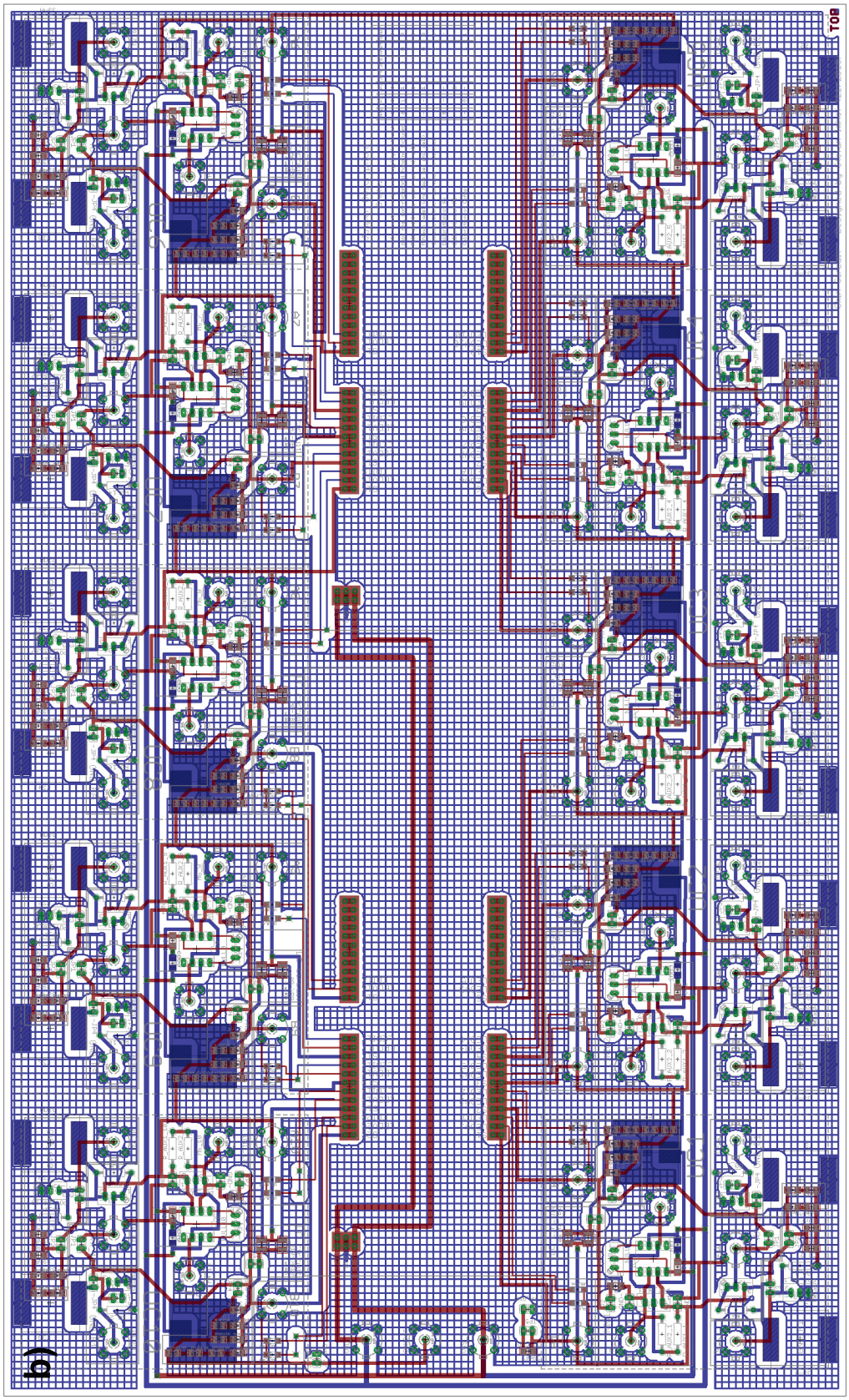

Circuit board of the 10 unit cell non-Hermitian, non-reciprocal SSH circuit (405 mm × 245 mm, FR4 1.55 mm, 105 µm copper). The nodes are arranged in a u-shape to have free space in the middle of the circuit board to attach additional piggyback boards with multiplexers for measurement automization and short lengths to make the chain periodic. The ground plane is located at the bottom side, the supply lines for the OpAmps are routed u-shaped on the bottom side, for the piggyback boards additional supply lines run in the middle of the circuit board to the corresponding connectors.

Figure A.2: Circuit diagram a) and printed circuit board design b) of the non-Hermitian, non-reciprocal SSH circuit.

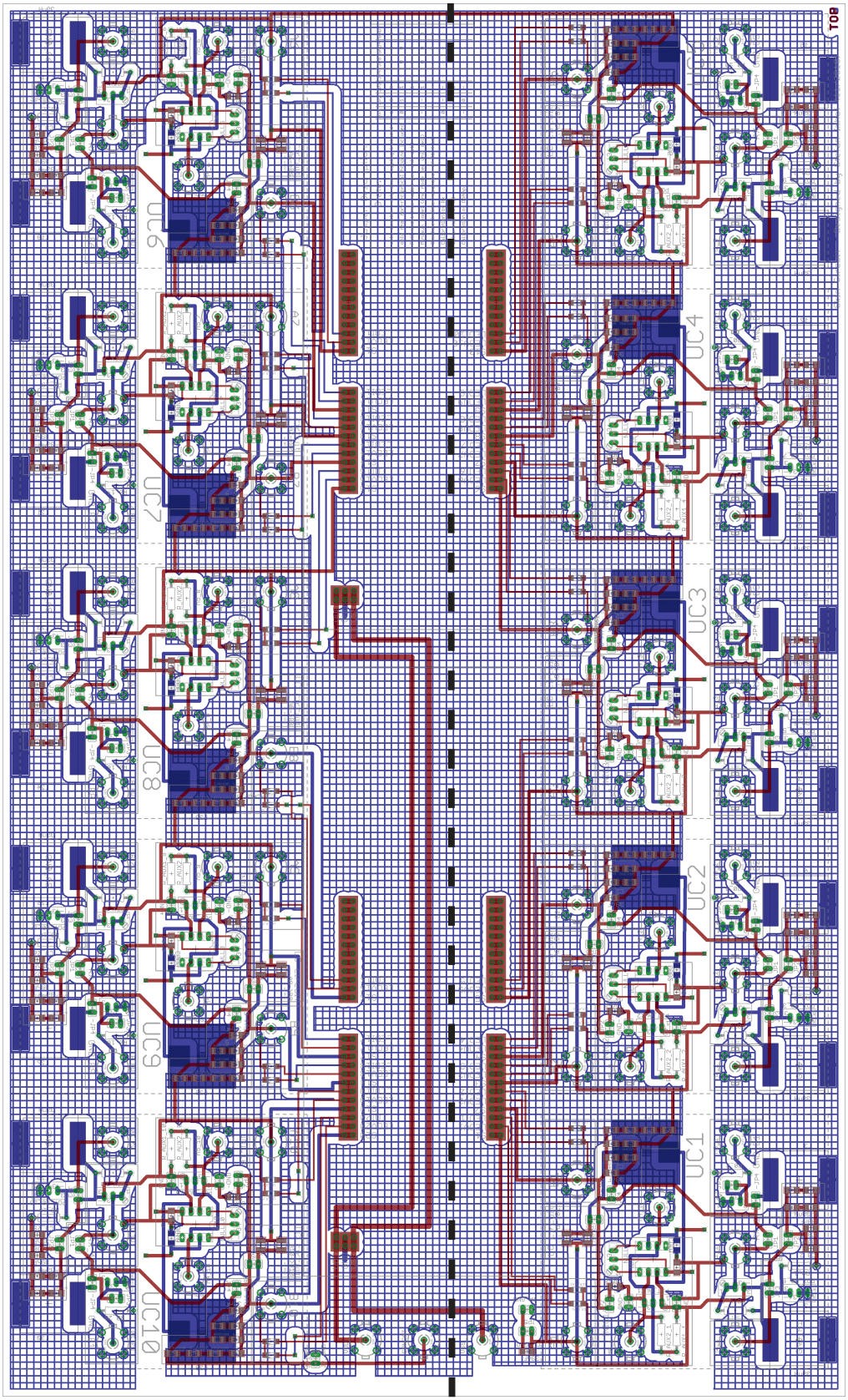

Figure A.3: Modified circuit board of the 10 unit cell non-Hermitian, non-reciprocal SSH circuit. The DC supply lines were milled out and the u-shaped geometry was cut in two halves along the dashed black line to be able to increase the spatial distance between the ends of the chain.

Considering that highly localized voltage responses combined with very low signals at the other end of the chain can eventually arise in this model a detailed investigation of signal couplings due to the circuit board was done. It could be figured out, that on a circuit board only equipped with BNC jacks to contact the conducting paths voltage couplings to nodes far away from the input in the order of 10^{-4} of the input voltage are present. This could be improved to 10^{-6} by milling out the DC supply lines of the circuit board, which were replaced by shielded coaxial cables routed several centimeters above and below the circuit board.
To eliminate further couplings on the circuit boards especially by inductive coupling of the inductors, the circuit boards were cut in the middle and reconnected to prevent couplings between the neighboring ends of the chain (see fig. A.3). Furthermore, each inductor was equipped with an additional shield made of adhesive aluminum tape and each half of the cut boards was placed on a metallic mesh isolated by plastic film. Additionally, the ground plane was bridged over the removed supply lines by air bridges to reduce long return paths along the slotted ground plane.

Circuit position	**Component label**	**Specifications**
L_0	shielded wire wound inductor SRP1770TA-390M [158]	Inductance $L = 39\,\mu\text{H} \pm 20\,\%$ at 100 kHz/1 V, range $30.0\,\mu\text{H} - 30.8\,\mu\text{H}$ pre-characterized at 91.9 kHz, DC resistance $R_{DC_{max}} = 48\,\text{m}\Omega$, saturation current $I_{sat,20\%} = 11\,\text{A}$
L_1	WE-HCI SMT High Current Inductor 74435561100 [153]	Inductance $L = 10\,\mu\text{H} \pm 20\,\%$ at 100 kHz/10 mA, range $9.495\,\mu\text{H} - 9.505\,\mu\text{H}$ pre-characterized at 91.9 kHz, DC resistance $R_{DC} = 6.9\,\text{m}\Omega \pm 8\,\%$, saturation current $I_{sat,10\%} = 10\,\text{A}$
C_2, C_3	MLCC C1210C154F5GACTU [159]	Capacity $C = 47\,\text{nF} \pm 1\,\%$, nominal DC voltage: 50 V, dielectric: C0G (NP0), case code: 1206
Bypass capacitor	MLCC C1206C104F3GACTU [154]	Capacity $C = 100\,\text{nF} \pm 1\,\%$, nominal DC voltage: 25 V, dielectric: C0G (NP0), case code: 1206
C_1	MLCC C1210C154F5GACTU [154]	Capacity $C = 150\,\text{nF} \pm 1\,\%$, nominal DC voltage: 50 V, dielectric: C0G (NP0), case code: 1210
C_{INIC}	MLCC C2220C474J5GACTU [154]	Capacity $C = 470\,\text{nF} \pm 5\,\%$, nominal DC voltage: 50 V, dielectric: C0G (NP0), case code: 2220
R_0	Trimmer Resistor 3296W-1-201LF [155]	Resistance $R = 200\,\Omega \pm 10\,\%$, number of turns: 25, power rating: 500 mW
Nulling poten-tiometer	Trimmer Resistor 3296W-1-502LF [155]	Resistance $R = 5\,\text{k}\Omega \pm 10\,\%$, number of turns: 25, power rating: 500 mW

R_x	Metal Film Resistor CMF5510R000BHEA [157]	Resistance $R = 10\,\Omega \pm 0.1\,\%$, power rating: 0.5 W, temperature coefficient: 50 ppm/K
R_0, R_{INIC}	Metal Film Resistor YR1B20RCC [160]	Resistance $R = 20\,\Omega \pm 0.1\,\%$, power rating: 0.25 W, temperature coefficient: 15 ppm/K
INIC	LT1363 Operational Amplifier [105]	Gain bandwidth: 70 MHz , slew rate: 1 000 V/µs, maximum supply current: 7.5 mA, unity-gain stable
Red LED indicator	LED 26-21/R6C-AR2T1LY/CA [85]	Chip material AlGaInP, forward voltage 1.7 V − 2.3 V, peak wavelength 632 nm, luminous intensity 140 mcd − 360 mcd, viewing angle 30°, case code: 1206
Green LED indicator	LED APTD3216LCGCK [84]	Chip material AlGaInP, forward voltage 1.9 V − 2.3 V, peak wavelength 570 nm, luminous intensity 12 mcd − 25 mcd, viewing angle 40°, case code: 1206
Node connector	BNC straight low profile PCB socket 5-1634503-1 [82]	Impedance: 50 Ω, maximum frequency: 4 GHz

Table A.3: Parts list of the non-Hermitian, non-reciprocal circuit.

A.3 Circuit boards for measurement automation

For measurement automation additional circuit boards shown in fig. A.4 where designed that can be plugged onto the model circuit (see fig.A.2). They host CMOS (complementary metal-oxide-semiconductor) analog multiplexers for routing the measurement signal and the current input to the corresponding nodes on the circuit board and switching the corresponding LED indicators. But as already explained at the investigation methods (sec. 2.3.4) the saved time due to the measurement automation is contrasted with a coupling of the measured nodes due to the multiplexer and the circuitry (see fig. 2.15). For a circuit with highly localized modes, as it is the case in the non-hermitian, non-reciprocal SSH circuit, this effect distorts the measurement results especially for a u-shaped circuit geometry (fig. A.2) where both ends of the chains are measured by the same multiplexer.

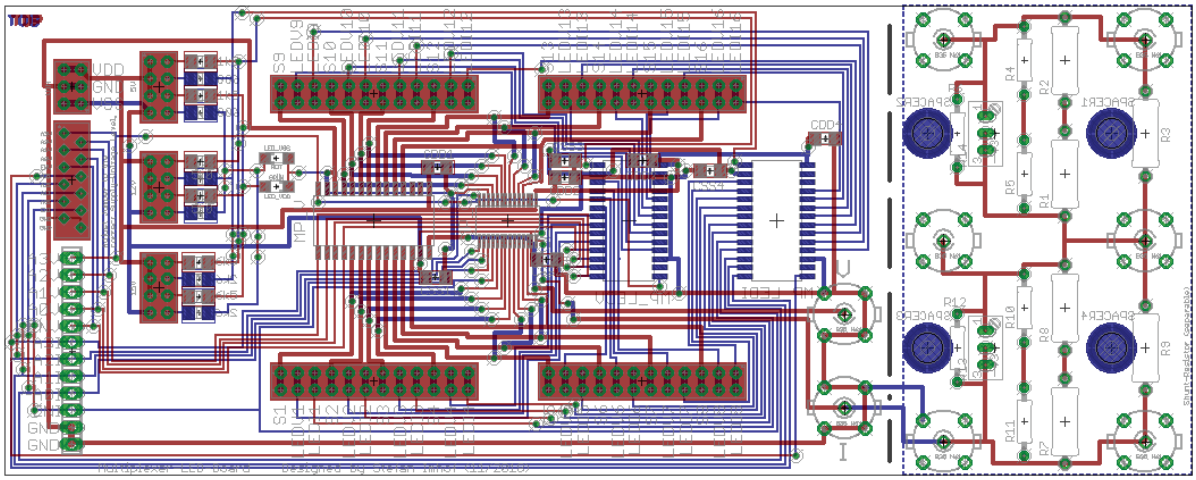

Figure A.4: PCB design of the 16 nodes multiplexer board for current input, voltage measurement and measurement indication with additional current sensing resistor circuit (top: red, bottom: blue). From left to right and top to bottom there are socket headers for the supply voltages (for each line two pins can be used in parallel), a connection block for digital control signals via ribbon cable, a screw terminal block for alternatively connecting the digital control signals, three rows of pin headers to be shortened with jumpers for selecting the supply voltage level and corresponding series resistors and indicator LEDs, 4 rows of socket headers (two pins in parallel for each connection, top and bottom in the middle of the circuit board) to connect the measurement signal and the measurement indication, a 16:1 channel multiplexer (SOIC (28) package) routing the voltage signal, a 16:1 channel multiplexer (TTSOP (28) package) to route the input current, two 16:1 channel multiplexer (SOIC (28) package, on the bottom) to control the voltage measurement and current input LEDs on the measurement board, two BNC jacks for connecting a voltage measurement device/current input and the optional current input sensing resistor circuit.

Circuit position	Component label	Specifications
Screw terminal block	PCB terminal block - MPT 0,5/12-2,54 - 1725753 [161]	12 pins, 2.54 mm pitch, 6 A nominal current, 160 V nominal voltage
Ribbon cable connector	WR-MM Female Angled Connector 690368171272 [83]	12 pins, 2.54 mm pitch, 1.5 A nominal current, 250 V AC working voltage, 10 mΩ max. contact resistance, 1 000 MΩ min. insulation resistance
Pin headers	WR-PHD 2.54 mm THT Dual Pin Header 6130XX21121 [80]	2.54 mm pitch, 3 A nominal current, 500 V AC maximum voltage, 20 mΩ max. contact resistance, 1 000 MΩ min. insulation resistance
Socket headers	WR-PHD 2.54 mm Dual Socket Header 6130XX21821 [79]	2.54 mm pitch, 3 A nominal current, 500 V AC maximum voltage, 20 mΩ max. contact resistance, 1 000 MΩ min. insulation resistance
Red LED indicator	LED 26-21/R6C-AR2T1LY/CA [85]	Chip material AlGaInP, forward voltage 1.7 V − 2.3 V, peak wavelength 632 nm, luminous intensity 140 mcd − 360 mcd, viewing angle 30°, case code: 1206
Green LED indicator	LED APTD3216LCGCK [84]	Chip material AlGaInP, forward voltage 1.9 V − 2.3 V, peak wavelength 570 nm, luminous intensity 12 mcd − 25 mcd, viewing angle 40°, case code: 1206
SMD resistor 620 Ω	Thin Film Resistor RT1206FRE07620RL [162]	Resistance $R = 620\,\Omega \pm 1\,\%$, temperature coefficient 50 ppm/K, power rating: 250 mW, case code 1206
SMD resistor 1.5 kΩ	Thick Film Resistor CRCW12061K50FKEA [163]	Resistance $R = 1.5\,\mathrm{k}\Omega \pm 1\,\%$, temperature coefficient 100 ppm/K, power rating: 250 mW, case code 1206
SMD resistor 2 kΩ	Thick Film Standard Power Resistor RMCF1206JT2K00TR-ND [164]	Resistance $R = 2\,\mathrm{k}\Omega \pm 5\,\%$, temperature coefficient 200 ppm/K, power rating: 250 mW, case code 1206
SMD resistor 2.7 kΩ	Thin Film Resistor RT1206FRE072K7L [162]	Resistance $R = 2.7\,\Omega \pm 1\,\%$, temperature coefficient 50 ppm/K, power rating: 250 mW, case code 1206
SMD resistor 4.7 kΩ	Thick Film Standard Power Resistor RMCF1206JT2K00TR-ND [164]	Resistance $R = 4.7\,\mathrm{k}\Omega \pm 5\,\%$, temperature coefficient 200 ppm/K, power rating: 250 mW, case code 1206
SMD resistor 6.49 kΩ	Thin Film Resistor ERA-8AEB6491V [165]	Resistance $R = 6.49\,\mathrm{k}\Omega \pm 0.1\,\%$, temperature coefficient 25 ppm/K, power rating: 250 mW, case code 1206

SOIC 28 multi-plexer	16:1 CMOS Multiplexer MUX36S16IDWR [166]	Supply range $\pm 5\,\mathrm{V} - \pm 18\,\mathrm{V}$ or $10\,\mathrm{V} - 36\,\mathrm{V}$, on-resistance $125\,\Omega$, on-capacitance 13.5 pF, transition time 97 ns, logic levels 2 V-V_{DD}
TSSOP 28 multi-plexer	16:1 iCMOS Multiplexer ADG1406BRUZ-ND [81]	Supply range $\pm 5\,\mathrm{V}$, 12 V or $\pm 15\,\mathrm{V}$, on-resistance $9.5\,\Omega$, on-capacitance 115 pF, transition time 105 ns, logic levels 2 V-V_{DD}
Bypass capacitor	MLCC C1206C104F3GACTU [154]	Capacity $C = 100\,\mathrm{nF} \pm 1\,\%$, nominal DC voltage: 25 V, dielectric: C0G (NP0), case code: 1206
BNC connector	BNC straight low profile PCB socket 5-1634503-1 [82]	Impedance: $50\,\Omega$, maximum frequency: 4 GHz

Table A.5: Parts list of the multiplexer board.

A.4 Non-linear SSH circuit

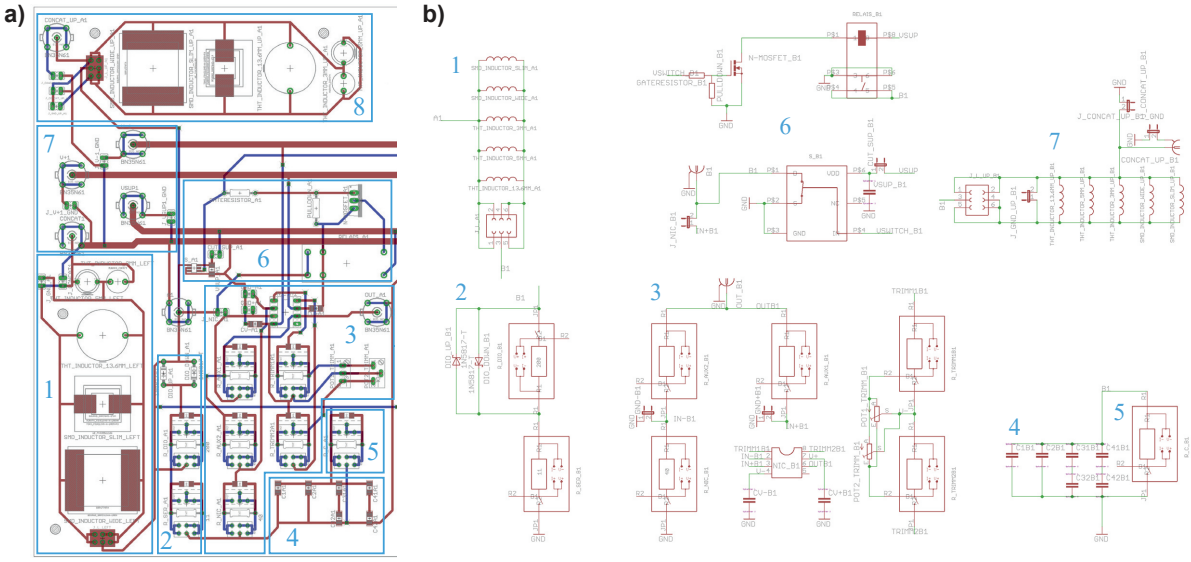

Figure A.5: Cutout of the circuitry of the non-linear topological circuit. The repeated nodes are designed in a modular fashion to be able to tune the circuit parameters after the circuit board fabrication. a): One node cutout of the PCB design. 1: Inductive coupling between the nodes, there are footprints for various leaded and SMD inductors, at the bottom 2x3 pin headers can be used to dis-/connect the building block from the circuit with a jumper (inner two pins) and to measure the impedance in a four-point kelvin configuration (outer four pins). 2: Diodes part (see fig. 4.22) of the non-linear resistance. The anti-parallel diodes are located a the top, the parallel (middle) and serial resistor (bottom) are made of a universal resistor footprint where the resistance can be made of SMD or THT (through hole technology) resistors or can be set by a potentiometer. Furthermore, the universal resistor has the same 2x3 pin headers to dis-/connect and measure on the board. 3: INIC part of the non-linear resistance. The resistors R_{FB} and R_{INIC} are implemented as universal resistors, the circuitry to trim the OpAmp output offset can be set by two universal resistors or potentiometer (middle right). 4: Several SMD footprints for capacitive grounding, 5: Additional universal grounding resistor (not used), 6: Switches to ground the node (not used), CMOS analog switch (left), MOSFET driven relay (right), 7: BNC connectors for positive/negative power supply of the OpAmps, for power supply of the switches and for connecting several boards in series, 8: Inductive coupling identical to 1 to connect in a 2D lattice configuration. b): One node of the schematic. It is made of repeated building blocks and the connection are defined by labeling the pins of the circuit. The numbering corresponds to the blocks explained in a).

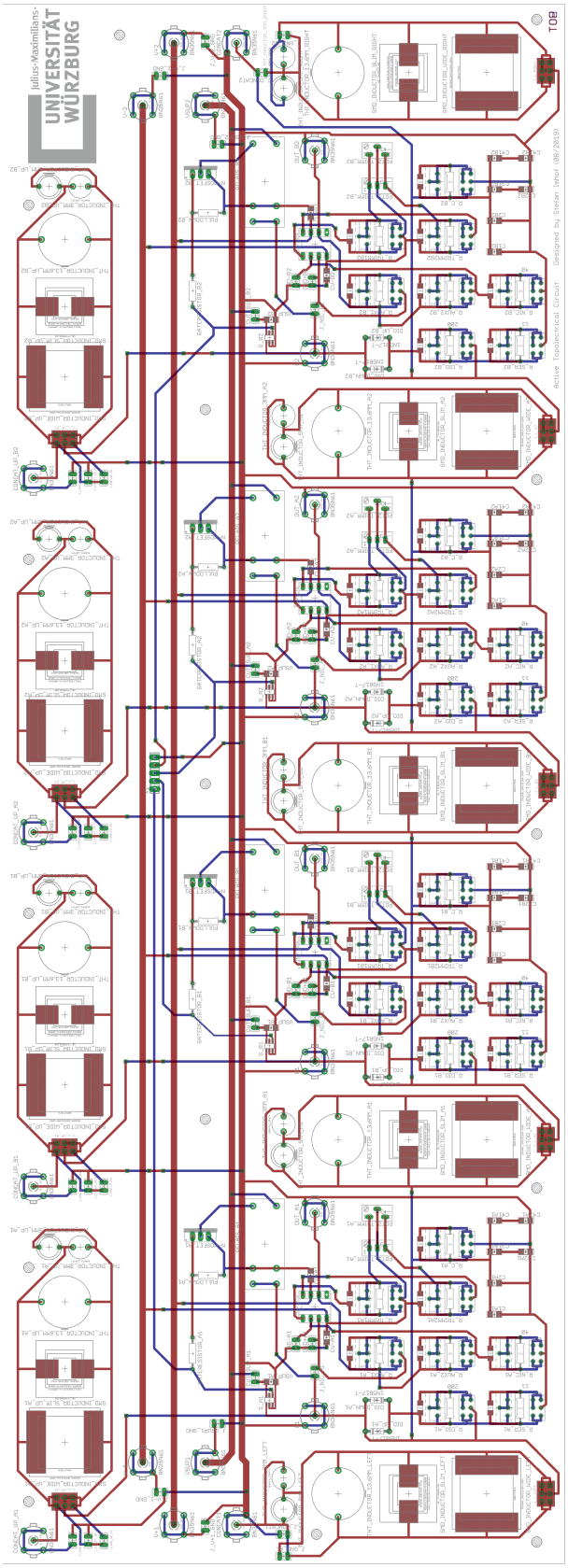

Figure A.6: Circuit board of the non-linear topological circuit (500 mm × 180 mm, FR4 1.55 mm, 70 µm copper). Four nodes (explained in detail in fig. A.5) are located at one circuit board. In the middle of the board between the supply lines a footprint for a screw terminal block is located to connect to computer-controlled hardware to control the switches (not used).

Circuit position	Component label	Specifications
Pin headers	WR-PHD 2.54 mm THT Dual Pin Header 6130XX21121 [80]	2.54 mm pitch, 3 A nominal current, 500 V AC maximum voltage, 20 mΩ max. contact resistance, 1 000 MΩ min. insulation resistance
L_1	Radial Lead Inductors 15152C [167]	Inductance $L = 1.5\,\mu\text{H} \pm 20\,\%$ at 10 kHz/0.1 V, range $1.368\,\mu\text{H} \pm 1\,\%$ pre-characterized at 89.4 kHz, DC resistance $R_{DC_{max}} = 3.48\,\text{m}\Omega$, max. DC current $I_{\text{DC,max}} = 14.9\,\text{A}$
L_2	Radial Lead RF Choke RL187-471J-RC [168]	Inductance $L = 10\,\mu\text{H} \pm 470\,\%$ at 796 kHz, $432.5\,\mu\text{H} \pm 1\,\%$ pre-characterized at 89.4 kHz, DC resistance $R_{DC} = 4.0\,\Omega$, max. DC current $I_{\text{DC,max}} = 0.2\,\text{A}$
C	MLCC C1206C104F3GACTU [154]	Capacity $C = 100\,\text{nF} \pm 1\,\%$, nominal DC voltage: 25 V, dielectric: C0G (NP0), case code: 1206
Nulling potentiometer	Trimmer Resistor 3296W-1-502LF [155]	Resistance $R = 5\,\text{k}\Omega \pm 10\,\%$, number of turns: 25, power rating: 500 mW
R_{ser}	Metal Film Resistor YR1B11RCC [169]	Resistance $R = 11\,\Omega \pm 0.1\,\%$, power rating: 0.25 W, temperature coefficient: 15 ppm/K
R_{par}	Metal Film Resistor YR1B40R2CC [170]	Resistance $R = 40.2\,\Omega \pm 0.1\,\%$, power rating: 0.25 W, temperature coefficient: 15 ppm/K
R_{INIC}	Metal Film Resistor YR1B200RCC [171]	Resistance $R = 200\,\Omega \pm 0.1\,\%$, power rating: 0.25 W, temperature coefficient: 15 ppm/K
R_{FB}	Metal Film Resistor CMF55500R00FEBF [172]	Resistance $R = 500\,\Omega \pm 1\,\%$, power rating: 0.25 W, temperature coefficient: 25 ppm/K
INIC	LT1363 Operational Amplifier [105]	Gain bandwidth: 70 MHz , slew rate: 1 000 V/µs, maximum supply current: 7.5 mA, unity-gain stable
Diode	Schottky Diode 1N5817 [173]	Average forward current 1 A, maximum forward voltage 450 mV, case: DO-41
Node connector	BNC straight low profile PCB socket 5-1634503-1 [82]	Impedance: 50 Ω, maximum frequency: 4 GHz

Table A.7: Parts list of the non-linear topological circuit.

Bibliography

[1] K. v. Klitzing, G. Dorda, and M. Pepper, *New method for High-Accuracy Determination of the Fine-Structure Constant Based on Quantized Hall Resistance*, Phys. Rev. Lett. **45** (1980), 494–497 https://link.aps.org/doi/10.1103/PhysRevLett.45.494.

[2] L. Landau, *Diamagnetismus der Metalle*, Zeitschrift für Physik **64** (1930), 629–637 https://doi.org/10.1007/BF01397213.

[3] D. J. Thouless, M. Kohmoto, M. P. Nightingale, and M. den Nijs, *Quantized Hall Conductance in a Two-Dimensional Periodic Potential*, Phys. Rev. Lett. **49** (1982), 405–408 https://link.aps.org/doi/10.1103/PhysRevLett.49.405.

[4] M. Born and V. Fock, *Beweis des Adiabatensatzes*, Zeitschrift für Physik **51** (1929), 165–180 https://doi.org/10.1007/BF01343193.

[5] M. V. Berry, *Quantal phase factors accompanying adiabatic changes*, Proceedings of the Royal Society of London. A. Mathematical and Physical Sciences **392** (1984), no. 1802, 45–57 https://royalsocietypublishing.org/doi/abs/10.1098/rspa.1984.0023.

[6] D. C. Tsui, H. L. Stormer, and A. C. Gossard, *Two-Dimensional Magnetotransport in the Extreme Quantum Limit*, Phys. Rev. Lett. **48** (1982), 1559–1562 https://link.aps.org/doi/10.1103/PhysRevLett.48.1559.

[7] R. B. Laughlin, *Anomalous Quantum Hall Effect: An Incompressible Quantum Fluid with Fractionally Charged Excitations*, Phys. Rev. Lett. **50** (1983), 1395–1398 https://link.aps.org/doi/10.1103/PhysRevLett.50.1395.

[8] F. D. M. Haldane, *Fractional Quantization of the Hall Effect: A Hierarchy of Incompressible Quantum Fluid States*, Phys. Rev. Lett. **51** (1983), 605–608 https://link.aps.org/doi/10.1103/PhysRevLett.51.605.

[9] Daniel Arovas, J. R. Schrieffer, and Frank Wilczek, *Fractional Statistics and the Quantum Hall Effect*, Phys. Rev. Lett. **53** (1984), 722–723 https://link.aps.org/doi/10.1103/PhysRevLett.53.722.

[10] F. D. M. Haldane, *Model for a Quantum Hall Effect without Landau Levels: Condensed-Matter Realization of the "Parity Anomaly"*, Phys. Rev. Lett. **61** (1988), 2015–2018 https://link.aps.org/doi/10.1103/PhysRevLett.61.2015.

[11] C.-Z. Chang et al., *Experimental Observation of the Quantum Anomalous Hall Effect in a Magnetic Topological Insulator*, Science **340** (2013), no. 6129, 167–170 http://science.sciencemag.org/content/340/6129/167.

[12] C. L. Kane and E. J. Mele, *Quantum Spin Hall Effect in Graphene*, Phys. Rev. Lett. **95** (2005), 226801 https://link.aps.org/doi/10.1103/PhysRevLett.95.226801.

[13] B. A. Bernevig and S.-C. Zhang, *Quantum spin hall effect*, Phys. Rev. Lett. **96** (2006), 106802 https://link.aps.org/doi/10.1103/PhysRevLett.96.106802.

[14] M. König et al., *Quantum Spin Hall Insulator State in HgTe Quantum Wells*, Science **318** (2007), no. 5851, 766–770 http://science.sciencemag.org/content/318/5851/766.

[15] M. Z. Hasan and C. L. Kane, *Colloquium: Topological insulators*, Rev. Mod. Phys. **82** (2010), 3045–3067
https://link.aps.org/doi/10.1103/RevModPhys.82.3045.

[16] B. A. Bernevig and T. L. Hughes, *Topological insulators and topological superconductors*, Princeton University Press, 2013.

[17] Wenchao Tian, Wenbo Yu, Jing Shi, and Yongkun Wang, *The property, preparation and application of topological insulators: a review*, Materials **10** (2017), no. 7, 814.

[18] S. A. Wolf, A. Y. Chtchelkanova, and D. M. Treger, *Spintronics - A retrospective and perspective*, IBM journal of research and development **50** (2006), no. 1, 101–110.

[19] M. He, H. Sun, and Q. L. He, *Topological insulator: Spintronics and quantum computations*, Frontiers of Physics **14** (2019), no. 4, 1–16.

[20] F. D. M. Haldane and S. Raghu, *Possible realization of directional optical waveguides in photonic crystals with broken time-reversal symmetry*, Physical review letters **100** (2008), no. 1, 013904.

[21] L. Lu, J. D. Joannopoulos, and M. Soljačić, *Topological photonics*, Nature photonics **8** (2014), no. 11, 821–829.

[22] T. Ozawa et al., *Topological photonics*, Reviews of Modern Physics **91** (2019), no. 1, 015006.

[23] A. B. Khanikaev and G. Shvets, *Two-dimensional topological photonics*, Nature photonics **11** (2017), no. 12, 763–773.

[24] D. Smirnova, D. Leykam, Y. Chong, and Y. Kivshar, *Nonlinear topological photonics*, Applied Physics Reviews **7** (2020), no. 2, 021306.

[25] Y. Ota et al., *Active topological photonics*, Nanophotonics **9** (2020), no. 3, 547–567.

[26] M. Hafezi, E. A. Demler, M. D. Lukin, and J. M. Taylor, *Robust optical delay lines with topological protection*, Nature Physics **7** (2011), no. 11, 907–912.

[27] Z. Yu and S. Fan, *Complete optical isolation created by indirect interband photonic transitions*, Nature photonics **3** (2009), no. 2, 91–94.

[28] M. A. Bandres et al., *Topological insulator laser: Experiments*, Science **359** (2018), no. 6381, eaar4005.

[29] G. Harari et al., *Topological insulator laser: theory*, Science **359** (2018), no. 6381, eaar4003.

[30] I. Bloch, J. Dalibard, and W. Zwerger, *Many-body physics with ultracold gases*, Reviews of modern physics **80** (2008), no. 3, 885.

[31] N. Goldman, J. C. Budich, and P. Zoller, *Topological quantum matter with ultracold gases in optical lattices*, Nature Physics **12** (2016), no. 7, 639–645.

[32] Y.-J. Lin et al., *Synthetic magnetic fields for ultracold neutral atoms*, Nature **462** (2009), no. 7273, 628–632.

[33] N. R. Cooper, J. Dalibard, and I. B. Spielman, *Topological bands for ultracold atoms*, Reviews of modern physics **91** (2019), no. 1, 015005.

[34] Zhaoju Yang et al., *Topological acoustics*, Physical review letters **114** (2015), no. 11, 114301.

[35] A. B. Khanikaev, R. Fleury, S. H. Mousavi, and A. Alu, *Topologically robust sound propagation in an angular-momentum-biased graphene-like resonator lattice*, Nature communications **6** (2015), no. 1, 1–7.

[36] E. Prodan and C. Prodan, *Topological phonon modes and their role in dynamic instability of microtubules*, Physical review letters **103** (2009), no. 24, 248101.

[37] C. L. Kane and T. C. Lubensky, *Topological boundary modes in isostatic lattices*, Nature Physics **10** (2014), no. 1, 39–45.

[38] R. Süsstrunk and S. D. Huber, *Observation of phononic helical edge states in a mechanical topological insulator*, Science **349** (2015), no. 6243, 47–50.

[39] S. D. Huber, *Topological mechanics*, Nature Physics **12** (2016), no. 7, 621–623.

[40] K. Bertoldi, V. Vitelli, J. Christensen, and M. Van Hecke, *Flexible mechanical metamaterials*, Nature Reviews Materials **2** (2017), no. 11, 1–11.

[41] T. Karzig, C.-E. Bardyn, N. H. Lindner, and G. Refael, *Topological polaritons*, Physical Review X **5** (2015), no. 3, 031001.

[42] S. Klembt et al., *Exciton-polariton topological insulator*, Nature **562** (2018), no. 7728, 552–556.

[43] Y. V. Kartashov and D. V. Skryabin, *Two-dimensional topological polariton laser*, Physical review letters **122** (2019), no. 8, 083902.

[44] M. D. Schroer et al., *Measuring a topological transition in an artificial spin-1/2 system*, Physical review letters **113** (2014), no. 5, 050402.

[45] P. Roushan et al., *Observation of topological transitions in interacting quantum circuits*, Nature **515** (2014), no. 7526, 241–244.

[46] J. Ningyuan et al., *Time-and site-resolved dynamics in a topological circuit*, Physical Review X **5** (2015), no. 2, 021031.

[47] V. V. Albert, L. I. Glazman, and L. Jiang, *Topological properties of linear circuit lattices*, Physical review letters **114** (2015), no. 17, 173902.

[48] H. Eleuch and I. Rotter, *Resonances in open quantum systems*, Physical Review A **95** (2017), no. 2, 022117.

[49] Z. Lin et al., *Unidirectional invisibility induced by $\mathcal{PT}$-symmetric periodic structures*, Physical Review Letters **106** (2011), no. 21, 213901.

[50] S. Longhi, *$\mathcal{PT}$-symmetric laser absorber*, Physical Review A **82** (2010), no. 3, 031801.

[51] H. Hodaei et al., *Enhanced sensitivity at higher-order exceptional points*, Nature **548** (2017), no. 7666, 187–191.

[52] B. Peng et al., *Parity-time-symmetric whispering-gallery microcavities*, Nature Physics **10** (2014), no. 5, 394–398.

[53] A. Guo et al., *Observation of $\mathcal{PT}$-symmetry breaking in complex optical potentials*, Physical review letters **103** (2009), no. 9, 093902.

[54] T. Yoshida and Y. Hatsugai, *Exceptional rings protected by emergent symmetry for mechanical systems*, Physical Review B **100** (2019), no. 5, 054109.

[55] D. R. Nelson and N. M. Shnerb, *Non-hermitian localization and population biology*, Physical Review E **58** (1998), no. 2, 1383.

[56] G. Kerg et al., *Non-normal recurrent neural network (nnrnn): learning long time dependencies while improving expressivity with transient dynamics*, Advances in neural information processing systems **32** (2019).

[57] T. Hofmann et al., *Chiral Voltage Propagation and Calibration in a Topolectrical Chern Circuit*, Phys. Rev. Lett. **122** (2019), 247702 `https://link.aps.org/doi/10.1103/PhysRevLett.122.247702`.

[58] W. P. Su, J. R. Schrieffer, and A. J. Heeger, *Solitons in polyacetylene*, Phys. Rev. Lett. **42** (1979), 1698–1701 `https://link.aps.org/doi/10.1103/PhysRevLett.42.1698`.

[59] T. Helbig et al., *Band structure engineering and reconstruction in electric circuit networks*, Phys. Rev. B **99** (2019), 161114 `https://link.aps.org/doi/10.1103/PhysRevB.99.161114`.

[60] W. A. Benalcazar, B. A. Bernevig, and T. L. Hughes, *Quantized electric multipole insulators*, Science **357** (2017), no. 6346, 61–66
http://science.sciencemag.org/content/357/6346/61.

[61] S. Imhof et al., *Topolectrical-circuit realization of topological corner modes*, Nature Physics **14** (2018), no. 9, 925
https://www.nature.com/articles/s41567-018-0246-1.

[62] A. Stegmaier et al., *Topological Defect Engineering and $\mathcal{PT}$ Symmetry in Non-Hermitian Electrical Circuits*, Phys. Rev. Lett. **126** (2021), 215302
https://link.aps.org/doi/10.1103/PhysRevLett.126.215302.

[63] T. Helbig et al., *Generalized bulk-boundary correspondence in non-Hermitian topolectrical circuits*, Nat. Phys. **16** (2020), 747–750.

[64] Balth. Van der Pol, *LXXXVIII. On "relaxation-oscillations"*, The London, Edinburgh, and Dublin Philosophical Magazine and Journal of Science **2** (1926), no. 11, 978–992.

[65] T. Kotwal et al., *Active topolectrical circuits*, Proceedings of the National Academy of Sciences **118** (2021), no. 32
https://www.pnas.org/content/118/32/e2106411118.

[66] S. Imhof, *Topolectrics - Topologische Zustände in linearen elektrischen Schaltkreisen*, Master's Thesis, 2018. Julius-Maximilians-Universität Würzburg.

[67] Özgür Ergül, *Introduction to Electrical Circuit Analysis*, John Wiley and Sons Ltd, 2017.

[68] C. H. Lee et al., *Topolectrical circuits*, Communications Physics **1** (2018), no. 1, 39
https://www.nature.com/articles/s42005-018-0035-2.

[69] T. Helbig, *Analysis of parity and time-reversal symmetric non-Hermitian physics in topolectrical circuits*, Master's Thesis, 2018. Julius-Maximilians-Universität Würzburg.

[70] T. Hofmann, *Topological States in Periodic Circuit Networks*, Master's Thesis, 2018. Julius-Maximilians-Universität Würzburg.

[71] A. Stegmaier, *Modeling Floquet Topological Insulators in Electrical Circuits*, Master's Thesis, 2019. Julius-Maximilians-Universität Würzburg.

[72] János K. Asbóth, László Oroszlány, and András Pályi, *A Short Course on Topological Insulators: Band Structure and Edge States in One andTwo Dimensions*, Springer International Publishing Switzerland, 2016.

[73] N. Batra and G. Sheet, *Physics with coffee and doughnuts*, Reson. **25** (2020), 765–786.

[74] R. E. Peierls, *Quantum theory of solids*, Clarendon Press, 1955.

[75] Zurich Instruments AG, *Principles of lock-in detection and the state of the art*, White Paper (2016).

[76] Stanford Research Systems, *About Lock-In Amplifiers*, Application Note #3
https://www.thinksrs.com/downloads/pdfs/applicationnotes/AboutLIAs.pdf.

[77] W.-K. Chen, *The Circuits and Filters Handbook: Passive, Active, and Digital filters*, Third Edition, CRC Press, Taylor & Francis Group, LLC, 2009.

[78] Keysight Technologies, *Impedance Measurement Handbook: A Guide to Measurement Technology and Techniques*, Application Note, 6th Edition.

[79] Würth Elektronik GmbH & Co. KG, *Website: WR-PHD 2.54 mm Dual Socket Header*
https://www.we-online.com/katalog/de/PHD_2_54_DUAL_SOCKET_HEADER_6130XX21821,
accessed: 14.06.2022

[80] ———, *Website: WR-PHD 2.54 mm THT Dual Pin Header*
https://www.we-online.com/katalog/de/PHD_2_54_THT_DUAL_PIN_HEADER_6130XX21121,
accessed: 14.06.2022

[81] Analog Devices Inc., *Data sheet:* 9.5 Ω R_{ON}*, 16-Channel, Differential 8-Channel,* ±*15 V/+12 V/*±*5 V iCMOS Multiplexers*
https://www.analog.com/media/en/technical-documentation/data-sheets/ADG1406_1407.pdf, accessed: 14.06.2022

[82] TE Connectivity, *Data sheet: BNC straight low profile PCB socket*
https://www.mouser.de/datasheet/2/418/7/ENG_CD_1634503_E-2014728.pdf, accessed: 14.06.2022

[83] Würth Elektronik GmbH & Co. KG, *Data sheet: PCB terminal block - MPT 0,5/12-2,54 - 1725753*
https://www.we-online.com/katalog/datasheet/690368171272.pdf, accessed: 14.06.2022

[84] Kingbright Electronic Co, Ltd, *Data sheet: APTD3216LCGCK 3.2 x 1.6 mm SMD Chip LED Lamp*
https://www.kingbrightusa.com/images/catalog/SPEC/APTD3216LCGCK.pdf, accessed: 14.06.2022

[85] Everlight Electronics Co., Ltd., *Data sheet: SMD - B 26-21/R6C-AR2T1LY/CA*
https://media.digikey.com/pdf/Data%20Sheets/Everlight%20PDFs/26-21-R6C-AR2T1LY-CA.pdf, accessed: 14.06.2022

[86] A. Kitaev, *Periodic table for topological insulators and superconductors*, AIP Conference Proceedings **1134** (2009), no. 1, 22–30
https://aip.scitation.org/doi/abs/10.1063/1.3149495.

[87] G. W. Semenoff, *Condensed-Matter Simulation of a Three-Dimensional Anomaly*, Phys. Rev. Lett. **53** (1984), 2449–2452
https://link.aps.org/doi/10.1103/PhysRevLett.53.2449.

[88] D. P. DiVincenzo and E. J. Mele, *Self-consistent effective-mass theory for intralayer screening in graphite intercalation compounds*, Phys. Rev. B **29** (1984), 1685–1694
https://link.aps.org/doi/10.1103/PhysRevB.29.1685.

[89] K. S. Novoselov et al., *Electric Field Effect in Atomically Thin Carbon Films*, Science **306** (2004), no. 5696, 666–669
https://www.science.org/doi/abs/10.1126/science.1102896.

[90] W. Jaskólski et al., *Edge states and flat bands in graphene nanoribbons with arbitrary geometries*, Phys. Rev. B **83** (2011), 235424
https://link.aps.org/doi/10.1103/PhysRevB.83.235424.

[91] D. J. Klein, *Graphitic polymer strips with edge states*, Chemical Physics Letters **217** (1994), no. 3, 261–265
https://www.sciencedirect.com/science/article/pii/0009261493E1378T.

[92] C. M. Bender and S. Boettcher, *Real Spectra in Non-Hermitian Hamiltonians Having* PT *Symmetry*, Phys. Rev. Lett. **80** (1998), 5243–5246
https://link.aps.org/doi/10.1103/PhysRevLett.80.5243.

[93] A. Mostafazadeh, *Pseudo-hermiticity versus* PT *symmetry: The necessary condition for the reality of the spectrum of a non-hermitian hamiltonian*, Journal of Mathematical Physics **43** (2002), no. 1, 205–214
https://doi.org/10.1063/1.1418246.

[94] Carl M. Bender et al., *PT Symmetry In Quantum and Classical Physics*, WORLD SCIENTIFIC (EUROPE), 2019.

[95] M.V. Berry, *Physics of nonhermitian degeneracies*, Czech. J. Phys. **54** (2004), 1039–1047
https://doi.org/10.1023/B:CJOP.0000044002.05657.04.

[96] W. D. Heiss, *The physics of exceptional points*, Journal of Physics A: Mathematical and Theoretical **45** (2012), no. 44, 444016
https://doi.org/10.1088/1751-8113/45/44/444016.

[97] C. Poli et al., *Selective enhancement of topologically induced interface states in a dielectric resonator chain*, Nat. Commun. **6** (2015), no. 1, 6710
https://doi.org/10.1038/ncomms7710.

[98] S. Weimann et al., *Topologically protected bound states in photonic parity–time-symmetric crystals*, Nature Mater. **16** (2017), no. 4, 433–438
https://doi.org/10.1038/nmat4811.

[99] L.-J. Lang, Y. Wang, H. Wang, and Y. D. Chong, *Effects of non-Hermiticity on Su-Schrieffer-Heeger defect states*, Phys. Rev. B **98** (2018), 094307
https://link.aps.org/doi/10.1103/PhysRevB.98.094307.

[100] C. H. Lee and R. Thomale, *Anatomy of skin modes and topology in non-hermitian systems*, Phys. Rev. B **99** (2019), 201103
https://link.aps.org/doi/10.1103/PhysRevB.99.201103.

[101] J. Zak, *Berry's phase for energy bands in solids*, Phys. Rev. Lett. **62** (1989), 2747–2750
https://link.aps.org/doi/10.1103/PhysRevLett.62.2747.

[102] S. Yao and Z. Wang, *Edge States and Topological Invariants of Non-Hermitian Systems*, Phys. Rev. Lett. **121** (2018), 086803
https://link.aps.org/doi/10.1103/PhysRevLett.121.086803.

[103] L. J. Peters, *Theory of Thermionic Vacuum Tube Circuits*, First Edition, McGraw-Hill Book Company, Inc., 1927.

[104] J. L. Merrill, *Theory of the negative impedance converter*, The Bell System Technical Journal **30** (1951), no. 1, 88–109.

[105] Analog Devices, Inc., *Data sheet: LT1363* 70 MHz, 1 000 V/µs *OpAmp*
https://www.analog.com/media/en/technical-documentation/data-sheets/1363fa.pdf,
accessed: 14.06.2022

[106] R. B. Laughlin, *Quantized Hall conductivity in two dimensions*, Phys. Rev. B **23** (1981), 5632–5633
https://link.aps.org/doi/10.1103/PhysRevB.23.5632.

[107] S. Longhi, *Nonadiabatic robust excitation transfer assisted by an imaginary gauge field*, Phys. Rev. A **95** (2017), 062122
https://link.aps.org/doi/10.1103/PhysRevA.95.062122.

[108] N. Hatano and D. R. Nelson, *Localization Transitions in Non-Hermitian Quantum Mechanics*, Phys. Rev. Lett. **77** (1996), 570–573
https://link.aps.org/doi/10.1103/PhysRevLett.77.570.

[109] Y. Xiong, *Why does bulk boundary correspondence fail in some non-hermitian topological models*, Journal of Physics Communications **2** (2018), no. 3, 035043
https://doi.org/10.1088/2399-6528/aab64a.

[110] M. P. Kennedy, *Experimental chaos from autonomous electronic circuits*, Philosophical Transactions of the Royal Society of London. Series A: Physical and Engineering Sciences **353** (1995), no. 1701, 13–32.

[111] B. B. Johnson, S. V. Dhople, A. O. Hamadeh, and P. T. Krein, *Synchronization of nonlinear oscillators in an LTI electrical power network*, IEEE Transactions on Circuits and Systems I: Regular Papers **61** (2014), no. 3, 834–844.

[112] S. H. Strogatz, *Nonlinear Dynamics and Chaos*, Perseus Books, 1994.

[113] D.W. Jordan and P. Smith, *Nonlinear Ordinary Differential Equations: An introduction for Scientists and Engineers*, Fourth Edition, Oxford University Press, 2007.

[114] V. A. Makarov, E. del Río, W. Ebeling, and M. G. Velarde, *Dissipative Toda-Rayleigh lattice and its oscillatory modes*, Phys. Rev. E **64** (2001), 036601
https://link.aps.org/doi/10.1103/PhysRevE.64.036601.

[115] G.-Q. Zhong, *Implementation of Chua's circuit with a cubic nonlinearity*, IEEE Transactions on Circuits and Systems I: Fundamental Theory and Applications **41** (1994), no. 12, 934–941.

[116] D. W. Storti and R. H. Rand, *Dynamics of two strongly coupled relaxation oscillators*, SIAM Journal on Applied Mathematics **46** (1986), no. 1, 56–67 http://www.jstor.org/stable/2101487.

[117] E Del Rio, VA Makarov, MG Velarde, and W Ebeling, *Mode transitions and wave propagation in a driven-dissipative toda-rayleigh ring*, Physical Review E **67** (2003), no. 5, 056208.

[118] F. G. Woodhouse, H. Ronellenfitsch, and J. Dunkel, *Autonomous actuation of zero modes in mechanical networks far from equilibrium*, Physical Review Letters **121** (2018), no. 17, 178001.

[119] A. Forrow, F. G. Woodhouse, and J. Dunkel, *Mode selection in compressible active flow networks*, Physical Review Letters **119** (2017), no. 2, 028102.

[120] H. Ronellenfitsch and J. Dunkel, *Spectral design of active mechanical and electrical metamaterials*, 2020 fourteenth international congress on artificial materials for novel wave phenomena (metamaterials), 2020, pp. 270–272.

[121] H. Ronellenfitsch et al., *Inverse design of discrete mechanical metamaterials*, Physical Review Materials **3** (2019), no. 9, 095201.

[122] J. W. S. Rayleigh, *The Theory of Sound, Dover Publications*, New York **344** (1945).

[123] S. Weidemann et al., *Topological funneling of light*, Science **368** (2020), no. 6488, 311–314.

[124] A. Regensburger et al., *Parity-time synthetic photonic lattices*, Nature **488** (2012), no. 167 https://www.nature.com/articles/nature11298.

[125] H. Ramezani et al., *Bypassing the bandwidth theorem with $\mathcal{PT}$ symmetry*, Physical Review A **85** (2012), no. 6, 062122.

[126] M. Kremer et al., *Demonstration of a two-dimensional $\mathcal{PT}$-symmetric crystal*, Nature communications **10** (2019), no. 1, 1–7.

[127] M. Brandenbourger, X. Locsin, E. Lerner, and C. Coulais, *Non-reciprocal robotic metamaterials*, Nature communications **10** (2019), no. 1, 1–8.

[128] E. Del Rio, V. A. Makarov, M. G. Velarde, and W. Ebeling, *Mode transitions and wave propagation in a driven-dissipative Toda-Rayleigh ring*, Physical Review E **67** (2003), no. 5, 056208.

[129] R. Haenel, T. Branch, and M. Franz, *Chern insulators for electromagnetic waves in electrical circuit networks*, Physical Review B **99** (2019), no. 23, 235110.

[130] M. Ezawa, *Electric circuits for non-Hermitian Chern insulators*, Physical Review B **100** (2019), no. 8, 081401.

[131] Y. Yang, D. Zhu, Z. H. Hang, and Y. D. Chong, *Observation of antichiral edge states in a circuit lattice*, Science China Physics, Mechanics & Astronomy **64** (2021), no. 5, 1–7.

[132] C. W. Peterson, W. A. Benalcazar, T. L. Hughes, and G. Bahl, *A quantized microwave quadrupole insulator with topologically protected corner states*, Nature **555** (2018), no. 7696, 346–350.

[133] M. Ezawa, *Higher-order topological electric circuits and topological corner resonance on the breathing kagome and pyrochlore lattices*, Physical Review B **98** (2018), no. 20, 201402.

[134] J. Bao et al., *Topoelectrical circuit octupole insulator with topologically protected corner states*, Physical Review B **100** (2019), no. 20, 201406.

[135] K. Luo, R. Yu, and H. Weng, *Topological nodal states in circuit lattice*, Research **2018** (2018).

[136] Y. Lu et al., *Probing the Berry curvature and Fermi arcs of a Weyl circuit*, Physical Review B **99** (2019), no. 2, 020302.

[137] C. H. Lee et al., *Imaging nodal knots in momentum space through topolectrical circuits*, Nature communications **11** (2020), no. 1, 1–13.

[138] S. M. Rafi-Ul-Islam, Z. B. Siu, C. Sun, and M. B. A. Jalil, *Strain-controlled current switching in Weyl semimetals*, Physical Review Applied **14** (2020), no. 3, 034007.

[139] Y. Wang, H. M. Price, B. Zhang, and Y. D. Chong, *Circuit implementation of a four-dimensional topological insulator*, Nature communications **11** (2020), no. 1, 1–7.

[140] H. Jiang et al., *Interplay of non-Hermitian skin effects and Anderson localization in nonreciprocal quasiperiodic lattices*, Physical Review B **100** (2019), no. 5, 054301.

[141] T. others Hofmann, *Reciprocal skin effect and its realization in a topolectrical circuit*, Physical Review Research **2** (2020), no. 2, 023265.

[142] X.-X. Zhang and M. Franz, *Non-Hermitian exceptional Landau quantization in electric circuits*, Physical Review Letters **124** (2020), no. 4, 046401.

[143] T. Yoshida, T. Mizoguchi, and Y. Hatsugai, *Mirror skin effect and its electric circuit simulation*, Physical Review Research **2** (2020), no. 2, 022062.

[144] L. Li, C. H. Lee, and J. Gong, *Impurity induced scale-free localization*, Communications Physics **4** (2021), no. 1, 1–9.

[145] N. H. Lindner, G. Refael, and V. Galitski, *Floquet topological insulator in semiconductor quantum wells*, Nature Physics **7** (2011), no. 6, 490–495.

[146] M. C. Rechtsman et al., *Photonic Floquet topological insulators*, Nature **496** (2013), no. 7444, 196–200.

[147] J. M. T. Thompson, H. B. Stewart, and R. Turner, *Nonlinear dynamics and chaos*, Computers in Physics **4** (1990), no. 5, 562–563.

[148] L. A. Aguirre and C. Letellier, *Modeling nonlinear dynamics and chaos: a review*, Mathematical Problems in Engineering **2009** (2009).

[149] E. Afshari and A. Hajimiri, *Nonlinear transmission lines for pulse shaping in silicon*, IEEE Journal of Solid-State Circuits **40** (2005), no. 3, 744–752.

[150] M. Ezawa, *Nonlinear Anderson localization in Toda lattices*, Journal of the Physical Society of Japan **90** (2021), no. 10, 104704.

[151] I. Boettcher et al., *Crystallography of hyperbolic lattices*, Physical Review B **105** (2022), no. 12, 125118.

[152] P. M. Lenggenhager et al., *Electric-circuit realization of a hyperbolic drum*, arXiv preprint arXiv:2109.01148 (2021).

[153] Würth Elektronik GmbH & Co. KG, *Data sheet: WE-HCI SMD Flat Wire High Current Inductor* `http://katalog.we-online.de/pbs/datasheet/74435561100.pdf`, accessed: 14.06.2022

[154] KEMET Corporation, *Data sheet: Surface Mount Multilayer Ceramic Chip Capacitors (SMD MLCCs) C0G Dielectric, 10 - 250 VDC (Commercial Grade)* `https://www.mouser.de/datasheet/2/212/KEM_C1003_C0G_SMD-1101588.pdf`, accessed: 14.06.2022

[155] Bourns, Inc., *Data sheet: 3296 - 3/8" Square Trimpot Trimming Potentiometer* `https://www.mouser.de/datasheet/2/54/3296-776415.pdf`, accessed: 14.06.2022

[156] Vishay Intertechnology, Inc., *Data sheet: Metal Film Resistors, Industrial Power, Precision, Flameproof* `https://www.mouser.de/datasheet/2/427/VISHS74561_1-2566210.pdf`, accessed: 14.06.2022

[157] ———, *Data sheet: Metal Film Resistors, Axial, Industrial, Precision* `https://www.mouser.de/datasheet/2/427/cmfind-1762971.pdf`, accessed: 14.06.2022

[158] Bourns, Inc., *Data sheet: SRP1770TA Series - Shielded Power Inductors* `https://www.mouser.de/datasheet/2/54/srp1770ta-1391594.pdf`, accessed: 14.06.2022

[159] KEMET Corporation, *Data sheet: Surface Mount Multilayer Ceramic Chip Capacitors (SMD MLCCs) ESD, C0G Dielectric, 25 - 250 VDC (Commercial & Automotive Grade)* https://www.mouser.de/datasheet/2/212/1/KEM_C1091_C0G_ESD-1140493.pdf, accessed: 14.06.2022

[160] TE Connectivity Ltd., *Data sheet:Precision Metal Film Fixed Resistors Type R Series* https://www.mouser.de/datasheet/2/418/4/NG_DS_1773265_A-722114.pdf, accessed: 14.06.2022

[161] PHOENIX CONTACT GmbH & Co. KG, *Data sheet: PCB terminal block - MPT 0,5/12-2,54 - 1725753* https://www.mouser.de/datasheet/2/324/4/1725753-1437518.pdf, accessed: 14.06.2022

[162] YAGEO Group, *Data sheet: THIN FILM CHIP RESISTORS, High precision - high stability, RT series* https://www.mouser.de/datasheet/2/447/PYu_RT_1_to_0_01_RoHS_L_11-1669912.pdf, accessed: 14.06.2022

[163] Vishay Intertechnology, Inc., *Data sheet: Standard Thick Film Chip Resistors* https://www.mouser.de/datasheet/2/427/dcrcwe3-1762152.pdf, accessed: 14.06.2022

[164] Stackpole Electronics, Inc., *Data sheet: RMCF / RMCP Series, General Purpose Thick Film Standard Power and High-Power Chip Resistor* https://www.seielect.com/catalog/sei-rmcf_rmcp.pdf, accessed: 14.06.2022

[165] Panasonic Corporation, *Data sheet: Metal Film (Thin Film) Chip Resistors, High Reliability Type* https://www.mouser.de/datasheet/2/315/AOA0000C307-1149632.pdf, accessed: 14.06.2022

[166] Texas Instruments Incorporated., *Data sheet: MUX36xxx 36-V, Low-Capacitance, Low-Leakage-Current, Precision Analog Multiplexers* https://www.ti.com/lit/gpn/mux36s16, accessed: 14.06.2022

[167] Murata Manufacturing Co., Ltd., *Data sheet: 1500 Series Radial Lead Inductors* https://www.mouser.de/datasheet/2/281/kmp_1500-46227.pdf, accessed: 14.06.2022

[168] Bourns, Inc., *Data sheet: RL187 Series - Radial Lead RF Choke* https://www.mouser.de/datasheet/2/54/RL187_series-777829.pdf, accessed: 14.06.2022

[169] TE Connectivity, *Data sheet: Precision Metal Film Fixed Resistors* https://www.mouser.de/datasheet/2/418/4/NG_DS_1773265_A-731863.pdf, accessed: 14.06.2022

[170] ———, *Data sheet: Precision Metal Film Fixed Resistors* https://www.mouser.de/datasheet/2/418/4/NG_DS_1773265_A-731968.pdf, accessed: 14.06.2022

[171] ———, *Data sheet: Precision Metal Film Fixed Resistors* https://www.mouser.de/datasheet/2/418/4/NG_DS_1773265_A-721213.pdf, accessed: 14.06.2022

[172] Vishay Intertechnology, Inc., *Data sheet: Metal Film Resistors, Axial, Industrial, Precision* https://www.mouser.de/datasheet/2/427/cmfind-1762971.pdf, accessed: 14.06.2022

[173] STMicroelectronics N.V., *Data sheet: 1N5817, 1N5818, 1N5819 Low drop power Schottky rectifier* https://www.mouser.de/datasheet/2/389/cd00001625-1795544.pdf, accessed: 14.06.2022

Acknowledgements

In the most cases a single person's work on such a fast moving research topic as topological metamaterials would be lost in the flood of novel scientific findings, if not supported by a broadly based but closely interconnected team. Therefore, I would like to thank everybody who became part of this team on our way to establish the topolectrical circuit platform in the scientific landscape:

My work on this project would not have been possible without the initiating ideas of Prof. Dr. Ching Hua Lee and Prof. Dr. Ronny Thomale and the willingness of Dr. Tobias Kießling, my supervisor, to invest a lot of time and manpower for the experimental investigation.
Next, I want to thank all people of the chair of Theoretical Physics 1 that have been involved in projects on topolectrical circuits, namely Tobias Helbig, Prof. Dr. Martin Greiter, Alexander Stegmaier, Dr. Lavi Upreti, Hendrik Hohmann, Alexander Fritzsche and Tobias Hofmann, to whom I would like to give special thanks due to his tireless efforts on discussing and proofreading this thesis.
Of course I also want to thank my colleagues from the Kießling group, especially Christian Berger, for his dedicated support to get the first projects off the ground quickly, Florian Bayer for technical introduction into circuit board design and measurement automation, Johannes Brehm for highly professional procurement of the best tools and every kind of circuit component, Vladimir Marković for providing skilled craftsmanship and superior working atmosphere and Hauke Brand for working full-time on the topolectrical circuits and taking over the processing of future projects.
In this context I further thank all members of the chair of Experimental Physics 3 who supported the Toplectrics project, first and foremost Dr. Mohamed Abdelghany for contributing his expertise in electrical engineering and chair holder Prof. Dr. Laurens Molenkamp for financial and technical support.
Furthermore, I am very grateful to all the research groups around the world who collaborated with us on various projects, namely Prof. Dr. Titus Neupert and his team at the University of Zurich, the group of Prof. Dr. Alexander Szameit at the Univerity of Rostock, Prof. Dr. Jörn Dunkel and his collaborators at the Massachusetts Institute of Technology and all groups of the Würzburg-Dresden ct.qmat Cluster of Excellence, which provided fruitful ideas and discussions.

Last but not least I wholeheartedly thank my girlfriend Jana for five years of long-distance relationship waiting for me to finish my academic education and my parents who taught me diligence, curiosity and perfectionism and also supported me financially and spatially even when I spontaneously decided to set up the laboratory at home during the COVID-19 pandemic. Special thanks also go to my brother-in-law Özkan, who provided his excellent English skills for the final proofreading of this thesis.